

TECHNISCHE UNIVERSITÄT MÜNCHEN

LEHRSTUHL FÜR FLUIDMECHANIK

FACHGEBIET GASDYNAMIK

**Compressible Dynamics of Cavitating
3-D Multi-Phase Flows**

İsmail Hakkı Sezal

Vollständiger Abdruck der von der Fakultät für Maschinenwesen der Technischen Universität München zur Erlangung des akademischen Grades eines

Doktor-Ingenieurs

genehmigten Dissertation.

Vorsitzender: Univ.-Prof. Dr.-Ing. habil. R. Schilling

Prüfer der Dissertation:

1. Univ.-Prof. Dr.-Ing. habil. G.H. Schnerr
2. Univ.-Prof. Dr.-Ing. habil. N.A. Adams

Die Dissertation wurde am 03.03.2009 bei der Technischen Universität München eingereicht und durch die Fakultät für Maschinenwesen am 24.06.2009 angenommen.

Acknowledgements

This Ph.D. thesis is the outcome of my research concluded at the *Fachgebiet Gasdynamik* of *Lehrstuhl für Fluidmechanik* at the *Technische Universität München*. During my employment at the university from 2004 until April 2008 and after I left my assistantship position many people have contributed in the work presented here and supported me throughout these years, whom I would like to address here.

First of all I want to express my sincere thanks to my supervisor, Prof. Dr.-Ing. habil. G.H. Schnerr for his guidance, insight and patience throughout this study. I shall also state my deepest appreciation and admiration about his exceptional enthusiasm and interest in my work. Our fruitful discussions on the subject made enormous contributions to this thesis.

Deepest gratitude are also due to the members of the examination committee; Prof. Dr.-Ing. habil. R. Schilling has willingly accepted the chairperson position and Prof. Dr.-Ing. habil. N.A. Adams has acted as my co-examiner with a great interest in the subject.

Next I would like to mention our remarkable team at the *Fachgebiet Gasdynamik* that I miss even today. In particular, my good old roommate and friend Steffen Schmidt; more than four years we shared not only the same office but most of the time the same challenges both at work and outside. His excellent knowledge in mathematics helped us a lot to build our scheme and understand the underlying theory in numerics. He was also always on my side and calmed all of us at the most needed and stressful times during the past years. Without his help this work could never have been completed. Thank you Steffen, I owe you so much! Then comes my good friend and colleague Nisar Al-Hasan; as soon as he joined our group we instantly started to work together and supported each other almost on everything. He was always the first person that I consulted whenever I needed assistance on any technical or official complication. Moreover, we shared lots of common interest that made us good friends. His driving force and encouragements helped me a lot to finish my thesis.

I also had the pleasure to work with Matthias Thalhamer and Marcus Giglmaier during their student theses. Matze parallelized our code and handled all the technical details to use the LRZ clusters. He also worked intensively on visualization efforts and processed huge amount of data, including the wonderful cover picture used in this thesis. Marcus helped us a lot in preparing the workshops and also printed my endless draft versions without any complaints.

Many thanks go to my colleagues at the Aerothermal Technologies Laboratory in GE Global Research - Europe; my former lab manager Dr.-Ing. Michael B. Schmitz has always supported and encouraged me to finish my thesis. Further thanks go to my

teammates and project leaders Dr. Alexander Simpson and Dr. Christian Aalburg, they were extremely understanding and helpful in all the matters related to both thesis and work. I would also like to mention my roommate Rodrigo Rodriguez-Erdmenger for his willingness to help on everything and our discussions on many subjects.

I am also grateful to KSB foundation, Stuttgart, who supported this project and financed it.

Finally, I would like to thank my family and my Meltem, for their invaluable patience, trust and encouragement during this thesis. They never stop believing in me even the times I have lost my confidence and hope.

Munich, August 2009

İsmail H. Sezal

Contents

Nomenclature	V
Abstract	IX
Zusammenfassung	XI
1 Introduction	1
1.1 Background	1
1.2 Motivation	1
1.2.1 Fluid Compressibility	2
1.2.2 Cavitation Phenomenon	4
1.2.2.1 Cavitation Types	6
1.2.2.2 Collapse Dynamics of Cavitation Bubbles	7
1.3 Numerical Motivation	9
1.4 Literature Overview	11
1.4.1 Theoretical Studies	11
1.4.2 Experimental Studies	12
1.4.3 Numerical Studies	17
1.5 Thesis Overview	19
2 Physical Model	21
2.1 Equilibrium vs. Non-equilibrium Processes	21
2.1.1 Flows with Non-equilibrium Effects	21
2.1.2 Vapor-liquid Equilibria	30
2.2 Effect of Molecular Viscosity and Turbulence	34
2.3 Governing Equations	36
2.3.1 Differential Form of the Equations	37
2.3.2 Integral Form of the Equations	38

2.4	Equilibrium Two-phase Model	40
2.4.1	Relaxation Time in Cavitating Flows	41
2.4.2	Integral Average Formulation	42
2.5	Equation of State and Speed of Sound	44
3	Numerical Method	55
3.1	Governing Equations	55
3.2	Geometry Definition	56
3.3	Convective Flux calculation	58
3.3.1	Riemann Problem	58
3.3.2	The HLLC Riemann solver	60
3.3.3	The AUSM Family of Methods	62
3.3.4	The Low Mach Number Problem	63
3.3.5	Modification for Liquid Flows - Hybrid Formulation	64
3.4	Higher Order Reconstruction	65
3.5	Time Integration	67
3.5.1	1st Order Time Integration	67
3.5.2	4-Stage Runge-Kutta Method	68
3.5.3	Time Step Calculation	69
3.6	Initial and Boundary Conditions	70
3.6.1	Initial Conditions	70
3.6.2	Boundary Conditions	71
3.6.2.1	Solid Walls	71
3.6.2.2	Periodic Boundaries	72
3.6.2.3	Inlet and Outlet Boundaries	73
4	Validation	77
4.1	1-D Shock Tube	77
4.1.1	Ideal Gas	77
4.1.2	Liquid Water	82
4.2	3-D Bubble Collapse	87
4.3	Discretization and Mesh Dependence of the Cavitation Regions	92
4.4	Validation Summary	96

5	Results and Discussion	97
5.1	Injection Nozzles	97
5.1.1	2-D Plane Injection Nozzle	98
5.1.1.1	Symmetry Break-up of the Flow Field	100
5.1.1.2	Cavitation Cycle	106
5.1.2	3-D Injection Nozzle with Swirl	109
5.1.3	3-D Injection Nozzle with Swirl and Divergence	114
5.1.4	3-D Multi-hole Injection Nozzle	118
5.2	Hydraulic Machinery	123
5.2.1	2-D NACA 0015 Hydrofoil	123
5.2.2	3-D NACA 0009 Twisted Wing - Half Wing Calculation	135
5.2.3	3-D NACA 0009 Twisted Wing - Full Wing Calculation	145
6	Conclusions	161
6.1	Summary	161
6.2	Recommendations for Further Development	162
	References	165
A	Physical Constants and Relations	175
A.1	Saturation Variables	175
A.2	Liquid and Gas Constants	176
B	Viscous Flow Formulation	179
B.1	Navier-Stokes Equations	179
B.2	Favre Averaged Navier-Stokes Equations	180
B.3	Single-phase Turbulence Modeling	184
B.3.1	Wilcox k - ω Model	184
B.4	Numerical Formulation	185
B.4.1	Nondimensionalization of the Variables	185
B.4.2	Governing Equations with k - ω Turbulence Model	186
B.4.3	Discussion about Two-phase Turbulence Modeling	187
B.4.4	Diffusive Flux Calculation	188
B.4.5	Boundary Conditions	189
B.5	Test Case Calculations for Single-phase Ideal Gas Flows	190
B.5.1	Laminar Flat Plate	190

B.5.2	Turbulent Flat Plate	191
B.5.3	RAE 2822 Airfoil	192
B.6	Outlook	194
C	CATUM Manual	195
C.1	Single-phase Inviscid Ideal Gas Calculation	200
C.2	Single-phase Inviscid Liquid Water Calculation	202
C.3	Two-phase Cavitating Hydrofoil Calculation	204

Nomenclature

Latin Symbols

c	$[m/s]$	Speed of sound
c	$[m]$	Chord length
c_e	$[m/s]$	Equilibrium speed of sound
c_f	$[-]$	Skin friction coefficient
c_D	$[-]$	Drag coefficient
$c_{D,p}$	$[-]$	Pressure drag coefficient
c_L	$[-]$	Lift coefficient
c_p	$[-]$	Pressure coefficient
c_p	$[J/kg \cdot K]$	Specific heat at constant pressure
c_v	$[J/kg \cdot K]$	Specific heat at constant volume
CFL	$[-]$	Courant-Friedrichs-Lewy number
e	$[J/kg]$	Mass-specific internal energy
E	$[J/kg]$	Total internal energy
f	$[1/s]$	Frequency
f	$[-]$	Favre mass-weighted operator
f	$[J/kg]$	Helmholtz free energy per unit mass
f_β, f_{β^*}	$[-]$	Turbulence model closure coefficients
\mathbf{f}	$[-]$	Vector for the convective fluxes in x -direction
\mathbf{f}_v	$[-]$	Vector for the viscous fluxes in x -direction
g	$[J/kg]$	Gibbs free energy per unit mass
\mathbf{g}	$[-]$	Vector for the convective fluxes in y -direction
\mathbf{g}_v	$[-]$	Vector for the viscous fluxes in y -direction
h	$[J/kg]$	Mass-specific enthalpy
H	$[J/kg]$	Total enthalpy
\mathbf{h}	$[-]$	Vector for the convective fluxes in z -direction
\mathbf{h}_v	$[-]$	Vector for the viscous fluxes in z -direction
k	$[J/kg]$	Turbulent kinetic energy
K	$[-]$	Runge-Kutta stage
l	$[m]$	Characteristic length
L	$[J/kg]$	Latent heat of vaporization
M	$[-]$	Mach number
\mathbf{n}	$[-]$	Normal vector
n_i	$[-]$	Maximum grid points in x -direction
n_j	$[-]$	Maximum grid points in y -direction
n_k	$[-]$	Maximum grid points in z -direction

p	[Pa]	Pressure
P	[$N/m^2 \cdot s$]	Turbulent production term
Pr	[-]	Prandtl number
Pr_T	[-]	Turbulent Prandtl number
q	[W/m^2]	Heat flux
\mathbf{q}	[-]	Vector of conserved variables
r	[m]	Radius
R	[m]	Bubble radius
R_0	[m]	Initial bubble radius
Re	[-]	Reynolds number
\mathbf{R}	[-]	Residual vector
s	[$J/kg \cdot K$]	Mass-specific entropy
\mathbf{s}	[-]	Source vector
\mathbf{S}	[m^2]	Surface area vector
S	[m/s]	Wave speeds in Riemann problem
S	[N/m]	Surface tension
S_{ij}	[$1/s$]	Strain tensor
St	[-]	Strouhal number
t	[s]	Time
T	[K]	Temperature
Tu	[m/s]	Turbulence intensity
u	[m/s]	Velocity component in x -direction
\mathbf{u}	[-]	Vector of primitive variables
v	[m/s]	Velocity component in y -direction
v	[m^3/kg]	Specific volume
V	[m^3]	Volume
w	[m/s]	Velocity component in z -direction
W	[-]	Weighting function in Galerkin method
x, y, z	[m]	Cartesian coordinates
x	[-]	Mass fraction of vapor

Greek Symbols

α	[-]	Void fraction
α	[$^\circ$]	Angle of attack
α_i	[-]	Runge-Kutta coefficient
β_0, β^*	[-]	Turbulence model closure coefficients
γ	[-]	Limiter function
Γ	[-]	Control volume surface
δ_{ij}	[-]	Kronecker delta
ϵ	[m^2/s^3]	Turbulent dissipation rate
κ	[-]	Specific heat capacity
λ	[$W/m \cdot K$]	Heat conductivity
λ_i	[-]	Eigenvalues of the equation system
μ	[$kg/m \cdot s$]	Dynamic viscosity

ν	$[m/s^2]$	Kinematic viscosity
ρ	$[kg/m^3]$	Density
σ_{ref}	$[-]$	Reference cavitation number
σ, σ^*	$[-]$	Turbulence model closure coefficients
τ	$[s]$	Relaxation time
τ_{ij}	$[N/m^2]$	Shear stress
ϕ	$[-]$	Pressure relaxation coefficient
χ_k, χ_ω	$[-]$	Turbulence model closure coefficients
Ψ	$[-]$	Mesh scale in cavitating flows
ω	$[1/s]$	Specific dissipation rate
Ω_{ij}	$[1/s]$	Rotation tensor
Ω	$[-]$	Control volume

Subscript Indices

0	Initial conditions
01	Total conditions
1/2	Interface value
e	Equilibrium condition
g	Gas
in	Inlet conditions
$init$	Initialization conditions
liq	Liquid
l, sat	Saturated liquid
L	Left value
max	Maximum value
min	Minimum value
out, mix	Mixed reflecting/non-reflecting boundary conditions
ref	Reference conditions
R	Right value
sat	Saturation conditions
T	Turbulent
vap	Vapor
v, sat	Saturated vapor
∞	Free stream or inlet condition

Superscript Indices

*	Equilibrium value
*	Star region value for the Riemann problem
*	Dimensionless variable
$ausm$	AUSM (Advection Upstream Splitting Method) Riemann solver
$hllc$	HLLC (Harten-Lax-van Leer Contact wave) Riemann solver
$hybrid$	Hybrid Riemann solver
n	Time instant
num	Numerical value

—	Mean value
\sim	Favre averaged value
'	Fluctuation in Reynolds averaging
"	Fluctuation in Favre averaging

All symbols that are not found in the list are defined in the text.

Abstract

The aim of this research is to model and analyze compressible 3-D cavitating liquid flows with special emphasis on the detection of shock formation and propagation. For that purpose the 3-D compressible finite volume flow solver **CATUM** (**CA**vitation **T**echnische **U**niversität **M**ünchen) is developed, which enables the simulation of unsteady 3-D liquid flows with phase transition at all Mach numbers. The compressible formulation of the full set of governing equations is solved by a modified Riemann approach, which is specially constructed to overcome the low Mach number problem. The phase transition is modeled according to equilibrium thermodynamics and it is validated against a series of test cases.

The CFD tool **CATUM** is then applied to various highly unsteady two-phase flows inside fuel injection systems and to the flow around hydrofoils. In order to resolve the wave dynamics that leads to acoustic cavitation as well as to detect regions of instantaneous high pressure loads, time steps down to nanoseconds are used in the calculations. Second order time and space discretizations are used throughout the simulations, as the geometrical complexity of the relevant applications restrict the usage of higher order schemes in terms of CPU requirements.

In the case of a multi-hole injection nozzle with an inlet pressure of 600 bar , a maximum pressure of about 2100 bar is observed inside the sack region and therefore ahead of the nozzle bore holes. Similarly, instantaneous local pressure peaks of the order of 100 bar are identified in the calculation around a 3-D twisted hydrofoil. These high intensity pressure loads are thought to be responsible for the erosive damage of the surfaces in such flows. Finally, symmetry break-up mechanism of the two-phase cavitating flows is investigated through a fully symmetric twisted wing. Moreover, in all the applications the time dependent development of vapor clouds, their shedding mechanism and the resulting unsteady variation of flow variables are discussed in detail and compared with the experimental results whenever possible.

Zusammenfassung

Der Inhalt dieser Arbeit ist die kompressible Modellierung und numerische Analyse von kavitierenden 3-D Flüssigkeitsströmungen einschließlich der durch Rekondensation initiierten Stoßbildung und Stoßausbreitung. Dafür wurde die Finite Volumen Methode **CATUM** (**CA**vitation **T**echnische **U**niversität **M**ünchen) entwickelt, die die Simulation von 3-D Strömungen mit Phasenübergang bei allen Machzahlen ermöglicht. Die kompressibel formulierten Bilanzgleichungen für Masse, Impuls und Energie werden unter Verwendung eines modifizierten Riemann Lösers, der das “low Mach number problem” umgeht, diskretisiert. Der Phasenwechsel wird durch thermodynamische Gleichgewichtsbeziehungen für Wasser, Wasserdampf und deren gesättigte Mischung modelliert.

Schwerpunkte der mit dem CFD Tool **CATUM** durchgeführten numerischen Analysen sind hoch instationäre Zweiphasenströmungen in Einspritzdüsen und um Schaufelmodelle. Zur zeitlichen Auflösung wellendynamischer Phänomene, wie akustische Kavitation und instantanen Druckspitzen, sind numerische Zeitschritte in der Größenordnung von 10^{-9} s erforderlich. Alle Simulationen werden mit hochauflösenden Diskretisierungen zweiter Ordnung in Raum und Zeit durchgeführt. Die hohe geometrische Komplexität der relevanten Anwendungen verhindert den Einsatz von Schemata höherer Ordnung, da diese die erforderlichen Rechenzeiten mindestens um den Faktor 30 erhöhen und somit nur für sehr einfache Testfälle praktikabel wären.

Die Simulation der kavitierenden Strömung in einer Mehrlochdüse bei 600 *bar* Vor- druck zeigt das Auftreten von instantanen Druckspitzen von 2100 *bar* stromauf der Spritzlöcher. Analog werden Druckspitzen in der Größenordnung von 100 *bar* bei der Simulation der kavitierenden Strömung um ein verwundenes Schaufelprofil identifiziert. Es wird davon ausgegangen, daß diese intensiven lokalen Druckspitzen an Bauteiloberflächen ein treibender Mechanismus für die erosive Schädigung sind. Anhand der Strömungssimulation um ein zur halben Spannweite symmetrisches Schaufelmodell wird die Instabilität kavitierender Strömungen und der resultierende Symmetriebruch der numerischen Lösung aufgezeigt und analysiert. Die zeitliche Entwicklung der Zweiphasengebiete, deren Ablöse- und Kollapsverhalten und das resultierende dynamische Verhalten des Strömungsgebiets werden im Detail dargestellt, analysiert und mit verfügbaren experimentellen Ergebnissen verglichen.

Chapter 1

Introduction

1.1 Background

This thesis work is the result of an ongoing research in the field of compressible formulation of liquid and two-phase flows where accurate time resolution of shock and wave dynamics in these flows is of fundamental interest. More specifically, in order to simulate such flows, first a 3-D compressible flow solver is developed for ideal gases. Subsequently, the code is modified to handle compressible liquid flows. Then, with the addition of two-phase modeling capability, it is extended to simulate the cavitation phenomenon. In the following sections, first some insight will be given on compressible flows, liquid compressibility and the cavitation phenomenon. Then, the numerical motivation behind this study will be explained briefly, followed by a literature survey on the subject and finally an overview of the thesis will be presented.

1.2 Motivation

The main physical motivation behind this research lies in understanding the unsteady compressible behavior of liquid flows, especially when phase transition (cavitation) takes place. As a natural consequence of compressibility, shock and expansion waves form and propagate inside the flow domain continuously. Accurate prediction of these highly unsteady flow phenomena is important in predicting the short time scale flow characteristics of the applications. Together with cavitation and subsequent re-condensation, a high temporal resolution is necessary to resolve the wave dynamics and detect regions of instantaneous high pressure loads resulting from violent collapses of cavitation regions. These pressure loads are thought to be responsible for the erosive damages in most of the applications that experience cavitation. The flow problems that are considered in the scope of this thesis are divided into two groups: The first group deals with micro-scale and high-speed applications like internal flows in fuel injection systems. Therefore, the required temporal resolution is extremely high, typically of the order of $\Delta t_{CFD} = 10^{-10} s$. The second group of flows exhibits low-speed and large-scale characteristics, where cavitating flows in hydraulic machinery such as ship propellers and pump or turbine blades are investigated. In both application groups, cavitation is an important and dominating feature of the flow field and, together with collapse

induced shocks, an accurate resolution and understanding of the flow phenomena is the physical motivation behind this study. Due to the dominance of inertia effects within the considered two-phase flows, viscous effects are neglected in the formulation of the problem and the conservation principles are expressed in terms of Euler equations.

1.2.1 Fluid Compressibility

By definition, flows undergoing density variations due to the imposed pressure field are characterized as compressible flows. Whereas in incompressible flows the density is assumed to be constant along a particle path. The density variation in a compressible fluid is a direct consequence of the pressure force exerted on the fluid particles. For a small element of fluid volume v , the pressure acting on the surfaces is p . If this pressure is increased with an infinitesimal amount of dp , the volume of the element will be correspondingly compressed by dv . Therefore, the compressibility of the fluid τ is defined as

$$\tau = -\frac{1}{v} \frac{dv}{dp}. \quad (1.1)$$

Since the volume is reduced, dv is a negative quantity [5]. Thus, a negative sign is added in front of the Eq. 1.1. This equation still needs some attention as the compression process normally is not adiabatic. Therefore, isothermal compressibility can be defined where the temperature of the fluid particle is kept constant

$$\tau_T = -\frac{1}{v} \left(\frac{\partial v}{\partial p} \right)_T. \quad (1.2)$$

This equation demonstrates an important physical condition. As the compressibility of a substance cannot be negative, following Eq. 1.2, the derivative $(\partial v / \partial p)_T$ must be **negative** for the complete thermodynamic range in consideration. This is a necessary condition for defining an equation of state and will be discussed in chapter 2 in detail.

Similarly, for adiabatic and reversible processes (without any dissipation mechanisms) isentropic compressibility can be defined as

$$\tau_s = -\frac{1}{v} \left(\frac{\partial v}{\partial p} \right)_s. \quad (1.3)$$

Equation 1.1 can be rewritten by using the density ρ of the fluid if v is defined as the specific volume of the fluid element, such that

$$\tau = \frac{1}{\rho} \frac{d\rho}{dp}. \quad (1.4)$$

Liquids have very low compressibility values compared to gases. Water, for example, at standard conditions has a compressibility value of $\tau_T = 5 \cdot 10^{-10} \text{ m}^2/N$, whereas for air the same value reads $\tau_T = 10^{-5} \text{ m}^2/N$. As a result, it seems reasonable to treat liquids as incompressible at first glance (where $\tau = 0$). But per definition, the description of waves and the resolution of wave propagation require the treatment of all fluid components as compressible substances, since the finite propagation speed of

the waves is defined by the equilibrium speed of sound c_e , which is a direct consequence of the isentropic compressibility of the fluid. This relation can be written as

$$c_e = \sqrt{\frac{1}{\rho\tau_s}}, \quad (1.5)$$

or equivalently the isentropic speed of sound in equilibrium flow is given by

$$c_e = \sqrt{\left. \frac{\partial p}{\partial \rho} \right|_s}. \quad (1.6)$$

The discussion on equilibrium conditions and equilibrium flow will be given in chapter 2; for the time being, one can assume $c = c_e$. Both definitions show that if compressibility is not taken into account, a finite wave propagation speed –speed of sound– cannot be defined, as $\tau = 0$ suggests $c \rightarrow \infty$.

Additionally, the importance and the necessity of treating liquids as compressible substances can be demonstrated by studying the “water hammer” problem, which is sometimes referred to as “Joukowski shock”. Here, an initially moving liquid is instantaneously stopped. The sudden deceleration of the flow velocity to $u = 0\text{ m/s}$ results in an upstream travelling shock. The strength of the pressure variation Δp across the shock can be approximated by **linearized 1-D acoustic theory** [138], where perturbations of the flow variables are used to derive the acoustic relations from the inviscid flow equations together with the assumption that the considered wave motion is isentropic. Therefore, following relation is obtained for the pressure variation

$$\Delta p \approx \rho c \Delta u. \quad (1.7)$$

It should be noted that this equation is derived from the linearized gasdynamic equations and therefore it assumes any change in pressure p causes an isentropic change in density ρ [5]. For an initial flow velocity of $u = 1\text{ m/s}$ at standard conditions the resulting pressure jump across the shock is 15 bar and the resulting shock Mach number is $M_s = 1.001$. Hence, the isentropic relation Eq. 1.7 is quite accurate. Whereas incompressible consideration for the pressure variation results in the following equation derived directly from the Bernoulli relation

$$\Delta p \approx \rho u \Delta u, \quad (1.8)$$

which shows that the hydrodynamic coupling scales with the convective velocity u in contrast to unsteady wave dynamics across a wave front in which the scaling is proportional to the speed of sound c .

The divergence-free condition in incompressible formulations does not permit the formation of pressure waves with finite propagation speeds and thus cannot model the pressure jump created by the unsteady wave motion. As a result, the “water hammer” problem demonstrates that even for a very slow liquid flow, compressibility is needed to be taken into account to resolve the wave dynamics and its consequences.

1.2.2 Cavitation Phenomenon

Another important difference of liquids over gases is that even though liquid is a continuous medium it breaks down under very low pressures and evaporates. This phenomenon is known as **cavitation**. Following this definition, it can be said that in cavitation the driving mechanism is the pressure decrease inside the flow field (Fig. 1.1). In a simplified consideration, as surrounding liquid shows only a very minor temperature change, isothermal path (blue line) can be assumed, i.e. temperature is taken as constant. But in the actual case, the process needs heat transfer and non-isothermal phase change occurs (red line). The difference $T - T'$ is called thermal delay in cav-

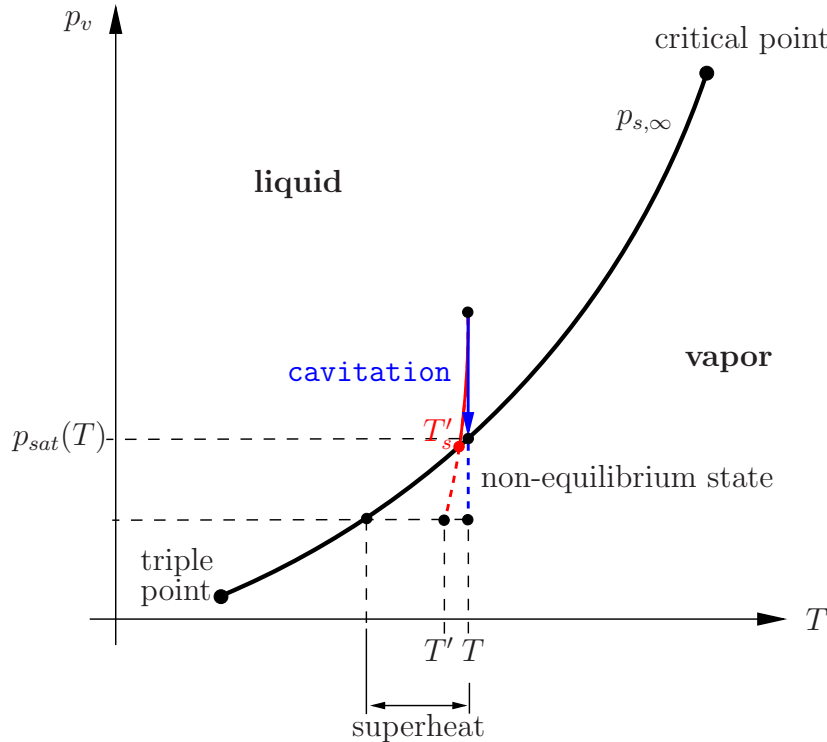


Figure 1.1: $p_v - T$ diagram for a general substance with emphasis on the cavitation process.

itation [30] and the path of the curve is **towards left hand side** (i.e. decreasing temperature). This is because the **surrounding liquid temperature decreases** as the liquid behaves like a heat source to complete the vaporization process. In order to resolve this behavior, the energy balance must be taken into account in the modeling strategy.

Even moderate convective accelerations in liquid flows can result in strong “negative pressure” gradients or tensions forcing the liquid to evaporate leading to “hydrodynamic cavitation”. However, cavitation can also occur in static or nearly static liquid through an oscillating pressure field or a moving expansion wave. This kind of cavitation is referred to as “acoustic cavitation” [135].

In both types of cavitation, the driving mechanism is the drop of the local pressure below some threshold value where liquid cohesion is no longer possible. This threshold value in most cases is the vapor pressure of the liquid at the given temperature. Therefore, the liquid immediately vaporizes. But this is not necessarily a requirement and deviations from the vapor pressure value can exist when a purified liquid is considered.

This situation is referred to as non-equilibrium state and represented by the dashed lines in Fig. 1.1. The detailed discussion on non-equilibrium and meta-stable states will be given in chapter 2.

The most important parameter of cavitating flows is the cavitation number σ_{ref} , which is defined as

$$\sigma_{ref} = \frac{p_{ref} - p_{sat}(T_{ref})}{\frac{1}{2}\rho_{liq}(p_{ref}, T_{ref}) \cdot u_{ref}^2}. \quad (1.9)$$

The cavitation number is defined with respect to the reference conditions of the flow field. The location of the reference values depends on the application that is considered and the corresponding experimental data present. But generally the reference conditions are defined at the inlet of the flow domain. A smaller value of the cavitation number σ_{ref} favors the possibility of cavitation.

The start of cavitation in a system is referred to as “**cavitation inception**” and defined by the critical cavitation number σ_i . It is a usual practice to expect cavitation at a location when the pressure drops to vapor pressure p_{sat} . However, as mentioned earlier, deviations from this value are possible and the real cavitation inception depends on different parameters such as fluid quality or initial gas content. Whereas, “**developed cavitation**” refers to a continuous situation of the steady or unsteady cavity with a significant effect on the flow dynamics and performance of the machines.

The second important parameter related with cavitation is the void fraction α , which is given by

$$\alpha = \frac{V_{vap}}{V_{ref}}. \quad (1.10)$$

This equation represents the vapor fraction inside a reference volume, V_{ref} . When this value is integrated through the whole domain, it gives the total amount of vapor volume with respect to the total volume of the flow domain.

Another important dimensionless parameter used in this thesis is the Strouhal number St . It relates the oscillating frequency to the reference velocity and the reference flow dimension, i.e.

$$St = \frac{f \cdot l}{u_{ref}}. \quad (1.11)$$

For an unsteady cavitating flow $f [Hz]$ is the unsteady shedding frequency, l is usually taken as the mean cavity length and u_{ref} is the flow velocity.

The Reynolds number $Re_{l_{ref}}$ defines the ratio of the inertial forces to the viscous forces and can be written as

$$Re_{l_{ref}} = \frac{\rho_{\infty} \cdot u_{ref} \cdot l_{ref}}{\mu_{\infty}}, \quad (1.12)$$

where ρ_{∞} and μ_{∞} are the density and the dynamic viscosity of the fluid respectively, u_{ref} is the reference velocity of the flow and l_{ref} is the reference or characteristic length of the flow problem. In cavitating nozzle flows the reference length is usually taken as the nozzle diameter, whereas for the flows around hydrofoils it is the chord length. As Eq. 1.12 suggests, the Reynolds number increases with decreasing viscosity and therefore, for flows with low viscosity fluids inertial forces dominate over the viscous forces. But the viscosity is still the controlling quantity for the flow attachment and

flow separation behaviors, so one should evaluate the flow field for such effects before neglecting the viscosity and assuming inviscid flow.

In terms of single bubble dynamics, the viscosity has a damping effect on the growth and collapse characteristics of the bubbles [49], [50]. But for the liquids with a small viscosity value like water ($\mu = 1.002 \cdot 10^{-3} \text{ Pa} \cdot \text{s}$ at $T = 293.15 \text{ K}, p = 1 \text{ bar}$) this damping effect is negligible [50]. The effect of viscosity and turbulence on cavitation will be discussed in chapter 2 in detail.

1.2.2.1 Cavitation Types

Once the cavitation starts to develop, it can take different forms depending on the profile shape, water quality, cavitation number and so on. Initially, it strongly depends on the non-cavitating flow structure and as it develops, the vapor structure disturbs and modifies the main flow also. The basic types of cavitating flows can be grouped as [30]:

- **Bubble cavitation:** This kind of cavitating flows consist of a small number of big bubbles, where the cavitation is seen in the regions of low pressure as a result of the rapid growth of initially present air nuclei. The bubbles are carried along the flow until they collapse and disappear as they enter areas of high pressure.

Fluid quality, especially the dissolved gas content of the flow, plays a big role on the quantity and the quality of the bubbles. Higher concentration of gas results in big bubbles, whereas lower concentration of dissolved gas results in a higher number of smaller bubbles [74].

- **Sheet Cavitation:** These cavities are often formed in the vicinity of the leading edge of wing type bodies, especially on the suction side of propeller blades and hydrofoils [67].
- **Supercavitation:** As the cavitation number decreases, the sheet cavity attached to the body grows and starts to surround a larger part of the body. When the whole solid body is totally enclosed in a vapor region, it is referred as supercavitation [30].
- **Cloud cavitation** is the cavitation regime consisting of many small bubbles (radius about 10^{-5} - 10^{-4} m) associated with intermediate pressure levels. It usually occurs when a partial or sheet cavity oscillates in length and periodically sheds clouds of vapor structure [57].
- **Vortex Cavitation:** Rotational structures generate low pressure regions like vortex cores or turbulent wakes inside the flow field. Such pressure drops can result in evaporation of the liquid and thus cavitation [58].

Different kinds of vortices exist depending on how they are produced. Well-defined, steady state vortices are usually attached to solid bodies and they are accompanied with circulation. Whereas the rotational coherent structures observed in the shear flows which are not attached to solid bodies are free and their life time is usually short due to viscous dissipation. Therefore, the character of the vortex cavity depends on how the vortex is created in the single-phase region.

Some experimental examples of the cavitation types discussed above are given in section 1.4.2. It should be noted that, in literature, with the exception of vortex cavitation, an exact distinction between the cavitation types does not exist. Especially the transition between cloud and bubble cavitation is not clear and most of the sheet cavitation applications are coupled with cloud cavitation and cloud shedding structures.

The flow problems that are considered in this investigation exhibit combined sheet and cloud cavitation behavior. In both application groups (injection nozzles and hydrofoils) initially a sheet cavity begins to develop at the surfaces where the local static pressure drops to the vapor pressure value. Subsequently, because of the flow dynamics of the problems, these sheet cavities grow and start to separate from the surface and form cloud cavitation with unsteady cloud shedding mechanism. Additionally, in one special case (section 5.1.4, 3-D multi-hole injection nozzle) the sheet cavity grows without breaking-up and forms a steady state supercavitation inside the nozzle bore hole.

Main effects of cavitation in hydraulic systems are related with the growth and collapse of the vapor regions that alter the flow characteristics, especially the pressure field, around the body. These effects can be summarized as

- decreasing the performance of the system, due to decrease in lift and increase in drag, reducing the turbomachinery efficiency
- production of noise and vibration
- instantaneous pressure loads on the body resulting from the collapse induced shocks
- erosion of solid surfaces.

1.2.2.2 Collapse Dynamics of Cavitation Bubbles

As of our primary interest, shock formation and related erosion effects can be depicted in the following basic sketch (Fig. 1.2). Assuming a pure vapor bubble already exists in a flow domain, because of the pressure imbalance between the bubble and the surrounding liquid ($p_{bubble} \ll p_{liquid}$), it starts to shrink and eventually collapses. This mechanism can be related to the water hammer problem, as the convective acceleration of the bubble surface during the collapse results in liquid flow towards the center of the bubble, and when the bubble collapses completely the impulse of the liquid collision at the center initiates a shock that propagates into the surrounding liquid. In this figure, three collapse situations are shown; an isolated bubble collapse and the resulting shock front (1), collapse of a bubble that is in contact with a solid surface (2) and interaction of a isolated bubble collapse with another bubble, which is in contact with a solid surface (3).

- 1) The isolated bubble collapse follows the description given above, where the imposed pressure difference initiates the collapse, and when the bubble collapses completely a shock forms and propagates into the surrounding liquid. Vogel et al. [125] measured in an experimental investigation peak pressures of the acoustic transients emitted during the bubble collapse and correlated them with the

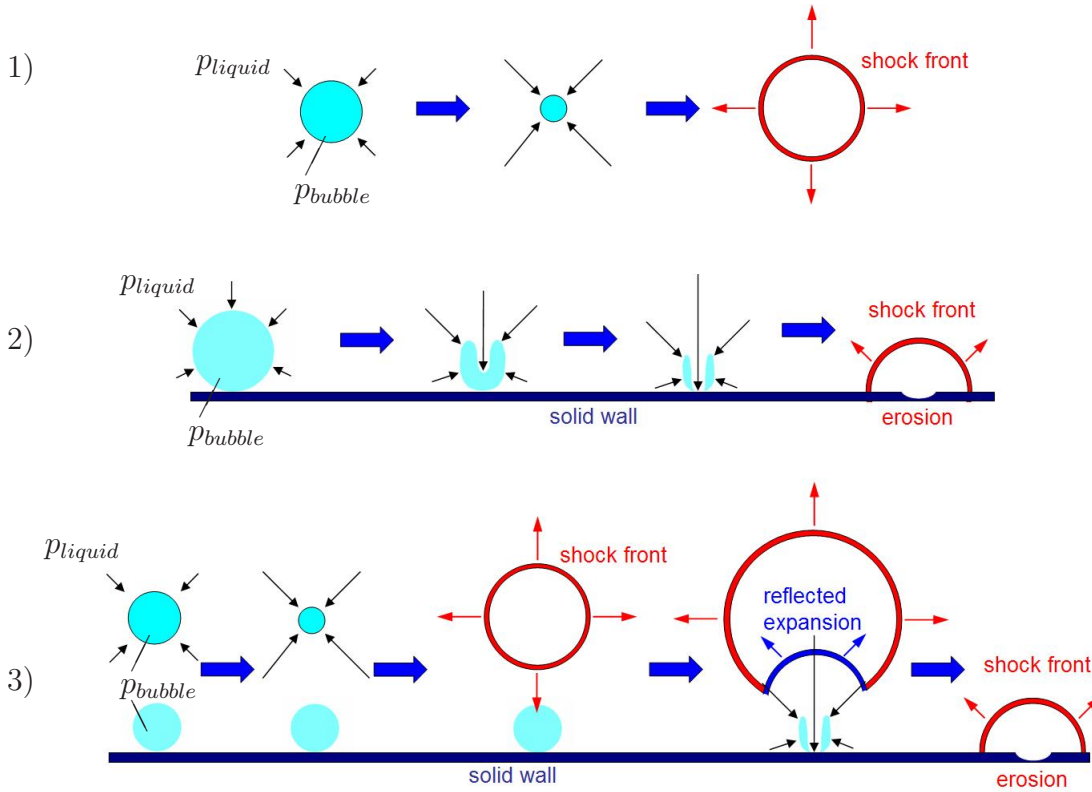


Figure 1.2: Representation of a pure vapor bubble collapse due to imposed pressure difference $p_{bubble} \ll p_{liquid}$. Collapse of an isolated bubble (1), isolated collapse situation near a solid surface (2), interaction of a isolated collapse with a bubble near a solid boundary (3).

initial bubble radius R_{max} . For an initial radius of $R_{max} = 2 \text{ mm}$ they reported a peak pressure of 150 bar behind the propagating shock.

- 2) The collapse of a bubble near a solid surface exhibits different characteristics than the isolated bubble. Because of the asymmetry of the problem, one side of the bubble accelerates inward more rapidly than the opposite side and this results in a liquid re-entrant micro-jet that is penetrating inside the bubble [13]. The speed of the re-entrant micro-jet is much higher in this case compared to the isolated bubble and together with the collapse mechanism described previously a more intense shock forms at the surface and propagates again into to the surrounding flow field. This highly localized high amplitude pressure increase at the solid surface due to the shock and the micro-jet results in material damage or **erosion**. Vogel et al. [125] and Philipp and Lauterborn [85] measured liquid jet velocities of the order of 100 m/s , when the bubble is directly in contact with the solid boundary. Depending on the shape of the tip of the liquid jet, “water hammer” pressures from 1500 bar up to 4500 bar are observed in the mentioned investigations. In addition to the liquid jet, Vogel et al. [125] found that the maximum pressure inside a collapsing bubble near the boundary can be as high as 2500 bar . Therefore, one can conclude that the combined effect of these two mechanism are responsible for the cavitation erosion [85].
- 3) Picture 3 of Fig. 1.2 depicts a situation where the shock emitted from the isolated bubble collapse interacts with another bubble in contact with a solid boundary. Tomita and Shima [118] observed similar cases and concluded that at the final

stages of a main collapse, tiny bubbles created earlier would be exposed to the high pressure pulse emitted by the main bubble and so they may collapse rapidly causing multiple impulsive pressure pulses that impinge on the solid surface. The collapse mechanism of these tiny bubbles close to the solid surface follows the description given above. In fact, the liquid jet velocities associated with this mechanism is considerably higher than the one discussed earlier. Tomita and Shima [118] reported that a shock with a strength of 50 *bar* hitting a gas bubble produces jets with a velocity of 200 – 370 *m/s*. Similarly, Dear and Field [25] have observed jets with velocities of 400 *m/s* after the cavity was struck by a shock with a strength of 2600 *bar*. The tiny bubbles at the surface and therefore the observed eroded area corresponds to a torus or a ring shape, which suggest that these tiny bubbles are produced by the reflected jet flows and the following expansion waves of the previous larger bubble collapses [85].

Although negative effects of cavitation are usually stressed, cavitation has also some favorable features. Especially with the help of ultrasonic devices, cavitation gained importance in the medical industry. One example for such an application is the extracorporeal shock wave lithotripsy, where collapse induced shocks are focused to break kidney stones [48]. Another example is the use of cavitating jets to clean surfaces. In addition to these, supercavitation is an important research topic for the military industry in order to develop low drag supercavitating torpedoes.

Cavitation is also a very important aspect of fuel injection systems of modern Diesel and Otto internal combustion engines. Recent developments in these systems include increasing pressure differences $\Delta p = p_{in} - p_{out}$ up to 2000 *bar*, as well as individual mass flow control strategies by pilot and multi-point injection with time scales of $\Delta t \leq 10^{-4}$ s. These conditions result in cavitation which is not avoidable in such systems. Therefore, control and optimization of cavitation in injection nozzles became an important research subject. Cavitation has a strong effect on spray formation and atomization, which is also associated with the efficiency of the combustion process [137]. It is also shown that supercavitation and turbulence will cause disturbances that will initiate atomization at the nozzle exit [19]. Moreover, with the help of swirling flow, cavitation region can be stabilized and moved away from the solid surfaces, where it causes erosion. Several 2-D and 3-D injection nozzle geometries are investigated in this thesis and their results will be discussed in chapter 5.

As explained briefly in the previous pages, cavitation is a technically very important subject in hydrodynamics and its prediction is crucial in the design phases of such devices. Therefore, an appropriate modeling strategy is needed for an accurate definition of the phase transition process. It is also known that, in comparison to pure fluid components, the speed of sound in two-phase mixtures decreases essentially by orders. The detailed discussion on two-phase modeling and the speed of sound will be given in chapter 2.

1.3 Numerical Motivation

Numerical simulation of cavitating flows is a long investigated subject. Methods based on the pressure correction technique are widely applied to simulate the periodic forma-

tion of the sheet cavity and its break-up dynamics for 2-D and 3-D applications [96], [109], where both phases are assumed to be incompressible. Chorin [21] introduced the artificial compressibility concept to solve incompressible flow equations as a hyperbolic system. In this method, the flow is still assumed to be incompressible but the solution procedure resembles the compressible treatment. Chen and Heister [20] presented a method based on this formulation to simulate 2-D cavitating flows, where the density of the liquid is taken as constant. Additionally, preconditioning techniques in combination with density based numerical methods enable the incorporation of compressibility effects for both phases. Furthermore, these methods allow for the simulation of low speed unsteady flows through the use of a dual time-stepping approach [111], [59].

Although these methods allow for the prediction of steady and unsteady flow characteristics based on the time scale of the convective velocity, they do not resolve wave dynamic effects. This is due to the fact that, preconditioning, when implemented alone, alters the physical propagation speed of waves and thus unsteady behavior is no longer contained in the solution. Although combination of preconditioning with dual time stepping algorithms reassures time accuracy on the time scale of the convective velocity, this approach is computationally not suitable for the resolution unsteady wave dynamics, which is the primary interest of the current study. For this reason, in the course of this thesis a 3-D compressible, block-parallel flow solver, **CATUM** (**CA**vitation **T**echnische **U**niversität **M**ünchen), is developed.

The compressible formulation of the flow allows for the hyperbolic treatment of the governing equations. Therefore, the time dependent flow characteristics are included in the solution procedure. It is known that Godunov type methods are well suited to calculate the numerical fluxes in the arising flow problem. These methods rely on approximate solutions of the Riemann problem across adjacent cells [119]. They can accurately reproduce even complicated wave structures and discontinuities. So far, this strategy and the resulting solution procedure are straightforward and well applied to aerodynamics or gas dynamics. However, as mentioned in the previous section, liquid flows undergo strong negative pressure gradients that enforce the liquid to break-up and cavitate, which results in a strong decrease of the sonic speed in two-phase regions.

As a result, when considering compressible liquid flows with phase transition, any proposed numerical model should accurately resolve a wide range of Mach number variations in the flow field as in two-phase regions with $M \gg 0$ and in the pure liquid phase with $M \rightarrow 0$. Moreover, as the compressible equation system with conservation of energy is coupled through an equation of state, a consistent and accurate equation of state should be defined for both pure phases, including the transition between the liquid and the vapor.

However, the classical approaches fail in the limit of multidimensional low Mach number flows (low Mach number problem) [38] and require substantial modifications to achieve accurate solutions in regions of pure liquid where $M \rightarrow 0$. Moreover, with respect to the high acoustic impedance $\rho \cdot c$ of liquids, the decrease of accuracy further intensifies. The details of the numerical model and the low Mach number problem will be given in chapter 3.

1.4 Literature Overview

Cavitation is a long known and an extensively studied phenomenon for different conditions and applications. It makes sense to classify these studies according to their theoretical, experimental or numerical origin.

1.4.1 Theoretical Studies

As already discussed in section 1.2.2, cavitation occurs due to pressure drop, when the local pressure exceeds the tensile strength of the liquid. The maximum tensile strength of the liquid without undergoing cavitation depends on the molecular properties as well as on the initial purity of the liquid. Some previous researchers tried to understand tension characteristics of the liquids, and thus cavitation inception through theoretical and experimental studies.

Theoretical analyses based on statistical thermodynamics overestimate the allowable tension as they consider a homogeneous nucleation process occurring on a molecular level [30]. Kinjo and Matsumoto [54] calculated the nucleation rate of cavitating bubbles using molecular dynamics and found nucleation rate to be eight orders of magnitude larger than that of the classical nucleation theory. As an example, simple theoretical modeling of a microscopic bubble with a diameter of an order of intermolecular distance (10^{-10} m) results in 7000 bar of tension, whereas the van der Waals equation predicts about 1000 bar at room temperature [134]. However, experimentally obtained tension levels are much lower than these estimated values even for artificially cleaned and degassed liquids. Trevena [120] pointed out in his survey paper various experimental methods and setups to measure the “negative pressures” in liquids. Accordingly, Briggs [14] found the breaking tension of distilled water as 277 bar, which is the highest experimental value ever reported. This value is still one order lower than the theoretical estimates, which suggests even cleaned water contains some foreign nuclei that result in heterogeneous nucleation [26]. Whereas untreated water or tap-water contains a large number of impurities which immediately results in the formation of vapor bubbles [12].

In terms of single bubble dynamics, theoretical formulations started with Besant [10] and his studies on the movement of an **empty** spherical bubble in an incompressible and inviscid liquid, where he predicted the pressure field in the liquid and the collapse time of the empty bubble [110]. Subsequently, Rayleigh [91] studied the same problem theoretically and derived its analytical formulation. Later, Plesset [86] modified the equation derived by Rayleigh by including surface tension and viscous effects. The resulting equation is known as the “Rayleigh-Plesset Equation” and governs the growth and collapse of a spherical bubble under the effect of a surrounding pressure field, which is filled with the **vapor** of the surrounding liquid (treated as **incompressible fluid**, i.e. $\rho_{liq} = const.$) and a **non-condensable gas** content.

$$R\ddot{R} + \frac{3}{2}\dot{R}^2 = \frac{p_{sat} - p_{\infty}(t)}{\rho_{liq}} + \frac{p_{g0}}{\rho_{liq}} \left(\frac{R_0}{R}\right)^{3\kappa} - \frac{2S}{\rho_{liq}R} - 4\nu_{liq}\frac{\dot{R}}{R}. \quad (1.13)$$

This equation describes the temporal evolution of the bubble radius R , where \dot{R} is the velocity of the bubble surface and \ddot{R} is the acceleration of it. p_{sat} is the vapor pressure

inside the bubble, $p_\infty(t)$ is the surrounding liquid pressure as a function of time, and ρ_{liq} is the liquid density. Therefore, the first term on the right hand side accounts for the pressure difference and hence represents the inertia effects. The second term stands for the non-condensable gas content inside the bubble, where p_{g0} is the initial gas pressure, R_0 is the initial bubble radius, and κ is the polytropic constant of the gas. The third term accounts for the surface tension S of the liquid and the last term is the effect of the liquid viscosity ν_{liq} . This equation is widely used in the literature with different levels of approximation to analyze the behavior of bubbles. Most of the attempts to solve this equation are numerical, therefore they will be discussed in section 1.4.3.

1.4.2 Experimental Studies

Experimental studies in cavitating flows can be divided into two classes. The first one concentrates on single or multiple bubble dynamics and analyze their growth, collapse and interaction mechanisms, while the second group focuses on flow applications and the resulting hydrodynamic cavitation properties rather than single bubble observations.

The collapse mechanism of the single isolated bubble has been extensively studied through experimental investigations. These experimental observations for the collapse of a single bubble as well as a bubble cloud demonstrate that violent shock structures occur [34]. In various papers Lauterborn investigated cavitation bubble dynamics [65]. The following picture series shows the production of a spherical bubble, its growth and subsequent collapse with a resolution of 75000 *fps*, i.e. time increment between two subsequent frames is $\Delta t_{pic} \approx 1.33 \cdot 10^{-5} s$. A laser pulse is used in the experiments to generate hot plasma inside a water tank that expands and initiates the bubble growth. The bubble contains **water vapor** and **non-condensable gas**, which is initially dissolved in the water.

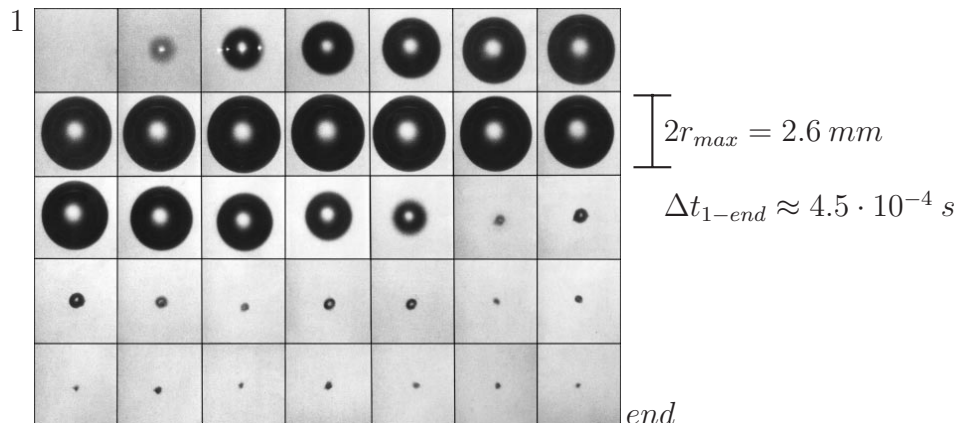


Figure 1.3: Growth and collapse of a spherical bubble initiated by a laser pulse in water, maximum bubble radius $r_{max} = 1.3 mm$, $\Delta t_{1-end} \approx 4.5 \cdot 10^{-4} s$. The bubble contains water vapor and non-condensable gas. Experiment by Lauterborn and Ohl [65].

Once the bubble reaches its maximum size, the pressure field imposed by the surrounding liquid forces it to collapse. The bubble does not collapse completely because of the

non-condensable gas content trapped inside, causing subsequent growth and collapses in a weakened manner. This behavior is referred to as “**rebounding**”.

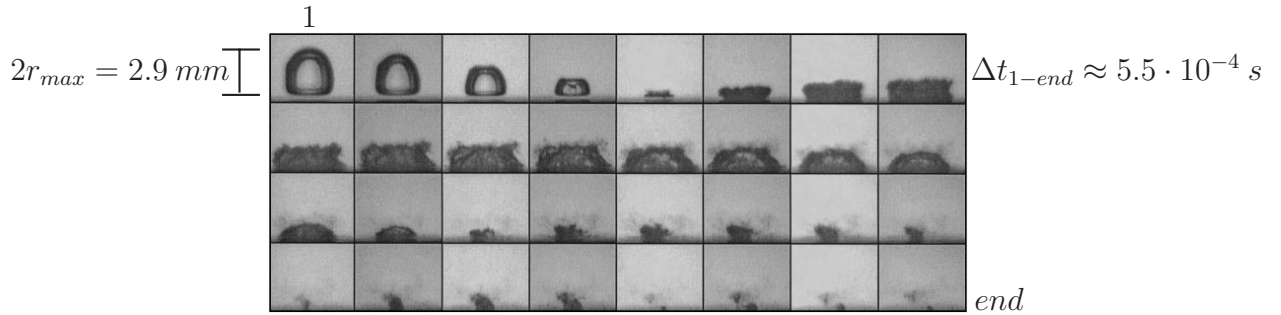


Figure 1.4: Collapse of a bubble near a solid surface; maximum bubble radius before first collapse $r_{max} = 1.45 \text{ mm}$, $\Delta t_{1-end} \approx 5.5 \cdot 10^{-4} \text{ s}$. The bubble contains water vapor and non-condensable gas. Experiment by Philipp and Lauterborn [85].

The second series (Fig. 1.4) depicts another bubble collapse situation near a solid wall [85] inside a water tank. The vapor bubble is initiated again using a laser pulse and analogous to the previous case it also contains some amount of non-condensable gas, which is initially dissolved in the water. Growth behavior of the bubble is similar to the previous case but the collapse characteristics are effected by the presence of the wall (model 2 in Fig. 1.2). During the collapse, the bubble interface near the wall flattens while a hollow develops on the opposite face. Thereby, a re-entrant jet forms that is directed towards the solid wall and finally strikes the solid wall. Because of the high velocity of the re-entrant jet, a shock forms and propagates into the liquid. This mechanism has already been discussed in section 1.2.2. Therefore, the solid surface undergoes a strong pressure force which is usually considered as a possible mechanism of cavitation erosion. Fujikawa and Akamatsu [34] reported shock intensities of the order of 100 bar in magnitude at the wall when the collapsing bubble is close to the surface. Philipp and Lauterborn [85] observed pressures up to several 10^4 bar acting on the material surface due to the collapse of bubbles which are in direct contact with the solid wall. The following series is again taken from Philipp and Lauterborn [85]

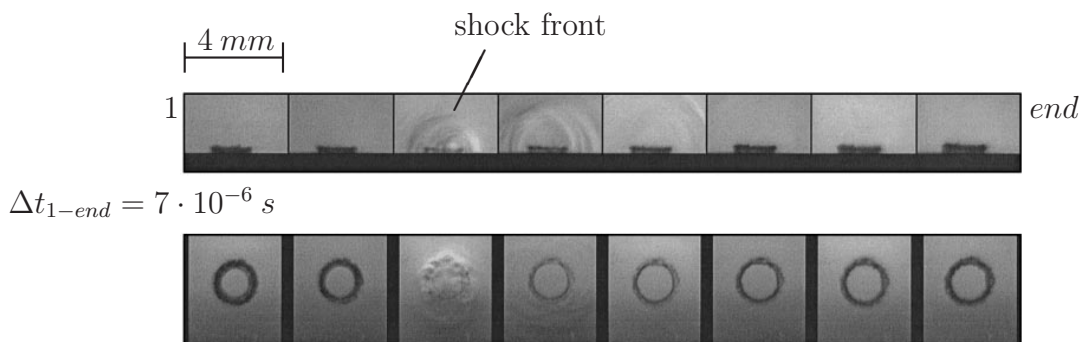


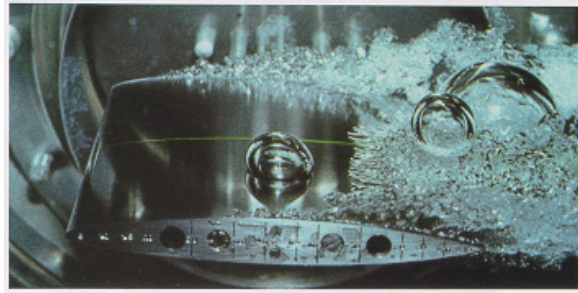
Figure 1.5: Emitted shock waves due to the collapse dynamics of a bubble near a solid surface. First row shows the side view and second row shows the top view. Maximum bubble radius before first collapse $r_{max} = 1.45 \text{ mm}$, $\Delta t_{1-end} = 7 \cdot 10^{-6} \text{ s}$. The bubble contains water vapor and non-condensable gas. Experiment by Philipp and Lauterborn [85].

and corresponds to a similar bubble collapse as given in Fig. 1.4 within a time interval of $\Delta t_{1-end} = 7 \cdot 10^{-6} \text{ s}$. Propagation of the shock front can be seen from the third

picture of the first row and the second row shows the situation from the top. During the collapse, a thick liquid jet forms and flows through the bubble forming a ring shape at the later stages of the collapse.

As stated earlier, the second class of experimental observations focus on cavitation in hydrodynamic applications which includes pump and turbine blades, ship propellers, underwater projectiles and injection nozzles of high pressure systems. Experiments related to pumps and propellers are mainly performed by using isolated 2-D or 3-D hydrofoil models in water channels. Depending on the experimental conditions, cavitation number and angle of attack, it is possible to observe sheet, cloud or supercavitation patterns. The following pictures are taken from the experiments of Franc and Michel [31], where different types of cavitation on a 2-D hydrofoil can be clearly seen.

These experiments are performed on a 2-D NACA 16012 hydrofoil at an almost constant Reynolds number with different cavitation numbers and angles of attack [31]. The first picture (Fig. 1.6) depicts traveling bubble cavitation together with cloud cavitation structures.

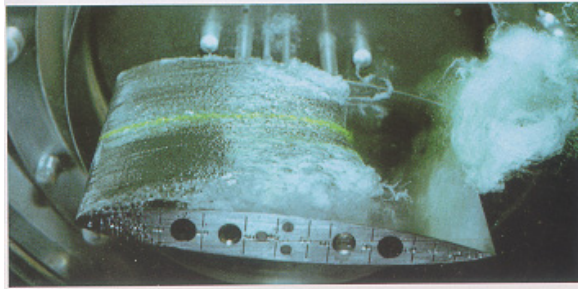


NACA 16012
 $Re_c = 10^6$, $\alpha = 17^\circ$
 $\sigma_{ref} = 1.2$, $c = 0.1 m$

Figure 1.6: Traveling bubble cavitation, NACA 16012 hydrofoil, chord length $c = 0.1 m$, $Re_c = 10^6$, $\sigma_{ref} = 1.2$, $\alpha = 17^\circ$. Experiment by Franc and Michel [31].



NACA 16012
 $Re_c = 10^6$, $\alpha = 11^\circ$
 $\sigma_{ref} = 0.81$, $c=0.1 m$



$Re_c = 6 \cdot 10^5$, $\alpha = 6^\circ$
 $\sigma_{ref} = 0.81$, $c=0.1 m$

Figure 1.7: Combined sheet and cloud cavitation, NACA 16012 hydrofoil, chord length $c = 0.1 m$, $Re_c = 10^6$, $\sigma_{ref} = 0.81$, $\alpha = 11^\circ$ (top), $Re_c = 6 \cdot 10^5$, $\sigma_{ref} = 0.81$, $\alpha = 6^\circ$ (bottom). Experiment by Franc and Michel [31].

Figure 1.7 demonstrates a sheet cavitation pattern near the leading edge of the foil with cloud shedding behavior over the trailing edge. In these pictures, the structure of the sheet cavitation and the cloud shedding pattern changes with the angle of attack.

For low values of the cavitation number, supercavitation can be observed independent of the angle of attack (Fig. 1.8).

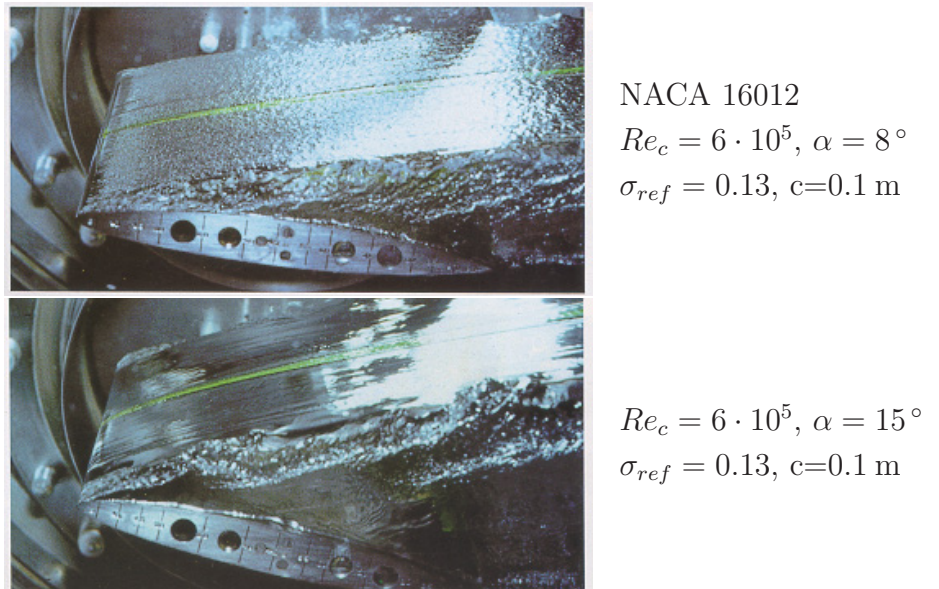


Figure 1.8: Supercavitation, NACA 16012 hydrofoil, chord length $c = 0.1$ m, $Re_c = 6 \cdot 10^5$, $\sigma_{ref} = 0.13$, $\alpha = 8^\circ$ (top), $\alpha = 15^\circ$ (bottom). Experiment by Franc and Michel [31].

As mentioned in section 1.2.2, another type of cavitation is the vortex cavitation, which is associated with rotational bodies as well as with vortex cores in free shear flows. An example of such a situation is given in Fig. 1.9.

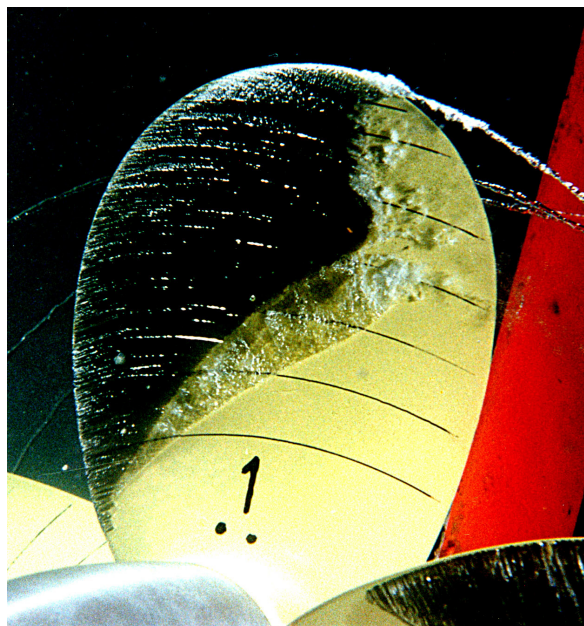


Figure 1.9: Vortex cavitation at the tip of a propeller blade and sheet cavitation on the blade surface of a ship propeller [58].

A ship propeller is investigated in the experiments [58]. Here, a vortical cavitation pattern is observed at the tip of the blade and sheet cavitation is visible on the blade surface.

In contrast to hydraulic machinery, cavitation in injection systems is much harder to observe due to their micro scale geometry. Observations of cavitation in large scale nozzles have shown the presence of cavitation bubbles and bubble clouds [19], [95]. Whereas Roosen et al. [93] observed sheet-type cavitation in small scale nozzles. Many authors have pointed out shedding of the cavitation region and unsteady behavior [100]. Chaves [19] also concluded that it is difficult to identify the structure of the cavitating flow, whether it is a sheet-type cavitation or cavitation cloud. Other investigations also confirmed that different types of cavitation structures can occur simultaneously inside the nozzle [75].

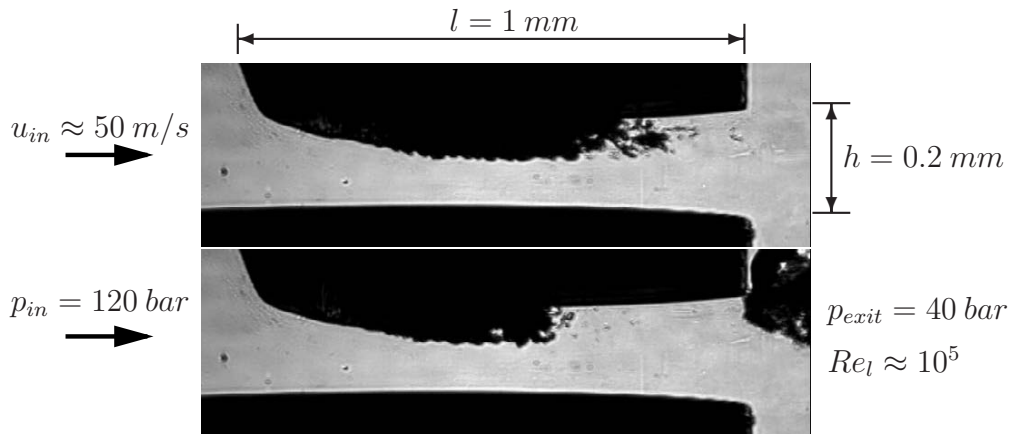


Figure 1.10: Experimental observation of cavitation in a 2-D planar injection nozzle at two time instants, $p_{in} = 120\text{ bar}$, $p_{exit} = 40\text{ bar}$. Experiment by Schmidt et al. [100].

The two pictures in Fig. 1.10 show cavitation regions inside a 2-D planar injection nozzle at two different time instants.

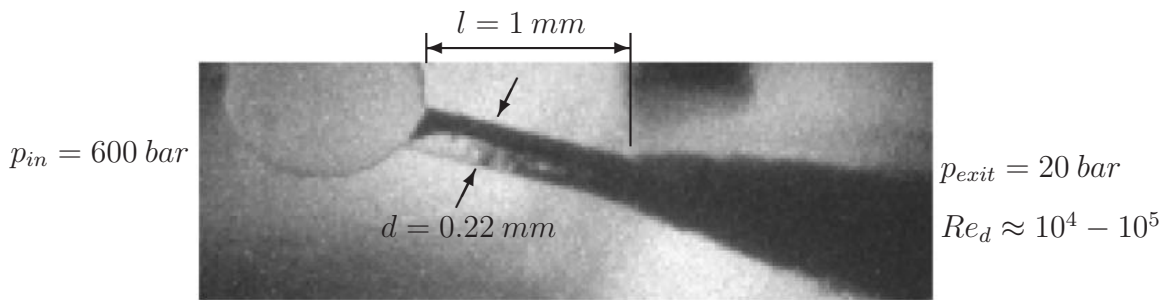


Figure 1.11: Cavitation pattern (dark area) inside a 3-D injection nozzle, bore hole connected to the side of the sack volume, $p_{in} = 600\text{ bar}$, $p_{exit} = 20\text{ bar}$. Experiment by Busch [15].

Busch [15] has experimentally investigated 3-D real-size single and multi-hole injection nozzles in his Ph.D. thesis. Figure 1.11 visualizes a 3-D injection nozzle with a single bore hole connected to the side wall of the sack volume. Here, the cavitation regions

inside the bore hole appear as dark regions, whereas the darker area outside the bore hole corresponds to the spray.

The last picture given by Fig. 1.12 clearly demonstrates the erosive effects of cavitation. The picture shows the leading edge of a propeller blade which is eroded due to the collapse of the cavitation structures. The eroded surface shows a typical roughness, illustrating that the erosion is due to many strong impacts on the surface concentrated on small areas [58].



Figure 1.12: Detail of an eroded ship propeller [58].

1.4.3 Numerical Studies

As shown in the previous section, measurements of cavitating flows are extremely difficult, especially in the case of injection systems, because of the micro-scales associated with the problem. Moreover, the liquid quality and the accuracy of the measurement instruments effect the overall results obtained from the experiments. For that reason, parallel to experimental investigations, numerical modeling of cavitating flows gained progress in recent years.

Earlier numerical attempts for the solution of cavitating flows consider the Rayleigh-Plesset equation (Eq. 1.13). Investigations focusing on single and multiple bubbles are referred to as bubble dynamics in the literature. Numerical investigations of single bubble dynamics are closely related to the previously mentioned theoretical work, as they serve for the physical understanding of the bubble growth and collapse problem for different boundary conditions. The pioneering work by Plesset and Prosperetti [87], Hickling and Plesset [43], Ivany and Hammit [49] and others [11],[88],[18] served as the fundamental understanding of the solution of the Rayleigh-Plesset equation, and therefore, of the bubble dynamics.

Another subgroup of bubble dynamics is the 1-D flow of bubbly liquids. In this case, the solution of the Rayleigh-Plesset equation is coupled with a 1-D or quasi 1-D flow

problem. The detailed investigation of such flow problems can be found in the work of Brennen [3] and Delale et al. [27].

Beside single bubble dynamics, different numerical models are developed for calculation of cavitating flows. They focus on the global flow character and cavitation patterns that are dominant in the flow field rather than the dynamics of single isolated bubbles. These models use different methods and different levels of approximation. There are two main approaches used to model two-phase flows according to their interpretation of the flow problem as single-fluid or multi-fluid domain.

Multi-fluid models assume different velocities, temperatures or pressures that can be present for the species. This is achieved by applying independent sets of continuity, momentum and energy equations for each phase. Therefore, simulations for dispersed non-equilibrium flows with defined internal structures and separate flow characteristics for every phase can be performed. However, these methods require the definition of appropriate closure and interface relations for each phase under consideration, which are usually empirical and problem dependent. Thus, these models are hard to implement and to verify for a wide variety of flow problems, especially for the calculation of three-dimensional transient cavitating flows in complex geometries. Saurel et al. [98] used multi-fluid models to calculate multi-phase and multi-material flows including cavitation.

Alternatively, two-phase modeling using single-fluid or “homogeneous mixture” approach is widely accepted and implemented. These models use one set of governing equations for all phases and accordingly, if needed, another transport equation is solved for the vapor fraction of the second phase. The single-fluid models can be divided into subgroups according to their definition of phase transition. In the first group, the cavitation model is based on the transport equation of the void fraction which has the following form

$$\frac{\partial(\rho_1\alpha_1)}{\partial t} + \frac{\partial(\rho_1\alpha_1u_j)}{\partial x_j} = S_{\alpha_1} . \quad (1.14)$$

Equation 1.14 governs the transport of phase 1 having a void fraction α_1 and density ρ_1 . The source term S_{α_1} on the right hand side of this equation is the defining parameter of the different models and it is a function of the fluid properties and of the phase transition process. In this approach the phase transition is assumed to occur in a **non-equilibrium process**, which is modeled through the definition of the source term. In the literature, different definitions are found for the source term. Empirical models for evaporation and re-condensation are encountered frequently in the work of Kunz et al. [59], Chen and Heister [20]. Additionally, source term formulations based on the Rayleigh-Plesset equation with some simplifications are also used to define the phase transition process. In previous studies by Schnerr [106], Yuan and Schnerr [137] and Sauer [96], the Rayleigh model is used as source term in an incompressible formulation. Alajbegovic et al. [4] also predict the evaporation and re-condensation rates by using a simplified Rayleigh model. It should be noted that these models include bubble dynamics with different levels of approximation to calculate the void fraction α value only. All the other aspects of bubble dynamics related to the growth and the collapse behavior of single bubbles are not included and not modeled in these approaches.

Another methodology in modeling the phase transition is to assume the phases in thermal equilibrium and define a mixture density to represent both phases, i.e. **equilibrium phase transition**. These kinds of models do not need an extra transport equation for the void fraction, and coupling of the equation system is achieved by a consistent equation of state. Most of these models use a barotropic definition of pressure, i.e. $p = p(\rho)$, therefore, the energy equation is not solved [56]. Hence, phase change is described as an isothermal process in this description. A more complex modeling can be proposed by considering the full set of governing equations, including the conservation of energy. This definition requires a consistent equation of state in the form of $p = p(\rho, T)$ for both phases. The distinction between the **equilibrium** and the **non-equilibrium** processes is discussed in chapter 2 in detail.

Additionally, commercial flow solvers are widely used in the industry to simulate cavitating flows. But the leading solver packages such as ANSYS-CFX and STAR-CD rely on pressure correction methods and they consider liquid flows as incompressible [7], [16]. In the area of internal combustion engine simulations, AVL-FIRE [9] is also a widely used and specialized commercial tool, which includes a multi-fluid model with interfacial closure relations to simulate cavitation. But again, like the previous ones the numerical algorithm is based on pressure correction methods and considers all the phases as incompressible. Therefore, all these mentioned commercial packages neglect compressibility effects and the related wave dynamics.

1.5 Thesis Overview

The current thesis is started as a development of a 3-D compressible, high-order, unsteady flow solver for gas dynamics. An unsplit finite volume method (FVM) is used for the solution of the full set of conservation equations of mass, momentum and energy on structured grids and flux calculation is carried out by the Riemann approach. Higher order spatial accuracy is achieved by using TVD/MUSCL type methods. A four stage Runge-Kutta method with enlarged stability region is used for temporal integration.

Once the initial code structure for ideal gases is finished, it is verified through various test cases such as 1-D shock-tube problems and 2-D airfoil and wing simulations. As the next step, the compressible liquid definition is included into the code. For that purpose, a detailed literature survey is carried out in order to find the most suitable equation of states. As a result, the modified Tait equation is chosen and implemented into the code to define the liquid water, which is the test fluid currently. Water shock tube experiments are used to verify the code with the chosen equation of state. Together with these modifications, the code is parallelized via multi-block structure using MPI libraries by Thalhamer [116].

As a last modification, in the scope of this thesis work but not the least, a two-phase modeling method based on the integral average quantities and equilibrium thermodynamics is included in the code, which resulted in our state of the art CFD-tool **CATUM** (**CA**vitation **T**echnische **U**niversitat **M**unchen). In the current state of the code, the vapor phase is defined by the ideal gas equation of state for water vapor, the liquid phase is defined by the modified Tait equation and for the mixture region saturation conditions are assumed.

Chapter 2 covers the physical aspects of the phase change process and introduces the governing equations. Together with the physical modeling, the chosen equation of state and the speed of sound calculation are discussed in detail. In chapter 3, the numerical modeling of the governing equations and the boundary treatments are explained.

To verify the developed solver, several standard test cases are considered in chapter 4. First, single-phase shock tube calculations for both ideal gas and liquid water are performed. Then, the proposed two-phase model is validated through the single bubble collapse problem and compared with the analytical solution of the Rayleigh-Plesset equation. Finally, the mesh and discretization dependence of the model is demonstrated by using a 2-D planar injection nozzle calculation.

Chapter 5 presents the simulation results from the applications. The first group belongs to 2-D and 3-D injection nozzles, which characterize the internal cavitating flow in high-speed, small-scale devices. The second group of applications focuses on hydrofoils that represent pump or turbine blades and ship propellers, which are mainly low-speed and large-scale devices. The results in this chapter are explained and discussed in detail and comparisons with the available experimental data are also presented.

Chapter 2

Physical Model

First we guess it. Then we compute the consequences of the guess to see what would be implied if the law we guess is right. Then we compare the result of the computation to nature, with experiment or experience, compare it directly with observation, to see if it works. If it disagrees with experiment it is wrong. In that simple statement is the key to science. It does not make any difference how beautiful your guess is. It does not make any difference how smart you are, who made the guess, or what your name is - if it disagrees with the experiment it is wrong. That is all there is to it. *Richard Feynman*

As cavitating flows involve a large variety of physical phenomena such as bubble dynamics, non-equilibrium thermodynamics, multi-phase turbulence and multi-phase wave and shock dynamics, its prediction is one of the most challenging tasks of modern CFD. Moreover, each physical aspect incorporates specific spatial and temporal scales depending on the considered flow field. Even the use of high performance computers does not presently enable simulations which resolve the combination of all these arising physical aspects, especially not for 3-D unsteady flows of typical technical applications. Therefore, suitable modeling strategies are needed for accurate simulation of the given flow problem. This chapter focuses on the physical definition of the considered flow problems and the corresponding physical modeling that is used by the numerical method.

2.1 Equilibrium vs. Non-equilibrium Processes

2.1.1 Flows with Non-equilibrium Effects

Before proposing any physical model, it is useful to clarify the meaning of equilibrium and non-equilibrium processes as they are encountered often in the literature. The following discussion in this subsection is based on chapter 7 of Vincenti [124] and it is extended in terms of cavitating flows. This analysis is divided into two parts. The first part considers a closed static system without any flow and in the second part an open system with a fluid flow through its boundaries is analyzed. In both cases, a micro scale system analysis of the order of an infinitesimal control volume is performed and then it is represented by a corresponding macro scale physical problem.

First we consider a **closed static system** where no flow is flowing through its boundaries. Figure 2.1 depicts an infinitesimal control volume corresponding to this system.

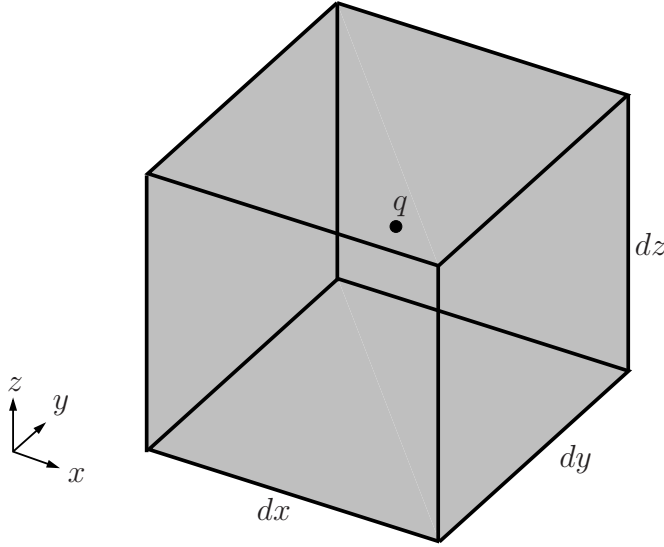


Figure 2.1: An infinitesimal closed control volume, without flow through its boundaries. q represents any variable produced or modified inside this control volume due to any thermodynamical or chemical process.

We can define a variable \mathbf{q} that is produced or modified inside this control volume due to any thermodynamical or chemical process and it denotes a general scalar non-equilibrium value per unit mass. In **cavitation**, due to the phase transition process, vapor is produced inside the control volume. Therefore q can be taken as the volume fraction α or the mass fraction x of the vapor, which are defined as

$$\alpha \equiv \frac{V_{vap}}{V_{tot}}, \quad x \equiv \frac{m_{vap}}{m_{tot}}. \quad (2.1)$$

The time rate of change of q inside the control volume can be written by using the generalized rate equation as follows

$$\left(\frac{dq}{dt} \right)_{int.proc} = \omega(\rho, T, q). \quad (2.2)$$

Here, ω defines the complete function in terms of thermodynamic state variables ρ , T and q . This equation represents an **internally occurring process** inside the control volume without any flow flowing through its boundaries as mentioned earlier, as the subscript “*int.proc*” suggests, and it can be reformulated for the definition of the local relaxation time $\tau(\rho, T, q)$. It is obvious that the function ω in Eq. 2.2 has the dimensions of q divided by time. Therefore, the partial derivative $(\partial\omega/\partial q)_{\rho, T}$ has the dimensions of time^{-1} , as the dimension of q is eliminated through the differentiation. As a result, the local relaxation time τ of the rate equation reads as

$$\tau(\rho, T, q) = -\frac{1}{(\partial\omega/\partial q)_{\rho, T}}. \quad (2.3)$$

The negative sign comes from the fact that the derivative in Eq. 2.3 is always negative [124]. Equation 2.2 can be rewritten in the following form

$$\left(\frac{dq}{dt}\right)_{int.proc} = \frac{\chi(\rho, T, q)}{\tau(\rho, T, q)}, \quad (2.4)$$

where the function $\chi(\rho, T, q)$ is given as

$$\chi(\rho, T, q) = -\frac{\omega}{(\partial\omega/\partial q)_{\rho, T}}. \quad (2.5)$$

Equation 2.5 is defined to represent the non-equilibrium rate equation as the ratio of two functions as given by Eq. 2.4.

Considering a situation where ρ and T are constant, an equilibrium state is possible and corresponds to the condition

$$\frac{dq}{dt} = \left(\frac{dq}{dt}\right)_{int.proc} = 0. \quad (2.6)$$

For all finite values of τ , an equilibrium value of q can be defined as q^* , which corresponds to

$$\chi(\rho, T, q^*) = 0, \quad (2.7)$$

$$q^* = q^*(\rho, T). \quad (2.8)$$

As a result, the equilibrium state of a system without flow suggests $(dq/dt)_{int.proc} = 0$ but it does not necessarily force the local relaxation time to be zero, i.e. $\tau = 0$. The discussion so far assumes a closed system without any flow flowing across its boundaries. At the macro system level this process can be interpreted through a piston-cylinder device as shown in Fig. 2.2 (left). We assume that initially the system contains only liquid water at constant temperature $T = 293.15 \text{ K}$. If the piston is gradually moved upwards while keeping the temperature constant, at some point the pressure inside the control volume reaches the vapor pressure value $p_{sat} = 2340 \text{ Pa}$ at that temperature and a phase change process from liquid to vapor would begin (point 1 on $p-v$ diagram, $\alpha_1 = x_1 = 0$). During the phase transition, both temperature and pressure are kept constant but the specific volume v increases. The piston-cylinder sketch in Fig. 2.2 corresponds to an intermediate state on the saturation line, where both liquid and vapor are present (point 2). From the sketch it can be interpreted that the vapor volume inside the cylinder is about two times the liquid volume, which corresponds to a vapor volume fraction of $\alpha_2 = 0.67$. At the given temperature $T = 293.15 \text{ K}$, this vapor volume fraction value leads to a vapor mass fraction of $x = 3.5 \cdot 10^{-5}$. The constant mass fraction line that passes through the considered state is also depicted in the $p-v$ diagram of Fig 2.2. At the end of the process all the fluid vaporizes

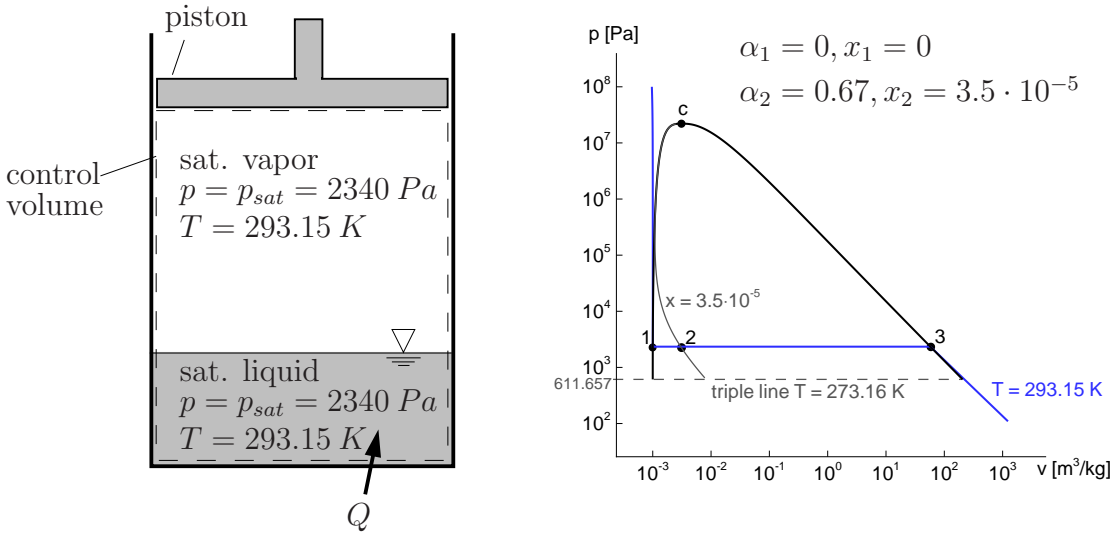


Figure 2.2: Equilibrium phase change process at constant temperature. Piston-cylinder device (left). Pressure reduced through the movement of the piston, heat transfer with surroundings is allowed. $p-v$ diagram of the phase change process (right), point 2 corresponds to depicted state of the piston-cylinder device.

and further reduction of pressure results in further increase in specific volume. This process corresponds to an equilibrium phase change, where the local relaxation time τ plays no role. Therefore, a phase change from liquid to vapor takes place through the constant pressure line as depicted in the $p-v$ diagram of Fig. 2.2. It should be noted that during this process the temperature of the system is kept constant by allowing the heat transfer with the surroundings. Therefore the entropy of the system increases during the vaporization process. A comparable analysis can be performed by considering the same process within an isolated piston-cylinder device, i.e. adiabatic

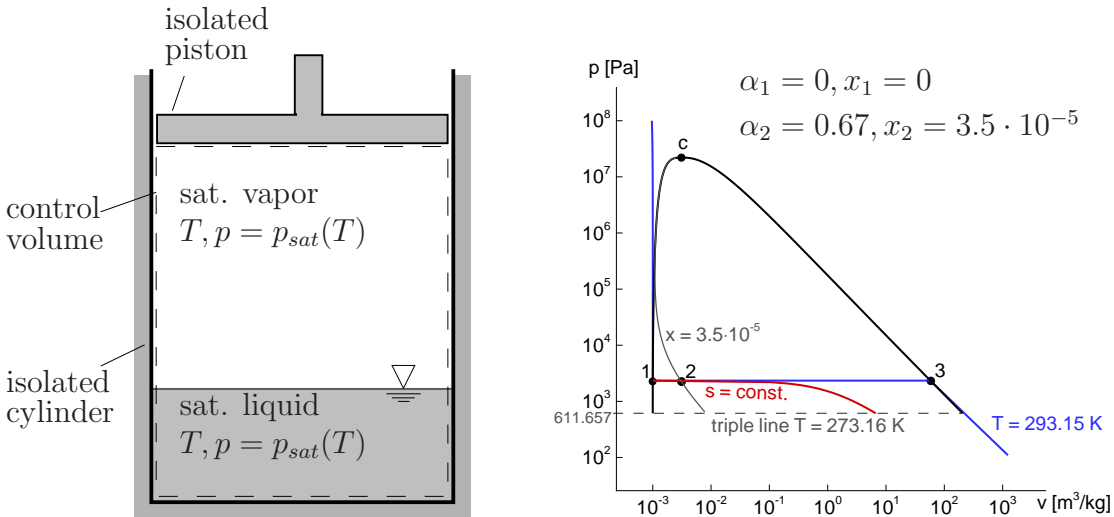


Figure 2.3: Equilibrium phase change process at constant entropy. Isolated piston-cylinder device (left). Pressure reduced through the movement of the piston, no heat transfer with surroundings is allowed. $p-v$ diagram of the phase change process (right), point 2 corresponds to depicted state of the piston-cylinder device, $\Delta T_{1-2} \approx 0.24 K$.

process (Fig. 2.3). Moreover, if the piston movement is slow enough then the overall process can be assumed as reversible and thus isentropic. In contrast to the previous case, in this idealized process the phase change occurs along the isentrope depicted as the red curve in Fig 2.3 (right). Therefore, the temperature is not constant anymore but **decreases** along the isentrope, so the system gets **colder** ($\Delta T_{1-2} \approx 0.24 K$) and the depicted state (point 2) now lies on the isentrope not on the isotherm. An important property of the isentropes in two-phase regions is that they have a negative slope in the $\log p - \log v$ diagram and they terminate at the triple line within the two-phase region. This observation is important, as in such an isolated piston-cylinder device a **complete vaporization** of the liquid is **not possible** through an isentropic process and it can only be achieved if the heat transfer is allowed with the surroundings as in the previous case. The maximum amount of vapor that can be produced in this process is limited by the triple line, where the isentrope terminates. For the considered initial conditions ($T_1 = 293.15 K$ and $p_1 = p_{sat} = 2340 Pa$) the maximum void fraction at the intersection of the isentrope and triple line is found as $\alpha_{max} = 0.99986$, which corresponds to maximum mass fraction of $x_{max} = 0.03239$.

In the second part we couple this closed system analysis with convective flow. For that purpose we assume a fluid flow without any dissipation mechanisms, which corresponds to the system of Euler equations of fluid dynamics. The assumption of **Euler flow** in terms of cavitating flows will be justified in section 2.2. For any standard flow without non-equilibrium effects, the set of Euler equations requires an equation of state as a closure relation. For equilibrium flows, the specific enthalpy in the form of $h = h(p, \rho)$ can be used as an equation of state. For non-equilibrium flows, a third variable should be introduced in order to specify this non-equilibrium process. So, the equation of the state takes the form $h = h(p, \rho, q)$, where q is a general scalar non-equilibrium variable per unit mass as discussed earlier. The addition of this new variable q requires an extra equation, namely a transport equation, as the change of this new variable is now influenced by the flow of the fluid. The following sketch shows an infinitesimal control volume, where the flow of the non-equilibrium variable q is shown.

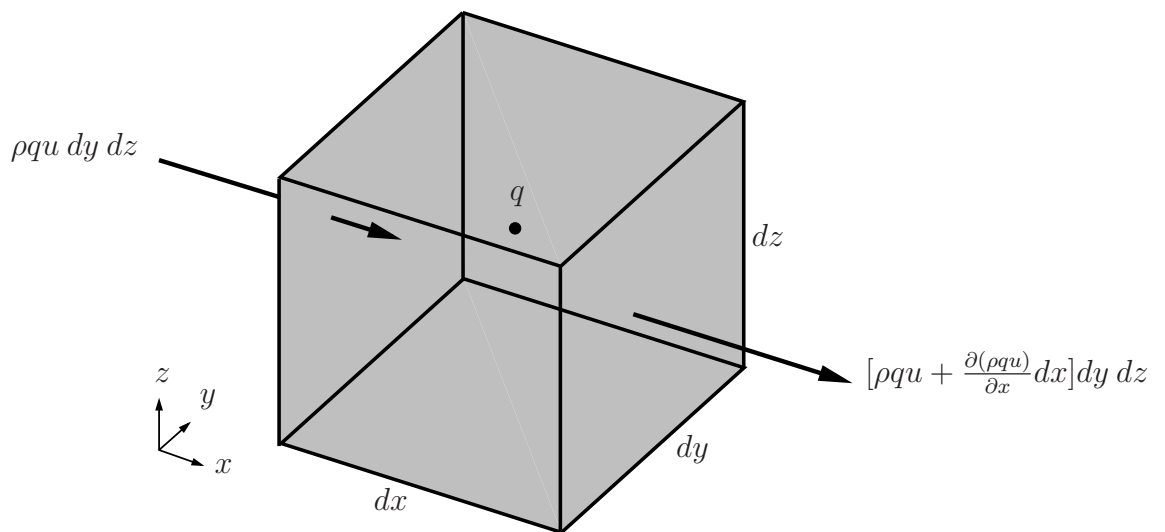


Figure 2.4: An open infinitesimal control volume showing the x -component of the flow of a non-equilibrium variable q .

Assuming that the non-equilibrium process is the same as in the static system previously defined, the transport equation takes the following form

$$\frac{\partial}{\partial t}(\rho q) + \frac{\partial}{\partial x_j}(\rho q u_j) = \rho \left(\frac{dq}{dt} \right)_{int.proc}, \quad (2.9)$$

The right hand side of this equation represents the time rate of change of q inside the control volume due to any internal process, as discussed previously, whilst the left hand side corresponds to the change of variable q due to the net inflow into the control volume. In fact, this equation resembles the transport equation given for the void fraction defined in Eq. 1.14, where $q = \alpha$. Repeating Eq. 1.14 here once more

$$\frac{\partial(\rho_1 \alpha_1)}{\partial t} + \frac{\partial(\rho_1 \alpha_1 u_j)}{\partial x_j} = S_{\alpha_1}. \quad (2.10)$$

Hence, the previously mentioned source term S_{α_1} is nothing but the rate equation of the non-equilibrium process. A similar transport equation was also used by Sauer [96] in his cavitation model to predict the vapor production in the calculations, i.e.

$$\frac{\partial \alpha}{\partial t} + \frac{\partial(\alpha u)}{\partial x} + \frac{\partial(\alpha v)}{\partial y} = \frac{n_0}{1 + n_0 \cdot \frac{4}{3}\pi R^3} \cdot \frac{d}{dt} \left(\frac{4}{3}\pi R^3 \right), \quad (2.11)$$

where n_0 is the nuclei concentration per unit volume of pure liquid and R is the bubble radius. It can be seen from this equation that the rate of the process is defined through the change in the bubble volume. One difference of this transport equation is that it does not include the transport of density ρ inside it, as Sauer assumed both phases are incompressible with the density of each phase being constant [96]. As a result, all three transport equations given by Eqs. 2.9 - 2.11 govern the same physical phenomenon of non-equilibrium flow, where the time rate of change of the non-equilibrium property inside the control volume is described by an additional transport equation. Moreover, in terms of cavitating flows this non-equilibrium variable can be taken as the void fraction α together with a corresponding source term depending on the modeling strategy.

In order to describe the properties of this transport equation and discuss the concept of the local relaxation time τ , we turn back to the general formulation Eq. 2.9 and rewrite it by using the definition given by 2.4

$$\frac{\partial}{\partial t}(\rho q) + \frac{\partial}{\partial x_j}(\rho q u_j) = \rho \frac{\chi(p, \rho, q)}{\tau(p, \rho, q)}. \quad (2.12)$$

The equation given above can be rearranged by using the substantial derivative, together with the definition of the continuity equation as

$$\frac{dq}{dt} = \frac{\chi(p, \rho, q)}{\tau(p, \rho, q)}. \quad (2.13)$$

In these equations, p and ρ are chosen as thermodynamic properties in accordance with the definition of the specific enthalpy proposed earlier.

The physical interpretation of Eq. 2.12 depends on the flow problem that is considered. This equation suggests that for any non-equilibrium flow, there should be a corresponding rate equation to describe the physical process. Flows with **non-equilibrium phase transition** (evaporation and condensation) are particularly good examples of such processes. **Condensation** of a steam or moist air due to rapid expansion of the fluid is a non-equilibrium process, which means that the time rate of nucleation is itself an internal process and needs to be modeled with an appropriate rate equation. Similarly, rapid expansion of a liquid flow can result in a metastable state where the pressure of the liquid drops below the saturation pressure without formation of the vapor phase, i.e. “liquid tension”. Therefore, non-equilibrium phase change takes place for the evaporation process which is defined by a rate equation for **cavitation** [75]. This behavior is already mentioned in chapter 1 and the thermodynamic background of these processes will be explained in the next section.

With the definitions of equilibrium and non-equilibrium processes, it is now possible to discuss the local relaxation time τ and to describe its physical meaning. If one performs perturbation analysis of Eq. 2.5 [124], one ends up with a formulation that reflects the physical interpretation of τ . The details of this analysis are beyond the scope of this thesis work. Hence, the quantity τ can be understood as the local relaxation time needed for the system to recover its equilibrium conditions for small departures of q from the equilibrium state q^* . It is of interest to examine the transport Eq. 2.12, when the relaxation time τ of the non-equilibrium process is negligibly small ($\tau \rightarrow 0$) or infinitely large ($\tau \rightarrow \infty$).

In the limit $\tau \rightarrow \infty$, the rate Eq. 2.13 shows that $dq/dt = 0$ for all values of χ . As a result, for an infinitely slow rate process, the value of q for a fluid element remains constant [124]. This process is regarded as “**frozen flow**”.

The limit $\tau \rightarrow 0$ is more interesting and it constitutes the base of the physical modeling used in this work. If we assume that dq/dt remains finite, it follows from Eq. 2.13 that $\chi \rightarrow 0$ as $\tau \rightarrow 0$, however contrary to the previous case this requires

$$\lim_{\substack{\tau \rightarrow 0 \\ \chi \rightarrow 0}} \frac{\chi}{\tau} = \text{finite} . \quad (2.14)$$

Moreover, in the consideration of the static system it was shown that $\chi(p, \rho, q) = 0$ defines the equilibrium value of q^* , i.e.

$$q \equiv q^*(p, \rho) . \quad (2.15)$$

As a result, the limit $\tau \rightarrow 0$ leads to the well known **equilibrium flow** of gas dynamics. Therefore, an infinitely fast rate process will lead to an instantaneous establishment of local equilibrium conditions as fluid elements move through the flow [124].

Similar to the previous discussion, we realize this process through a cavitating hydrofoil calculation as depicted by Fig. 2.5 (top). Because of the acceleration of the liquid flow over the foil suction side, the local pressure value drops to the vapor pressure and cavitation takes place as shown by the void fraction α values in the figure. The details of the two-phase model is explained later in this chapter but as already mentioned in chapter 1, in an actual process during cavitation the surrounding liquid temperature decreases as the liquid behaves like a heat source to complete the vaporization process.

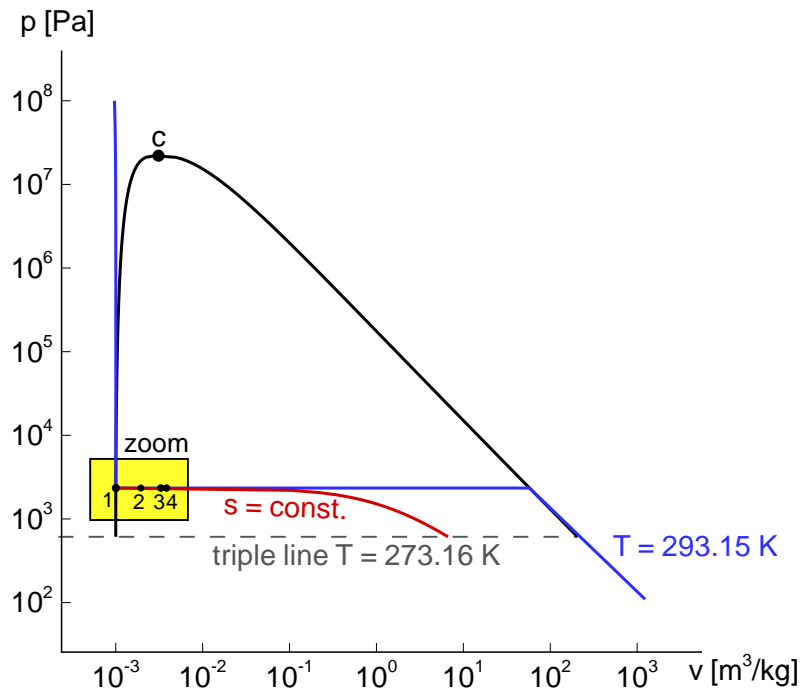
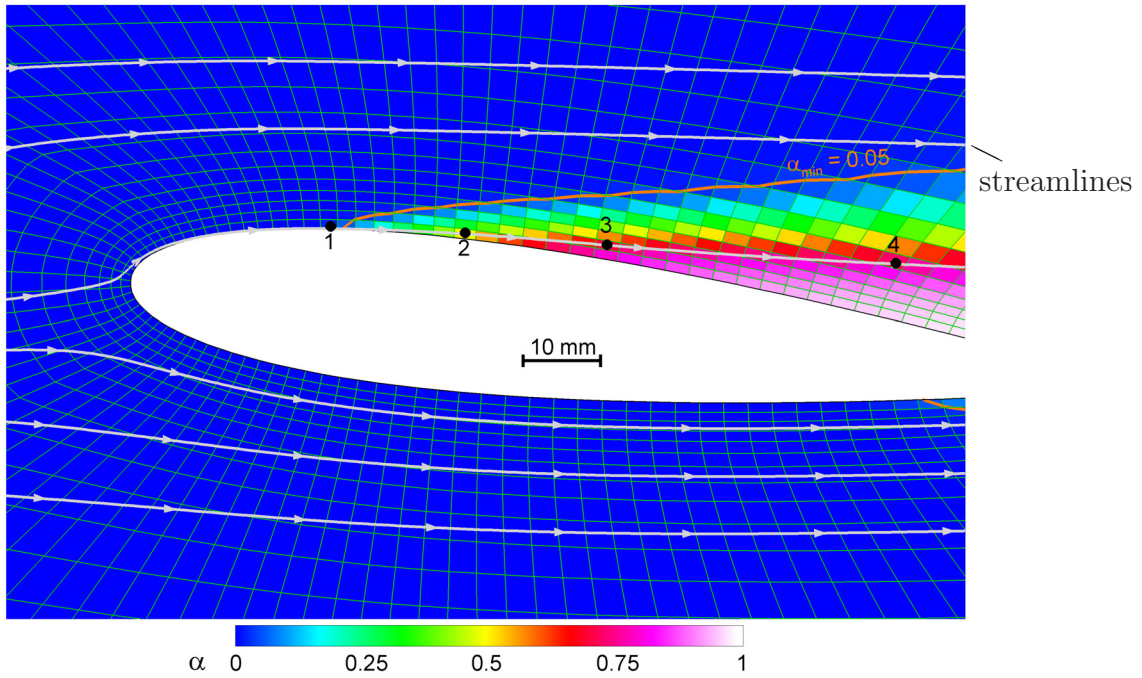


Figure 2.5: Cavitating flow over a 2-D hydrofoil, void fraction α and streamlines (top). Corresponding $p - v$ diagram of the phase change process. 2-D NACA 0009 hydrofoil, chord length $c = 0.13 \text{ m}$, angle of attack $\alpha = 6^\circ$, channel height 0.3 m , channel length 0.6 m . Water inflow from left to right, inlet conditions $u_{in} = 12 \text{ m/s}$, $T_{init} = 293 \text{ K}$, outlet condition $p_{out,mix} = 0.5 \text{ bar}$, Euler flow with equilibrium phase change, $\Delta T_{1-4} \approx 0.4 \text{ K}$.

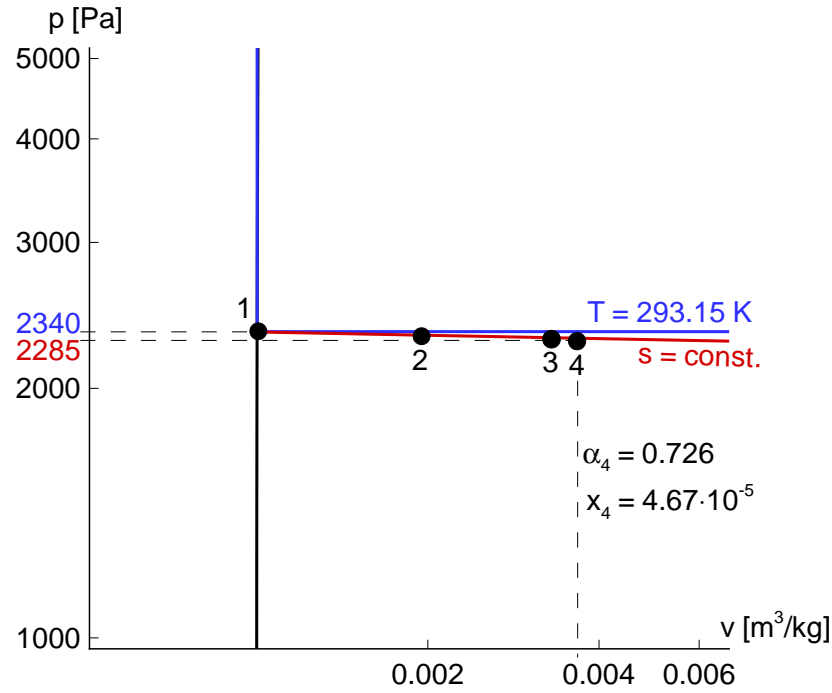


Figure 2.6: Zoomed area of the $p - v$ diagram given in Fig. 2.5. The points 1-4 correspond to the cell values on the depicted streamline, $\Delta T_{1-4} \approx 0.4 \text{ K}$, $\Delta p_{1-4} \approx 55 \text{ Pa}$.

This phenomenon is also seen in the calculation and as we move along the streamline shown in the figure, the temperature decreases from point 1 to point 4 and the void fraction increases. Figure 2.5 (bottom) shows the process in the $p - v$ diagram. In the calculation the temperature difference between points 1 and 4 is extremely small, i.e. $\Delta T_{1-4} \approx 0.4 \text{ K}$. Moreover, as there is no heat transfer to the system from outside, analogous to the closed system discussion given earlier, the process follows the isentrope depicted by the red curve. As the temperature difference is not recognizable, a zoomed in view of the yellow boxed area is given in Fig. 2.6. Here one can see that the depicted points follow the isentrope and the last point corresponds to a void fraction value of $\alpha = 0.726$ or a mass fraction value of $x = 4.67 \cdot 10^{-5}$. This calculation and the implemented model are based on the equilibrium flow assumption. The motivation of this assumption will be discussed in section 2.4.1. But from the discussion so far, we can conclude that, **in a steady-state Euler flow the equilibrium phase change along a streamline follows the isentrope and thus the mentioned process is isentropic.**

It should also be noted that **equilibrium flow** is different from the **equilibrium conditions** in a closed system. Equilibrium conditions assumes $dq/dt = 0$ for all values of τ , whereas in equilibrium flow $dq^*/dt \neq 0$ and $\tau = 0$. Accordingly, equilibrium flow can involve changes in q as a result of species production due to the effects of the flow field or the convective flow.

Thus, considering any internal process occurring during the flow one can postulate the following definitions:

- **Non-equilibrium flow** means that the time rate of the internal process is im-

portant within the time scale of the flow and it should be therefore modeled (by means of new transport equations and time dependent source terms).

- **Equilibrium flow** means that the time rate of this internal process is vanishingly small and it is therefore not taken into account in the formulations of such problems.

2.1.2 Vapor-liquid Equilibria

In conjunction with the discussion in the previous section, thermodynamics of the phase transition processes, especially the vapor-liquid equilibria, will be discussed here.

Thermodynamically distinct phases of pure substances can be visualized through phase diagrams where equilibrium conditions or phase boundaries are characterized by curved lines. The following p - v - T diagram of water represents the solid, liquid and vapor phases together with co-existence regions [81].

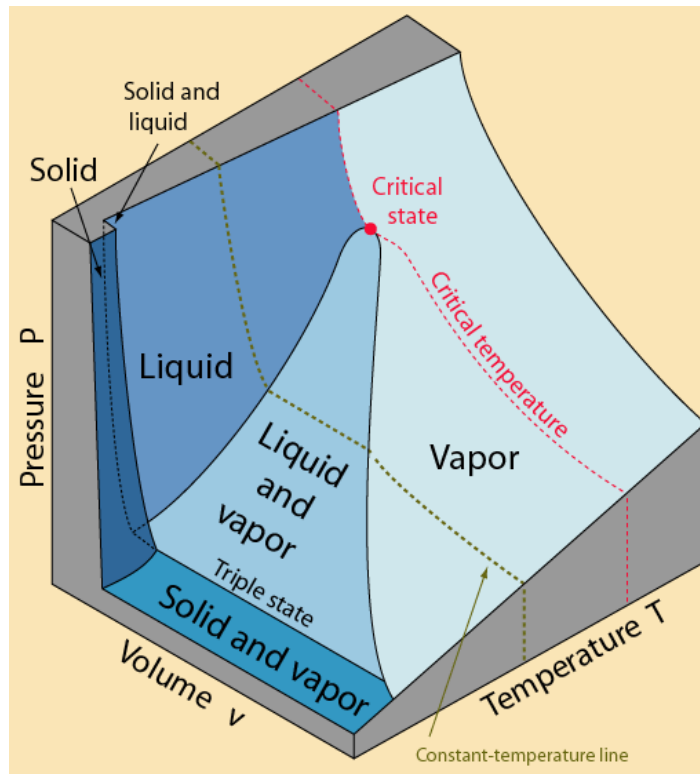


Figure 2.7: Representative p - v - T surface for water. The axes show pressure p , specific volume v and temperature T [81].

The p - v - T surface given in Fig. 2.7 requires further consideration. The equilibrium condition given by the horizontal line connecting the two ends of the co-existence curve is not always experienced in real applications. The best known example of such a process is often seen in steam turbines, where a supersaturated vapor state can occur although the phase diagram suggests that vapor should condense so that liquid and vapor should coexist in equilibrium. This supersaturated state is referred to as **metastable state**.

Similarly, another metastable state can be observed by the overexpansion of the liquid phase. This case has already been mentioned and discussed in chapter 1 as liquid tension, where the liquid expands below the saturation pressure without forming the vapor phase. In such processes, even “negative pressures” (or tension) can be observed for short periods of time.

In order to clarify the discussion of the metastable states, one can consider the isotherms of the $p - v$ diagram. This can be done by considering a general equation of state such as the van der Waals equation. This equation describes the isotherms inside the liquid-vapor equilibrium region not with horizontal lines but allows metastable states. Figure 2.8 depicts corresponding sub-critical isotherms T_1 and T_2 following the van der Waals equation. Moreover, one can connect the maxima and the minima of the van der Waals isotherms to the critical point. The resulting left hand side curve XQc is referred to as the **liquid spinodal line** and the right hand side curve ZSc is referred to as the **vapor spinodal line**.

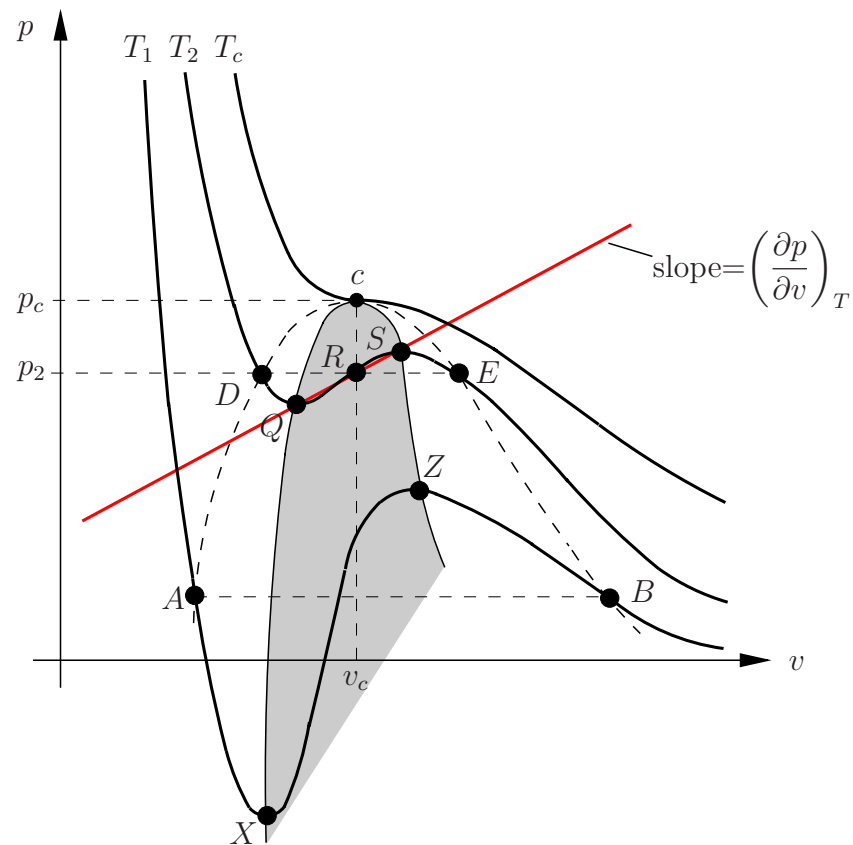


Figure 2.8: The isotherms of the $p - v$ diagram following the analytical expression of the van der Waals equation. The equilibrium behavior is given by DE and AB . DQ and AX represent the overexpansion of the liquid, SE and ZB correspond to the supersaturation of the vapor. The grey area bounded by the spinodal lines depicts physically not-allowable states (see Eq. 2.17 or 2.26).

If one considers the T_2 isotherm, the analytical solution gives the $DQRSE$ curve, whereas equilibrium phase change takes place along the horizontal line DE , where the pressure is constant and equal to p_2 . In order to see the physical limitations on the theoretical isotherms, we consider the straight red line passing through the points Q

and S , such that it connects the minimum and maximum points of the considered isotherm. From the figure it can be seen that the slope of this line is positive and is equal to $(\partial p/\partial v)_T$. Recalling the definition of the isothermal compressibility, which was derived in chapter 1 as

$$\tau_T = -\frac{1}{v} \left(\frac{\partial v}{\partial p} \right)_T. \quad (2.16)$$

We have already concluded in chapter 1 that as the compressibility of a substance cannot be negative, following Eq. 2.16, the derivative $(\partial v/\partial p)_T$ must be **negative** for the complete thermodynamic range in consideration, i.e.

$$\left(\frac{\partial v}{\partial p} \right)_T \leq 0. \quad (2.17)$$

The positive slope portions of the van der Waals isotherms (QRS and XZ lines) violate this condition and therefore they define **physically not-allowable states**. As a result, the grey area in Fig. 2.8, bounded by the spinodal lines depicts non-physical conditions.

One can end up with the same conclusion by considering the fundamental thermodynamic laws. Maxwell introduced a way for finding the vapor pressure from the isotherms of the analytical equations [77]. Thus, the Gibbs free energy per unit mass for a pure phase is defined as

$$g = h - Ts. \quad (2.18)$$

When unit mass of a liquid is vaporized, the change of Gibbs free energy is given by

$$g_v - g_l = \int v dp, \quad (2.19)$$

where the integration is carried along the $DQRSE$ portion of the isotherm. By definition, when the vapor and liquid are in equilibrium the Gibbs free energy of the phases are equal to each other, i.e. $g_l = g_v$. Therefore, the integral in the Eq. 2.19 reduces to zero. This means that the area bounded by the curve DQR and the line DR should be equal to the area between the curve RSE and the line RE .

Although equilibrium phase transition takes place through the line DE , previously discussed metastable states can also be realized on the isotherms. The segment SE of the isotherm T_2 corresponds to the supersaturation states and, similarly, the segment DQ corresponds to the states of overexpansion. Moreover, “negative pressures” that lead to liquid tension are observed through the AX segment of the T_1 isotherm. It should be noted that these isotherms follow analytical expressions and do not always resemble physical behavior. In order to relate the analytical expression to physical observations, one must consider the thermodynamic constraints. Thereby, the Helmholtz free energy per unit mass is defined as

$$f = e - Ts. \quad (2.20)$$

The second law of thermodynamics states that a stable state has the minimum value of Helmholtz free energy f with respect to variations at constant temperature and volume [45]. An isothermal variation of Helmholtz free energy with respect to specific volume v is plotted in Fig. 2.9.

If point a corresponds to any stable state of a substance, alterations from this point are possible via isothermal expansion or isothermal compression. Thereby, a new state

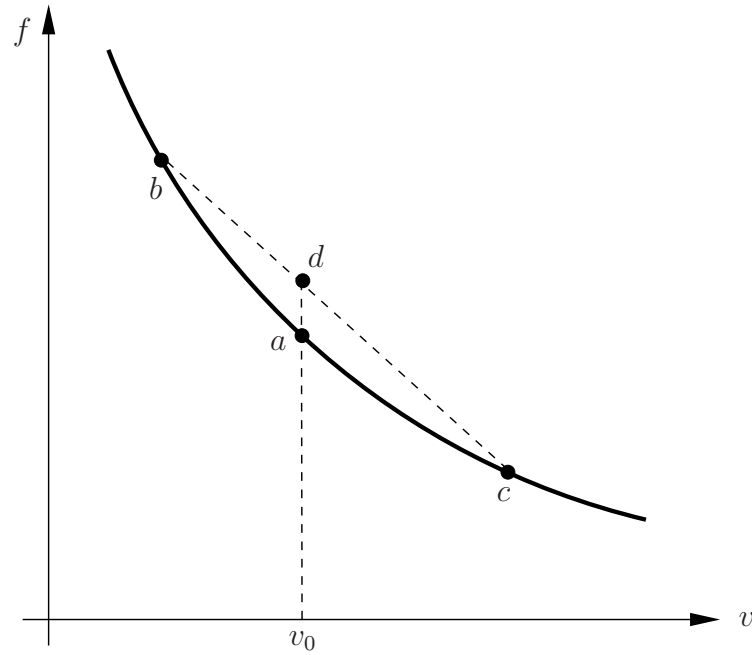


Figure 2.9: Isothermal variation of the Helmholtz free energy f with respect to specific volume v for a stable system.

can be achieved by compressing a portion of the system to point b and expanding the remaining portion to point c by ensuring the total volume remains the same. The resulting Helmholtz free energy value of the new state is given by point d . It is seen from the figure that the new state d has a higher Helmholtz free energy, hence it is unstable. If the curve was concave downward, the new state would have a lower Helmholtz free energy and would be more stable. Thus, we conclude that the concave upward curve given by Fig 2.9 satisfies the following Eq.

$$\left(\frac{\partial^2 f}{\partial v^2}\right)_T \geq 0 \quad (2.21)$$

and envelopes a series of stable states. A small change in Helmholtz free energy (Eq. 2.20) is given by

$$df = de - d(Ts) = de - Tds - sdT. \quad (2.22)$$

From the first law of thermodynamics it is known that

$$de = Tds - pdv. \quad (2.23)$$

Combining the equations 2.22 and 2.23, one obtains

$$df = -sdT - pdv. \quad (2.24)$$

For the isothermal process discussed previously where $dT = 0$, the change in Helmholtz free energy with respect to the specific volume v becomes

$$\left(\frac{\partial f}{\partial v}\right)_T = -p. \quad (2.25)$$

Comparing the equations 2.21 and 2.25, one can conclude that

$$\left(\frac{\partial p}{\partial v}\right)_T \leq 0. \quad (2.26)$$

As expected we end up with the same conclusion as in the previous analysis. Equations 2.17 or 2.26 are important in understanding the physical behavior of the phase change process. It states that any equation of state in the form $p = p(v, T)$ can represent a series of allowable states **if, and only if**, the condition given by Eq. 2.26 is **satisfied**. Otherwise, the system would be unstable with respect to any infinitesimal density fluctuation. This was already discussed in the first part, where the analytical isotherms plotted in Fig. 2.8 were analyzed with respect to their slopes. It is clear that the portions DQ and SE have negative slopes, therefore they satisfy Eq. 2.26 and thus represent the stable states of the system with respect to small fluctuations in the density. These regions correspond to the metastable states of overexpansion and supersaturation respectively, while the portions QRS and XZ have positive slopes, i.e. $(\partial p/\partial v)_T > 0$, which means that the states described by these segments are not even metastable and in fact they are physically **not defined**, as already explained earlier.

2.2 Effect of Molecular Viscosity and Turbulence

Viscosity can be defined as “the macroscopic effect of the momentum transport taking place in the molecular level in a fluid domain” [124] and it tends to damp out the flow perturbations inside the flow field [76]. As already given in chapter 1, for a given fluid, viscosity is measured by using the coefficient of dynamic viscosity μ or by using the kinematic viscosity $\nu = \mu/\rho$.

In terms of **single bubble dynamics**, viscosity plays a role in the final stages of the collapse only when the bubble radius is of the order of $10^{-7} m$ [30]. Such a spatial resolution in a numerical simulation is hardly applicable in the flow problems that are considered. Moreover, Ivany et al. [49], [50] investigated the growth and collapse of cavitation bubbles and found out that the damping effect of viscosity can be neglected in low viscous fluids like water.

In terms of **flow dynamics**, in the applications that are considered, it is known a priori from the experiments or from the previous simulations that the corresponding **single-phase liquid flows** do not separate and therefore the boundary layer is **attached**. As a result, the global flow will experience only a **weak displacement effect**, as long as the boundary layers are thin and remain attached. Similarly in the **unsteady developed cavitation dynamics**, which is the main topic in this investigation, the cloud shedding behavior, their collapse mechanisms and the resulting shock and wave dynamics are all driven by the **inertia effects** and therefore viscosity plays a minor role.

In order to demonstrate the effects of viscosity on the flow dynamics we can consider the Reynolds number, which is defined in chapter 1 as

$$Re_{l_{ref}} = \frac{\rho_{\infty} \cdot u_{ref} \cdot l_{ref}}{\mu_{\infty}}. \quad (2.27)$$

In wall bounded flows the thickness of the viscous boundary layer can be written as a function of the Reynolds number [99], [129]. Depending on the nature of the flow (laminar or turbulent) boundary layer thicknesses for a flat plate flow can be approximated as follows [99]

$$\frac{\delta_{lam}}{x} = \frac{5.0}{\sqrt{Re_x}}, \quad (2.28)$$

$$\frac{\delta_{tur}}{x} = \frac{0.37}{\sqrt[5]{Re_x}}. \quad (2.29)$$

It should be noted that these equations are approximations for flat plate flows but they can be used to determine the length scale of the boundary layers associated with the considered flow problems.

In hydrofoil calculations the reference velocity is $u_{ref} = 10 - 50 \text{ m/s}$ and the reference length is the chord length of the hydrofoils, which is on the order of $c \approx 0.1 \text{ m}$. In a **single-phase water flow** with viscosity $\mu_\infty = 1.002 \cdot 10^{-3} \text{ Pa} \cdot \text{s}$ and density $\rho_\infty = 998 \text{ kg/m}^3$, the Reynolds number turns out to be $Re = 1.0 \cdot 10^6 - 5.0 \cdot 10^6$. Using equations 2.28 and 2.29 laminar and turbulent boundary layer thicknesses at the end of the hydrofoil are found as $\delta_{lam} = 5 \cdot 10^{-4} \text{ m}$ and $\delta_{tur} = 2.3 \cdot 10^{-3} \text{ m}$ respectively.

A similar analysis for the injection nozzles with bore lengths of the order of 10^{-3} m and with a reference velocity of $u_{ref} = 100 \text{ m/s}$ results in laminar and turbulent boundary layer thicknesses $\delta_{lam} = 1.6 \cdot 10^{-5} \text{ m}$ and $\delta_{tur} = 3.9 \cdot 10^{-5} \text{ m}$ respectively. However, due to the extremely short length scales (bore hole length $l \approx 10^{-3} \text{ m}$ and diameter $d \approx 2 - 4 \cdot 10^{-4} \text{ m}$), the flow cannot fully develop inside the bore hole - the boundary layers remain thin and do not merge. Therefore, the flow is most likely to be of transitional type.

Both studies show that the boundary layers in the considered single-phase water flows are thin with respect to the characteristic dimensions of the flow domains and high Reynolds numbers associated with the flow conditions suggest that only weak displacement effect is expected in the unseparated single-phase flow. But as high Reynolds numbers drive the flow field into the turbulent regime, one should consider the effect of turbulence on cavitating flows. A pressure fluctuation level due to turbulence can be determined by using the definition of turbulence intensity Tu as

$$Tu = \frac{\sqrt{u' \cdot u'}}{\bar{u}}, \quad (2.30)$$

where \bar{u} is the mean velocity of the flow and u' is the turbulent fluctuation velocity [131]. The turbulent pressure fluctuation can be approximated as

$$p' \approx \frac{1}{2} \rho u'^2. \quad (2.31)$$

In the injection nozzle calculations that will be presented in chapter 5, the flow accelerates at the nozzle throat and reduces the turbulence effects inside the bore hole. Therefore, one can assume that the flow has a weak turbulence intensity Tu on the order of $\sim 10^{-3}$, i.e.

$$Tu = \frac{\sqrt{u' \cdot u'}}{\bar{u}} \approx 10^{-3}. \quad (2.32)$$

For a mean velocity of $\bar{u} = 100 \text{ m/s}$, the turbulent fluctuation velocity u' can be found by using the above equation as $|u'| = 0.1 \text{ m/s}$. This velocity corresponds to a pressure fluctuation which can be approximated as

$$p' \approx \frac{1}{2} \rho u'^2 = \frac{1}{2} \cdot 1000 \cdot 0.1^2 = 5 \text{ Pa} . \quad (2.33)$$

This pressure fluctuation can also be interpreted in terms of the change in the cavitation number of the considered flow problem, i.e.

$$\Delta\sigma_{Tu} = \mp \frac{p'}{\frac{1}{2} \rho_\infty \cdot u_\infty^2} , \quad (2.34)$$

Therefore for the given injection nozzle calculation the change in the cavitation number due to turbulence can be estimated as $\Delta\sigma_{Tu} = \mp 0.0001$. As a result the effect of turbulence in cavitating flows can be neglected if $\Delta\sigma_{Tu} \ll \sigma_{min}$, where σ_{min} is the minimum cavitation number in the flow field.

In terms of cavitating flows, the viscosity tends to decrease the critical cavitation number as it slows down the growth of individual bubbles through the damping effect mentioned earlier [96]. The decrease in critical cavitation number alters the cavitation inception behavior and it is significant for the flows where flow separation exists. The experiments of Arakeri [8] showed that laminar separation on a wall provides a site for cavitation inception and by eliminating the laminar separation they could control the inception. Similarly, Franc and Michel [31] found that a well developed cavity always detaches downstream of the laminar separation of the boundary layer and the existence of separation generates conditions that the cavity can remain attached to the wall. If the boundary layer does not separate, the cavity is affected by the upcoming flow and cannot remain attached [30].

As mentioned earlier, in the applications that are considered in this thesis, unsteady cavitation dynamics, cloud shedding and their collapse mechanisms are of primary interest together with the shock and wave dynamics inside the flow field. All these mentioned effects are inertia controlled [32], [92] and therefore viscosity plays a minor role.

Nonetheless, substantial care should be taken into account when neglecting viscosity in flows, where viscous separation is likely to occur. To ensure that the unsteady two-phase flow dynamics and related cloud shedding mechanisms are dominated by inertia effects, one must a priori verify that the single-phase flow for the same geometry and flow conditions remains attached at all times. This can be checked either by experimental observations or Navier-Stokes simulations of the flow field. For 2-D and 3-D hydrofoil flows that are presented in chapter 5, experimental observations show that viscous separation does not occur in single-phase flow [32], [96], whilst for the considered injection nozzle geometry, viscous flow simulations ensure that the flow remains attached inside the bore hole [107], [137].

2.3 Governing Equations

The focus of the present thesis work can be stated as the development of a new multi-purpose solution package for compressible flow dynamics including pure liquids and

phase transition, chemical reaction and heat addition. The phase transition process from liquid to vapor is modeled by assuming **equilibrium flow** and for the preliminary development, following the discussion given in the previous subsection, viscosity is neglected and the conservation principles are expressed by the Euler equations. However, the inclusion of dissipative mechanisms into the model is easily possible; this will be shortly presented in appendix B for single-phase ideal gas flows.

2.3.1 Differential Form of the Equations

The differential form of the Euler equations in the vector form without body forces can be written as

$$\frac{\partial \mathbf{q}}{\partial t} + \frac{\partial \mathbf{f}}{\partial x} + \frac{\partial \mathbf{g}}{\partial y} + \frac{\partial \mathbf{h}}{\partial z} = 0, \quad (2.35)$$

where \mathbf{q} is the vector of conserved quantities and \mathbf{f} , \mathbf{g} and \mathbf{h} are the physical flux vectors at each spatial direction x, y and z given by

$$\mathbf{q} = \begin{pmatrix} \rho \\ \rho u \\ \rho v \\ \rho w \\ \rho E \end{pmatrix}, \quad \mathbf{f} = \begin{pmatrix} \rho u \\ \rho u^2 + p \\ \rho uv \\ \rho uw \\ \rho uH \end{pmatrix}, \quad \mathbf{g} = \begin{pmatrix} \rho v \\ \rho vu \\ \rho v^2 + p \\ \rho vw \\ \rho vH \end{pmatrix}, \quad \mathbf{h} = \begin{pmatrix} \rho w \\ \rho wu \\ \rho wv \\ \rho w^2 + p \\ \rho wH \end{pmatrix}. \quad (2.36)$$

Total energy E and total enthalpy H are defined as

$$E = e + \frac{1}{2}(u^2 + v^2 + w^2), \quad (2.37)$$

$$H = h + \frac{1}{2}(u^2 + v^2 + w^2) = E + \frac{p}{\rho}, \quad (2.38)$$

where e is the specific internal energy and h is the specific enthalpy per unit mass. In addition to the above given relations, the set of Euler equations requires the definition of a closure relation to couple the energy equation with the momentum equation. This closure relation in the case of Euler equations is the **equation of state** of the considered fluid. Therefore, for a single-phase flow an equation of state in the form, $e = e(p, \rho)$ is necessary and sufficient. If the considered fluid is not chemically reacting (i.e. equilibrium flow) and if the intermolecular forces are ignored the resulting system is called thermally perfect and specific internal energy and specific enthalpy are functions of the temperature only [5], i.e.

$$\begin{aligned} e &= e(T), \\ h &= h(T). \end{aligned} \quad (2.39)$$

Similarly for a thermally perfect system, specific heats at constant pressure c_p and at constant volume c_v are also functions of temperature only and following relations hold

$$\begin{aligned} de &= c_v dT, \\ dh &= c_p dT. \end{aligned} \quad (2.40)$$

Moreover, if the specific heats are constant, the system is called calorically perfect and following equations can be written

$$\begin{aligned} e &= c_v T, \\ h &= c_p T, \\ p &= (\kappa - 1)\rho e, \end{aligned} \tag{2.41}$$

where κ is the ratio of the specific heats as $\kappa = c_p/c_v$.

As the flow problems that are considered in this thesis involve cavitating two-phase flows with water and water vapor, each phase should be represented correctly. **Water vapor** can be treated as a thermally perfect gas [17] and therefore, specific internal energy and specific enthalpy are the functions of temperature only. For **liquid water** perfect gas assumption is not valid and a suitable equation of state is needed in order to close the equation system. Similarly, for the **cavitating two-phase flows**, an equation of state is needed for the complete thermodynamic range from liquid to vapor phase including the mixture state. A complete description of the cavitation modeling and the equation of states of the phases will be given in the following sections (see section 2.5).

The three flux components \mathbf{f} , \mathbf{g} and \mathbf{h} in equations 2.35 and 2.36 can be written in a single flux vector by using the unsplit formulation for the Euler equations as [119]

$$F_i(\mathbf{q}) = \rho u_i \cdot \begin{vmatrix} 1 \\ u \\ v \\ w \\ E \end{vmatrix} + p \cdot \begin{vmatrix} 0 \\ \delta_{1i} \\ \delta_{2i} \\ \delta_{3i} \\ u_i \end{vmatrix}. \tag{2.42}$$

In this equation $F_i(\mathbf{q})$ is the physical flux in coordinate direction x_i , u_i denotes the velocity vector components at each coordinate direction as $u_i = (u \ v \ w)^T$ and δ_{ij} denotes the Kronecker symbol. Thus, the differential or point-wise form of Eq. 2.35 reads

$$\frac{\partial}{\partial t} \mathbf{q} + \sum_{i=1}^3 \frac{\partial}{\partial x_i} F_i(\mathbf{q}) = 0. \tag{2.43}$$

2.3.2 Integral Form of the Equations

The differential form of the Euler equations (2.35 or 2.43) is valid only if the flow variables are differentiable and continuous through the whole flow domain. However, in order to model shock and wave dynamics in compressible flows and to represent phase boundaries in cavitating flows, we have to take the arising discontinuities into consideration. Therefore, the weak form or so-called integral form of the Euler equations should be used.

To define the weak formulation for the equation system given by Eq. 2.35 or 2.43, first we consider the following conservation law of the form

$$\frac{\partial U}{\partial t} + \nabla \cdot \mathbf{F} = Q, \tag{2.44}$$

where \mathbf{F} is the flux vector containing only convective contributions in the domain Ω bounded by $\Gamma = \Gamma_0 \cup \Gamma_1$ with the following initial and boundary conditions [44]

$$\begin{aligned} U(\mathbf{x}, 0) &= U_0(\mathbf{x}) & t = 0, x \in \Omega, \\ U(\mathbf{x}, t) &= U_1(\mathbf{x}) & t \geq 0, x \in \Gamma_0, \\ F_n &= g & t \geq 0, x \in \Gamma_1, \end{aligned} \quad (2.45)$$

where $F_n = g$ is the boundary value of the flux vector. Defining a weak formulation with a weighting function W on Γ_0 leads to

$$\int_{\Omega} \frac{\partial U}{\partial t} W d\Omega + \int_{\Omega} (\nabla \cdot \mathbf{F}) W d\Omega = \int_{\Omega} Q W d\Omega. \quad (2.46)$$

This method is originally derived for the finite element Galerkin method [82], where Eq. 2.46 is solved at every node J of a subdomain Ω_J with a weighting function equal to a interpolation function at that node, i.e. $W = N_J$ [44]. We consider the following arbitrary subdomain (or **control volume**) Ω_J corresponding to node J , which is located at the center of the domain.

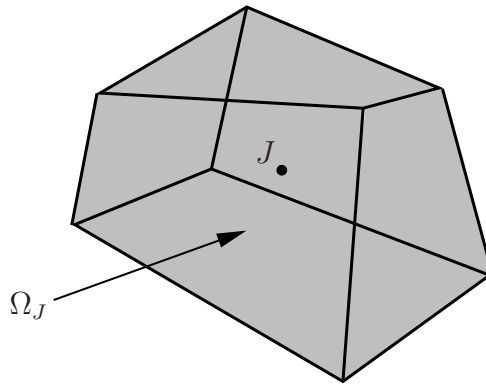


Figure 2.10: An arbitrary control volume Ω_J and corresponding cell center J .

By defining the weighting function as

$$\begin{aligned} W_J(\mathbf{x}) &= 0 & \mathbf{x} \notin \Omega_J, \\ W_J(\mathbf{x}) &= 1 & \mathbf{x} \in \Omega_J, \end{aligned} \quad (2.47)$$

Eq. 2.46 becomes

$$\int_{\Omega_J} \frac{\partial U}{\partial t} d\Omega + \int_{\Omega_J} (\nabla \cdot \mathbf{F}) d\Omega = \int_{\Omega_J} Q d\Omega. \quad (2.48)$$

Gauss theorem can be applied to the flux term, which leads to the conservation equation in integral form written for each subdomain Ω_J bounded by the corresponding closed surface Γ_J having an outward normal vector \mathbf{S} .

$$\int_{\Omega_J} \frac{\partial U}{\partial t} d\Omega + \oint_{\Gamma_J} \mathbf{F} \cdot d\mathbf{S} = \int_{\Omega_J} Q d\Omega. \quad (2.49)$$

As the derivative and integral are interchangeable, the above equation can also be written as

$$\frac{\partial}{\partial t} \int_{\Omega_J} U d\Omega + \oint_{\Gamma_J} \mathbf{F} \cdot d\mathbf{S} = \int_{\Omega_J} Q d\Omega. \quad (2.50)$$

If the physical problem or the equation system does not involve any source terms, i.e. $Q = 0$, the equation simplifies to

$$\frac{\partial}{\partial t} \int_{\Omega_J} U d\Omega + \oint_{\Gamma_J} \mathbf{F} \cdot d\mathbf{S} = 0. \quad (2.51)$$

These resulting two equations are the integral conservation form of the general differential conservation equation given by Eq. 2.44. As the system of the Euler equations is also in the conservation form and it mimics Eq. 2.44 with $U = \mathbf{q}$, $\mathbf{F} = \sum_{i=1}^3 F_i(\mathbf{q})$ and $Q = 0$, one can write

$$\frac{\partial}{\partial t} \int_{\Omega_J} \mathbf{q} d\Omega + \oint_{\Gamma_J} \sum_{i=1}^3 F_i(\mathbf{q}) \cdot d\mathbf{S} = 0. \quad (2.52)$$

Equation 2.52 is the weak formulation of the system of Euler equations and it can be replaced by its discrete form, where the volume integral is expressed as its averaged values in cell J such that $\mathbf{q}_J = A_J(\mathbf{q})$, where $A_J(\mathbf{q})$ is the cell average operator defined as

$$A_J(\mathbf{q}) \equiv \frac{1}{\Omega_J} \int_{\Omega_J} \mathbf{q} d\Omega, \quad (2.53)$$

and the surface integral is replaced by a sum over all the bounding faces Γ_J of the considered volume Ω_J

$$\frac{d}{dt} \mathbf{q}_J + \sum_{\Gamma_J} \sum_{i=1}^3 F_i(\mathbf{q}) \cdot \Delta\mathbf{S} = 0. \quad (2.54)$$

Equation 2.54 is the discrete form of the governing equations for a flow domain divided into finite control volumes of Ω_J . This equation is valid for any type of multi-component and multi-phase inviscid flow, even if the species do not share a common pressure, temperature or velocity. The solution of the flow problem requires an appropriate numerical discretization scheme, which will be explained in detail in chapter 3.

2.4 Equilibrium Two-phase Model

As stated in chapter 1, various methods are applicable to model the phase transition associated with cavitating flows. The focus of the present thesis work relies on compressible dynamics and the corresponding wave propagation phenomena in such flows.

Therefore, the proposed model should correctly resolve the arising two-phase regions as well as the wave propagation throughout the flow domain.

The weak formulation given in the previous section allows for the computation of integral average values of the flow variables in each computational cell. Once the flow variables are determined according to the arising flow field, phase transition should be taken into account.

2.4.1 Relaxation Time in Cavitating Flows

Overexpansion of the liquid phase and the corresponding liquid tension properties have already been discussed in the previous sections. One must consider these metastable states before proposing a phase transition model. In that sense, the time scale of the convective and wave motion should be taken into account.

It is known that traveling expansion waves may cause tension and therefore metastable states in the liquid before the equilibrium condition is reached [53]. The cavitating shock tube experiments of Bode et al. [12] showed that the maximum tension is closely related to the initial purity of the water. These experiments have demonstrated that an increase in the initial cavitation nuclei density in the liquid tends to diminish pressure oscillations including tension. Moreover, Trevena [120] suggested that, by using processes such as boiling and de-ionization, the allowable liquid tension of water can be increased significantly and meta-stable states far beyond saturation conditions can be observed. As a comparison, an analytical estimate together with an experimental observation for the relaxation time of the tensile stress is given by Kendrinskii [53], where cavitation in a vertically accelerated tube is investigated. In the experiment, cavitation is produced near the bottom of a vertical tube filled with liquid when the tube is suddenly accelerated downward by an impact. The experiment is simulated numerically by using a one-dimensional model by Kendrinskii [53], where in the model an infinitesimally small initial gas content and radius ($\alpha_0 = 10^{-10}$ and $R_0 = 1 \cdot 10^{-6} m$) are considered with an expansion wave of a strength of 300 bar. For these conditions, the relaxation time of the tensile stresses in the cavitating liquid turns out to be of order of $10^{-8} s$. This value is obtained for a relatively low gas content that is normally not applicable to real systems [120], [12] and thus the relaxation time decreases significantly with increasing the initial gas content of the water. Accordingly, tap water does not show this meta-stable behavior where the large number of impurities immediately results in heterogeneous nucleation [26] and thus in the formation of vapor bubbles.

As a result, the pressure relaxation time from meta-stable state to stable state is extremely short when compared with both the convective and the acoustic time scales of the flows that are considered in the current investigation. Furthermore, the development of the cavitation zone is mainly determined by the velocity of the fluid and the phase change process is considered to be fast enough that an instantaneous establishment of the equilibrium conditions is reached, i.e. $\tau \rightarrow 0$ (see the discussion in section 2.1.1). Due to this equilibrium assumption, meta-stable states are neglected in the proposed two-phase model. Consequently, the coexistence of both phases implies that the Clausius-Clapeyron relation holds, i.e. $p = p_{sat}(T)$. Moreover, following the analysis given in section 2.1.1, if there is no heat transfer between the system and the surroundings, the phase change from liquid to vapor takes place along the isentropes

of the $p - v$ diagram. Therefore, the temperature of the system **decreases**. As the isentropes have negative slope in the $\log p - \log v$ plane and they terminate at the triple line within the two-phase region, the current model does not allow the full vaporization of the liquid phase. It was also shown previously that **if the Euler flow is steady, the equilibrium phase change along a streamline follows the isentrope and thus the process is isentropic.**

2.4.2 Integral Average Formulation

In this subsection, the physical consequence of Eq. 2.54 on the flow field and two-phase domains will be discussed. As already introduced in chapter 1, the void fraction α can be written as

$$\alpha = \frac{V_{vap}}{V_{cell}}. \quad (2.55)$$

This equation gives the ratio of the vapor volume in a computational cell to the total volume of the cell; it does not contain any sub-grid information such as the structure of the vapor inside the cell or the bubble radius. In the following figure two identical control volumes are considered.

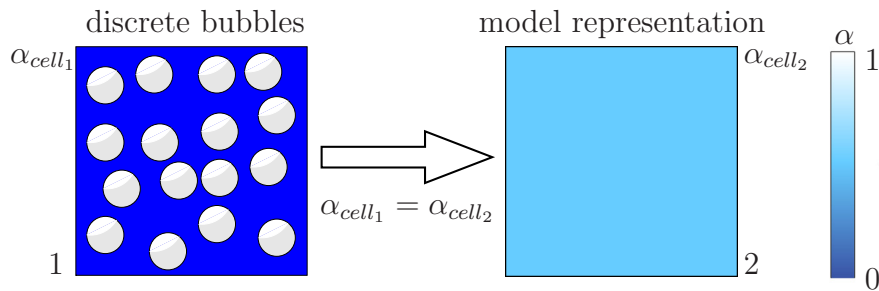


Figure 2.11: Physical situation and model representation of a control volume with vapor content.

The control volume on the left hand side depicts a possible physical situation with discrete bubbles of equal size. It should be noted that this is not the only possible situation and any kind of bubble size and distribution is possible in a physical system. The integral average formulation given in the previous section allows for defining the cell average values for the flow variables. Therefore, the void fraction value of the computational cell on the right hand side of Fig. 2.11 corresponds to the total void fraction value of the discrete bubble structures seen in the left picture, i.e. $\alpha_{cell_1} = \alpha_{cell_2}$. As a result, sub-grid structures are not modeled but their effects are included in the integral average formulation, so that no additional specification of small scale structures (radius, number density, etc.) is required. This is an important advantage of **CATUM**, as these parameters are problem dependent and their determination is hardly possible and requires complex experimental techniques.

The discretization of the flow domain through fixed control volumes of Ω_J introduces a local length scale l_J , which can be defined as $l_J \equiv \sqrt[3]{\Omega_J}$. In the case of cavitating bubbly liquid flow, the resolution of two-phase features depends on the fraction $\Psi = R/l_J$ of the bubble radius R and the induced length scale l_J . If $\Psi \ll 1$ the model resembles the average behavior of a mixture, while it fully resolves single bubbles if $\Psi \gg 1$.

Using Eq. 2.53, the integral average of the conservative variables, \mathbf{q} , inside the control volume Ω_J are defined as

$$\begin{aligned}\bar{\rho} &= \frac{1}{\Omega_J} \int_{\Omega_J} \rho \, d\Omega, \\ \overline{\rho u_i} &= \frac{1}{\Omega_J} \int_{\Omega_J} (\rho u_i) \, d\Omega, \\ \overline{\rho E} &= \frac{1}{\Omega_J} \int_{\Omega_J} (\rho E) \, d\Omega.\end{aligned}\tag{2.56}$$

The average specific internal energy \bar{e} follows from the average total energy by subtracting the specific kinetic energy such that

$$\bar{e} = \frac{1}{\bar{\rho}} \left(\overline{\rho E} - \frac{1}{2} \frac{\sum_{i=1}^3 (\overline{\rho u_i})^2}{\bar{\rho}} \right).\tag{2.57}$$

As the physical model is based on the integral average quantities that are evaluated in each computational cell, all variables follow this definition. Therefore, one can drop the bar over the variables and use the usual representation.

Assuming consistent initial and boundary data are strictly available, at each instant of time, the solution of the system Eq. 2.54 gives the average density ρ_J , velocity \mathbf{u} and total energy E_J within the cell Ω_J . However, the calculation of pressure, p_J requires additional model equations depending on the phase or the model under consideration.

It is important to note that the formulation given by Eqs. 2.56 and 2.57 does not distinguish if the considered flow is an ideal gas flow, liquid water flow or cavitating two-phase flow. Therefore, it is applicable to any flow type that is under consideration, as long as correct closure relations are defined depending on the flow type.

For the two-phase domains, integral average formulation together with thermodynamic equilibrium suggest that the average density ρ_J within cell Ω_J is a convex combination of temperature dependent saturation densities $\rho_{l,sat}(T_J)$, $\rho_{v,sat}(T_J)$ of liquid and vapor. Using the void fraction α , the average density ρ_J is defined as

$$\rho_J = \alpha_J \cdot \rho_{v,sat}(T_J) + (1 - \alpha_J) \cdot \rho_{l,sat}(T_J).\tag{2.58}$$

Following the above equation, the void fraction α_J of the considered control volume is found directly from

$$\alpha_J = \frac{\rho_J - \rho_{l,sat}(T_J)}{\rho_{v,sat}(T_J) - \rho_{l,sat}(T_J)}.\tag{2.59}$$

By using the vapor mass fraction x_J , the internal energy e_J of the considered control volume is given by

$$x_J \cdot \rho_J = \alpha_J \cdot \rho_{v,sat}(T_J),\tag{2.60}$$

$$e_J = x_J \cdot e_{v,sat}(T_J) + (1 - x_J) \cdot e_{l,sat}(T_J).\tag{2.61}$$

In accordance with the thermodynamic equilibrium, the average pressure for the two-phase domains is simply the saturation pressure at the given temperature, as

$$p_J = p_{sat}(T_J).\tag{2.62}$$

As a result, the unknown quantities T_J , α_J , x_J and p_J are found as solutions of the system given by Eqs. 2.58-2.62. The temperature dependent saturation conditions are modeled according to the Oldenbourg polynomials [83], given in A.1. Therefore, the required closure relation in the case of two-phase flow is completely defined. The numerical implementation of the solution procedure will be given in chapter 3.

2.5 Equation of State and Speed of Sound

In the previous section the two-phase modeling strategy for the cavitating flows is explained, which is defined by the saturation conditions of the liquid. This section will focus on the equation of state and the sonic speed definitions that are used in the model.

As mentioned earlier, the set of Euler equations requires definition of a closure relation to couple the energy equation with the momentum equation. This closure relation is the equation of state of the considered fluid. For ideal gas flows these relations are already given in section 2.3.1. Whereas for liquid flows these relations are not that straightforward and accurate. For this reason, a detailed survey and analysis is needed to decide on an equation of state to model the behavior of the liquid. In the current state of the solver, liquid water is used as the test fluid, so the investigated equations of state are compared with the available water data. The reference data for water and water vapor is taken from the IAPWS - International Association for the Properties of Water and Steam [47].

An often encountered equation of state for liquids is the stiffened equation of state or sometimes called ‘‘Tammann Equation’’, given by

$$p = p(\rho, e) = (\gamma - 1)\rho e - \gamma p_c. \quad (2.63)$$

The advantage of this equation is its simple form and resemblance to the ideal gas equation of state 2.41. The values of constants p_c and γ are liquid dependent. In [84] these constants are given for water as; $\gamma = 2.8$ and $p_c = 8.5 \times 10^8 Pa$. This EOS is suitable for describing **pure** liquids **without** phase change at high pressures and for liquid flows undergoing non-isentropic processes like underwater explosions or blast waves [51].

The second equation of state under consideration is the famous Tait equation, which has different forms in literature. The usual representation given by Thompson [117] is

$$p = p(\rho) = B \left[\left(\frac{\rho}{\rho_0} \right)^n - 1 \right] + p_0. \quad (2.64)$$

In this equation, B is a weak function of entropy and usually taken as constant, ρ_0 , p_0 and n are constants depending on the liquid. For water these constants are defined as $B = 3.3 \times 10^8 Pa$, $n = 7.15$ and $\rho_0 = 1000 kg/m^3$ [84]. Although the given form of the Tait equation is quite accurate for water up to 25000 bar [51], it is not applicable to the current formulation, as it describes a barotropic process, i.e. $p = p(\rho)$, where temperature dependence is neglected. Hence, the calculation of the energy equation becomes redundant. Saurel et al. [97] suggest a modification to Tait equation

by including the temperature dependency through replacing the constant reference properties with temperature dependent saturation pressure and corresponding liquid saturation density, such that

$$p = p(\rho, T) = B \left[\left(\frac{\rho}{\rho_{l,sat}(T)} \right)^n - 1 \right] + p_{sat}(T). \quad (2.65)$$

This equation will be referred to as the **modified Tait equation** from this point on. A caloric equation of state that is thermodynamically consistent with the Tait equation is given by

$$e = e(T) = c_{v,liq} \cdot (T - T_{ref}) + e_{l0}, \quad (2.66)$$

where $c_{v,liq}$ is the specific heat of water at constant volume, which is taken as constant $c_{v,liq} = 4186 \text{ J/kg} \cdot \text{K}$, $T_{ref} = 273.15 \text{ K}$ is the reference temperature and e_{l0} is the reference energy at this temperature (617 J/kg) [97]. In order to define a stable thermodynamical system, Eq. 2.65 must satisfy the following condition given in Eq. 2.26

$$\left(\frac{\partial p}{\partial v} \right)_T \leq 0. \quad (2.67)$$

Rewriting Eq. 2.65 using $v = 1/\rho$

$$p = p(v, T) = B \left[\left(\frac{1/v}{\rho_{l,sat}(T)} \right)^n - 1 \right] + p_{sat}(T) \quad (2.68)$$

and as differentiation is performed at constant temperature, saturation functions in Eq. 2.68 can be replaced by constants, i.e.

$$p = p(v, T) = B \left[\left(\frac{1/v}{C_1} \right)^n - 1 \right] + C_2. \quad (2.69)$$

Thus,

$$\begin{aligned} \left(\frac{\partial p}{\partial v} \right)_T &= \frac{\partial}{\partial v} \Big|_T \left\{ B \left[\left(\frac{1/v}{C_1} \right)^n - 1 \right] + C_2 \right\} \\ &= \frac{B}{C_1^n} \frac{\partial}{\partial v} \Big|_T \left(\frac{1}{v^n} \right) \\ &= -n \frac{1}{v^{n+1}} \frac{B}{C_1^n}. \end{aligned} \quad (2.70)$$

Let us consider each term in this equation individually; B and n are the constants of the Tait equation and $B > 0$, $n > 0$. We defined $C_1 = \rho_{l,sat}(T)$ which cannot be negative, and v is the specific volume of the fluid and always positive. As a result, as $-n$ is negative, the derivative is also negative and therefore the condition given by Eq. 2.67 is satisfied. This means that the modified Tait equation represents a series of stable thermodynamic states.

Before deciding on one of the equations given above, one should also test the accuracy of these equations for the thermodynamic ranges in question. In the following graphs (Figs. 2.12 and 2.13) all three equations are compared with the IAPWS data for two different temperatures.

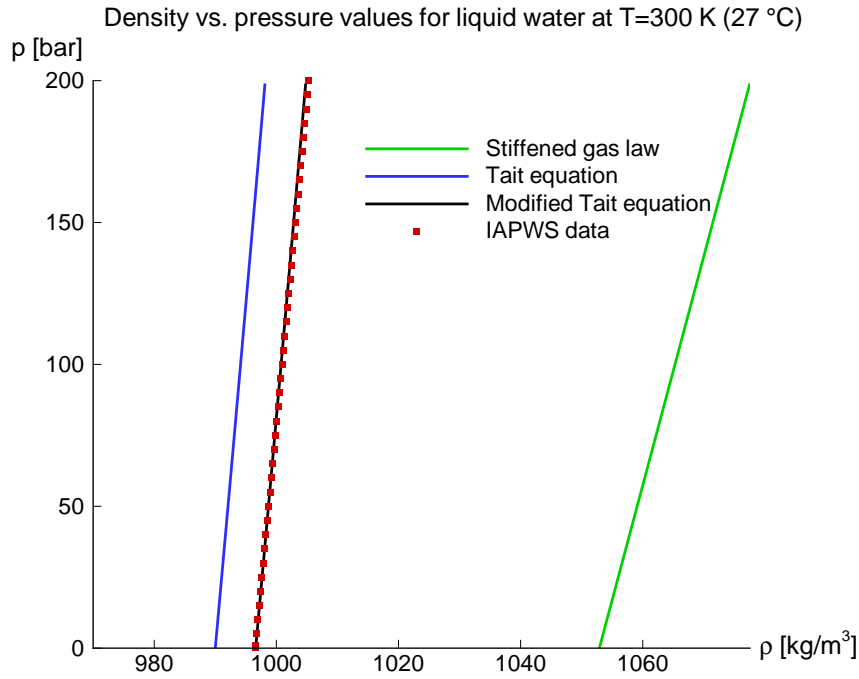


Figure 2.12: Comparison of the pressure vs. density values for the stiffened gas equation, Tait equation and modified Tait equation with the IAPWS data for $T = 300\text{ K}$.

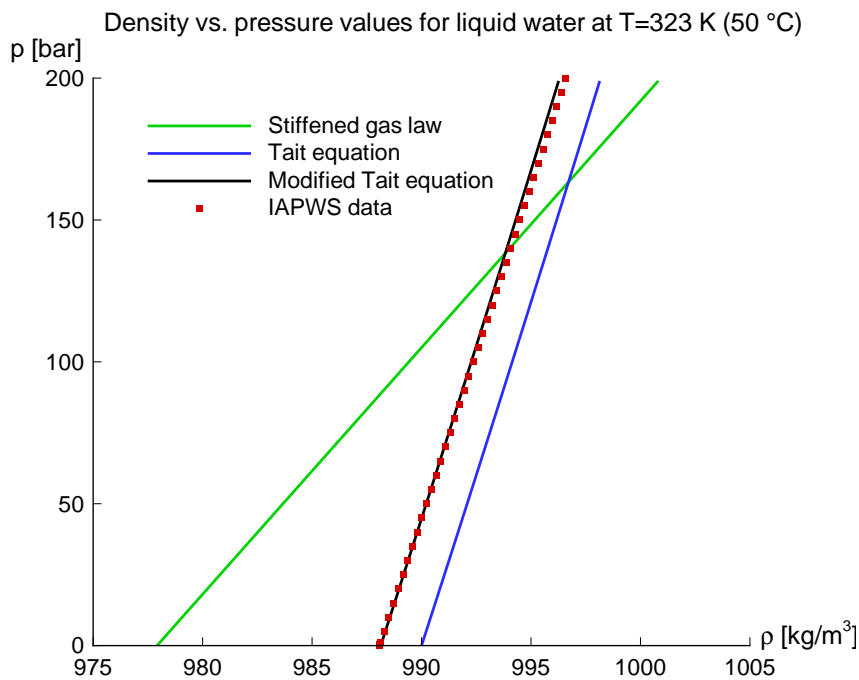


Figure 2.13: Comparison of the pressure vs. density values for the stiffened gas equation, Tait equation and modified Tait equation with the IAPWS data for $T = 323\text{ K}$.

Both figures clearly show that the modified Tait equation is far superior to the stiffened equation of state and the standard Tait equation. Moreover, the modified Tait equation is the only model that provides a continuous connection to the saturation conditions. Although the stiffened equation of state can be improved by adjusting the constants in the equation, it still can not predict the correct behavior and is therefore not applicable to the current investigation.

Table 2.1 shows the maximum error of each equation of state with respect to the IAPWS data for the investigated pressure range (0 – 200 bar) and temperatures ($T = 300\text{ K}, 323\text{ K}$).

Table 2.1: Maximum error of density for each equation of state with respect to the IAPWS data for **liquid water** in the investigated pressure range 0 – 200 bar.

Temperature	300 K	323 K
Stiffened EOS	72 kg/m ³ (7.16 %)	9.8 kg/m ³ (1.00 %)
Tait EOS	7.1 kg/m ³ (0.71 %)	1.9 kg/m ³ (0.19 %)
Modified Tait EOS	0.44 kg/m ³ (0.04 %)	0.3 kg/m ³ (0.03 %)

For the pure water vapor phase, the following well known ideal gas equation of state definition is used,

$$p = \rho RT, \quad (2.71)$$

together with a caloric equation of state in the form

$$e = c_{v,vap} \cdot (T - T_{ref}) + L_{vap,ref} + e_{l0}. \quad (2.72)$$

In the equations given above, R is the specific gas constant of the fluid, which is given by $R = \mathcal{R}/\mathcal{M}$, where \mathcal{M} is the molecular weight in kg/mol and \mathcal{R} is the universal gas constant ($\mathcal{R} = 8.31451\text{ J/mol} \cdot \text{K}$). For water $\mathcal{M} = 18.015 \cdot 10^{-3}\text{ kg/mol}$ and $R = 461.5\text{ J/kg} \cdot \text{K}$. In Eq. 2.72 $c_{v,vap}$ is the specific heat of water vapor at constant volume, $L_{vap,ref}$ is the latent heat of vaporization at T_{ref} and e_{l0} is the constant in the equation, which is given by $e_{l0} = 617\text{ J/kg}$. For the calculations, the reference temperature is chosen as $T_{ref} = 273.15\text{ K}$ and the corresponding latent heat of vaporization for water is $L_{vap,ref} = 2501.3 \cdot 10^3\text{ J/kg}$. In Fig. 2.14 a comparison of ideal gas values with the IAPWS data for the water vapor at $T = 293.15\text{ K}$ is presented.

Figure 2.14 verifies the accuracy of the ideal gas equation in the case of water vapor. Therefore, together with the previously given saturation state and liquid water definitions, the equation of state formulation for the whole range of interest is completed. In Fig. 2.15 the p - v behavior of the combined equation of state is plotted for all the phases, together with the IAPWS data for comparison. The saturation curve (green line) is obtained by the temperature dependent saturation functions given in A.1.

Both the modified Tait equation and the proposed two-phase model are based on temperature dependent saturation functions of the fluid under consideration. The constants of the Tait equation for various fluids can be found in literature (see Thompson [117]). Therefore, the two-phase formulation applicable to any liquid as long as the saturation conditions can be expressed by temperature dependent functions and if the constants in the Tait equation are known.

After completing the definition of an applicable equation of state as the numerical solution procedure requires, a sonic speed formulation is needed for all phases under consideration. The equation for the isentropic speed of sound in equilibrium flow is already given in chapter 1 as

$$c = \sqrt{\left. \frac{\partial p}{\partial \rho} \right|_s}. \quad (2.73)$$

Density vs. pressure values for water vapor at $T=293.15\text{ K}$ (20°C)

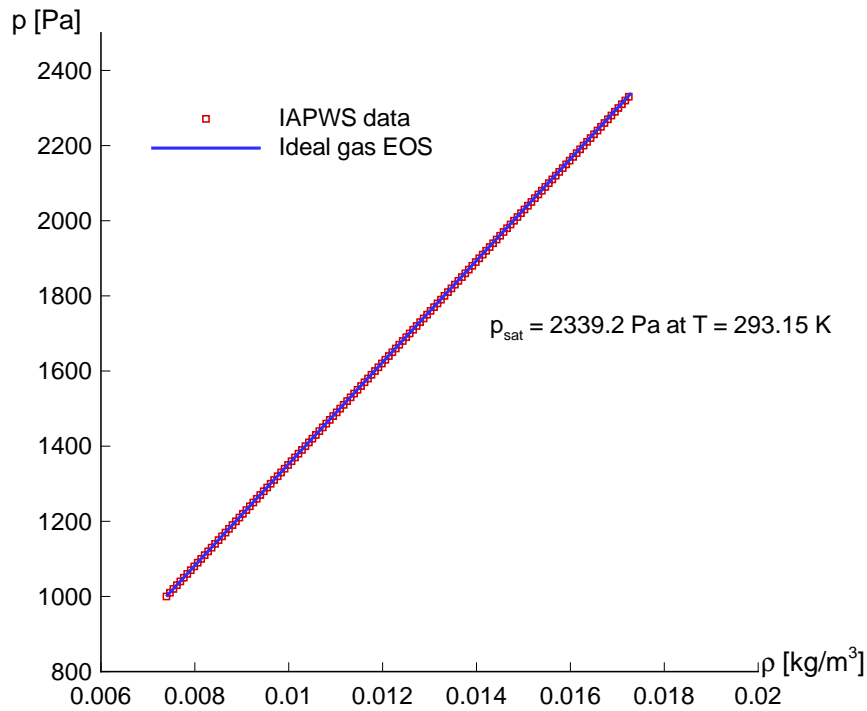


Figure 2.14: Pressure vs. density values for water vapor. Solid line: ideal gas equation, red squares: IAPWS data for $T = 293.15\text{ K}$.

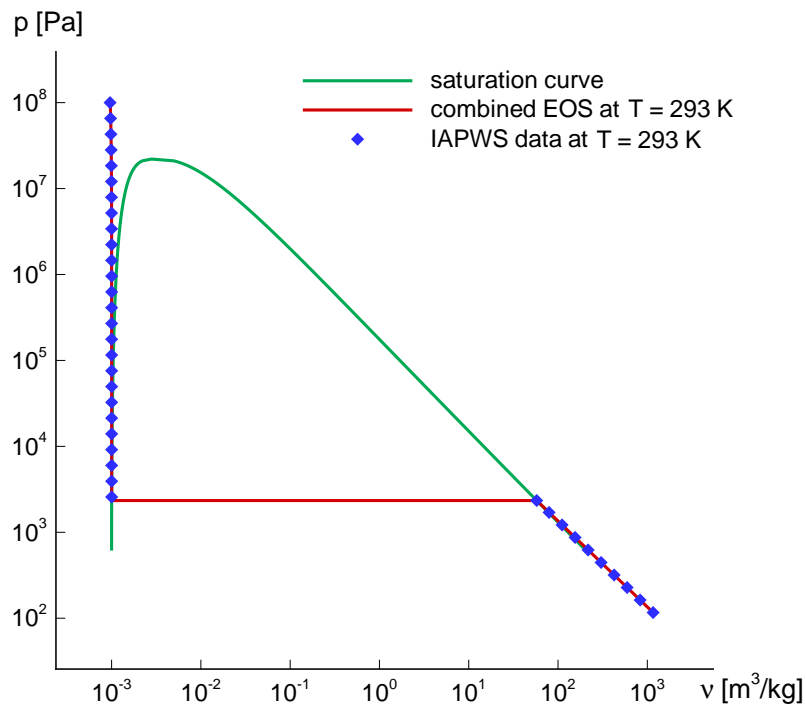


Figure 2.15: Combined equation of state, together with IAPWS data at $T = 293\text{ K}$. The green line depicts the saturation curve obtained by the temperature dependent saturation functions.

This equation is not limited to the ideal gas case and valid for the whole thermodynamic range as long as the the thermodynamic states are in equilibrium. For pure vapor domains, the sonic speed formulation is rather trivial. Using the ideal gas definition together with Eq. 2.73 results in the following formula for the speed of sound

$$c = \sqrt{\kappa RT}. \quad (2.74)$$

The values of κ and R depend on the ideal gas under consideration. For air $\kappa = 1.4$, $R = 287.1 \text{ J/kg} \cdot \text{K}$; for water vapor $\kappa = 1.327$, $R = 461.5 \text{ J/kg} \cdot \text{K}$.

Similarly, the speed of sound for liquid water can also be determined from Eq. 2.73. Using the modified Tait equation given by Eq. 2.65, the sonic speed can be efficiently and accurately approximated by the following relation

$$c_{liq} = \sqrt{\frac{n}{\rho}(p + B)}. \quad (2.75)$$

This completes the definition of sonic speed for single-phases. In two-phase domains, however, this definition is not that straightforward and needs more attention. The following definition, which is named as Wallis formula [126], is often encountered in literature and associated with two-phase flows in many sources [55]

$$\frac{1}{\rho \cdot c^2} = \frac{\alpha}{\rho_{vap} \cdot c_{vap}^2} + \frac{1 - \alpha}{\rho_{liq} \cdot c_{liq}^2}, \quad (2.76)$$

where ρ is the mixture density and c is the mixture speed of sound. This equation gives the equilibrium speed of sound in **two-component** flows like air/water mixtures, where phase transition does not occur, i.e. the mass fraction of each component remains **constant** [13]. When the flow undergoes a phase transition process, this definition still can be used, but it would result in the **frozen speed of sound** in two-phase flow.

The following investigation is given in Franc and Michel [30] in detail. Considering a homogeneous mixture of water and water vapor in **equilibrium**, a pressure variation of δp induces phase transition to occur. Accordingly, if the mass of liquid decreases by δm through vaporization, the same amount of mass is transferred to the vapor phase. Using Eq. 2.73 and after some manipulation [30] the **equilibrium speed of sound in two-phase flow** becomes

$$\frac{1}{\rho \cdot c^2} \cong \frac{\alpha}{\rho_{vap} \cdot c_{vap}^2} + \frac{1 - \alpha}{\rho_{liq} \cdot c_{liq}^2} - \frac{\delta m}{\rho_{vap} \cdot \delta p}. \quad (2.77)$$

For an adiabatic process, the heat balance is given by the latent heat of vaporization L_{vap} and the temperature difference δT :

$$\delta m L_{vap} = -(1 - \alpha)\rho_{liq} c_{p,liq} \delta T, \quad (2.78)$$

which can be rearranged

$$\frac{\delta m}{\delta p} = -\frac{(1 - \alpha)\rho_{liq} c_{p,liq}}{L_{vap}} \frac{\delta T}{\delta p}. \quad (2.79)$$

From the Clapeyron relation it is known that [17]

$$\left(\frac{\partial p}{\partial T}\right)_{sat} = \frac{L_{vap}}{T(v_{vap} - v_{liq})}, \quad (2.80)$$

as $v_{liq} \ll v_{vap}$, one can write

$$\left(\frac{\partial p}{\partial T}\right)_{sat} \cong \frac{L_{vap}}{Tv_{vap}} = \frac{L_{vap} \rho_{vap}}{T}. \quad (2.81)$$

Substituting Eq. 2.81 into 2.77 finally gives

$$\frac{1}{\rho \cdot c^2} \cong \frac{\alpha}{\rho_{vap} \cdot c_{vap}^2} + \frac{1 - \alpha}{\rho_{liq} \cdot c_{liq}^2} + \frac{(1 - \alpha)\rho_{liq} c_{p,liq} T}{(\rho_{vap} \cdot L_{vap})^2}. \quad (2.82)$$

Equation 2.82 is the definition of the mixture speed of sound in the case of phase transition. Except in cases where the void fraction is close to one, the last term dominates the sonic speed. The following figure depicts the comparison of the mixture

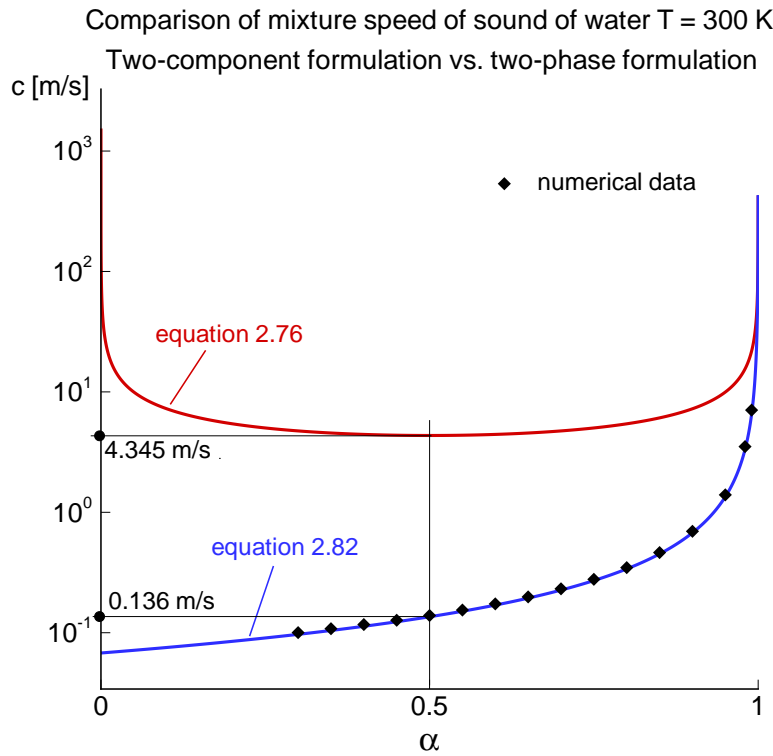


Figure 2.16: Comparison of mixture speed of sound of water/water vapor, two-component formulation (red line - Eq. 2.76), two-phase formulation (blue line - Eq. 2.82). Black points correspond to calculated mixture sonic speeds in a numerical experiment performed for different void fraction values.

speed of sound for water and water vapor with and without phase transition (Eqs. 2.82 and 2.76 respectively).

Figure 2.16 shows the difference between the two formulations. For a void fraction of 50%, Eq. 2.76 gives a value of 4.345 m/s, whereas, if the phase transition is taken

into account by using Eq. 2.82, the sonic speed is found out to be 0.136 m/s . As a result, the sonic speed in two-phase domains is governed by Eq. 2.82 (blue line) and hence it determines the physical propagation speed of the sonic waves. Additionally, to see the accuracy of Eq. 2.82 and to check the consistency of the developed code, a numerical experiment is performed. Thereby the propagation speed of a pressure pulse is measured in a rectangular numerical domain for different void fraction values. The black points in Fig. 2.16 correspond to these numerically calculated mixture sonic speeds. As it is seen, they match perfectly to the analytical expression given by Eq. 2.82.

The jump on the speed of sound as $\alpha \rightarrow 0$ in two-phase formulation is due to the last term in Eq. 2.82 and can be explained by examining the $p - v$ diagram and the corresponding isentropes. The following figure presents the $p - v$ diagram of water as we have already investigated at the beginning of the chapter.

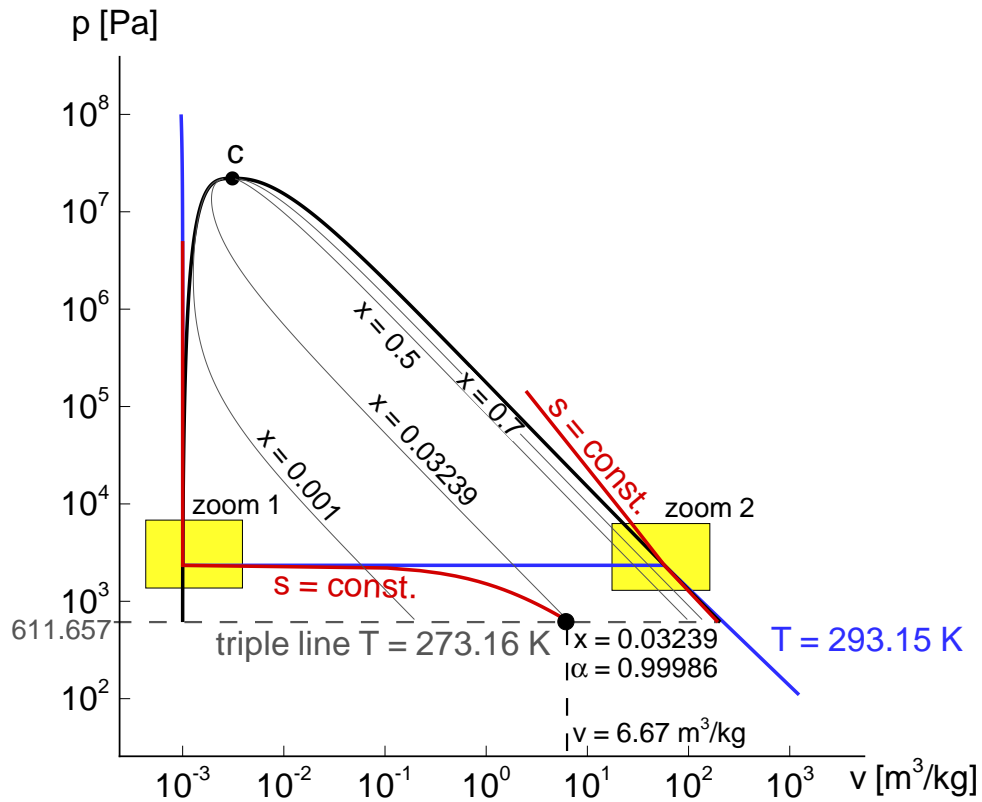


Figure 2.17: $p - v$ diagram of water including the isentropes corresponding to the saturation liquid and saturation vapor states together with vapor quality lines.

Considering the general form of the equation for the isentropic speed of sound in equilibrium flow, which was given earlier as

$$c = \sqrt{\left. \frac{\partial p}{\partial \rho} \right|_s}. \quad (2.83)$$

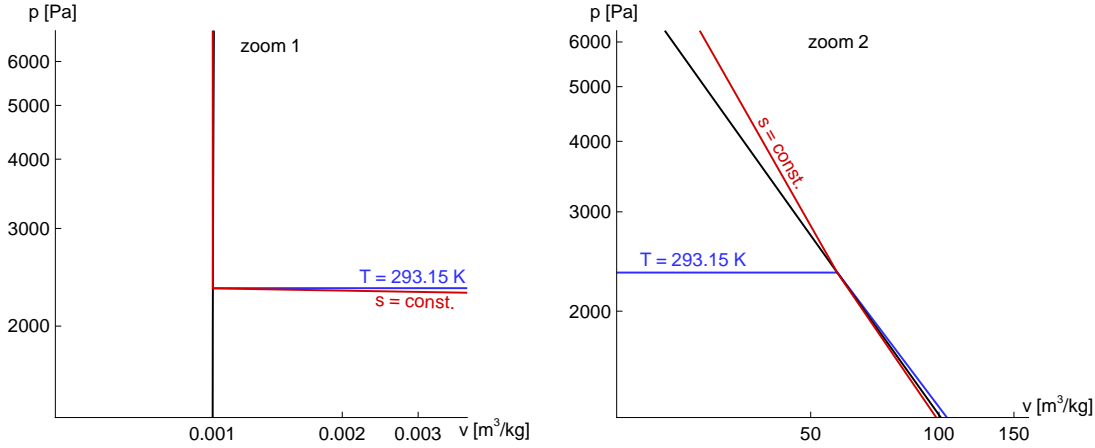


Figure 2.18: Zoomed view of the $p - v$ diagram of water including the isentropes corresponding to the saturation liquid (zoom 1) and saturation vapor states (zoom 2).

Rewriting this equation in terms of the specific volume v results in

$$c = \sqrt{-v^2 \left. \frac{\partial p}{\partial v} \right|_s}. \quad (2.84)$$

Therefore, the speed of sound is defined by the derivative of the pressure p with respect to the specific volume v over an isentrop. If we examine Figs. 2.17 or 2.18-left we observe that the isentrop coming from the pure liquid phase has a discontinuity in the first derivative at the saturated liquid state. Due to this discontinuity the pressure is not differentiable at that point and thus the mixture speed of sound experiences a jump as $\alpha \rightarrow 0$. The isentrop coming from the pure vapor phase experiences only a minor discontinuity as it passes through the saturated vapor point see Fig. 2.18-right. Mathematically, this minor discontinuity results in a jump as $\alpha \rightarrow 1$, but such a jump is not observed in Fig. 2.16. The reason therefore is that the derivation of Eq. 2.82 is approximate - it does not consider mass transfer from vapor into liquid as this effect is negligible for $\alpha < \alpha_{max} \approx 0.999$. The inclusion of the mass transfer from vapor to liquid in the derivation would result in a α dependent term on the right hand side of Eq. 2.82 and would cause a minor jump when $\alpha = 1$ as well (see Brennen [13]). Therefore, this equation is accurate for α very close to 1, i.e. $0 < \alpha < \alpha_{max} \approx 0.999$.

Although Eq. 2.82 is relevant for the calculation of the physical propagation speed in two-phase domains, Eq. 2.76 is used as mixture sonic speed in the numerical scheme. This distinction is important and should be cleared here; as it will be presented in the next chapter, the numerical scheme uses a sonic speed while calculating the convective fluxes. This sonic speed is purely a numerical variable and defines the **numerical dissipation** included in the scheme which is proportional to $\rho c \Delta u$. Therefore, using two-component formulation (Eq. 2.76) will result in a higher sonic speed, and thus a larger numerical dissipation. So overestimating the speed of sound stabilizes the scheme, while an underestimation destabilizes it. As a result, a slight overestimation is preferred, i.e.

$$c_{num} > c_{phys} \quad \rightarrow \quad \text{otherwise unstable} \quad (2.85)$$

Once again, when physical values of sonic speed or Mach number are presented or

mentioned in any test case, it means that they are approximated according to the definition of the local speed of sound given by Eq. 2.73.

The behavior of the mixture speed of sound in two-phase flows with respect to temperature is also of interest in this study. Therefore, in Fig. 2.19 the mixture speed of sound is compared for different temperatures, $T = 300 - 480 K$. As it can be seen in the figure, when the temperature increases, the curves shift upward, therefore the mixture speed of sound increases. As an example, for a void fraction of 50%, $c = 0.136 m/s$ at $T = 300 K$, whereas $c = 35.04 m/s$ when $T = 480 K$.

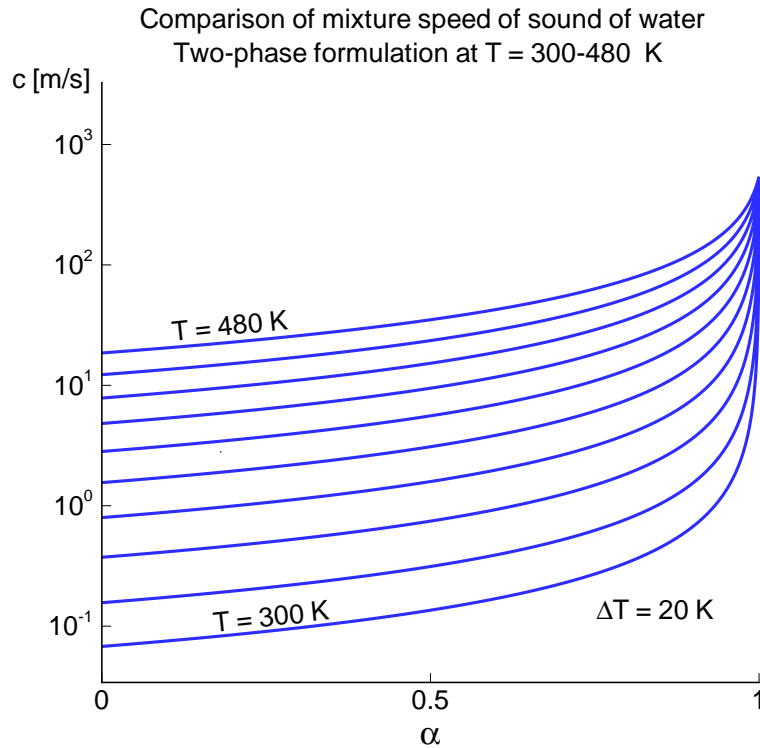


Figure 2.19: Comparison of the mixture speed of sound for temperatures $T = 300 - 480 K$, $\Delta T = 20 K$, calculated by Eq. 2.82.

This figure has also the same behavior as the previous one and includes discontinuities when $\alpha \rightarrow 0$. As discussed above, this is due to different character of the isentropes at the saturation states.

Chapter 3

Numerical Method

The governing equations of fluid dynamics constitute a coupled non-linear differential equation system, of which closed form analytical solutions cannot be achieved. Therefore, with the help of increasing computer power, computational fluid dynamics, namely CFD, provides methods for the numerical simulation of fluid flows. These methods depend on the considered flow problem and the desired level of physical approximation.

This chapter will present the details of the applied numerical method according to the physical modeling described in the previous chapter.

3.1 Governing Equations

The set of Euler equations together with the model dependent closure relations have already been given in chapter 2. The numerical model is based on the weak or integral formulation of the governing equations, as they allow for the arising discontinuities inside the flow field in comparison to the differential form.

The discrete form of the governing equations for a flow domain divided into finite control volumes of Ω_J was given as follows

$$\frac{d}{dt} \mathbf{q}_J + \sum_{\Gamma_J} \sum_{i=1}^3 F_i(\mathbf{q}) \cdot \Delta \mathbf{S} = 0, \quad (3.1)$$

where

$$\mathbf{q} = \begin{pmatrix} \rho \\ \rho u \\ \rho v \\ \rho w \\ \rho E \end{pmatrix}, \quad F_i(\mathbf{q}) = \rho u_i \cdot \begin{pmatrix} 1 \\ u \\ v \\ w \\ E \end{pmatrix} + p \cdot \begin{pmatrix} 0 \\ \delta_{1i} \\ \delta_{2i} \\ \delta_{3i} \\ u_i \end{pmatrix}. \quad (3.2)$$

3.2 Geometry Definition

The physical model explained in the previous section is based on the integral average quantities that are evaluated in each computational cell. As a result, the system given by Eq. 3.1 is evaluated at each finite control volume depicted in the following figure.

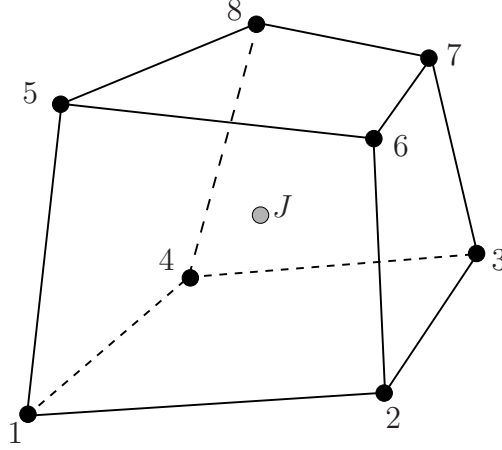


Figure 3.1: The sketch of a finite control volume Ω_J . Typical grid geometry.

The flow domain consists of non-overlapping hexahedra cells in ijk order as the example given above, i.e. for any point p it can be written

$$\begin{aligned}
 p_{i,j,k} &\equiv p_1, & p_{i,j,k+1} &\equiv p_5, \\
 p_{i+1,j,k} &\equiv p_2, & p_{i+1,j,k+1} &\equiv p_6, \\
 p_{i+1,j+1,k} &\equiv p_3, & p_{i+1,j+1,k+1} &\equiv p_7, \\
 p_{i,j+1,k} &\equiv p_4, & p_{i,j+1,k+1} &\equiv p_8.
 \end{aligned} \tag{3.3}$$

The ijk ordering of the flow domain is the necessary condition for structured grids and its numerical implementation is straightforward when compared to unstructured grids, as no neighborhood information or connectivity table is needed. Moreover, structured grids are more efficient from a CFD point of view, in terms of accuracy, CPU time and memory requirement [44]. In the newly developed code, the cell-center approach is used, where the unknown flow variables are defined at the centers of the cells and the convective fluxes are calculated through each cell surface. The center point J is designated after the lowest corner, i.e. $J \equiv i, j, k$. The finite volume formulation requires calculation of every cell volume and surface areas of each cell. As seen in Fig. 3.1 the points are not necessarily co-planar. The surface area calculation is performed according to Fig. 3.2. The area of the surface Γ_{5678} can be calculated by using vectors \mathbf{x}_{68} and \mathbf{x}_{57} . Hence the area is given by

$$\Gamma_{5678} = \frac{1}{2} \|\mathbf{x}_{68} \times \mathbf{x}_{57}\|, \tag{3.4}$$

whereas the corresponding normal vector of the surface is

$$\mathbf{n}_{5678} = \frac{\mathbf{x}_{68} \times \mathbf{x}_{57}}{\|\mathbf{x}_{68} \times \mathbf{x}_{57}\|}. \tag{3.5}$$

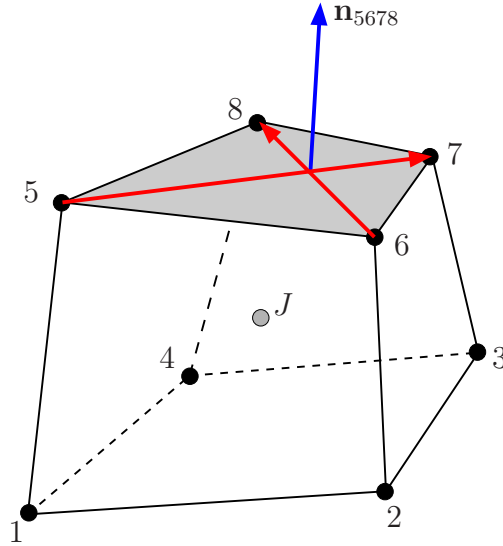


Figure 3.2: Surface area of Γ_{5678} and corresponding normal vector \mathbf{n}_{5678} .

The volume Ω_J of the given hexahedral cell can be estimated with different formulas. In this investigation, following Fig. 3.3 the considered cell is divided into 12 tetrahedra using the cell center J , which is found by arithmetic averaging of all corner nodes.

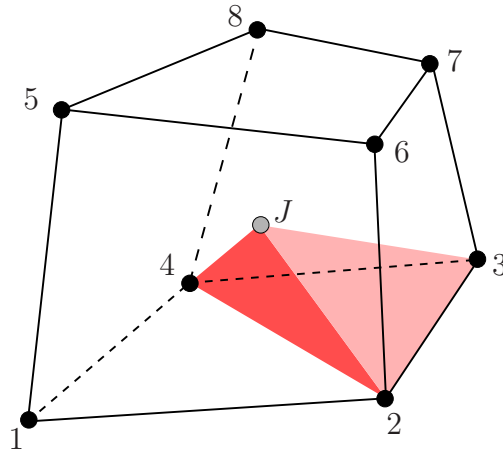


Figure 3.3: Partitioning of the control volume Ω_J into tetrahedra volumes using the cell center J .

The volume of the given red tetrahedron is calculated as [44]

$$\Omega_{J234} = \frac{1}{6} \mathbf{x}_{J2} \cdot (\mathbf{x}_{23} \times \mathbf{x}_{34}), \quad (3.6)$$

similarly the opposite volume is

$$\Omega_{J124} = \frac{1}{6} \mathbf{x}_{J1} \cdot (\mathbf{x}_{12} \times \mathbf{x}_{24}). \quad (3.7)$$

Therefore, each face of the hexahedron corresponds to two tetrahedra volumes, so the total volume Ω_J is found by adding all the tetrahedra volumes.

3.3 Convective Flux calculation

The numerical solution procedure requires the calculation of fluxes through each cell interface, which is defined by two-dimensional surfaces with a given normal vector as explained in the previous section. Among the wide variety of methods that have been developed for the solution of the flow equations, the Godunov approach [36] is employed in the current solver. In this approach approximate solutions of the Euler equations for a local region of the flow are pieced together to form the general solution of a flow field [6]. The local solution mentioned is found by solving the approximate solution of the Riemann problem at the interface, which is discussed in the next subsection.

3.3.1 Riemann Problem

The Riemann problem is a special type of initial value problem for a given partial differential equation, where the initial data has a jump discontinuity [60]. Moreover for a time dependent, strictly hyperbolic system, the solution of the 1-D Riemann problem consists of waves propagating in the $(x - t)$ plane. Furthermore, hyperbolicity guarantees that all the eigenvalues of the equation system are real. A detailed mathematical analysis of the Riemann problem is outside the scope of this thesis but the readers are encouraged to refer to Toro [119] or Laney [60].

The solution of the Riemann problem for Euler equations involves three elementary wave types that are known from gas dynamics: shock, expansion wave and contact discontinuity. The set of 3-D Euler equations is rotational invariant [119]. This property of the Euler equations and the definition of the Riemann problem allow for the use of a x -split form of the equations for a 3-D Riemann problem, which is given by the following initial value problem with Eq. 3.2 evaluated in x -direction

$$\frac{\partial \mathbf{q}}{\partial t} + \frac{F(\mathbf{q})}{\partial x} = 0, \quad (3.8)$$

with

$$\mathbf{q}(x, 0) = \begin{cases} \mathbf{q}_L & x < 0 \\ \mathbf{q}_R & x > 0 \end{cases}, \quad (3.9)$$

where

$$\mathbf{q} = \begin{pmatrix} \rho \\ \rho u \\ \rho v \\ \rho w \\ \rho E \end{pmatrix}, \quad F(\mathbf{q}) = \begin{pmatrix} \rho u \\ \rho u^2 + p \\ \rho uv \\ \rho uw \\ \rho uH \end{pmatrix}, \quad (3.10)$$

and \mathbf{q}_L and \mathbf{q}_R correspond to the left and right states respectively. One can consider the x -split system as the component of the flux function in x -direction in a 3-D flow domain. Therefore, finding the solution of the Riemann problem for the split 3-D equations is in fact the same as finding the solution for the corresponding 1-D Riemann problem. The following figure depicts this situation for two computational cells in x -direction for a 3-D domain. The 1-D Riemann problem is evaluated through the grey surface.

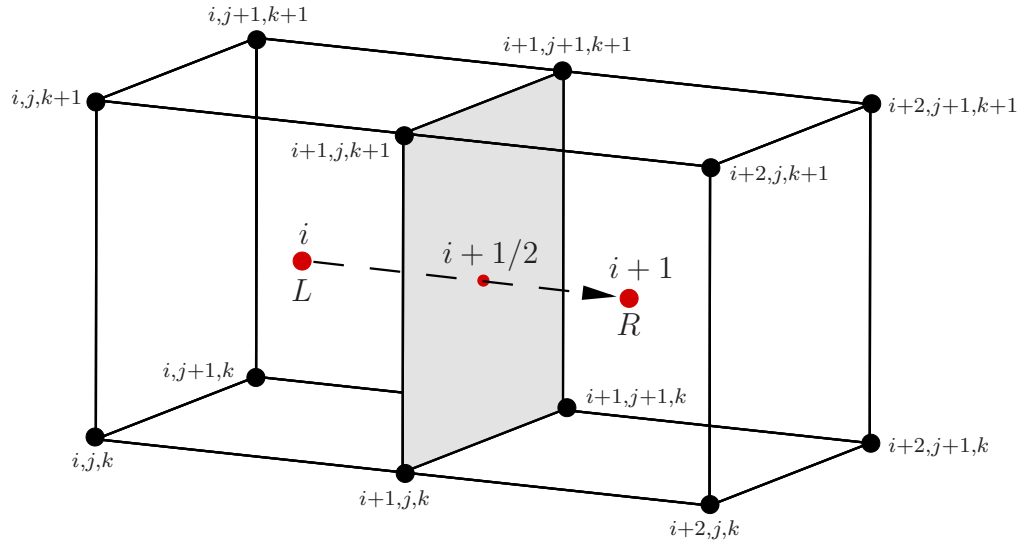


Figure 3.4: Discretization of the 3-D numerical domain. The x -split numerical flux is calculated through the grey surface, $i + 1/2$, from the left state L, i to the right state $R, i + 1$.

As can be seen in Fig. 3.4, the x -split numerical flux is calculated through the grey surface, $i + 1/2$, which can be written from Eq. 3.1 as follows

$$\frac{d}{dt} \mathbf{q}_i = -F(\mathbf{q}_{i+1/2}^{num}) \cdot \mathbf{S}_{i+1/2}, \quad (3.11)$$

where the vector $\mathbf{S}_{i+1/2}$ gives the surface area and its normal direction of the cell interface. Therefore, in order to obtain the numerical result one needs to determine the numerical flux function $F(\mathbf{q}_{i+1/2}^{num})$. As stated earlier, among many other methods the Godunov approach is chosen, where $F(\mathbf{q}_{i+1/2}^{num})$ is given by the solution of the local Riemann problem. The advantage of x -splitting of the Riemann problem is that it is only needed to evaluate the same set of the equations through each face of the computational cell separately and then add them together.

The solution of the Riemann problem with specified left and right states for x -split 3-D Euler equations results in a three-wave structure, which is shown in Fig. 3.5. Each of these waves correspond to eigenvalues of the equation system, given by

$$\begin{aligned} \lambda_1 &= u - c \\ \lambda_2 &= u \\ \lambda_3 &= u \\ \lambda_4 &= u \\ \lambda_5 &= u + c. \end{aligned} \quad (3.12)$$

The **exact solution of the Riemann problem** is possible through iterative methods as long as the chosen equation of state ensures the hyperbolicity of the equation system. But, as it is needed at every interface between the computational cells, for practical

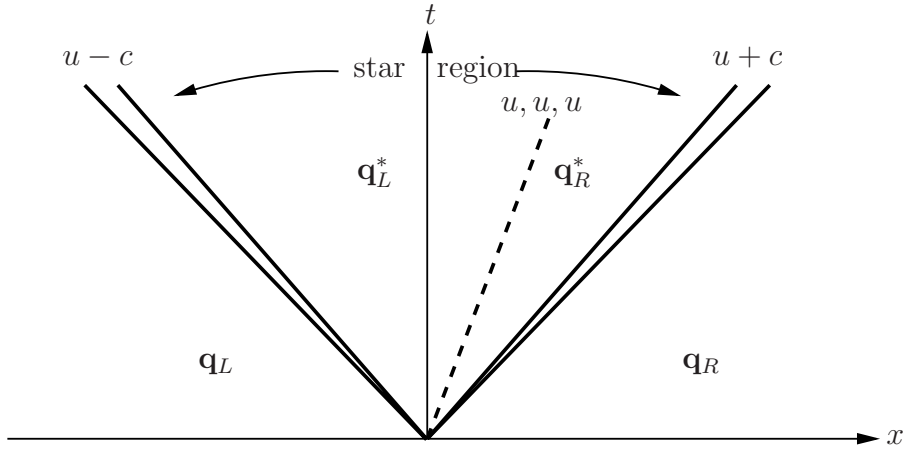


Figure 3.5: Structure of the x -split 3-D Riemann problem.

applications **approximate Riemann solvers** are developed, which are explicit and time efficient. In the following two subsections two of such approximate Riemann solvers are considered.

3.3.2 The HLLC Riemann solver

Among a number of approximate Riemann solvers the HLLC (Harten-Lax-van Leer Contact wave) method has an advantage of capturing all three-wave families, therefore the complete structure of the exact solution is obtained. Figure 3.6 shows the three-wave structure of the HLLC solver with wave speeds S_L , S_R and S^* .

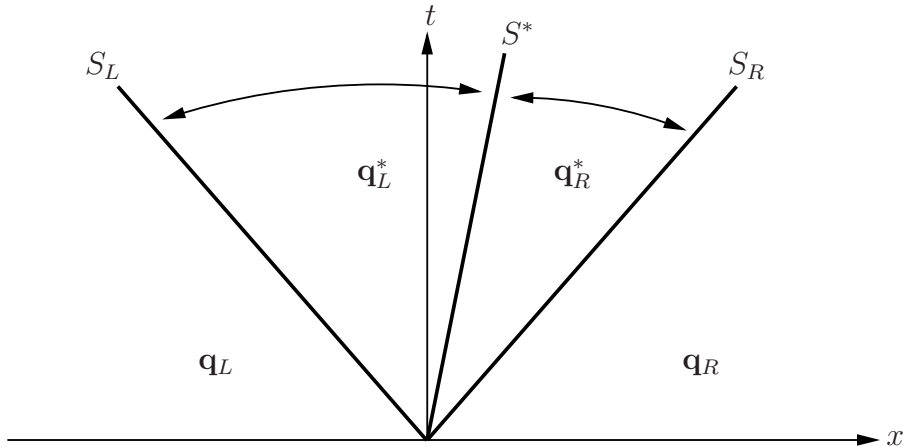


Figure 3.6: HLLC approximate Riemann solver. The solution in the star region consists of two states separated from each other by a middle wave of speed S^* .

The derivation of the HLLC method follows from the integral form of the equations [119], which is not given here. Using the Rankine-Hugoniot relations over each wave one can write

$$\begin{aligned}
 F(\mathbf{q}_L^*) &= F(\mathbf{q}_L) + S_L(\mathbf{q}_L^* - \mathbf{q}_L) \\
 F(\mathbf{q}_R^*) &= F(\mathbf{q}_L^*) + S^*(\mathbf{q}_R^* - \mathbf{q}_L^*) \\
 F(\mathbf{q}_R^*) &= F(\mathbf{q}_R) + S_R(\mathbf{q}_R^* - \mathbf{q}_R).
 \end{aligned} \tag{3.13}$$

The aim is to find the left and right vectors \mathbf{q}_L^* and \mathbf{q}_R^* so that the fluxes $F(\mathbf{q}_L^*)$ and $F(\mathbf{q}_R^*)$ can be determined from the equations given above. The following conditions for primitive variables are imposed in the approximate Riemann solver

$$\begin{aligned}
u_L^* &= u_R^* = u^* \\
p_L^* &= p_R^* = p^* \\
v_L^* &= v_L \\
v_R^* &= v_R \\
w_L^* &= w_L \\
w_R^* &= w_R \\
S^* &= u^* .
\end{aligned} \tag{3.14}$$

Substituting the conditions given by Eq. 3.14 into the Rankine-Hugoniot relations (Eq. 3.13) gives the solution vector for the star region as

$$\mathbf{q}_K^* = \rho_K \left(\frac{S_K - u_K}{S_K - S^*} \right) \begin{bmatrix} 1 \\ S^* \\ v_K \\ w_K \\ \frac{E_K}{\rho_K} + (S^* - u_K) \left[S^* + \frac{p_K}{\rho_K(S_K - u_K)} \right] \end{bmatrix}, \tag{3.15}$$

with $K = L$ and $K = R$. Thereby, the fluxes $F(\mathbf{q}_L^*)$ and $F(\mathbf{q}_R^*)$ are completely defined. Hence, the flux function of the HLLC method can be written as

$$F(\mathbf{q}_{i+\frac{1}{2}}^{hllc}) = \begin{cases} F(\mathbf{q}_L) & 0 \leq S_L \\ F(\mathbf{q}_L^*) = F(\mathbf{q}_L) + S_L(\mathbf{q}_L^* - \mathbf{q}_L) & S_L \leq 0 \leq S^* \\ F(\mathbf{q}_R^*) = F(\mathbf{q}_R) + S_R(\mathbf{q}_R^* - \mathbf{q}_R) & S^* \leq 0 \leq S_R \\ F(\mathbf{q}_R) & 0 \geq S_R \end{cases}. \tag{3.16}$$

To complete the HLLC Riemann solver one must define the wave speeds S_L , S_R and S^* . The following formulas are often encountered in literature [119] and thus implemented in the code

$$\begin{aligned}
S_L &\equiv \min(u_L - c_L, u_R - c_R) \\
S_R &\equiv \max(u_L + c_L, u_R + c_R) \\
S^* &\equiv \frac{p_R - p_L + \rho_L u_L (S_L - u_L) - \rho_R u_R (S_R - u_R)}{\rho_L (S_L - u_L) - \rho_R (S_R - u_R)}.
\end{aligned} \tag{3.17}$$

As HLLC Riemann solver captures the complete structure of the exact solution, the ideal gas calculations are performed by using it without any modifications.

3.3.3 The AUSM Family of Methods

The AUSM (Advection Upstream Splitting Method) scheme dates back to 1993 when it was first published by Liou and Steffen [70]. From that time on, it was highly celebrated for its straightforward formulation with robustness and improved by its original author and several others [71], [73]. The AUSM method falls into the group of methods that are called flux vector splitting (FVS), where the numerical flux function is split into a positive and negative part

$$F(\mathbf{q}) = F^+(\mathbf{q}_L) + F^-(\mathbf{q}_R). \quad (3.18)$$

The main idea in the advection upstream splitting method is to divide the numerical flux into a convective flux part and a pressure flux part, i.e.

$$F(\mathbf{q}) = F^c(\mathbf{q}) + \mathbf{p} = \dot{m}\boldsymbol{\psi} + \mathbf{p}, \quad (3.19)$$

where

$$\boldsymbol{\psi} = \begin{pmatrix} 1 \\ u \\ v \\ w \\ H \end{pmatrix}, \quad \mathbf{p} = \begin{pmatrix} 0 \\ p \\ 0 \\ 0 \\ 0 \end{pmatrix}, \quad (3.20)$$

and

$$\dot{m} = \rho u = \rho c M. \quad (3.21)$$

Following the previous definition of the numerical flux function, Eq. 3.19 is evaluated at the cell interface $i + 1/2$,

$$F(\mathbf{q}_{i+\frac{1}{2}}^{ausm}) = \dot{m}_{1/2}\boldsymbol{\psi}_{1/2} + \mathbf{p}_{1/2}, \quad (3.22)$$

with

$$\boldsymbol{\psi}_{1/2} = \begin{cases} \boldsymbol{\psi}_L & \dot{m}_{1/2} > 0 \\ \boldsymbol{\psi}_R & \dot{m}_{1/2} \leq 0 \end{cases}, \quad \text{and} \quad \dot{m}_{1/2} = c_{1/2}M_{1/2} \cdot \begin{cases} \rho_L & M_{1/2} > 0 \\ \rho_R & M_{1/2} \leq 0 \end{cases}. \quad (3.23)$$

The interface relations are defined as follows

$$M_{1/2} = \mathcal{M}^+(M_L) + \mathcal{M}^-(M_R) \quad (3.24)$$

$$p_{1/2} = \mathcal{P}^+(M_L)p_L + \mathcal{P}^-(M_R)p_R, \quad (3.25)$$

where

$$M_L = \frac{u_L}{c_{1/2}}, \quad M_R = \frac{u_R}{c_{1/2}}, \quad (3.26)$$

and interface speed of sound $c_{1/2}$ is given by

$$c_{1/2} = \frac{1}{2}(c_L + c_R). \quad (3.27)$$

The split Mach number and pressure functions \mathcal{M} and \mathcal{P} are given by [72] as

$$\mathcal{M}^\pm(M) = \begin{cases} \frac{1}{2}(M \pm |M|) & |M| \geq 1 \\ \pm \frac{1}{2}(M \pm 1)^2 \pm \frac{1}{8}(M^2 - 1)^2 & |M| < 1 \end{cases}, \quad (3.28)$$

$$\mathcal{P}^\pm(M) = \begin{cases} \frac{1}{2}(1 \pm \text{sign}(M)) & |M| \geq 1 \\ \frac{1}{4}(M \pm 1)^2(2 \mp M) \pm \frac{3}{16}(M^2 - 1)^2 & |M| < 1 \end{cases}. \quad (3.29)$$

3.3.4 The Low Mach Number Problem

The framework discussed in previous subsections is well developed for the simulation of steady and unsteady compressible aerodynamics of moderate and high Mach number flows as well as for the investigation of wave propagation phenomena including sharp and accurate shock capturing in unsteady flows. Furthermore, methods based on Eq. 3.11 are conservative by construction and enable efficient time dependent simulations. Contrary to pressure based approaches, all fluxes are calculated without the need for sub-iterations. However, Godunov type methods fail in the limit of multidimensional low Mach number flows (**low Mach number problem**) [38], [78], [79] and require substantial modification to overcome the low Mach number problem. Otherwise, the accuracy and the convergence of the Godunov approximation significantly decreases if the Mach number is in the weakly compressible regime, $M \lesssim 0.1$. The slow convergence is associated with the large difference between the acoustic wave speed $|\mathbf{u}| + c$ and the convective flow speed u . The stiffness of the equation system is defined by the condition number C , which is defined by the ratio of the largest eigenvalue of the system to the smallest one, i.e.

$$C = \frac{|\mathbf{u}| + c}{|\mathbf{u}|} = 1 + \frac{1}{M}. \quad (3.30)$$

As the maximum time step is limited by the fastest wave speed $|\mathbf{u}| + c$ (see subsection 3.5.3), a larger condition number, where $M \rightarrow 0$, reduces the convergence rate of the numerical scheme.

On the other hand, the decrease of accuracy is associated with the incorrect estimation of the numerical dissipation in standard schemes in the low Mach number limit [38]. In particular due to the high acoustic impedance of liquids, the decrease of accuracy is further intensified. In order to demonstrate this failure we consider the definition of the interface pressure in the Godunov approach. If the variations of the state variables are smooth, any method based on compatibility relations or on Rankine-Hugoniot relations will lead to an interface pressure definition comparable to

$$p^* = \frac{p_L + p_R}{2} + \frac{u_L - u_R}{2} \bar{\rho} \bar{c}, \quad (3.31)$$

where $\bar{\rho}$ and \bar{c} are the average density and speed of sound respectively. As can be seen in Eq. 3.31 this coupling is weighted by the acoustic impedance, which is close to a constant value if the Mach number remains small within the flow field. Moreover, this

second term in Eq. 3.31 adds to the numerical dissipation in the numerical scheme. To demonstrate the failure of this equation a very simple accelerating flow is considered, where the total pressure p_0 is constant and the average speed of sound is taken as $\bar{c} = 1500 \text{ m/s}$ with the following left and right states

$$\begin{aligned} p_L &= 1 \text{ bar} & u_L &= 10 \text{ m/s} & \rho_L &= 1000 \text{ kg/m}^3 \\ p_R &= 0.95 \text{ bar} & u_R &= 10.5 \text{ m/s} & \rho_R &\approx 1000 \text{ kg/m}^3. \end{aligned} \quad (3.32)$$

Application of Eq. 3.31 results in an interface pressure of

$$p^* = -2.78 \text{ bar}, \quad (3.33)$$

which is obviously wrong. The obtained pressure value indicates the difficulty to calculate the numerical pressure flux for a smooth water flow. Therefore, one can conclude that the calculated interface pressure p^* is extremely sensitive even to small variations in the velocity field, as the Godunov approach treats all variations as discrete jumps. Thus, the low Mach number problem is directly related to the numerical approximation of the interface pressure p^* based on the compatibility relations.

In numerics, preconditioning methods are frequently used to handle stiff equation systems [44]. The main idea of this method is to multiply the time derivative term with a suitable preconditioning matrix, which alters the eigenvalues of the system and reduces the acoustic wave speed to the order of the convective one. Chorin [21] introduced the artificial compressibility method for incompressible flows, where he included an artificial time derivative of pressure in the continuity equation. This method is regarded as one of the first preconditioning techniques used in computational fluid dynamics. Later on several different other preconditioning techniques are introduced by Turkel [121], [122], Turkel et al. [123] and others [128]. As mentioned earlier, preconditioning alters the physical propagation speed of waves and thus, the unsteady behavior is no longer physical, so it is applicable only to **steady state problems**. Combination of preconditioning with dual time stepping algorithms reassures time accuracy of the problem on the time scale of the convective velocity, so unsteady calculations can be performed in order to resolve **unsteady convective motion** [128]. In this methodology during each physical time step Δt , the system of preconditioned equations are solved in artificial or pseudo time steps $\Delta \tau$ to reach a steady state in pseudo time. As physical time steps of the order of acoustic time scale is needed, dual time stepping methods are computationally **not applicable** for the resolution of **unsteady wave dynamics**, which is the primary interest of the current study.

3.3.5 Modification for Liquid Flows - Hybrid Formulation

As can be seen from the previous section, the standard formulations used in Godunov approach fail in calculating the interface pressure in smooth flow conditions when the acoustic impedance of the medium is extremely large. Moreover, preconditioning methods are not suitable for the flow problems and time scales that are considered in this investigation.

To understand the behavior of the numerical flux better, Schmidt et al. [103] investigated Eq. 3.31 numerically and concluded that the numerical error that is introduced by the application of Eq. 3.31 grows inversely proportional to the Mach number M_∞

as long as the number of cells N is kept constant. As a result, in order to use this equation it would require a factor of $N \sim M_\infty^{-1}$ mesh points in every direction, which is not practical for the calculations that are investigated here.

In order to overcome the low Mach number problem Schmidt et al. [103] introduced a modified numerical flux for cavitating liquid flow, which is developed by using an asymptotically consistent pressure flux definition, i.e.

$$p^* = \frac{p_L + p_R}{2}, \quad (3.34)$$

and a corresponding velocity flux u^* as

$$u^* = \frac{\rho_L c_L u_L + \rho_R c_R u_R + p_L - p_R}{\rho_L c_L + \rho_R c_R}. \quad (3.35)$$

The hybrid formulation is developed by using the idea of pressure and velocity splitting as in the AUSM method. Therefore, the numerical flux function for the x -split system takes the following form

$$F(\mathbf{q}_{i+\frac{1}{2}}^{hybrid}) = \rho_i u^* \begin{vmatrix} 1 \\ u^* \\ v_i \\ w_i \\ E_i \end{vmatrix} + p^* \begin{vmatrix} 0 \\ 1 \\ 0 \\ 0 \\ u^* \end{vmatrix}. \quad (3.36)$$

The proposed pressure flux definition does not contain the coupling of pressure and velocity which causes the low Mach number problem. Although this definition is slightly less dissipative than the standard approximate Riemann approaches, the numerical stability is well preserved in our simulations. Thus, one can conclude that the definition of u^* includes sufficient coupling of pressure and velocity. The underlying mathematical analysis and the asymptotical expansion of the governing equations are beyond the scope of this thesis and can be found in the literature [38], [78]. A detailed discussion of the implemented hybrid scheme is given in the Ph.D. thesis of Schmidt [104].

3.4 Higher Order Reconstruction

As explained earlier while calculating the numerical flux the local Riemann problem is evaluated at cell interfaces by using the left and right states. Until now, in the formulation primitive variables at the cell centers of the corresponding left and right states are used as they were (Fig. 3.4), i.e.

$$\begin{aligned} \mathbf{u}_{i+1/2}^L &= \mathbf{u}_i \\ \mathbf{u}_{i+1/2}^R &= \mathbf{u}_{i+1}, \end{aligned} \quad (3.37)$$

where \mathbf{u} is the vector of primitive variables, i.e. $\mathbf{u} = (\rho u v w p)^T$. This methodology results in first order accuracy in spatial directions. In order to achieve higher order accuracies in space, several methods have been proposed over the years for Riemann

solvers [60] based on extrapolating the left and right states by using the values of the neighboring computational cells. Following Shu [112] second order linear reconstruction can be written as

$$\begin{aligned} \mathbf{u}_{i+1/2}^L &= \frac{1}{2}\mathbf{u}_i + \frac{1}{2}\mathbf{u}_{i+1} & \mathbf{u}_{i+1/2}^L &= \frac{3}{2}\mathbf{u}_i - \frac{1}{2}\mathbf{u}_{i-1} \\ \mathbf{u}_{i+1/2}^R &= \frac{1}{2}\mathbf{u}_i + \frac{1}{2}\mathbf{u}_{i+1} & \mathbf{u}_{i+1/2}^R &= \frac{3}{2}\mathbf{u}_{i+1} - \frac{1}{2}\mathbf{u}_{i+2} . \end{aligned} \quad (3.38)$$

As long as the solution is smooth and not experiencing any kind of jumps (shocks, contact discontinuities or phase boundaries) the formula given above or higher order reconstructions with more points are applicable. But if the flow field is not smooth, the above and similar linear reconstructions result in oscillations of the calculated variables.

Van Leer introduced the idea of modifying the piece-wise constant data in the first-order Godunov method [66]. This technique is referred to as MUSCL (Monotone Upstream-Centered Schemes for Conservation Laws) or variable extrapolation approach. Combined with TVD (Total Variation Diminishing) methods, non-linear higher order reconstructions are possible without the problems stated earlier [119]. TVD methods ensure that as a result of reconstruction, no new extrema may be created and the value of a local minimum increases, whereas the value of a local maximum decreases. Hence, total variation is a decreasing function in time [40], [68]. The total variation of a scalar ϕ for a piece-wise constant function is given as

$$TV(\phi) = \sum_{i=-\infty}^{\infty} |\phi_{i+1} - \phi_i| . \quad (3.39)$$

Therefore, the TVD reconstructed function $\tilde{\phi}^n(x, t_n)$ of the scalar ϕ fulfills the following relation

$$TV(\tilde{\phi}^n(x, t_n)) \leq TV(\phi_i(t_n)) . \quad (3.40)$$

Based on the mathematical formulation and definitions found in literature [60], [119] various TVD-limiters are defined. A TVD limiter can be written as follows

$$\begin{aligned} s_{i,L} &\equiv \mathbf{u}_i - \mathbf{u}_{i-1} \\ s_{i,R} &\equiv \mathbf{u}_{i+1} - \mathbf{u}_i , \end{aligned} \quad (3.41)$$

where $s_{i,L}$ and $s_{i,R}$ are left and right sided slopes of the primitive variable inside a cell. The slope function r_i is therefore

$$r_i \equiv \frac{s_{i,L}}{s_{i,R}} = \frac{\mathbf{u}_i - \mathbf{u}_{i-1}}{\mathbf{u}_{i+1} - \mathbf{u}_i} . \quad (3.42)$$

The following limiter functions $\gamma(r_i)$ are implemented in the code

$$\begin{aligned}
\text{Minmod} \quad \gamma(r_i) &= \max(0, \min(1, r_i)) \\
\text{Superbee} \quad \gamma(r_i) &= \max(0, \min(1, 2r_i), \min(r_i, 2)) \\
\text{VanAlbada} \quad \gamma(r_i) &= \frac{\max(0, r_i) \cdot (1 + r_i)}{(1 + r_i^2)} \\
\text{VanLeer} \quad \gamma(r_i) &= \frac{\max(0, 2r_i)}{(1 + |r_i|)} \\
\text{MC} \quad \gamma(r_i) &= \max(0, \min(\frac{1 + r_i}{2}, 2, 2r_i)) .
\end{aligned}$$

These are only a few and the most popular of the limiters that can be found in literature [69] and it is always possible to derive a combination of those according to the numerical needs. The resulting TVD reconstruction of the primitive variables inside the cell i is therefore given by

$$\mathbf{u}(x) = \mathbf{u}_i + \frac{(x - x_i) \cdot s_{i,R}}{x_{i+1/2} - x_{i-1/2}} \gamma(r_i) \quad \text{with} \quad x \in [x_{i-1/2}, x_{i+1/2}] . \quad (3.43)$$

In the simulations, unless otherwise stated or smooth solutions without any discontinuities are expected (for example subsonic single-phase liquid flows), always higher order non-linear MUSCL/TVD type reconstructions are used.

3.5 Time Integration

The semi-discrete form of the governing equations given by Eq. 3.1 allows for the calculation of the numerical fluxes at a fixed point in time, which is mostly referred to as method of lines [60]. The advantage of this method is that one can independently combine any kind of temporal and spatial discretization schemes. Since the compressible Euler equations are hyperbolic in time, time-marching methods are applicable both for steady and unsteady flow problems.

3.5.1 1st Order Time Integration

The simplest method for marching the solution in time is the first order explicit method or sometimes called Euler method. In Eq. 3.11 the time operator is evaluated through the first order forward method and the flux function is evaluated at the cell interfaces at $i + 1/2$ and $i - 1/2$ for the x -split equations

$$\frac{\mathbf{q}_i^{n+1} - \mathbf{q}_i^n}{\Delta t} = \frac{F(\mathbf{q}_{i+1/2}^n) - F(\mathbf{q}_{i-1/2}^n)}{\Delta x} , \quad (3.44)$$

or

$$\mathbf{q}_i^{n+1} = \mathbf{q}_i^n - \frac{\Delta t}{\Delta x} [F(\mathbf{q}_{i+1/2}^n) - F(\mathbf{q}_{i-1/2}^n)] , \quad (3.45)$$

where $n+1$ corresponds to the next time instant, $t+\Delta t$, Δx is the cell size in x -direction and the flux function includes changes from both of the interfaces in the x -direction. The time step Δt is determined from Courant-Friedrichs-Lewy (*CFL*) criteria, which will be explained in subsection 3.5.3. As x -splitting includes changes only in the x -direction, for a 3-D problem the contributions from all the cell faces should be included into the flux function. Following the notation introduced in chapter 2, the 3-D form of Eq. 3.45 can be written as

$$\begin{aligned} \mathbf{q}_{i,j,k}^{n+1} = \mathbf{q}_{i,j,k}^n - \frac{\Delta t_{i,j,k}}{\Delta V_{i,j,k}} [& F(\mathbf{q}_{i+1/2,j,k}^n) - F(\mathbf{q}_{i-1/2,j,k}^n) \\ & + F(\mathbf{q}_{i,j+1/2,k}^n) - F(\mathbf{q}_{i,j-1/2,k}^n) \\ & + F(\mathbf{q}_{i,j,k+1/2}^n) - F(\mathbf{q}_{i,j,k-1/2}^n)] , \end{aligned} \quad (3.46)$$

where $\Delta V_{i,j,k}$ is the volume of the cell i, j, k and $\Delta t_{i,j,k}$ is the time step calculated for the same cell.

3.5.2 4-Stage Runge-Kutta Method

First order time integration is not enough in most of the calculations, especially if the unsteady behavior of the flow field is of interest.

Compared to the Euler method described earlier, the Runge-Kutta schemes achieve high orders of accuracy by introducing multiple stages. These methods have been first applied to the solution of Euler equations in the well known paper from Jameson et al. [52] and are further developed and used in highly efficient numerical codes [44].

The basic idea of Runge-Kutta methods is to evaluate the right-hand side of Eq. 3.11 at several values of \mathbf{q} in the interval between t and $t+\Delta t$ and then combine them to obtain a high order approximation of \mathbf{q}^{n+1} . The number of intermediate levels corresponds to the stage of the Runge-Kutta method [44].

In this thesis, to optimize memory usage, a low-storage Runge-Kutta method is applied. For a K stage scheme it is given by

$$\begin{aligned} \mathbf{q}_{i,j,k}^{(0)} &= \mathbf{q}_{i,j,k}^n \\ \mathbf{q}_{i,j,k}^{(1)} &= \mathbf{q}_{i,j,k}^n - \alpha_1 \frac{\Delta t_{i,j,k}}{\Delta V_{i,j,k}} \mathbf{R}_{i,j,k}^{(0)} \\ \mathbf{q}_{i,j,k}^{(2)} &= \mathbf{q}_{i,j,k}^n - \alpha_2 \frac{\Delta t_{i,j,k}}{\Delta V_{i,j,k}} \mathbf{R}_{i,j,k}^{(1)} \\ &\vdots \\ \mathbf{q}_{i,j,k}^{(K)} &= \mathbf{q}_{i,j,k}^n - \alpha_K \frac{\Delta t_{i,j,k}}{\Delta V_{i,j,k}} \mathbf{R}_{i,j,k}^{(K-1)} \\ \mathbf{q}_{i,j,k}^{n+1} &= \mathbf{q}_{i,j,k}^n - \frac{\Delta t_{i,j,k}}{\Delta V_{i,j,k}} \mathbf{R}_{i,j,k}^{(K)} , \end{aligned} \quad (3.47)$$

where α_i is the coefficient of the i th stage and R is the residual vector following Eq. 3.46 of the previous subsection

$$\begin{aligned} \mathbf{R}_{i,j,k}^n = & [F(\mathbf{q}_{i+1/2,j,k}^n) - F(\mathbf{q}_{i-1/2,j,k}^n) + F(\mathbf{q}_{i,j+1/2,k}^n) \\ & - F(\mathbf{q}_{i,j-1/2,k}^n) + F(\mathbf{q}_{i,j,k+1/2}^n) - F(\mathbf{q}_{i,j,k-1/2}^n)] . \end{aligned} \quad (3.48)$$

In the current version of the code, the following second-order accurate 4-stage Runge-Kutta method is employed

$$\begin{aligned} \mathbf{q}_{i,j,k}^{(1)} &= \mathbf{q}_{i,j,k}^n - 0.11 \frac{\Delta t_{i,j,k}}{\Delta V_{i,j,k}} \mathbf{R}_{i,j,k}^{(n)} \\ \mathbf{q}_{i,j,k}^{(2)} &= \mathbf{q}_{i,j,k}^n - 0.2766 \frac{\Delta t_{i,j,k}}{\Delta V_{i,j,k}} \mathbf{R}_{i,j,k}^{(1)} \\ \mathbf{q}_{i,j,k}^{(3)} &= \mathbf{q}_{i,j,k}^n - 0.5 \frac{\Delta t_{i,j,k}}{\Delta V_{i,j,k}} \mathbf{R}_{i,j,k}^{(2)} \\ \mathbf{q}_{i,j,k}^{n+1} &= \mathbf{q}_{i,j,k}^n - \frac{\Delta t_{i,j,k}}{\Delta V_{i,j,k}} \mathbf{R}_{i,j,k}^{(3)} . \end{aligned} \quad (3.49)$$

The coefficients α_K are chosen such that the stability of the scheme is improved. The corresponding stability analysis of the scheme is performed by Schmidt [101].

3.5.3 Time Step Calculation

The prediction of the time step Δt is one of the most important aspects of a flow solver. As we are mainly interested in unsteady short time-scale behavior of the applications, we implemented two explicit time integration schemes as discussed in the previous subsections. Explicit time integration schemes are relatively easy to implement and they are computationally efficient as no matrix operations are needed. But on the other hand because of the stability concerns, the applicable time step is limited. On a 1-D basis the *CFL* (Courant-Friedrichs-Lewy) condition states that Δt must be less than or at most equal to the time it takes the fastest wave to move from one grid point to the next one [6]. One can consider a 1-D problem with grid points i and $i+1$ separated with a distance of Δx . Assuming a right running wave with velocity of λ_1 and a left running wave with a velocity of λ_2 , the *CFL* condition imposes that

$$\Delta t = \min \left(\frac{\Delta x}{|\lambda_1|}, \frac{\Delta x}{|\lambda_2|} \right) , \quad (3.50)$$

therefore the *CFL* number is defined as

$$CFL \equiv \frac{\Delta t}{\Delta x} \lambda_{max} \leq 1 . \quad (3.51)$$

Whereas for a 3-D problem waves propagate in every direction inside the computational cell, so one must consider all the possible wave speeds and directions. It was stated in

section 3.3.3 that the eigenvalues of the Euler equations correspond to the wave speeds of the problem. If one examines Eq. 3.12, the fastest wave speed corresponds to $u + c$ for a x -split system. Therefore one can propose the following definitions for the fastest wave speeds in a 3-D problem

$$\begin{aligned}\lambda_x &\equiv |u| + c \\ \lambda_y &\equiv |v| + c \\ \lambda_z &\equiv |w| + c.\end{aligned}\tag{3.52}$$

Following Eq. 3.52, the CFL numbers in three space directions can be written as

$$CFL_x = \frac{\Delta t}{\Delta x} \lambda_x, \quad CFL_y = \frac{\Delta t}{\Delta y} \lambda_y, \quad CFL_z = \frac{\Delta t}{\Delta z} \lambda_z.\tag{3.53}$$

In 3-D domains, the CFL numbers can be written using the following definition

$$CFL_x = \frac{\Delta t}{\Delta x} \frac{\Delta y \Delta z}{\Delta y \Delta z} \lambda_x = \Delta t \frac{\Delta y \Delta z}{\Delta V} \lambda_x,\tag{3.54}$$

therefore the time step should be restricted according to

$$\Delta t_{i,j,k} = CFL \min \left(\frac{\Delta V_{i,j,k}}{3 \Delta y \Delta z \lambda_x}, \frac{\Delta V_{i,j,k}}{3 \Delta x \Delta z \lambda_y}, \frac{\Delta V_{i,j,k}}{3 \Delta x \Delta y \lambda_z} \right).\tag{3.55}$$

The factor 3 comes from the three space dimension that waves can propagate. In 2-D problems the time step is found analogous to Eq. 3.55 with factor 2 in the denominator. In the simulations depending on spatial reconstruction, for first order time integration maximum CFL number of 0.9 and for RK4 method a maximum of 1.7 – 1.9 are used.

The formulation explained above determines a different time step at each computational cell, depending on the corresponding wave speeds and cell size, which is called **local time stepping**. This approach, which accelerates the simulation, is favorable in steady-state calculations. But for unsteady calculations the whole flow field should be integrated with the same time step, without destroying the stability condition. Because of this reason, for unsteady calculations the smallest time step in the domain is found and used for all the cells. This approach is referred to as **global time stepping**.

3.6 Initial and Boundary Conditions

3.6.1 Initial Conditions

Initialization of a numerical domain is crucial in the sense of starting a stable solution and minimizing the calculation time. The initialization of the domain depends on the type of flow problem (external or internal).

For external flows the domain can be initialized by far field values. For internal flows, on the other hand various options are possible, while the easiest way is to use the inlet

conditions for the whole domain. Alternatively, exit pressure and inlet velocity can also be used for initialization.

3.6.2 Boundary Conditions

For inviscid flows three types of boundary conditions are implemented in **CATUM**. Solid walls represent the geometry of the investigated body, thus they are purely physical, whilst inlet and outlet boundaries define the outer limits of the numerical domain, so they are purely numerical. In addition to those, periodic boundaries are also used in the code to simplify and accelerate the solution of symmetric problems.

3.6.2.1 Solid Walls

Physically, impermeable solid surfaces in inviscid flows have only one property, which is the flow tangency condition. This property also satisfies the no-penetration condition without restricting the flow in any other way. In particular a solid surface may be replaced by an image or ghost-flow [60]. In this investigation, all boundaries are treated with two ghost-cells, in order to be consistent for higher order reconstructions of flow variables also at the boundaries. For a simplified 2-D case, wall boundary is demonstrated in Fig. 3.7.

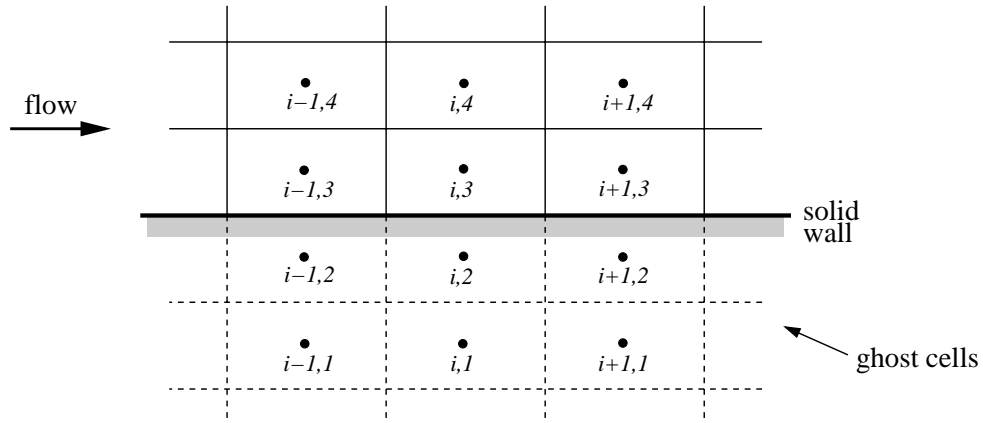


Figure 3.7: 2-D representation of the numerical discretization of solid wall boundaries.

The flow tangency condition is satisfied by the following relation

$$\mathbf{v} \cdot \mathbf{n} = 0, \quad (3.56)$$

where \mathbf{v} is the average velocity vector on the wall and \mathbf{n} is the wall normal. The best practice for constructing the ghost-flow is reflection, where scalar quantities reflect symmetrically onto the ghost-region and vector quantities such as velocity reflect with a change in sign [60]. Therefore, following Fig. 3.7, ghost-cell values for cell $(i, 2)$ are

defined as follows

$$\begin{aligned}\rho_{i,2} &= \rho_{i,3} \\ \mathbf{v}_{i,2} &= \mathbf{v}_{i,3} - 2\mathbf{n}_{i,3} \cdot (\mathbf{v}_{i,3} \cdot \mathbf{n}_{i,3}) \\ p_{i,2} &= p_{i,3},\end{aligned}\tag{3.57}$$

and for cell $(i, 1)$

$$\begin{aligned}\rho_{i,1} &= \rho_{i,4} \\ \mathbf{v}_{i,1} &= \mathbf{v}_{i,4} - 2\mathbf{n}_{i,4} \cdot (\mathbf{v}_{i,4} \cdot \mathbf{n}_{i,4}) \\ p_{i,1} &= p_{i,4}.\end{aligned}\tag{3.58}$$

Schmidt [101] has further improved wall boundary conditions by considering the curvature of the solid surface, where a pressure gradient function is implemented in the wall normal direction depending on the curvature.

3.6.2.2 Periodic Boundaries

Periodic boundaries are used to simplify and accelerate the simulations of symmetric flow problems such as circular pipe flows, where every quadrant is assumed to have exactly the same flow field. They are also needed for the connectivity plane of c - or o -grids, which are often used for the simulations of wing type bodies.

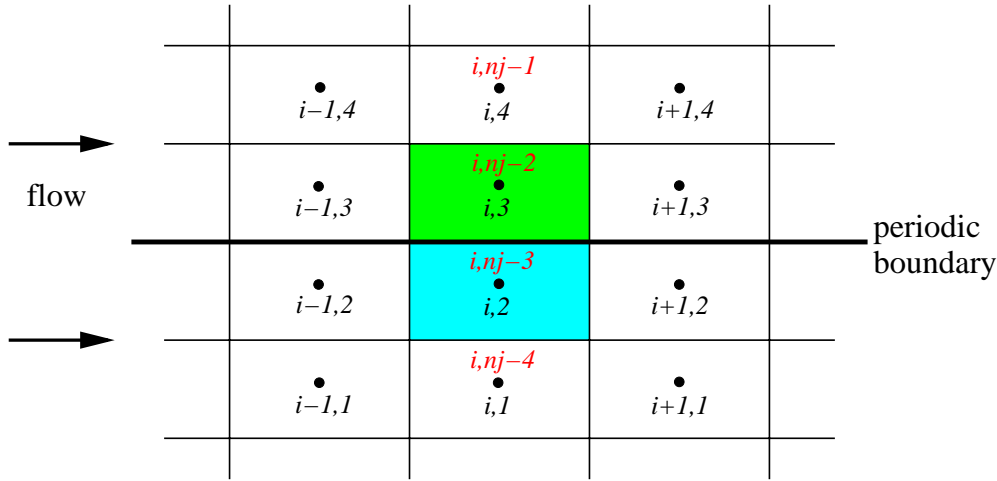


Figure 3.8: 2-D representation of the numerical discretization of periodic boundaries in y -direction. The **last cell** $(i, nj - 3)$ and the **first cell** $(i, 3)$ are adjacent to each other.

The periodic boundary condition is implemented again by considering the ghost-cell method explained earlier. The main idea behind periodic boundaries is that in the direction where periodicity is assumed, the **last cell** and the **first cell** are adjacent to each other. Figure 3.8 depicts a situation where the flow domain has a periodic boundary in y -direction. Therefore, the ghost-cells in both directions coincide with the normal cells. Such that, $(i, 1) \rightarrow (i, nj - 4)$, $(i, 2) \rightarrow (i, nj - 3)$, $(i, nj - 2) \rightarrow (i, 3)$ and $(i, nj - 1) \rightarrow (i, 4)$. Hence, the boundary values are set as follows

$$\begin{aligned}
\rho_{i,2} &= \rho_{i,nj-3}, \\
\mathbf{v}_{i,2} &= \mathbf{v}_{i,nj-3}, \\
p_{i,2} &= p_{i,nj-3},
\end{aligned} \tag{3.59}$$

and

$$\begin{aligned}
\rho_{i,1} &= \rho_{i,nj-4}, \\
\mathbf{v}_{i,1} &= \mathbf{v}_{i,nj-4}, \\
p_{i,1} &= p_{i,nj-4}.
\end{aligned} \tag{3.60}$$

3.6.2.3 Inlet and Outlet Boundaries

As before, two ghost-cells are used again to determine the flow variables at the inlet and outlet boundaries. Figure 3.9 shows this method for a simplified 2-D case.

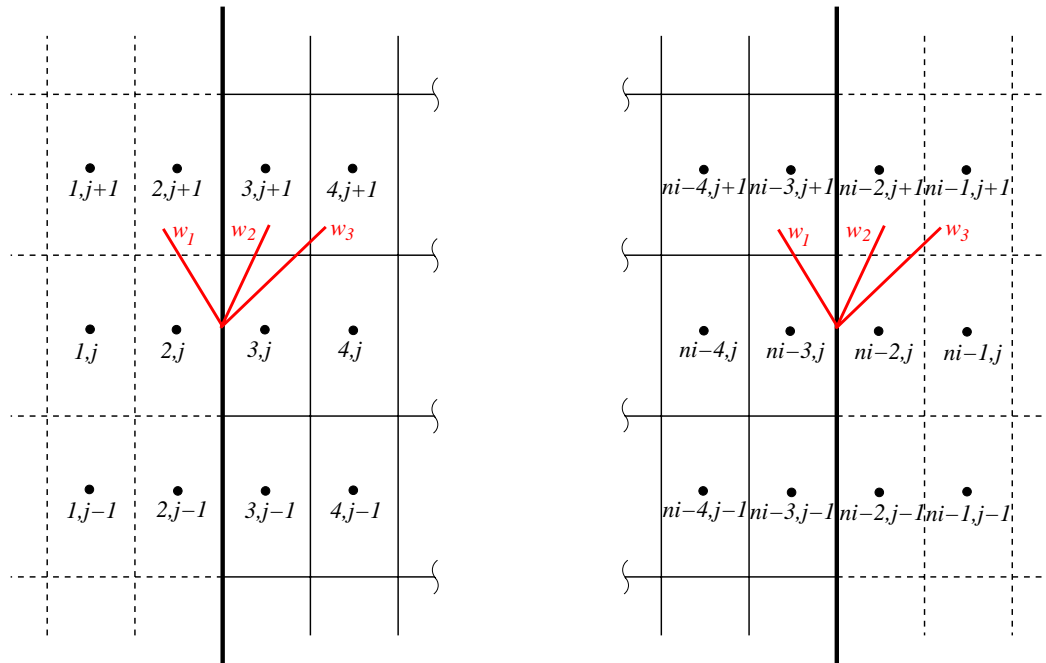


Figure 3.9: 2-D representation of the numerical discretization of inlet and outlet boundaries in x -direction. Red lines represent the propagation direction of the waves given by Eq. 3.61 for subsonic inlet and outlet condition

The one-dimensional characteristic theory is usually applied when considering inlet and outlet boundaries [60]. The number of physical variables that have to be imposed at a boundary depends on the propagation properties of the system, especially on the information propagated from the boundary towards the inside of the flow field [44]. According to the wave propagation properties, the number of required physical boundary conditions are determined depending on the type of the boundary, which is summarized in Table 3.1.

Table 3.1: Number of required boundary conditions according to one-dimensional characteristic treatment.

	subsonic	supersonic
inlet	2	3
outlet	1	0

However, from the numerical point of view in order to solve the equation system at the boundary, information about all the variables is needed in addition to physical conditions. This additional information is determined numerically. It is important to note that this discussion is based on one-dimensional characteristic theory and therefore the total number of variables to be determined is 3, i.e. density, pressure and velocity.

Supersonic inlet and outlet boundary conditions are easiest to consider. For a supersonic inlet no information can propagate in upstream direction, so all the information comes from the outside domain. Therefore, the inlet variables are simply the physical inlet conditions of the flow field. Whereas for a supersonic outlet no information can propagate into the numerical domain, so all the boundary values are determined numerically using the inside values.

For a subsonic outlet, only one condition is needed to be specified and in most of the practical applications exit or back pressure is used a physical boundary condition.

The subsonic inlet boundary condition requires most consideration among all. From Table 3.1 it can be seen that one boundary condition needs to be calculated and two must be specified (see Fig. 3.9). Characteristic variables and primitive variables are related to each other by using the following differential form

$$\begin{aligned}
 dw_1 &= du - \frac{dp}{\rho c}, \\
 dw_2 &= d\rho - \frac{dp}{c^2}, \\
 dw_3 &= du + \frac{dp}{\rho c}.
 \end{aligned}
 \tag{3.61}$$

In this equation the characteristic variables w_1 , w_2 and w_3 correspond to wave speeds $u - c$, u and $u + c$ respectively. Therefore for a subsonic inflow, $u < c$, w_1 carries the information from the internal domain to the inlet boundary and hence it should not be specified. This observation concludes that the specification of both u and p in the subsonic inlet results in a ill-posed problem. For a well-posed subsonic inlet boundary condition either the (ρ, p) or (ρ, u) pair should be chosen as a physical condition [60]. Once the physical boundary conditions are decided, they are simply set in the corresponding ghost-cell in the code.

The discussion so far was focused on which physical boundary conditions should be specified according to the nature of the boundary. The next step is to determine numerical boundary conditions. One method is simply to use first or second order extrapolations of the inner variables to calculate the values in the ghost-cells. As an

example, density and velocity in the ghost-cell $(ni - 2, j)$ can be approximated as

$$\begin{aligned}\rho_{ni-2,j} &= 2\rho_{ni-3,j} - \rho_{ni-4,j}, \\ u_{ni-2,j} &= 2u_{ni-3,j} - u_{ni-4,j}.\end{aligned}\quad (3.62)$$

Specifying a constant pressure at the inlet or outlet boundaries cause significant problems, as waves cannot propagate through the boundaries and reflect back into the flow field, which can damage the numerical solution. To overcome this problem, non-reflecting boundary conditions for inlet and outlet can be used, which are based on Riemann-invariants of the one-dimensional characteristic theory [44]. To illustrate this method, one can consider a subsonic outlet, where the first relation of Eq. 3.61 corresponds to the $u - c$ characteristic, which propagates into the flow field. Rewriting this relation by using difference operator gives

$$\Delta w_1 = \Delta u - \frac{\Delta p}{\rho c}.\quad (3.63)$$

Evaluating this equation at the outlet boundary $(ni - 2, j)$ and assuming constant far field values as $u_\infty = 0$ and $p_\infty = \text{const}$ one gets

$$\Delta w_1 = (u_\infty - u_{ni-2,j}) - \frac{p_\infty - p_{ni-2,j}}{\rho_\infty c_\infty}.\quad (3.64)$$

To solve this equation, dw_1 must be specified. A typical choice is $dw_1 = 0$ [60]; with $u_\infty = 0$, Eq. 3.64 reduces to

$$p_{ni-2,j} = p_\infty + \rho_\infty c_\infty u_{ni-2,j}.\quad (3.65)$$

Together with the extrapolations given by Eq. 3.62, Eq. 3.65 results in a purely non-reflecting boundary condition, which is applicable to free-stream calculations directly. But particularly for cavitation calculations non-reflecting boundary conditions are unsuitable, as they do not provide a time-averaged constant boundary value due to the continuous wave propagation through the boundaries. On the other hand, a reflecting boundary condition can damage the numerical solution inside the flow domain, as mentioned earlier. These facts are taken into account by the use of essentially non-reflective or mixed reflecting/non-reflecting conditions. Based on the idea proposed by Rudy and Strickwerda [94] the physical boundary conditions at the inlet and outlet are relaxed during the solution procedure. For **steady state** calculations a relaxation formula for the mixed reflecting/non-reflecting outlet pressure can be written as follows

$$p_{out,mix} = p_{ni-2,j} = \phi p_\infty + (1 - \phi)p_{ni-3,j},\quad (3.66)$$

similarly at the inlet

$$p_{in,mix} = p_{2,j} = \phi p_\infty + (1 - \phi)p_{3,j},\quad (3.67)$$

where $\phi > 0$ is the relaxation coefficient and depends on the problem and flow conditions.

For **unsteady** inlet and outlet boundaries the formulation of mixed reflecting/non-reflecting boundary condition needs more attention, as the effect of the unsteady wave

propagation at the boundaries should also be taken into account. In this case, the relaxation coefficient ϕ is a function of the time step of the calculation, i.e.

$$\phi = \frac{c \cdot \Delta t_{CFD}}{l}, \quad (3.68)$$

where c is the speed of sound, l is the cell length and Δt_{CFD} is the global time step used in the calculation. Let the superscripts $+$ and $-$ denote the values of the current and the previous instants in time respectively, the pressure and velocity at the inlet boundary are given by

$$p_{in,mix}^+ = p_{2,j}^+ = \frac{p_{2,j}^- + 0.5 \cdot \phi \cdot [p_{3,j} + p_{2,j}^- + \rho_{2,j}^- \cdot c_{2,j}^- \cdot (u_\infty - u_{3,j})]}{1 + \phi}, \quad (3.69)$$

$$u_{in,mix}^+ = u_{2,j}^+ = \frac{u_{2,j}^- + 0.5 \cdot \phi \cdot \left[\frac{p_{2,j}^- - p_{3,j}}{\rho_{2,j}^- \cdot c_{2,j}^-} + u_\infty + u_{3,j} \right]}{1 + \phi}, \quad (3.70)$$

similarly for the outlet boundary

$$p_{out,mix}^+ = p_{ni-2,j}^+ = \frac{p_{ni-2,j}^- + 0.5 \cdot \phi \cdot [p_{ni-3,j} + p_\infty + \rho_{ni-2,j}^- \cdot c_{ni-2,j}^- \cdot (u_{ni-3,j} - u_{ni-2,j}^-)]}{1 + \phi}, \quad (3.71)$$

$$u_{out,mix}^+ = u_{2,j}^+ = \frac{u_{2,j}^- + 0.5 \cdot \phi \cdot \left[\frac{p_{ni-3,j} - p_\infty}{\rho_{2,j}^- \cdot c_{2,j}^-} + u_{ni-2,j}^- + u_{ni-3,j} \right]}{1 + \phi}. \quad (3.72)$$

In both cases the specification of the average density is performed by the modified Tait model and numerical inlet and outlet boundaries are assumed to be located far from two-phase domains.

Once all the ghost-cell values are determined according to their boundary condition type, the flux calculation is performed through the boundaries by using the Riemann approach as explained before. Moreover, implementing two ghost-cells in every direction allows for higher order reconstruction even for the boundary variables.

Chapter 4

Validation

In order to validate the developed code several test cases have been performed. The first test cases focus on the fundamental validation of the code through numerical shock tube examples of ideal gas flow and liquid water. Then, the proposed two-phase model is compared with the solution of the Rayleigh-Plesset equation for the collapse of an isolated single bubble filled with water vapor only. Finally, the importance of the order of the discretization and the effects of the mesh resolution are demonstrated by 2-D injection nozzle calculations.

4.1 1-D Shock Tube

4.1.1 Ideal Gas

The first two shock tube test cases are often used in the validation of numerical methods that involve ideal gas flows. These tests were first suggested by Sod [113] and are usually referred to as Sod's test problems in the literature. They consist of initially specified left and right states separated at $t_0 = 0$ s similar to the real shock tube setup where a membrane or a valve divides the flow domain. The computational flow domain is depicted in Fig. 4.1. The tube is assumed to be infinitely long, which means that the initiated waves travel through the tube without being disturbed by numerical boundary conditions.

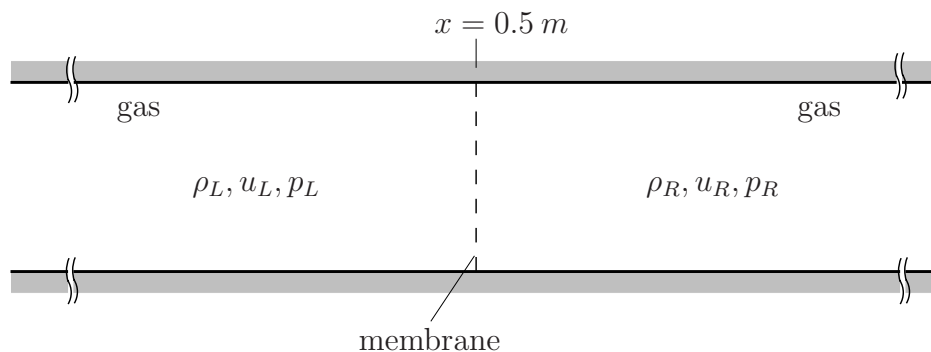


Figure 4.1: Representation of shock tube problem for ideal gas test cases. Flow domain at $t_0 = 0$ s.

The first test case has the following initial conditions

$$\mathbf{w}(x, 0) = \begin{cases} \mathbf{w}_L & x < 0 \\ \mathbf{w}_R & x \geq 0 \end{cases} \quad (4.1)$$

where \mathbf{w} is the vector of primitive variables given by

$$\mathbf{w}_L = \begin{vmatrix} \rho_L \\ u_L \\ p_L \end{vmatrix} = \begin{vmatrix} 1 \text{ kg/m}^3 \\ 0 \text{ m/s} \\ 100000 \text{ Pa} \end{vmatrix}, \quad (4.2)$$

$$\mathbf{w}_R = \begin{vmatrix} \rho_R \\ u_R \\ p_R \end{vmatrix} = \begin{vmatrix} 0.125 \text{ kg/m}^3 \\ 0 \text{ m/s} \\ 10000 \text{ Pa} \end{vmatrix}.$$

The solution of this case consists of a left expansion wave, a contact surface and a right running shock. Numerical calculations are performed in the spatial domain $0 \leq x \leq 1 \text{ m}$ with 100 equidistant computational cells. Figure 4.2 shows the solution profiles for pressure (left) and density (right) at time $t = 6.0 \cdot 10^{-3} \text{ s}$. These profiles correspond to first order discretization in space and time. As ideal gas flow is considered, non-modified flux formulation is chosen here.

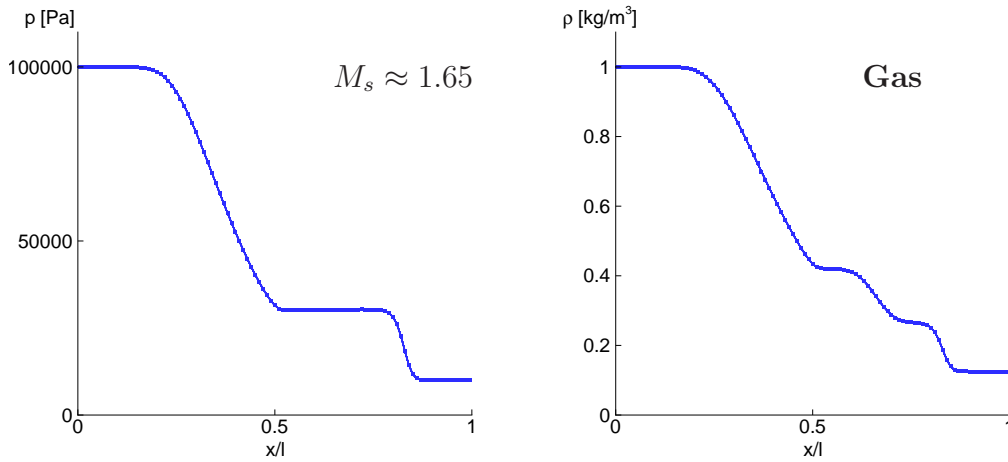


Figure 4.2: Numerically obtained pressure p and density ρ profiles at $t = 6.0 \cdot 10^{-3} \text{ s}$. **First order calculation in space and time.** Initial conditions: $\rho_L = 1 \text{ kg/m}^3$, $\rho_R = 0.125 \text{ kg/m}^3$, $p_L = 100000 \text{ Pa}$, $p_R = 10000 \text{ Pa}$, $u_L = u_R = 0 \text{ m/s}$, initial discontinuity at $x = 0.5 \text{ m}$, tube length 1 m , 100 mesh points.

The density profile in Fig. 4.2 shows all three wave structures that are present in the problem. The smearing of the discontinuous waves (contact surface and shock) is caused by the first order discretization of the problem. The following figure depicts the same situation calculated by second order scheme with four-stage Runge-Kutta time integration and Van-Leer limiter, where smearing is avoided and the discontinuities are resolved as sharp interfaces.

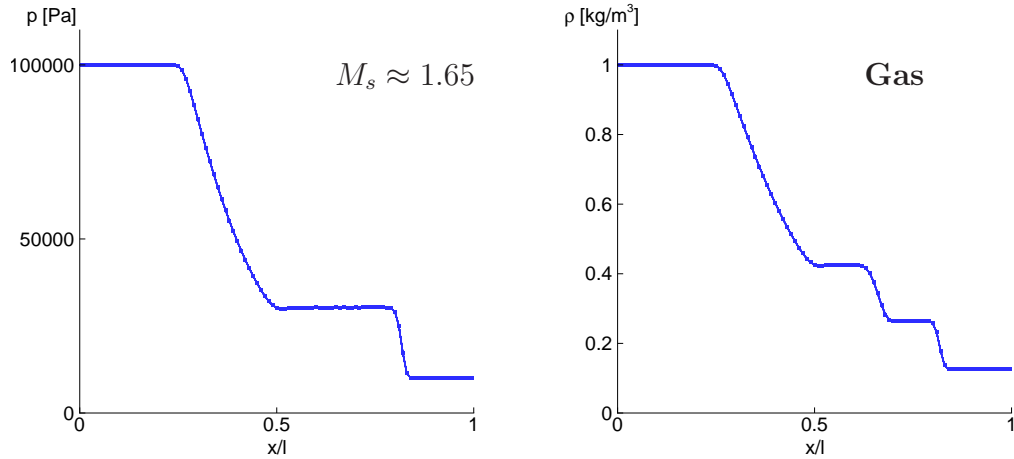


Figure 4.3: Numerically obtained pressure p and density ρ profiles at $t = 6.0 \cdot 10^{-3} s$. **Second order calculation with Van-Leer limiter and 4-stage Runge-Kutta scheme.** Initial conditions: $\rho_L = 1 kg/m^3$, $\rho_R = 0.125 kg/m^3$, $p_L = 100000 Pa$, $p_R = 10000 Pa$, $u_L = u_R = 0 m/s$, initial discontinuity at $x = 0.5 m$, tube length $1 m$, 100 mesh points.

The second shock tube example is somewhat more challenging than the first one and some numerical methods fail to resolve the physical solution. The initial conditions are given for this case as

$$\mathbf{w}(x, 0) = \begin{cases} \mathbf{w}_L & x < 0 \\ \mathbf{w}_R & x \geq 0 \end{cases} \quad (4.3)$$

where \mathbf{w} is

$$\mathbf{w}_L = \begin{vmatrix} \rho_L \\ u_L \\ p_L \end{vmatrix} = \begin{vmatrix} 1 kg/m^3 \\ 0 m/s \\ 100000 Pa \end{vmatrix}, \quad (4.4)$$

$$\mathbf{w}_R = \begin{vmatrix} \rho_R \\ u_R \\ p_R \end{vmatrix} = \begin{vmatrix} 0.01 kg/m^3 \\ 0 m/s \\ 1000 Pa \end{vmatrix}.$$

As the previous test case, the solution of this problem also consists of an expansion wave, a contact surface and a right running shock. The small separation distance between the shock and contact surface makes it difficult for the numerical model to resolve both of them smoothly. Moreover, both the expansion wave and the shock contain sonic points, which can cause problems with some solvers. Together with the large initial pressure ratio between the left and right states, the difficulty of the test case increases. The following figure gives the pressure and density profiles for the first order calculation at $t = 3.32 \cdot 10^{-3} s$.

As in the previous test case, the first order results suffer from the smearing of the discontinuities but this time it is much more intensified. Moreover, as seen in the density profile, it is obvious that the numerical method experiences difficulty resolving the three-wave structure as they are very close to each other. The sonic point in

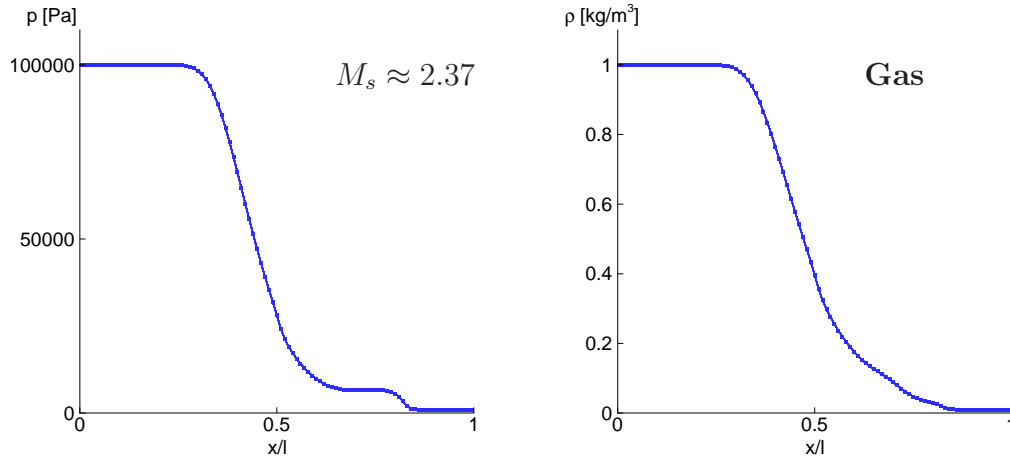


Figure 4.4: Numerically obtained pressure p and density ρ profiles at $t = 3.32 \cdot 10^{-3}$ s. **First order calculation in space and time, 100 mesh points.** Initial conditions: $\rho_L = 1$ kg/m³, $\rho_R = 0.01$ kg/m³, $p_L = 100000$ Pa, $p_R = 1000$ Pa, $u_L = u_R = 0$ m/s, initial discontinuity at $x = 0.5$ m, tube length 1 m.

the expansion wave can be observed at $x = 0.5$. Whereas the second order results given by Fig. 4.5 show the improvement in the resolution of the waves, and their structures are visible. It should be noted that, although second order results have a better quality, smearing effects in the discontinuities still exist. This is due to the relatively coarse mesh used in the calculation. The effect of the mesh resolution on capturing the discontinuous interfaces like contact surface and shock is demonstrated in Fig 4.6, where 250 mesh points are used in the same domain.

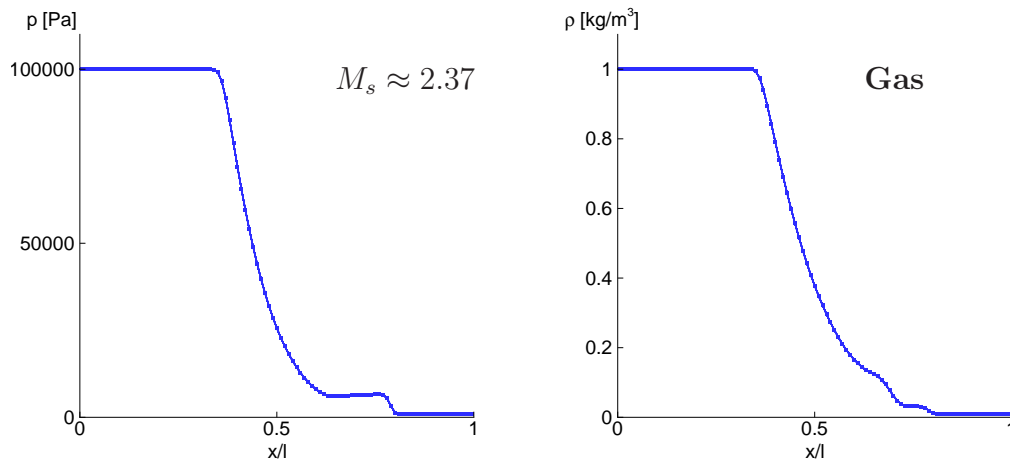


Figure 4.5: Numerically obtained pressure p and density ρ profiles at $t = 3.32 \cdot 10^{-3}$ s. **Second order calculation with Van-Leer limiter and 4-stage Runge-Kutta scheme, 100 mesh points.** Initial conditions: $\rho_L = 1$ kg/m³, $\rho_R = 0.01$ kg/m³, $p_L = 100000$ Pa, $p_R = 1000$ Pa, $u_L = u_R = 0$ m/s, initial discontinuity at $x = 0.5$ m, tube length 1 m.

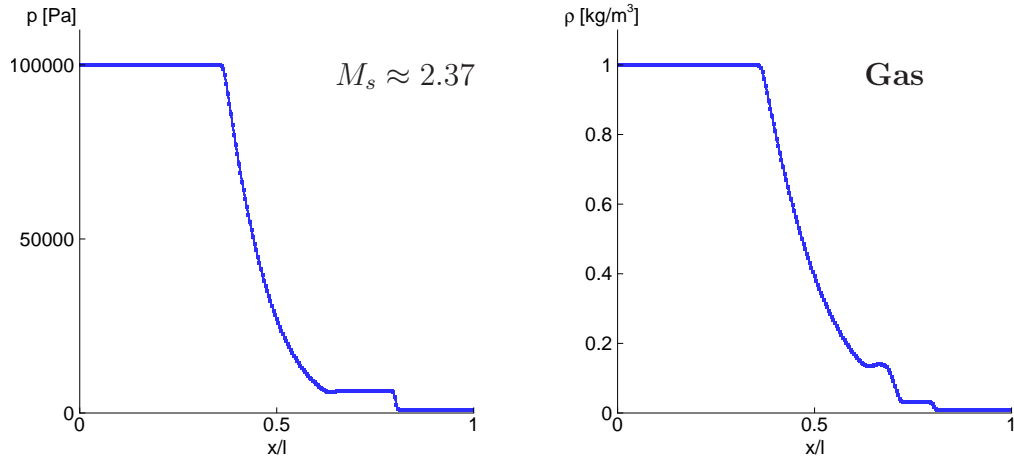


Figure 4.6: Numerically obtained pressure p and density ρ profiles at $t = 3.32 \cdot 10^{-3} s$. **Second order calculation with Van-Leer limiter and 4-stage Runge-Kutta scheme, 250 mesh points.** Initial conditions: $\rho_L = 1 \text{ kg/m}^3$, $\rho_R = 0.01 \text{ kg/m}^3$, $p_L = 100000 \text{ Pa}$, $p_R = 1000 \text{ Pa}$, $u_L = u_R = 0 \text{ m/s}$, initial discontinuity at $x = 0.5 \text{ m}$, tube length 1 m .

The final ideal gas shock tube experiment is given by Toro [119] and referred to as a very severe test problem. The solution contains a left expansion wave, a contact surface and a right running shock. Originally, this test case was investigated by Woodward and Collela [133] as a blast wave problem. Here, only the left half of this problem is considered. Like the previous cases, the initial conditions are given as

$$\mathbf{w}(x, 0) = \begin{cases} \mathbf{w}_L & x < 0 \\ \mathbf{w}_R & x \geq 0 \end{cases} \quad (4.5)$$

with

$$\mathbf{w}_L = \begin{vmatrix} \rho_L \\ u_L \\ p_L \end{vmatrix} = \begin{vmatrix} 1 \text{ kg/m}^3 \\ 0 \text{ m/s} \\ 1000 \text{ Pa} \end{vmatrix}, \quad (4.6)$$

$$\mathbf{w}_R = \begin{vmatrix} \rho_R \\ u_R \\ p_R \end{vmatrix} = \begin{vmatrix} 0.01 \text{ kg/m}^3 \\ 0 \text{ m/s} \\ 1000 \text{ Pa} \end{vmatrix}.$$

As the test case is extremely challenging, a finer mesh with 500 points is used and second order results for pressure and density are presented only in Fig 4.7.

The solid line shows the results of the reference calculation obtained with the same method on a grid with 5000 cells, while the blue dots correspond to the calculation with 500 mesh points. As can be seen in the pressure profile, expansion wave and shock are captured within a couple of cells at the correct locations. The contact surface is also not smeared out and resolved as a sharp interface as seen in the density profile. But it experiences numerical overshoot associated with the second order reconstruction of Van-Leer. This effect can also be seen in the pressure profile as a small oscillation, where the contact surface is located.

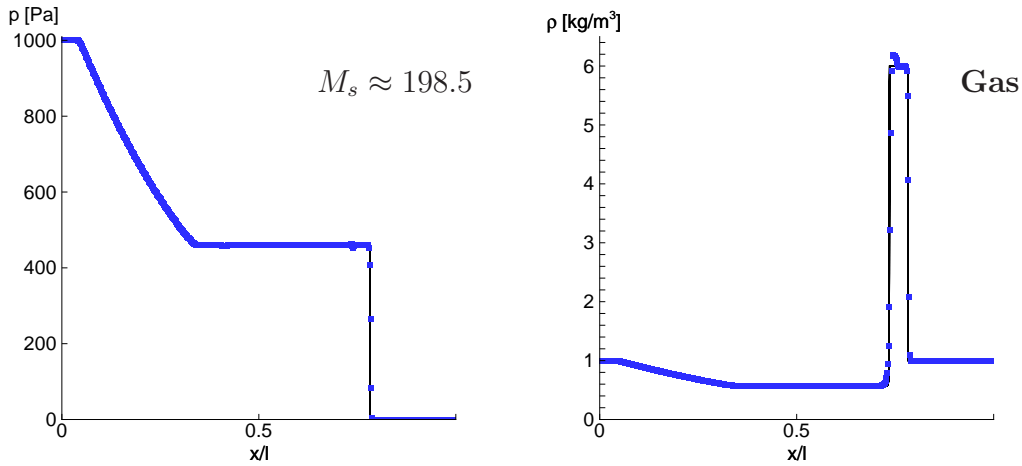


Figure 4.7: Numerically obtained pressure p and density ρ profiles at $t = 0.012$ s. **Second order calculation with Van-Leer limiter and 4-stage Runge-Kutta scheme, 500 mesh points.** Black line corresponds to reference calculation with 5000 mesh points. Initial conditions: $\rho_L = 1$ kg/m³, $\rho_R = 1$ kg/m³, $p_L = 1000$ Pa, $p_R = 0.01$ Pa, $u_L = u_R = 0$ m/s, initial discontinuity at $x = 0.5$ m, tube length 1 m.

The ideal gas shock tube test cases considered in this subsection are encountered often in the literature and used to test inviscid flow solvers. It is shown that the developed code accurately captures the discontinuities in these tests. But the resolution of the interfaces is highly dependent on the mesh and the accuracy of the solver scheme that is used.

4.1.2 Liquid Water

Single-phase Shock Tube

In this subsection, shock tube problems with liquid water are considered. These test cases are important to demonstrate the potential of the method to capture and predict wave dynamics in compressible liquid flows.

The first test case is very similar to the Sods shock tube experiments. A 1-D tube of length 1 m is assumed to be filled with liquid water at 293 K. The tube is initially divided into two regions of length $l/2$ as before. The initial conditions are depicted in Fig. 4.8 and given as

$$\mathbf{w}(x, 0) = \begin{cases} \mathbf{w}_L & x < 0 \\ \mathbf{w}_R & x \geq 0 \end{cases}, \quad (4.7)$$

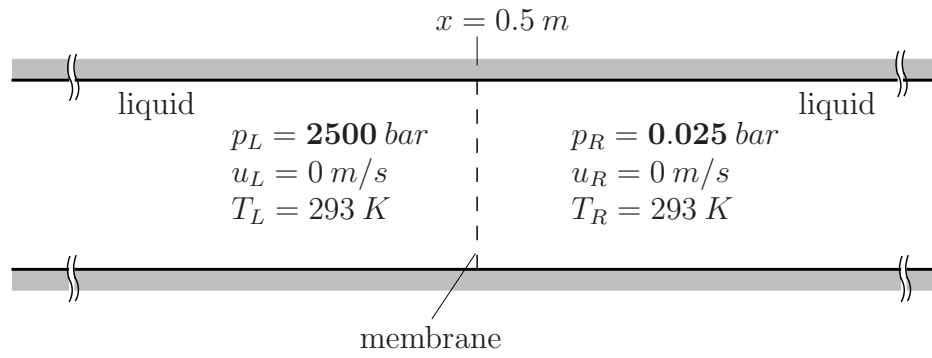


Figure 4.8: Representation of first shock tube problem for **single-phase liquid flow**. Flow domain at $t_0 = 0$ s.

with

$$\mathbf{w}_L = \begin{vmatrix} p_L \\ u_L \\ T_L \end{vmatrix} = \begin{vmatrix} 2500 \text{ bar} \\ 0 \text{ m/s} \\ 293 \text{ K} \end{vmatrix}, \quad (4.8)$$

$$\mathbf{w}_R = \begin{vmatrix} p_R \\ u_R \\ T_R \end{vmatrix} = \begin{vmatrix} 0.025 \text{ bar} \\ 0 \text{ m/s} \\ 293 \text{ K} \end{vmatrix}.$$

The flow is initially at rest ($u_L = u_R = 0$ m/s) and the densities on both sides are determined by Eq. 2.65. The numerical domain is divided into 250 equidistant computational cells. Figure 4.9 depicts the pressure and velocity profiles for the given conditions.

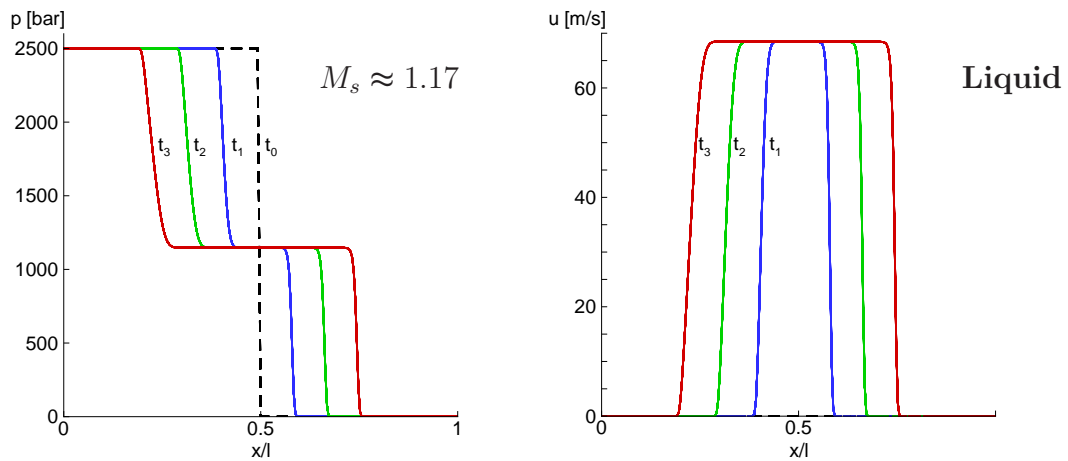


Figure 4.9: Numerically obtained pressure p and velocity u for 4 equidistant instants in time ($t_0 = 0$ s, $\Delta t = 4.9 \cdot 10^{-5}$ s). **Second order calculation with minmod limiter and 4-stage Runge-Kutta scheme, 250 mesh points.** Initial conditions: $p_L = 2500$ bar, $p_R \approx p_{sat} = 0.025$ bar, $T_L = T_R = 293$ K, $u_L = u_R = 0$ m/s, initial discontinuity at $x = 0.5$ m, tube length 1 m.

On the left of Fig. 4.9 the pressure is plotted for three instants in time, which shows the

shock and the rarefaction wave that are captured without the presence of overshoots. Due to the high acoustic impedance of $O(10^6)$ of the liquid, the convective velocity u reaches hardly 70 m/s (Fig. 4.9 - right). The shock Mach number M_s for the presumed pressure ratio is still rather small, $M_s \approx 1.17$.

The second liquid shock tube test focuses on the resolution of the contact discontinuity. This is important in the sense of cavitating flows, as the phase interfaces behave like contact a surface. A traveling contact surface is simulated by initializing the domain with different left and right temperatures and a constant velocity, which is depicted in Fig. 4.10.

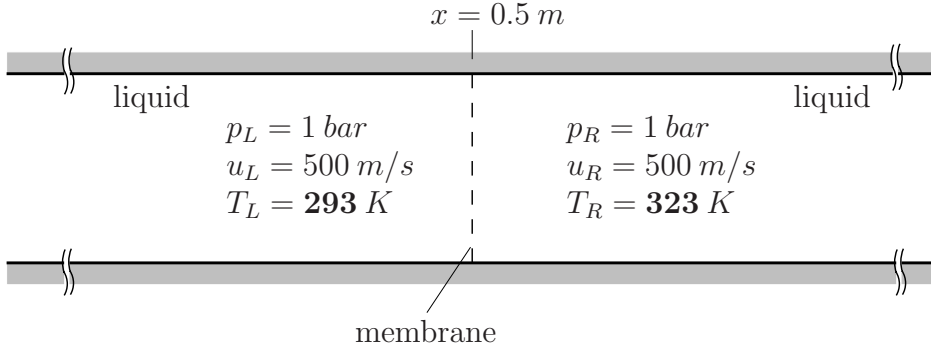


Figure 4.10: Representation of second shock tube problem for **single-phase liquid flow**. Flow domain at $t_0 = 0\text{ s}$.

The initial conditions are given as

$$\mathbf{w}(x, 0) = \begin{cases} \mathbf{w}_L & x < 0 \\ \mathbf{w}_R & x \geq 0 \end{cases} \quad (4.9)$$

with

$$\mathbf{w}_L = \begin{vmatrix} p_L \\ u_L \\ T_L \end{vmatrix} = \begin{vmatrix} 1\text{ bar} \\ 500\text{ m/s} \\ 293\text{ K} \end{vmatrix}, \quad (4.10)$$

$$\mathbf{w}_R = \begin{vmatrix} p_R \\ u_R \\ T_R \end{vmatrix} = \begin{vmatrix} 1\text{ bar} \\ 500\text{ m/s} \\ 323\text{ K} \end{vmatrix}.$$

The densities on both sides are determined by Eq. 2.65. Figure 4.11 depicts the temperature for three instants in time. The initial discontinuity of the temperature (see Fig. 4.11) is well preserved although the pressure and the velocity experience oscillations due to the form of the modified Tait model. This is because the pressure cannot be represented by a function in the form $p = c_1 \rho e + c_2$, where c_1 and c_2 are constants [44].

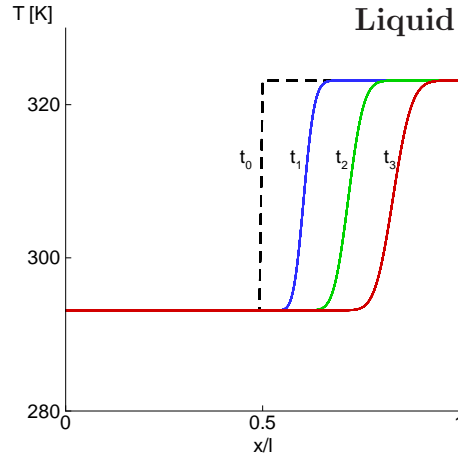


Figure 4.11: Numerically obtained temperature T for 4 equidistant instants in time ($t_0 = 0$ s, $\Delta t = 2.2 \cdot 10^{-3}$ s). **Second order calculation with minmod limiter and 4-stage Runge-Kutta scheme, 250 mesh points.** Initial conditions: $T_L = 293$ K, $T_R = 323$ K, $p_L = p_R = 1$ bar, $u_L = u_R = 500$ m/s, initial discontinuity at $x = 0.5$ m, tube length 1 m.

Two-phase Shock Tube

The two-phase shock tube example uses the phase transition model and the combined equation of state definition that were introduced in chapter 2. The decrease of density below the saturation density and therefore evaporation of the pure liquid phase is enforced by **two symmetric expansion waves** moving opposite to each other with 10 m/s. The domain is the same as in the previous test cases, $0 \leq x \leq 1$ m (Fig. 4.12), discretized by 250 mesh points.

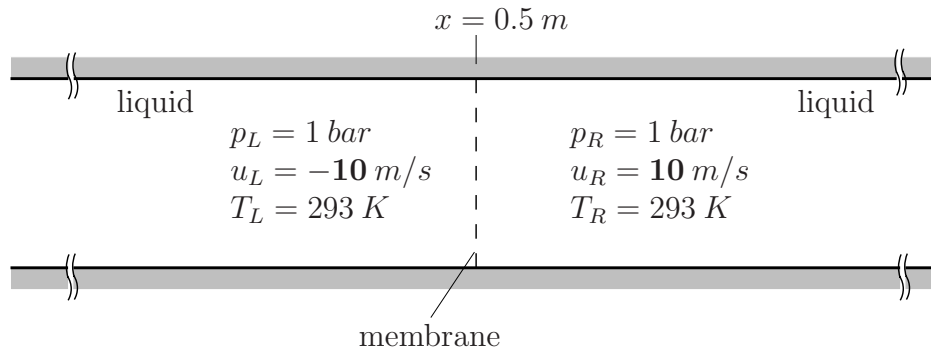


Figure 4.12: Representation of shock tube problem for **two-phase calculation**. Flow domain at $t_0 = 0$ s.

The initial conditions in the tube is as follows

$$\mathbf{w}(x, 0) = \begin{cases} \mathbf{w}_L & x < 0 \\ \mathbf{w}_R & x \geq 0 \end{cases} \quad (4.11)$$

with

$$\mathbf{w}_L = \begin{vmatrix} p_L \\ u_L \\ T_L \end{vmatrix} = \begin{vmatrix} 1 \text{ bar} \\ -10 \text{ m/s} \\ 293 \text{ K} \end{vmatrix}, \quad (4.12)$$

$$\mathbf{w}_R = \begin{vmatrix} p_R \\ u_R \\ T_R \end{vmatrix} = \begin{vmatrix} 1 \text{ bar} \\ 10 \text{ m/s} \\ 293 \text{ K} \end{vmatrix}.$$

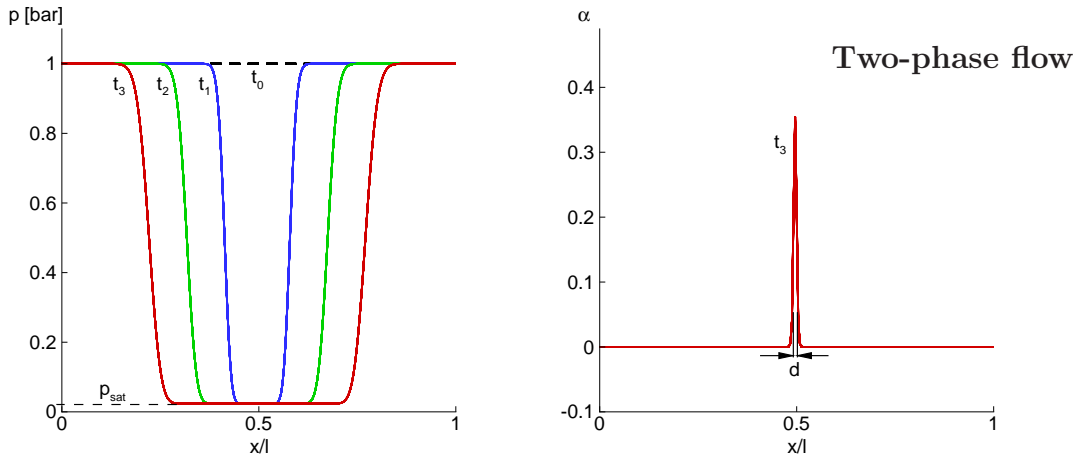


Figure 4.13: Numerically obtained pressure p for 4 equidistant instants in time ($t_0 = 0 \text{ s}$, $\Delta t = 6.0 \cdot 10^{-3} \text{ s}$) and void fraction α at $t_3 = 1.8 \cdot 10^{-4} \text{ s}$. **Second order calculation with minmod limiter and 4-stage Runge-Kutta scheme, 250 mesh points.** Initial conditions: $u_L = -10 \text{ m/s}$, $u_R = 10 \text{ m/s}$, $p_L = p_R = 1 \text{ bar}$, $T_L = T_R = 293 \text{ K}$, initial discontinuity at $x = 0.5 \text{ m}$, tube length 1 m .

In figure 4.13 the resulting pressure and void fraction profiles are shown. Because of the initially enforced velocity field, two expansion waves initiate at $x = 0.5 \text{ m}$ and propagate against each other. The expansion is strong enough for the pressure to drop instantly to vapor pressure and evaporation of the liquid is observed as the void fraction α suggests. As expansion waves propagate against each other, contact waves initiate in the region between them and propagate with the convective velocity of the flow which can be estimated by the linearized acoustic theory given in chapter 1 by

$$\Delta p \approx \rho c \Delta u, \quad (4.13)$$

or

$$\Delta u \approx \frac{\Delta p}{\rho c}. \quad (4.14)$$

The pressure decreases from 1 bar to vapor pressure $p_{sat} = 2340 \text{ Pa}$ across the rarefaction wave. Using the conditions ahead of the wave (ρ_{liq} and c_{liq}) and initial velocity of 10 m/s gives the velocity of the contact wave as 9.935 m/s . This is the velocity of the convective motion, which corresponds also to the propagation speed of the vapor region and results in $d \approx 0.004 \text{ m}$.

4.2 3-D Bubble Collapse

Single- and two-phase compressible liquid formulation has been tested in the previous sections using numerical shock tube experiments. In this section, the proposed two-phase model will be investigated for an isolated single bubble collapse.

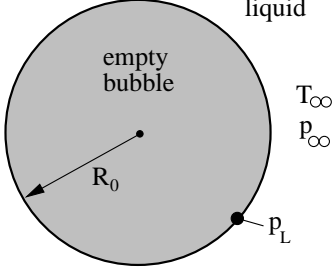
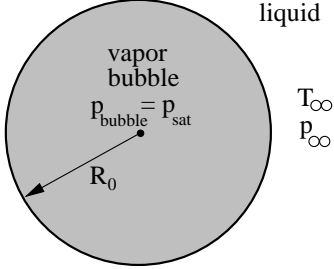
As already mentioned in chapter 1, the collapse mechanism of a single isolated bubble has been extensively studied theoretically and experimentally by numerous research groups for different conditions [34], [65], [85].

The growth and collapse dynamics of a spherical bubble are governed by the Rayleigh-Plesset equation given by 1.13. This equation can be simplified in the absence of viscous effects and surface tension. Following Young [135] we consider an **empty spherical bubble** for the analytical solution of the bubble collapse, which is governed by

$$R\ddot{R} + \frac{3}{2}\dot{R}^2 = \frac{p_L - p_\infty(t)}{\rho_{liq}}, \quad (4.15)$$

where p_L is the pressure in the liquid at the bubble wall [135]. In the analytical solution we assume that the pressure at the bubble wall is equal to the vapor pressure and is constant, i.e. $p_L = p_{sat}(T_\infty) = 2340 \text{ Pa}$. The flow conditions and the properties of the analytical model and the numerical code are summarized in the following table

Table 4.1: Comparison of the flow conditions and model assumptions for the analytical model and **CATUM** simulation.

Rayleigh-Plesset solution	CATUM simulation
 <p>“empty bubble” inviscid no gas content no surface tension incompressible (liquid) $p_\infty = 1 \text{ bar}$ $T_\infty = 293 \text{ K}$ $p_L = p_{sat}(T_\infty) = 2340 \text{ Pa}$ $R_0 = 0.4 \text{ mm}$</p>	 <p>pure vapor bubble inviscid no gas content no surface tension compressible (liquid and vapor) $p_\infty = 1 \text{ bar}$ $T_\infty = 293 \text{ K}$ $p_{bubble} = p_{sat}$ $R_0 = 0.4 \text{ mm}$</p>

By using Eq. 4.15, the temporal evolution of the bubble radius $R(t)$ can be calculated for a given initial radius R_0 and an enforced pressure difference between the bubble

wall and the surrounding liquid. The collapse of an **empty spherical bubble** defined by the incompressible, inviscid Rayleigh-Plesset equation without surface tension and without gas content is referred to as “Besant problem” in the literature [10].

In the numerical calculation a **pure vapor bubble** is considered. It is known from the theory and the observations that a vapor bubble initially in equilibrium with the surrounding liquid at $t_0 = 0$ and $p_{\infty,0} = p_{sat}$ will start to collapse if the pressure in the liquid is raised to $p_{\infty} > p_{sat}$ by $t > 0$ and held constant at the boundaries of the liquid domain (at infinity). The bubble collapses completely in this situation within the so called Rayleigh time $t_{Rayleigh}$.

In the calculation, a spherical vapor region is constructed in a 3-D flow domain. The resolution of the region corresponds to a discrete bubble in contrast to the application simulations where the resolution in space is restricted to large scale structures such as bubble clouds. The following picture depicts the initial vapor region that is constructed to calculate the bubble collapse.

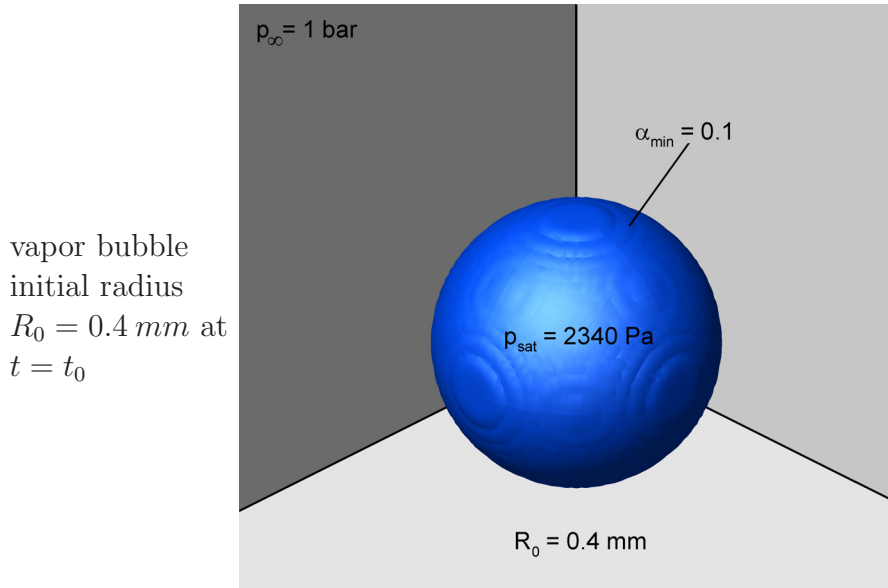


Figure 4.14: Isolated pure vapor bubble, initial radius $R_0 = 0.4 \text{ mm}$ at $t = t_0$. Bubble surface visualized by iso-surfaces of void fraction $\alpha_{min} = 0.1$.

The numerical boundaries are located 25 diameters away from the bubble and the corresponding boundary conditions model constant pressure $p_{\infty} = 1.0 \text{ bar}$ and $T_{\infty} = 293 \text{ K}$ at infinity. The pressure inside the bubble is given by the vapor pressure $p_{sat} = 2340 \text{ Pa}$ at $T_{\infty} = 293 \text{ K}$. The initial radius of the vapor bubble is $R_0 = 0.4 \text{ mm}$ and the grid resolution of $l_J = 0.02 \text{ mm}$ results in $\Psi = 20$ with respect to R_0 ; hence, the initially defined bubble is fully resolved (see section 2.4.2). Figure 4.15 shows the meridional plane of the discretization domain with the corresponding mesh.

The bubble interface is defined by the variation of void fraction values from $\alpha = 0.99$ inside the bubble and $\alpha = 0$ in the surrounding liquid, according to the defined initial radius R_0 .

Based on the *CFL* requirement stated in chapter 3 the applied numerical time step in this problem is of the order of $\Delta t = 6.5 \text{ nanoseconds}$. Although the numerical method includes compressibility effects, the results are compared with the solution

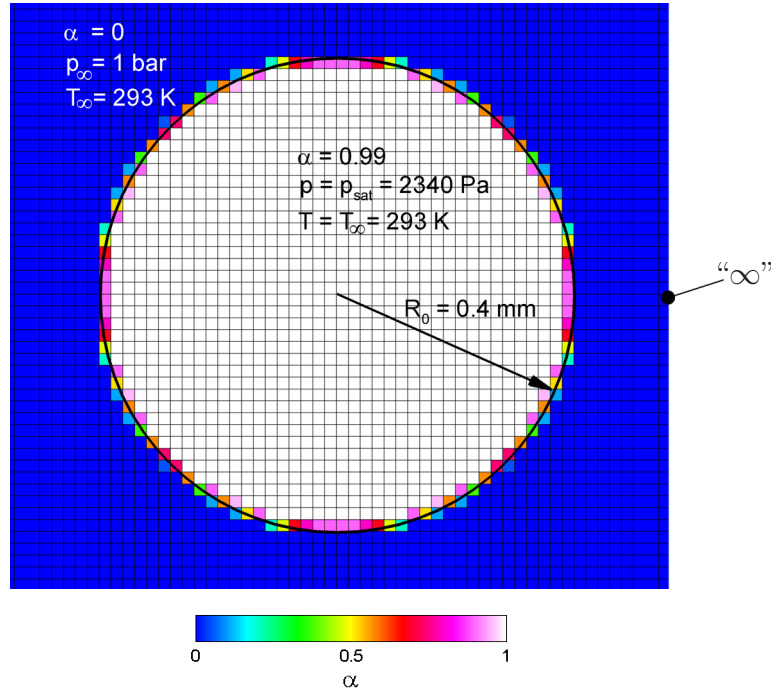


Figure 4.15: 3-D bubble structure at initialization, $t_0 = 0$ s, meridional plane of the discretization domain. $p_\infty = 1.0$ bar and $T_\infty = 293$ K, $R_0 = 0.4$ mm, $p_{sat} = 2340$ Pa at $T_\infty = 293$ K. Mesh resolution corresponds to $\Psi = 20$.

of the incompressible Rayleigh-Plesset model. This comparison is motivated by the analytical investigation of Gilmore [35], where it is demonstrated that the incorporation of liquid compressibility results in only a slight increase of the dimensionless collapse time of 0.5% as compared to the incompressible model. Moreover, as stated by Franc and Michel [30], surface tension is negligible in the collapse for the initial radius of $R_0 = 0.4$ mm considered here. The collapse time of the bubble can be found from Eq. 4.15 by rewriting the left hand side and taking $p_L = p_{sat}$ as

$$\frac{1}{2\dot{R}R^2} \frac{d}{dt} [\dot{R}^2 R^3] = \frac{p_{sat} - p_\infty(t)}{\rho_{liq}} \quad (4.16)$$

$$\frac{d}{dt} [\dot{R}^2 R^3] = 2\dot{R}R^2 \left(\frac{p_{sat} - p_\infty(t)}{\rho_{liq}} \right). \quad (4.17)$$

Integrating the above equation

$$\int \frac{d}{dt} [\dot{R}^2 R^3] dt = \int 2\dot{R}R^2 \left(\frac{p_{sat} - p_\infty(t)}{\rho_{liq}} \right) dt \quad (4.18)$$

$$\dot{R}^2 R^3 = 2 \frac{p_{sat} - p_\infty(t)}{\rho_{liq}} \int_0^t \dot{R}R^2 dt \quad (4.19)$$

$$\dot{R}^2 R^3 = 2 \frac{p_{sat} - p_\infty(t)}{\rho_{liq}} \cdot \frac{R^3 - R_0^3}{3} \quad (4.20)$$

or

$$\frac{dR}{dt} = -\sqrt{\frac{2}{3} \frac{p_{sat} - p_\infty(t)}{\rho_{liq}} \left(1 - \frac{R_0^3}{R^3} \right)}. \quad (4.21)$$

As during the collapse $dR/dt < 0$, the sign inside the square root can be changed

$$\frac{dR}{dt} = -\sqrt{\frac{2}{3} \frac{p_{sat} - p_{\infty}(t)}{\rho_{liq}} \left(\frac{R_0^3}{R^3} - 1 \right)}. \quad (4.22)$$

Rearranging this equation and integrating from R_0 to 0 for collapse time $t_{Rayleigh}$ gives

$$\frac{dR}{\sqrt{\frac{R_0^3}{R} - 1}} = -\frac{2}{3} \sqrt{\frac{p_{sat} - p_{\infty}(t)}{\rho_{liq}}} dt \quad (4.23)$$

$$\int_{R_0}^0 \frac{dR}{\sqrt{\frac{R_0^3}{R} - 1}} = -\frac{2}{3} \sqrt{\frac{p_{sat} - p_{\infty}(t)}{\rho_{liq}}} \int_0^{t_{Rayleigh}} dt \quad (4.24)$$

$$\int_{R_0}^0 \frac{dR}{\sqrt{\frac{R_0^3}{R} - 1}} = -\frac{2}{3} \sqrt{\frac{p_{sat} - p_{\infty}(t)}{\rho_{liq}}} \cdot t_{Rayleigh}. \quad (4.25)$$

The integral on the left hand side can be evaluated through factorial gamma function, which gives [30]

$$t_{Rayleigh} \cong 0.915 R_0 \sqrt{\frac{\rho_{liq}}{p_{\infty} - p_{sat}}}. \quad (4.26)$$

Figure 4.16 shows the time dependent evolution of the normalized bubble radius with respect to the time normalized by the Rayleigh time $t_{Rayleigh}$. The solid line corresponds

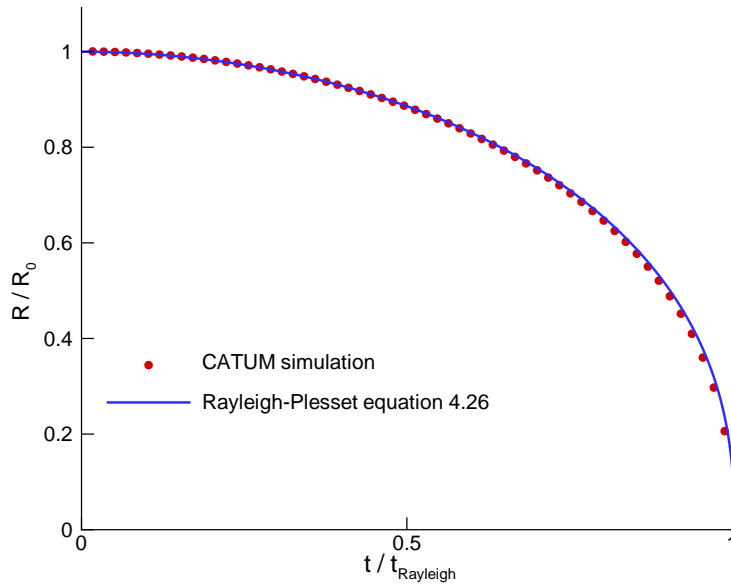


Figure 4.16: Comparison of simulation and bubble dynamics for a single bubble collapse. Evolution of dimensionless radius R/R_0 with respect to dimensionless time $t/t_{Rayleigh}$ from simulation (dots) and solution of the Rayleigh-Plesset equation for the collapse of a spherical vapor bubble, $\Delta t_{CFD} = 6.5 \cdot 10^{-9}$ s.

to the solution of the Rayleigh-Plesset equation and the dots represent the results of the **CATUM** simulation. The collapse velocity $|\dot{R}|$ can be approximated from Eq. 4.22 when $R \rightarrow 0$ as

$$\left| \frac{dR}{dt} \right| \cong \frac{2}{3} \frac{p_{sat} - p_{\infty}(t)}{\rho_{liq}} \left(\frac{R_0}{R} \right)^{3/2}, \quad (4.27)$$

or

$$|\dot{R}| \cong 0.747 \frac{R_0}{t_{Rayleigh}} \left(\frac{R_0}{R} \right)^{3/2}. \quad (4.28)$$

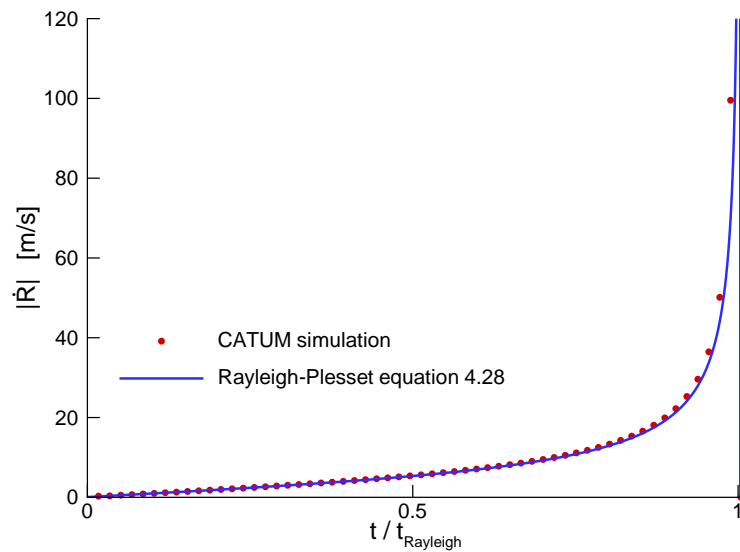


Figure 4.17: Comparison of simulation and bubble dynamics for a single bubble collapse. Evolution of collapse velocity $|\dot{R}|$ with respect to dimensionless time $t/t_{Rayleigh}$ from simulation (dots) and solution of the Rayleigh-Plesset equation for the collapse of a spherical vapor bubble, $\Delta t_{CFD} = 6.5 \cdot 10^{-9} s$.

In both of the figures, the solid line corresponds to the solution of the Rayleigh-Plesset equation and the dots represent the results of the 3-D compressible simulation. The agreement of both data sets demonstrates the ability of the numerical method to accurately predict the collapse dynamics of the single bubble. Therefore, the model reduces to the Rayleigh-Plesset dynamics for the Besant problem.

During the collapse, the liquid accelerates towards the center of the bubble and initiates the formation of an outward propagating shock when it impacts at the center of the recondensed bubble. The intensity of the shock is related to the impact velocity of the liquid. For the presumed initial conditions and the defined spatial resolution, the obtained maximum instantaneous pressure reaches 1040 *bar* within the control volume located at the center of the domain. In accordance to the theory, the spherical shock then propagates into the surrounding liquid and attenuates inversely proportional to its distance from the origin. Due to the high acoustic impedance of the liquid, the shock speed is only slightly supersonic. This shock intensity is driven by the inertia effects and the viscosity plays a minor role on the underlying dynamics.

4.3 Discretization and Mesh Dependence of the Cavitation Regions

In the previous section an isolated single bubble collapse was considered. In that case, the mesh resolution ($\Delta x = 0.02 \text{ mm}$) was fine enough to resolve a single bubble with an initial radius of $R_0 = 0.4 \text{ mm}$. This test is performed in order to validate the proposed model in the limit of single bubble dynamics. But, as mentioned earlier, the main aim in the current study is to predict the unsteady cavitation characteristics of relevant applications. Therefore, the resolution of single bubbles for these applications is not possible. In this case the implemented “homogeneous mixture model” assumes an average behavior of the cavitation regions, which are described by the thermodynamical properties.

At this point, we discuss the effects as well as the limits of the mesh resolution and of the discretization scheme on the resolved structures. Figure 4.18 depicts four calculations of a 2-D injection nozzle geometry; the flow conditions in all of the calculations are the same, with a fixed inlet pressure of $p_{in} = 80 \text{ bar}$ and an outlet pressure of $p_{out,mix} = 26 \text{ bar}$, which is the mixed reflecting/non-reflecting approach as described in chapter 3.

The first row in Fig. 4.18 shows the meshes used in the calculation. The second row and the third row correspond to calculations performed by 1st order time and space discretization and 2nd order time and space discretization respectively. Figure 4.18 gives an overview on the mesh and discretization dependence of the flow problem. At first glance, it can be seen that, by using a higher order scheme, cavitation regions grow and become highly unsteady. Moreover, the results obtained with the fine mesh show high fragmentation and small-scale structures, especially in the second order calculation. But the frequencies of the shedding cycles are nearly equal ($f \approx 62 \text{ Hz}$ coarse mesh, $f \approx 61 \text{ Hz}$ fine mesh) for both meshes. Additionally, we have seen in several other test cases that large scale cavitation structures are grid convergent and show comparable dynamic behavior. Whereas, the small scale structures fragment continuously as the mesh is refined. This suggests that the order of the discretization has a stronger effect on the global cavitation dynamics than the mesh resolution. Therefore, higher order numerical schemes are necessary to resolve and predict unsteady cavitation dynamics. However the commercial solver packages Fluent and ANSYS-CFX apply a first order discretization to the void fraction transport equation due to stability reasons. In our implementation we apply the minmod limiter on the density field in order to ensure second order discretization in smooth regions. We investigated to use of higher order WENO schemes for the density field as well, but it turned out that this results in overshoots in the regions of steep density gradients, especially at the closure region of sheet cavities. Therefore, we propose to apply the minmod limiter for the density field together with a less dissipative second order reconstruction for the velocity field (like van-Leer limiter). Overall the spatial discretization is thus limited to second order due to the sensitivity of the density field.

The observed mesh dependence of the arising small-scale structures (see Fig. 4.18) raises the question of the physical limits due to the mesh refinement. The limit on the mesh refinement is purely physical and depends also on the flow characteristics. Therefore, we assume that it would be possible to perform simulations for any finite number of grid cells, and we ask for arising violations of the physical aspects. It turns

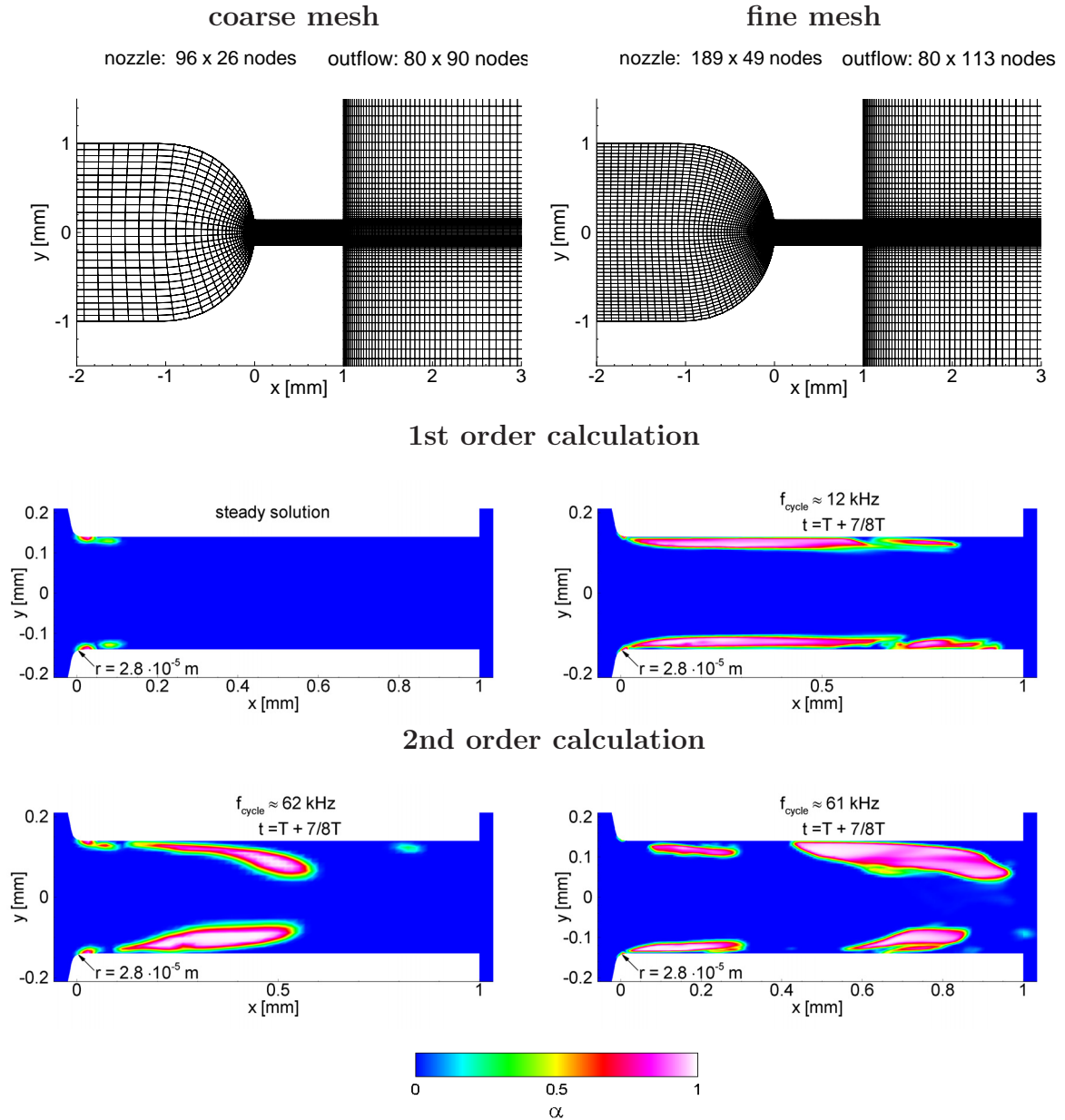


Figure 4.18: Representation of the mesh and discretization dependence of the cavitation regions. 2-D injection nozzle calculation, inlet pressure $p_{in} = 80 \text{ bar}$, outlet pressure of $p_{out,mix} = 26 \text{ bar}$. First row: coarse mesh (left), fine mesh (right); second row: 1st order time and space discretization (left: coarse mesh, right: fine mesh); third row: 2nd order time and space discretization (left: coarse mesh, right: fine mesh).

out that the first limitation is given by the neglected effects of the surface tension.

The effect of the surface tension is investigated for two cases. In the first case, presuming that the mesh resolution resolves single bubbles of radius R , the bubble is assumed to be in **mechanical equilibrium** with its surroundings, which is regarded as the **static condition**. Following the Young-Laplace equation [135] the static condition of a spherical bubble containing pure vapor only requires the following relation to be satisfied

$$p_{sat} = p_{\infty} + \frac{2S}{R}, \quad (4.29)$$

where p_{sat} is the vapor pressure, p_{∞} is the pressure of the surrounding liquid domain and S is the surface tension of the liquid. For water and water vapor at room temperature these values are $p_{sat} = 2340 \text{ Pa}$ and $S = 0.072 \text{ N/m}$. Then the pressure difference due to the surface tension can be written as

$$\Delta p = p_{sat} - p_{\infty} = \frac{2S}{R}. \quad (4.30)$$

It can be seen from this equation that the smaller the bubble radius is, the larger the effect of the surface tension on the pressure difference that maintains the mechanical equilibrium. In order to give a numerical estimation, if we consider static equilibrium condition of a spherical bubble with a radius of $r = 1 \cdot 10^{-5} \text{ m}$ at 20°C the above given formula results in

$$2340 - p_{\infty} = \frac{2 \times 0.072}{1 \cdot 10^{-5}}, \quad (4.31)$$

$$p_{\infty} = -12060 \text{ Pa}. \quad (4.32)$$

Equation 4.32 shows that a “negative” surrounding pressure value is required to maintain the static equilibrium condition. This means that the surrounding liquid has to be in **tension**. As already discussed in chapters 1 and 2 such “negative” pressures and deviations from the saturation conditions are associated with thermodynamic non-equilibrium states (see Fig. 1.1) and they are not considered in the implemented physical model. Therefore, surface tension effect is not included in the model and in the calculations presented in this thesis. The following table demonstrates the effect of the surface tension on the pressure difference that maintains the mechanical equilibrium for different bubble radii.

Table 4.2: The effect of different bubble radii on the pressure difference that maintains the mechanical equilibrium according to Eq. 4.30.

Radius	$5 \cdot 10^{-3} \text{ m}$	$1 \cdot 10^{-3} \text{ m}$	$1 \cdot 10^{-4} \text{ m}$	$1 \cdot 10^{-5} \text{ m}$
Δp	28.8 Pa	144 Pa	1440 Pa	14400 Pa

As in the calculations the fragmented cavitation regions are resolved, the smallest mesh size in these regions could correspond to tiny single bubbles, where the surface tension may influence the flow dynamics. In order to conclude if the surface tension is significant for a given calculation, one should investigate the flow conditions together with the mesh resolution. Table 4.3 summarizes the smallest mesh sizes encountered in the calculations that will be presented in the next chapter together with the pressure differences that maintain the mechanical equilibrium when these meshes correspond to single “resolved bubbles”.

The injection nozzle calculation that is considered in this section has the smallest mesh size around the inlet of the bore hole of the order of $6 \cdot 10^{-6} \text{ m}$, which is also the smallest mesh size encountered among all the calculations that are performed in this thesis. Therefore it is the most critical flow problem in terms of the possible effects of the surface tension. According to the mechanical equilibrium discussion given above, if an isolated single mesh apart from the cavitation regions is filled with vapor, it would correspond to a tiny single bubble with a radius on the order of that mesh size. Following Eq. 4.30, this mesh size ($6 \cdot 10^{-6} \text{ m}$) would result in a pressure difference of

Table 4.3: The smallest mesh sizes encountered in different calculations and the equivalent pressure differences that maintain the mechanical equilibrium when these meshes correspond to single “resolved bubbles”.

calculation	2-D injection nozzle	3-D injection nozzle	2-D hydrofoil	3-D wing
smallest mesh size	$6 \cdot 10^{-6} m$	$1 \cdot 10^{-5} m$	$5 \cdot 10^{-4} m$	$1 \cdot 10^{-3} m$
corresponding Δp of the “resolved bubble”	24000 Pa	14400 Pa	288 Pa	144 Pa

$\Delta p = 24000 Pa$. When compared with the inlet pressure of $p_{in} = 80 bar$, it is clear that the effect of this pressure difference can be neglected. Moreover, as it can be seen from table 4.3 that in hydrofoil calculations the smallest mesh size is on the order of $5 \cdot 10^{-4} - 10^{-3} m$ which corresponds to a pressure difference of $O(10^2) Pa$. This value is also not significant when compared with the inlet conditions of these problems.

In the second case, we analyze the effect of the surface tension on the **collapse dynamics**. It was mentioned in the previous subsection that the surface tension can be neglected during the collapse for the initial radius considered here. The collapse velocity given in the previous section (Eq. 4.22) can be rewritten by including the surface tension effect as follows [30]

$$\frac{dR}{dt} = -\sqrt{\frac{2 p_{sat} - p_{\infty}(t)}{3 \rho_{liq}} \left(\frac{R_0^3}{R^3} - 1 \right) + \frac{2S}{\rho_{liq} R_0} \frac{R_0^3}{R^3} \left(1 - \frac{R^2}{R_0^2} \right)}, \quad (4.33)$$

or

$$\frac{dR}{dt} = -\sqrt{\frac{2 p_{sat} - p_{\infty}(t)}{3 \rho_{liq}} \left(\frac{R_0^3}{R^3} - 1 \right) + \frac{2S}{\rho_{liq} R_0} \left(\frac{R_0^3}{R^3} - \frac{R_0}{R} \right)}. \quad (4.34)$$

As initially $R = R_0$, the two terms inside the square root can be compared by using their coefficients. Thus, the accelerating effect of surface tension becomes significant if

$$\frac{2S}{\rho_{liq} R_0} > \frac{2 p_{sat} - p_{\infty}(t)}{3 \rho_{liq}}, \quad (4.35)$$

or

$$R_0 < \frac{3S}{p_{\infty} - p_{sat}}, \quad (4.36)$$

Therefore, at standard conditions, $p_{\infty} = 1 bar$, $T_{\infty} = 293.15 K$ and $p_{sat} = 2340 Pa$ with $S = 0.072 N/m$, the surface tension must be considered if

$$R_0 < 2.2 \cdot 10^{-6} m = 2.2 \mu m. \quad (4.37)$$

Thus, when the mesh resolution is smaller than this value, the fragmented cavitation regions correspond to tiny single bubbles that surface tension is no longer negligible and influences the collapse dynamics. As a result, in the current model the limit given by Eq. 4.36 is considered when refining the computational grid.

Similar to the mechanical equilibrium analysis given earlier, we again consider 2-D injection nozzle problem in terms of collapse dynamics. If we assume that the liquid pressure p_∞ that surrounds the cavity regions is also of the order of the inlet pressure $p_{in} = 80 \text{ bar}$, Eq. 4.36 results in a limiting radius of $R_0 \approx 2.7 \cdot 10^{-8} \text{ m}$. This value is two orders smaller than the smallest mesh size in this example, thus the effect of the surface tension on the collapse dynamics can also be neglected.

4.4 Validation Summary

Before presenting any results, it is necessary to validate a newly developed code. In this chapter, the convective flux definition and ability to resolve sharp discontinuities of **CATUM** was tested via a series of numerical shock tube test cases for gas and liquid water flows. It was shown that the code accurately captures and resolves the wave propagation even for severe test cases. The quality of the solution strongly depends on the mesh resolution and the order of the scheme that is used.

To validate the two-phase model proposed earlier, several additional tests were also performed. In the first case, a cavitating shock tube was considered, where two opposite running expansion waves are used to initiate evaporation. In the second test, an isolated single bubble collapse was considered and compared with the solution of the Rayleigh-Plesset equation. This case showed a perfect match for the collapse time, the bubble radius evolution and the collapse velocity with respect to the theory.

Finally, the mesh and discretization dependence of the cavitating flow field was demonstrated by using a 2-D injection nozzle calculation. The fragmentation and the cavitation dynamics showed that a higher order discretization is needed to resolve such flow features.

Second order time and space discretizations are used throughout all the validation cases. It is possible to implement third or higher order WENO schemes for the 1-D shock tube problems, but the geometrical complexity of the 3-D applications restrict the usage of higher order schemes in terms of CPU requirements. For comparison, the required numerical effort to realize third order accuracy in space and time increases by a factor of 30 for the considered 3-D applications (see also the discussion in section 5.2.3, page 159).

The results that will be presented in the next chapter will also serve as validation for the developed code and the proposed phase transition model, as various experimental comparisons are included.

Chapter 5

Results and Discussion

In the previous chapter the developed solver and the proposed two-phase model were validated through a series of single and multi-phase liquid flow test cases together with numerical shock tube experiments. This chapter presents the results from the applications that are considered in the scope of this thesis. These applications can be divided into two main categories according to their physical and flow properties. The first category focuses on the flow dynamics inside the fuel injection systems, which are characterized by high-speed, micro-scale flows. The second application area focuses on the flows around hydrodynamic machinery such as pump or turbine blades as well as ship propellers. In the following sections, results of 2-D and 3-D injection nozzle simulations and hydrofoil calculations will be presented.

5.1 Injection Nozzles

Control and optimization of cavitation in injection nozzles are subjects of intense research and development. Because of the pressure differences $\Delta p = p_{in} - p_{out}$ up to 2000 *bar* and unsteady excitation according to the frequency of the motor cycle it is obvious that wave dynamics plays a dominant role. Moreover, individual mass flow control strategies by pilot and multi-point injection systems operate within the time scales of $\Delta t \leq 10^{-4} s$. Therefore, the arising flow field inside the injection nozzle experiences variations on multiple time scales together with both hydrodynamic and acoustic cavitation. As wave dynamics and hydrodynamics are strictly coupled, a separate consideration of these scales is not possible. Hence, numerical time steps Δt_{CFD} of the order of $10^{-10} s$ are necessary to ensure the complete resolution of hydrodynamics and wave dynamics within the numerical simulation. Beside these flow dynamic scales, the injection cycle introduces a time scale $\Delta t_{injec} = 10^{-3} s$ as well. Consequently, the dynamic phase transition processes like cavitation and recondensation can be experienced within all considered time scales $10^{-10} \leq \Delta t \leq 10^{-3} s$.

Due to typical bore hole diameters of the order of 0.1 – 0.3 *mm*, experimental investigations are difficult and limited. Therefore, detailed studies of the flow field require numerical simulations [4].

5.1.1 2-D Plane Injection Nozzle

As a first test case and for comparison with the previous research done by Yuan and Schnerr [137] the cavitating flow through a 2-D planar injection nozzle is simulated. This nozzle geometry was also used in the experiments of Roosen et al. [93].

Figure 5.1 shows the layout and the discretization of the computational domain. The computational mesh for the full injection nozzle is obtained by mirroring the lower half with respect to the center line of the domain. Hence, a **perfectly symmetric mesh** is constructed. Even for this symmetric mesh, an asymmetric flow solution can be observed because of the strong gradients associated with the two-phase flow. This phenomenon will be discussed in section 5.1.1.1 in detail.

The inlet pressure p_{in} is kept constant and at the outflow domain a mixed non-reflecting/reflecting boundary condition $p_{out,mix}$ is applied (see chapter 3). The size of the nozzle bore hole is given by the total height of 0.28 mm and the length of 1.0 mm . With respect to cavitation, the radius of wall curvature at the inlet of the nozzle is one of the most sensitive parameters of this problem. Rounding the edge with a radius $r = 2.8 \cdot 10^{-5}\text{ m}$ ensures that the single-phase viscous flow remains attached in this inlet region. This important fact has been controlled by additional single-phase Navier-Stokes simulations [136]. Otherwise, strong interaction of viscous separation and cavitation cannot be excluded, i.e. conditions which make reasonable conclusions difficult.

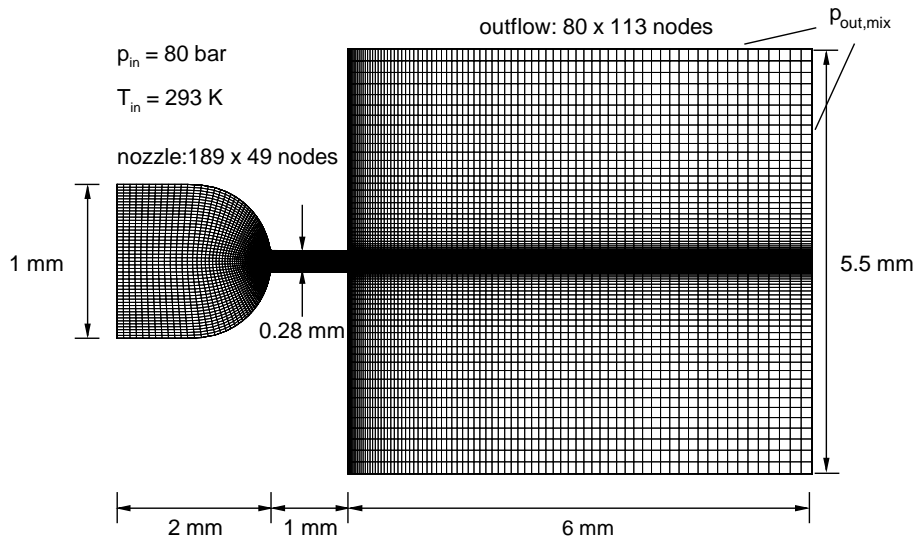


Figure 5.1: 2-D injection nozzle grid with outflow domain and corresponding boundary conditions.

The numerical domain includes the nozzle as well as the outflow region. The initial conditions for the entire numerical domain model liquid water at rest at temperature $T_{init} = 293\text{ K}$ and pressure $p_{out,mix} = 26\text{ bar}$. At the inlet we prescribe $p_{in} = 80\text{ bar}$. This moderate pressure ratio $80/26\text{ bar}$ is typical for direct injection in Otto engines (FSI - Fuel Stratified Injection). Due to the initially prescribed pressure jump $\Delta p = p_{in} - p_{out,mix} = 54\text{ bar}$ at the inlet, a shock wave propagates through the nozzle and initiates the convective motion.

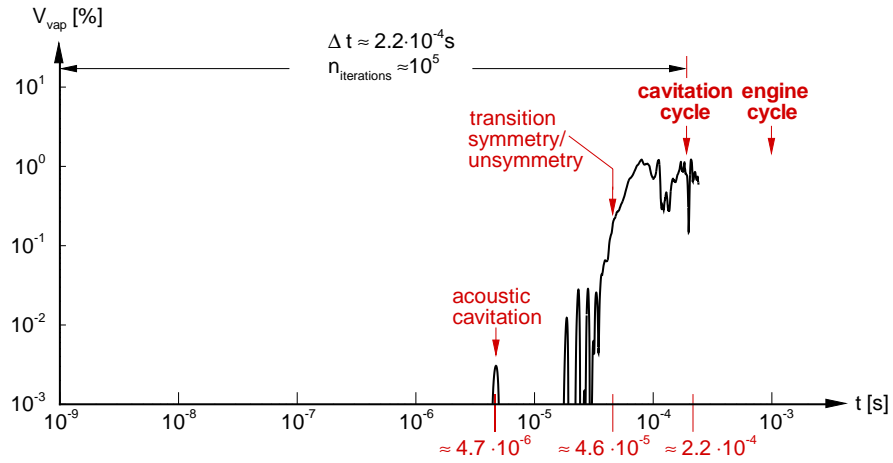


Figure 5.2: Time history of the integrated vapor volume V_{vap} [% total volume of the computational domain], $p_{in} = 80 \text{ bar}$, $p_{out,mix} = 26 \text{ bar}$, $T_{init} = 293 \text{ K}$, $\Delta t_{CFD} = 10^{-9} \text{ s}$, second order in space and in time.

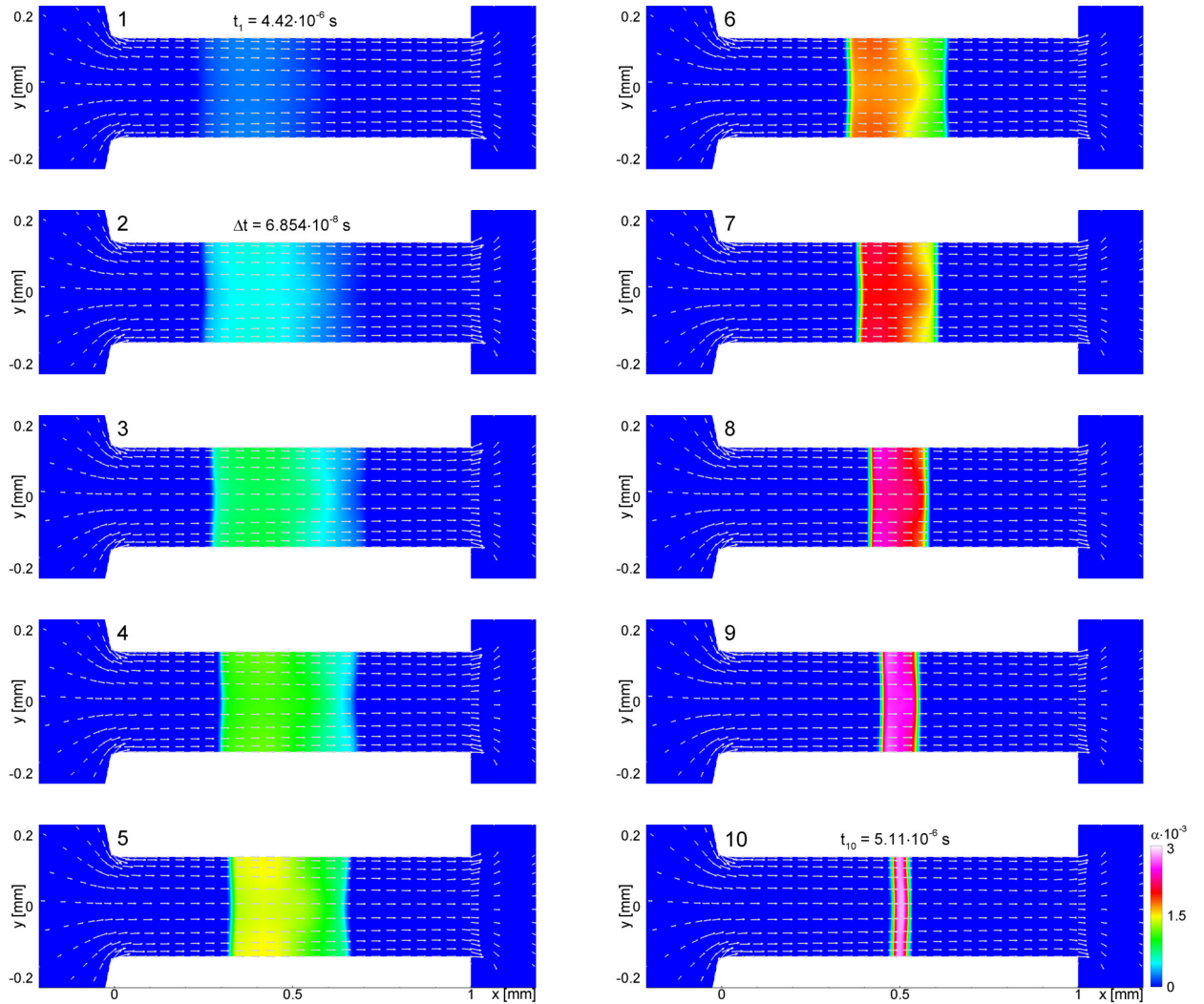


Figure 5.3: Vapor volume fraction α due to acoustic cavitation inside the bore hole at $t_1 = 4.42 \cdot 10^{-6} \text{ s}$, time interval $\Delta t_{1-10} = 6.90 \cdot 10^{-7} \text{ s}$, $p_{in} = 80 \text{ bar}$, $p_{out,mix} = 26 \text{ bar}$, $T_{init} = 293 \text{ K}$, $\Delta t_{CFD} = 10^{-9} \text{ s}$, second order in space and in time.

In Fig. 5.2 the time history of the vapor formation V_{vap} inside the flow domain is shown. This graph clarifies the various time scales experienced during an injection process. A typical engine cycle corresponds to 10^{-3} s and the cavitation cycle has a time scale of the order of 10^{-4} s. Two additional time scales are introduced into the flow due to the imposed wave motion. Both of them are short time scale characteristics of the flow field and experienced during the start-up phase.

As the shock reaches the exit of the bore hole, a reflected rarefaction wave forms and propagates upstream through the throat. The interaction of the hydrodynamic flow acceleration with the pressure drop due to rarefaction waves enforces acoustic cavitation around time $t \approx 4.7 \cdot 10^{-6}$ s (Fig. 5.2).

Within $\Delta t \approx 10^{-6}$ s the evaporated domain recondenses completely. The sequence of 10 pictures in Fig. 5.3 represents a time interval of $\Delta t_{1-10} = 6.90 \cdot 10^{-7}$ s, beginning at $t_1 = 4.42 \cdot 10^{-6}$ s. In this series, acoustic cavitation is visualized by the vapor volume fraction α . It can be seen from this figure that in the region between two expansion waves vapor develops and acoustic cavitation takes place. From Pic. 1 to Pic. 4 the region grows as the expansion waves move farther away from each other. Starting with picture 5, reflected compression waves interact with the cavitating region and compress it. Although due to the compression the region shrinks in size, the absolute value of the vapor volume fraction increases as a direct consequence of the volume reduction. Picture 10 depicts the maximum vapor fraction reached during this wave induced cavitation process. As compression waves move further towards each other and finally collide, all the vapor recondenses and the acoustic cavitation process ends. It should also be noted that the resulting maximum vapor volume fraction value is of the order of 10^{-3} . This is because the pressure drop due to the expansion wave is weak as compared to the hydrodynamic acceleration.

5.1.1.1 Symmetry Break-up of the Flow Field

Further acceleration of the flow field results in hydrodynamic cavitation at the inlet of the bore hole (Pic. 1 Fig. 5.4). In Pics. 2-3 of Fig. 5.4 the onset of a flow instability that leads to asymmetric collapses at the closure region of the cavities (Pics. 5-6 of Fig. 5.4) is observed. The time increment between the pictures is $\Delta t_{pic} = 3.425 \cdot 10^{-8}$ s; this emphasizes the short time dynamics of this micro scale two-phase flow. The asymmetry of the collapse induced shocks is depicted in Pics. 7-9 of Fig. 5.4. The further attenuation and propagation of these first asymmetric shocks drive the entire flow topology towards global asymmetry with highly non-predictable random behavior (Pics. 10-12 of Fig. 5.4). The graph of the integrated vapor volume, Fig. 5.2, also demonstrates this highly random, non-periodic flow character.

The predicted break-up of the symmetry is interesting by its own right, especially with respect to the inviscid nature of the governing equations. Therefore, this phenomenon is investigated in detail. By introducing ‘‘corresponding sensor cells’’ positioned at two symmetrically located finite volumes at the entry region of the bore hole (see Fig. 5.5), pressure signals are recorded during the whole simulation. Figure 5.6 depicts the normalized static pressure difference Δp in logarithmic scale given by

$$\log_{10}(\Delta p + \varepsilon) = \log_{10} \left(\frac{|p_{up} - p_{low}|}{p_{01}} + \varepsilon \right), \quad (5.1)$$

recorded at the given two monitor points. The pressure difference value is normalized by the inlet total pressure p_{01} and a cut-off value of $\varepsilon = 10^{-9}$ is used to avoid the zero point in log scale. This pressure difference is a way to measure the asymmetry of the flow field. It also shows the development of the instabilities in the domain. Strong gradients like phase change or shocks around the monitor points cause local extrema of the pressure signals.

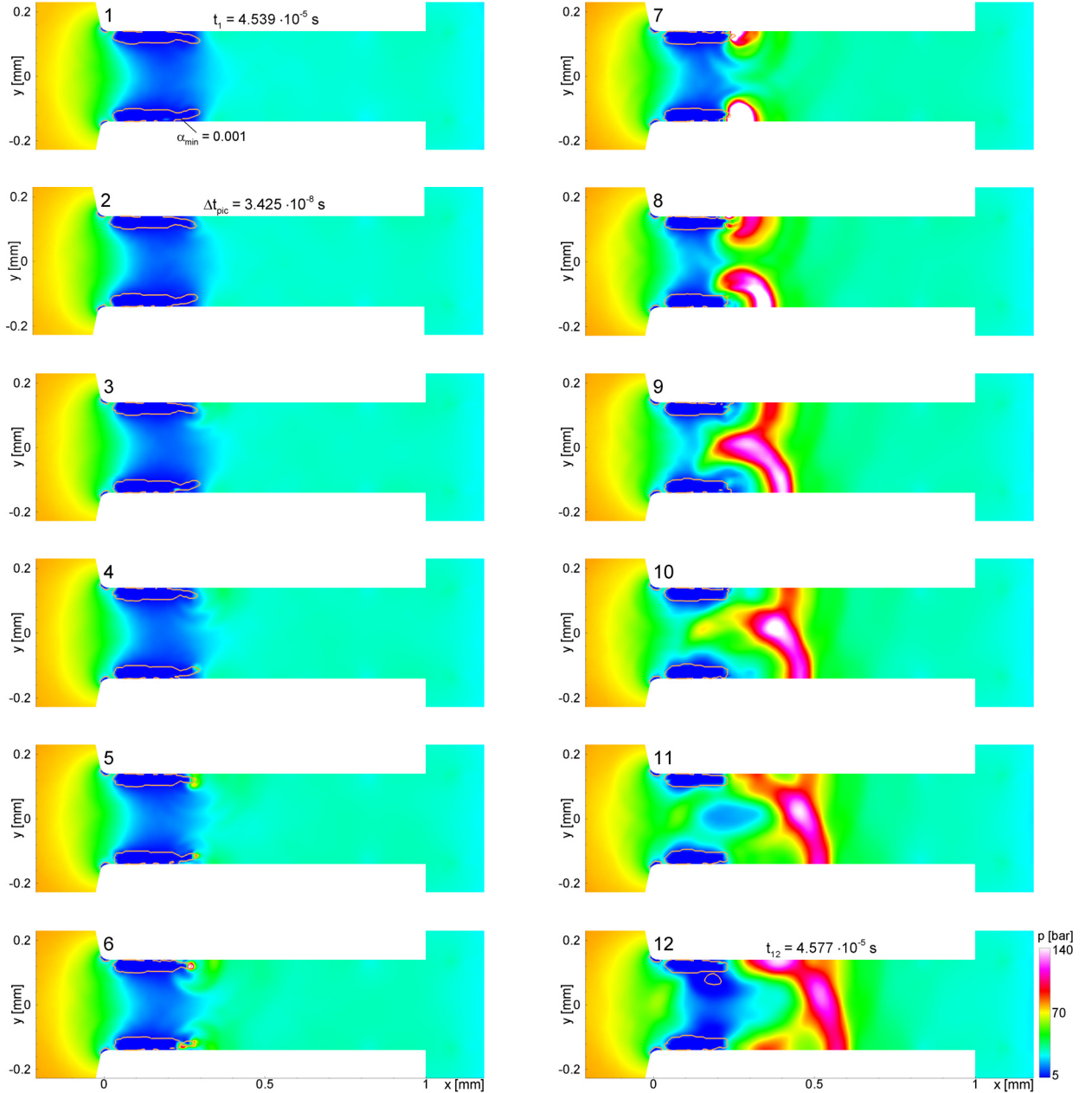


Figure 5.4: Static pressure contours and cavitation regions (orange lines $\alpha_{min} = 0.001$), transient re-arrangement from symmetric to asymmetric cavitation at $t_1 = 4.539 \cdot 10^{-5} s$, time interval $\Delta t_{1-12} = 3.8 \cdot 10^{-7} s$, $p_{in} = 80 bar$, $p_{out,mix} = 26 bar$, $T_{init} = 293 K$, $\Delta t_{CFD} = 10^{-9} s$, second order in space and in time.

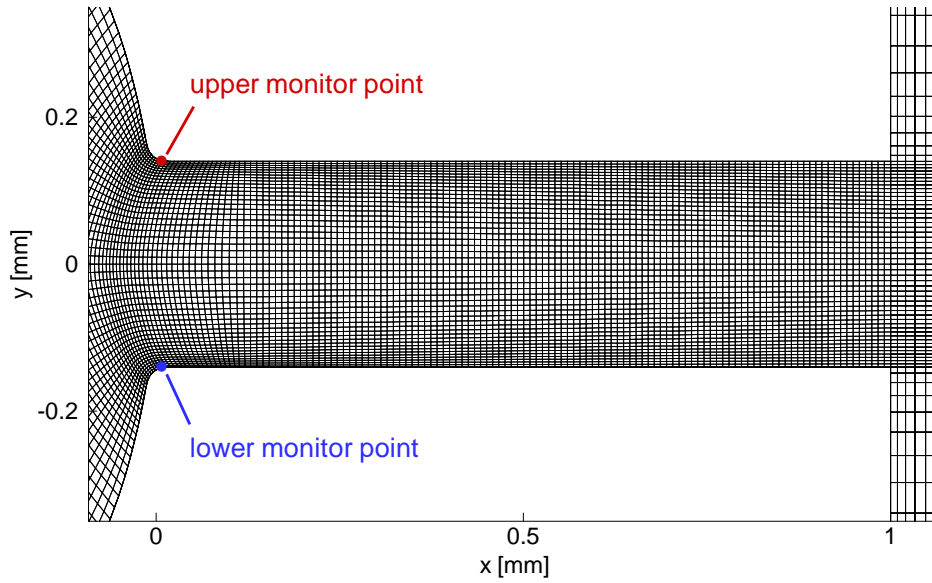


Figure 5.5: Upper and lower monitor points, located at the upper and the lower walls - symmetrically to the axis of the bore hole, $p_{in} = 80 \text{ bar}$, $p_{out,mix} = 26 \text{ bar}$, $T_{init} = 293 \text{ K}$, $\Delta t_{CFD} = 10^{-9} \text{ s}$.

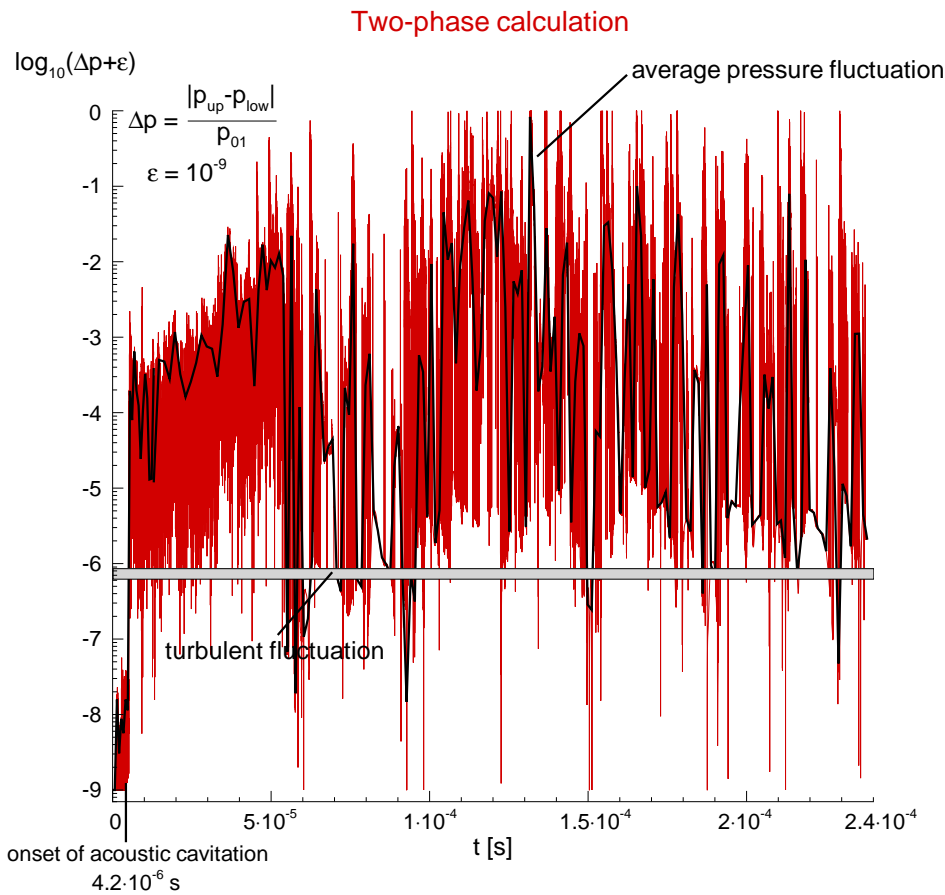


Figure 5.6: Time dependent normalized static pressure difference Δp , **two-phase calculation**, logarithmic scale, $p_{in} \approx p_{01} = 80 \text{ bar}$, $p_{out,mix} = 26 \text{ bar}$, $T_{init} = 293 \text{ K}$, $\Delta t_{CFD} = 10^{-9} \text{ s}$, second order in space and in time.

Figure 5.6 clearly shows that the instability in the flow field starts to grow already from the beginning of the simulation and it fluctuates continuously as the transient solution proceeds. A pressure fluctuation level due to turbulence is estimated for the considered flow conditions. Due to the acceleration of the flow through the nozzle of the bore hole, one can assume that the flow has a weak turbulence intensity Tu on the order of $\sim 10^{-3}$, i.e.

$$Tu = \frac{\sqrt{u' \cdot u'}}{\bar{u}} \approx 10^{-3} . \quad (5.2)$$

For a mean velocity of $\bar{u} = 100 \text{ m/s}$, the turbulent fluctuation velocity u' can be found by using the above equation as $|u'| = 0.1 \text{ m/s}$. This velocity corresponds to a pressure fluctuation which can be approximated as

$$p' \approx \frac{1}{2} \rho u'^2 = \frac{1}{2} \cdot 1000 \cdot 0.1^2 = 5 \text{ Pa} . \quad (5.3)$$

Normalizing this value with respect to the inlet total pressure $p_{01} \approx 80 \text{ bar}$ and taking the logarithm of it results in the gray bars depicted in Figs. 5.6 and 5.7.

In order to exclude the effect of phase transition on the break-up, a **single-phase** simulation using exactly the same numerical algorithm but without taking the phase

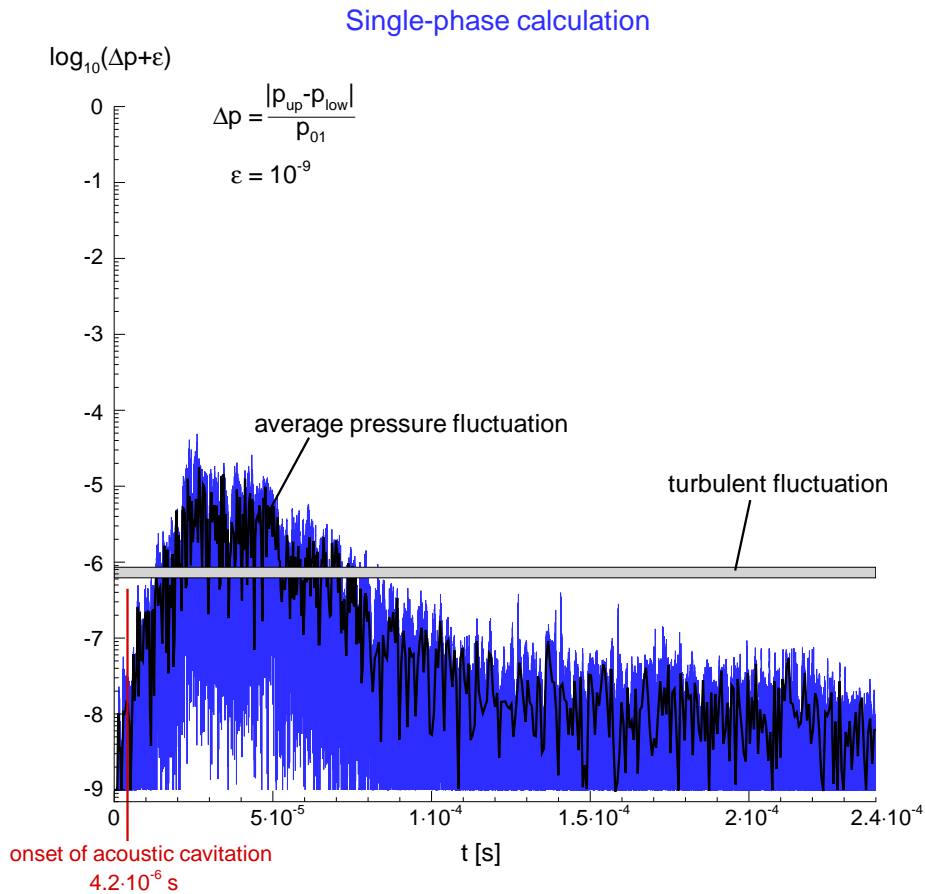


Figure 5.7: Time dependent normalized static pressure difference Δp , **single-phase calculation**, logarithmic scale, $p_{in} \approx p_{01} = 80 \text{ bar}$, $p_{out,mix} = 26 \text{ bar}$, $T_{init} = 293 \text{ K}$, $\Delta t_{CFD} = 10^{-9} \text{ s}$, second order in space and in time.

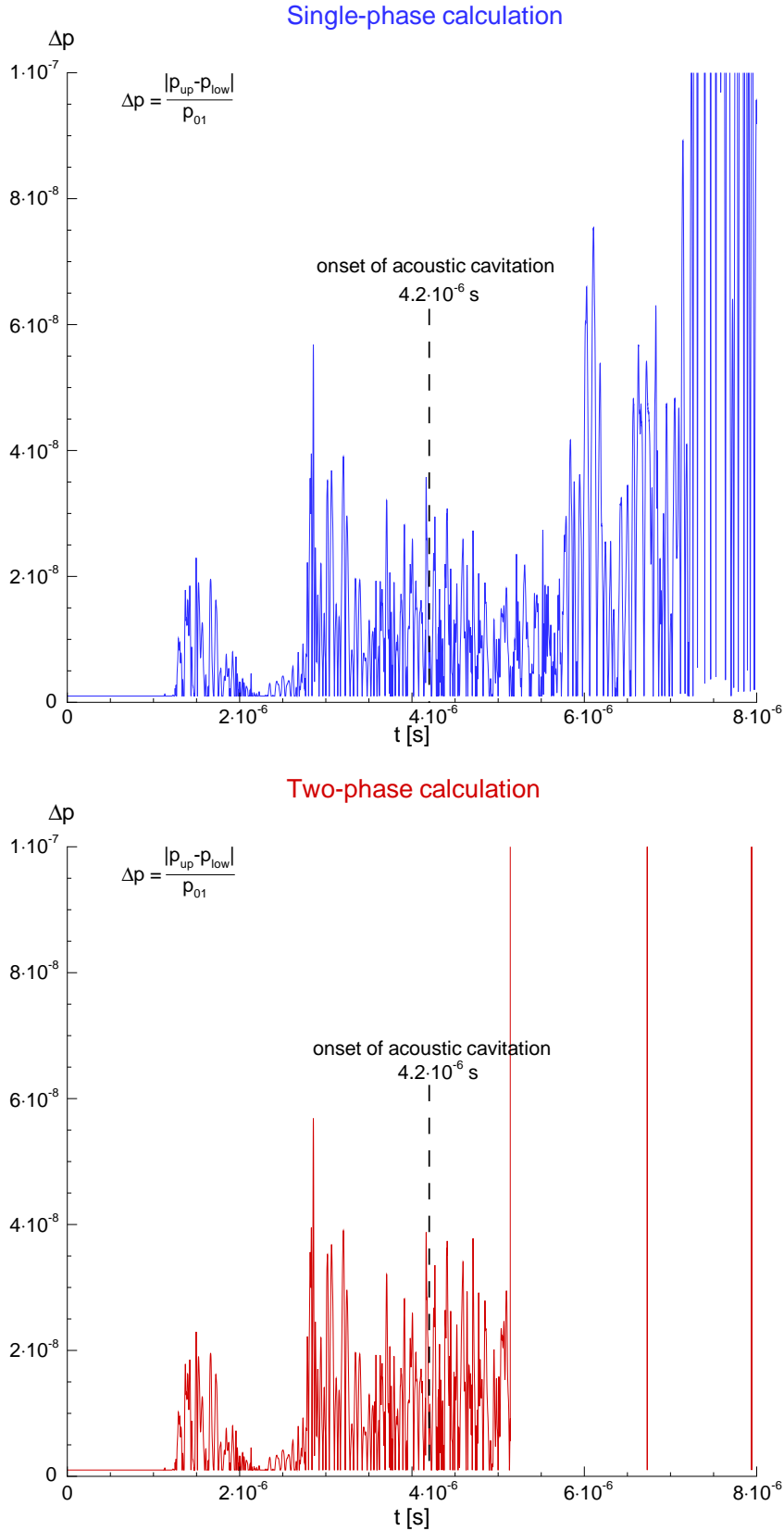


Figure 5.8: Close-up views of time dependent normalized static pressure difference Δp , $0 \leq t \leq 8 \cdot 10^{-6} \text{ s}$, **single-phase calculation** (top), **two-phase calculation** (bottom), linear scale, $p_{in} \approx p_{01} = 80 \text{ bar}$, $p_{out,mix} = 26 \text{ bar}$, $T_{init} = 293 \text{ K}$, $\Delta t_{CFD} = 10^{-9} \text{ s}$, second order in space and in time.

change into account (pure liquid flow) is also performed. Again, the same perfectly symmetric grid, which was generated by mirroring the lower half with respect to the nozzle axis, is used together with the same initial and boundary conditions. Figure 5.7 shows the normalized pressure difference recorded at the monitor points in logarithmic scale.

As seen in the Fig. 5.7 the numerical noise arising in the single-phase simulation initially grows during the time evolution and decays during the transient process towards the steady state solution. The steady state solution still contains a small amount of noise of the order of 10^{-10} for any normalized quantity. This noise does not further reduce due to unavoidable numerical round-off errors. However, the numerically predicted flow field is symmetric up to the mentioned order and remains stable. Global asymmetries are not observed within single-phase simulations.

The difference of the recorded pressure signals in the single- and in the two-phase simulations are compared in the previous two figures for $0 \leq t \leq 8 \cdot 10^{-6} \text{ s}$. It can be seen from Fig. 5.8 that the numerical noise arising in both simulations is identical as long as there is no cavitation present, i.e. the two-phase simulation is not yet affected by phase transition. In the previous section it is shown that due to wave propagation inside the bore hole, acoustic cavitation forms and within a very short time interval ($\approx 10^{-6} \text{ s}$) it recondenses completely forming pressure waves propagating in both directions. When this pressure wave reaches the monitor points, it causes an unbalanced pressure increase and therefore, the numerical noise arising in two-phase simulation is intensified, which causes the sudden peaks after the onset of acoustic cavitation as depicted in Fig. 5.8 (bottom). The maximum magnitude of these peaks reach $0.1 - 0.15 \text{ bar}$, which is outside the scale of the figure. Moreover, it is seen from the results that before acoustic cavitation occurs, the flow variables that are calculated inside the upper and lower monitor control volumes are exactly the same.

As a result, it is seen that the considered single-phase flow is stable within small perturbations (numerical noise), whereas, the corresponding two-phase flow shows an instable behavior. It is therefore important to distinguish between the numerical origin of the instability (that is the occurrence of the numerical noise due to round-off errors, compiler settings, internal processor routines, etc.) and the resulting behavior of the governing equations. The compatibility relations for the Euler equations imply that the variation of acoustic impedance $\delta(\rho c)$ is a measure of the non-linearity due to compressibility. The acoustic impedance is nearly constant for single-phase flows but it varies several orders of magnitude in two-phase flows (see Fig. 2.16 and chapter 3). Therefore, it is reasonable to associate the observed instability in two-phase calculations to the increased non-linearity due to compressibility and is therefore not controlled by viscosity effects.

It should be also noted that the discussed symmetry break-up analysis is performed on the same computer with same compiler settings both for the single-phase and two-phase calculations. Repetition of these calculations on the same computer gives exactly the same results, as expected. But repetition on different architectures or with different compiler settings or on different computers can result in a completely different time history of the recorded pressure signals, as every computer has different machine accuracy and internal routines.

5.1.1.2 Cavitation Cycle

Figure 5.9 is the enlarged plot of the total vapor volume integrated within the entire computational domain and shows the investigated cavitation cycle with a time interval of $\Delta t_{cycle} = 1.639 \cdot 10^{-5} s$. The sequence of 8 void fraction pictures in Fig. 5.10 represents this cavitation cycle with a shedding frequency of $f_{cycle} \approx 61 kHz$. It can be easily seen from the pictures that, although the flow topology in the upper and in the lower halves of the nozzle is at some instances similar, it is completely unsymmetrical. The mass flow defect due to cavitation is an important parameter for the operating conditions of injection nozzles and for the efficiency of the engine. In this calculation the time dependent fluctuation of this quantity, normalized with the single-phase reference value, is $\Delta \dot{m} / \dot{m}_{single-phase} = 18\% \pm 5\%$. This value is in good agreement with the observations of Chaves et al. [19].

The flow within the cavitation cycles experiences violent shock structures due to collapses. Figure 5.11 (top) depicts the instantaneous flow field corresponding to a violent collapse at $t = 1.992 \cdot 10^{-4} s$, which is given by the first black point in Fig. 5.9 respectively close to picture 1 of Fig. 5.10. The pressure behind the shock is $314 bar$, which is more than one order higher than the outflow static pressure. The corresponding shock Mach number is $M_s = 1.01$. Similarly, in the bottom picture of Fig. 5.11, formation of a circular shock front within the free shear layer of the external flow is observed. This time the maximum pressure behind the shock is $264 bar$ and this collapse corresponds to the time instant $t = 2.330 \cdot 10^{-4} s$.

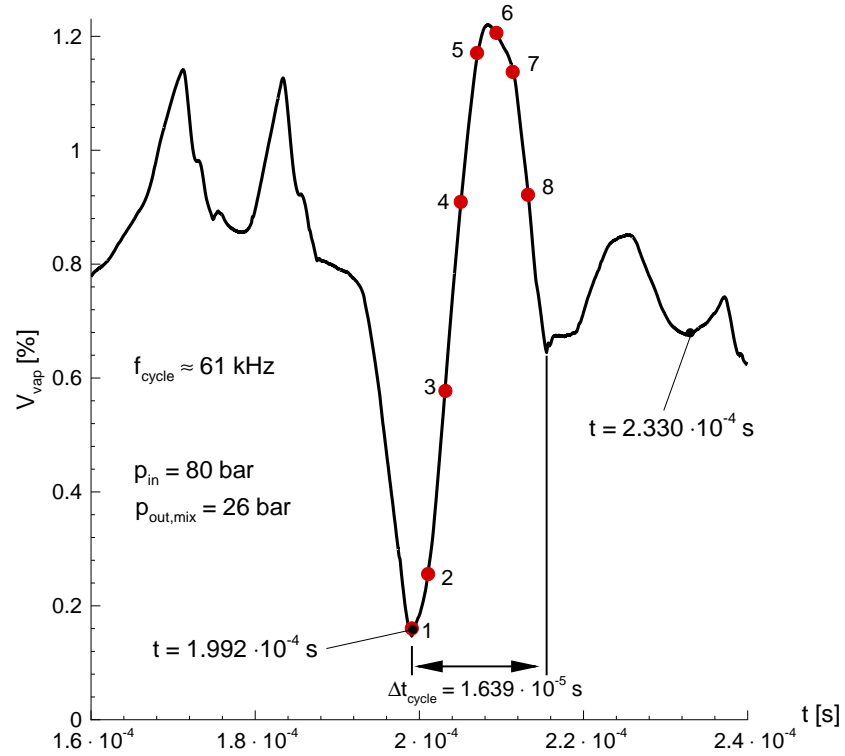


Figure 5.9: Time history of the integrated vapor volume V_{vap} , $p_{in} = 80\text{bar}$, $p_{out,mix} = 26\text{bar}$, $T_{init} = 293\text{K}$, $\Delta t_{CFD} = 10^{-9}\text{s}$, second order in space and in time.

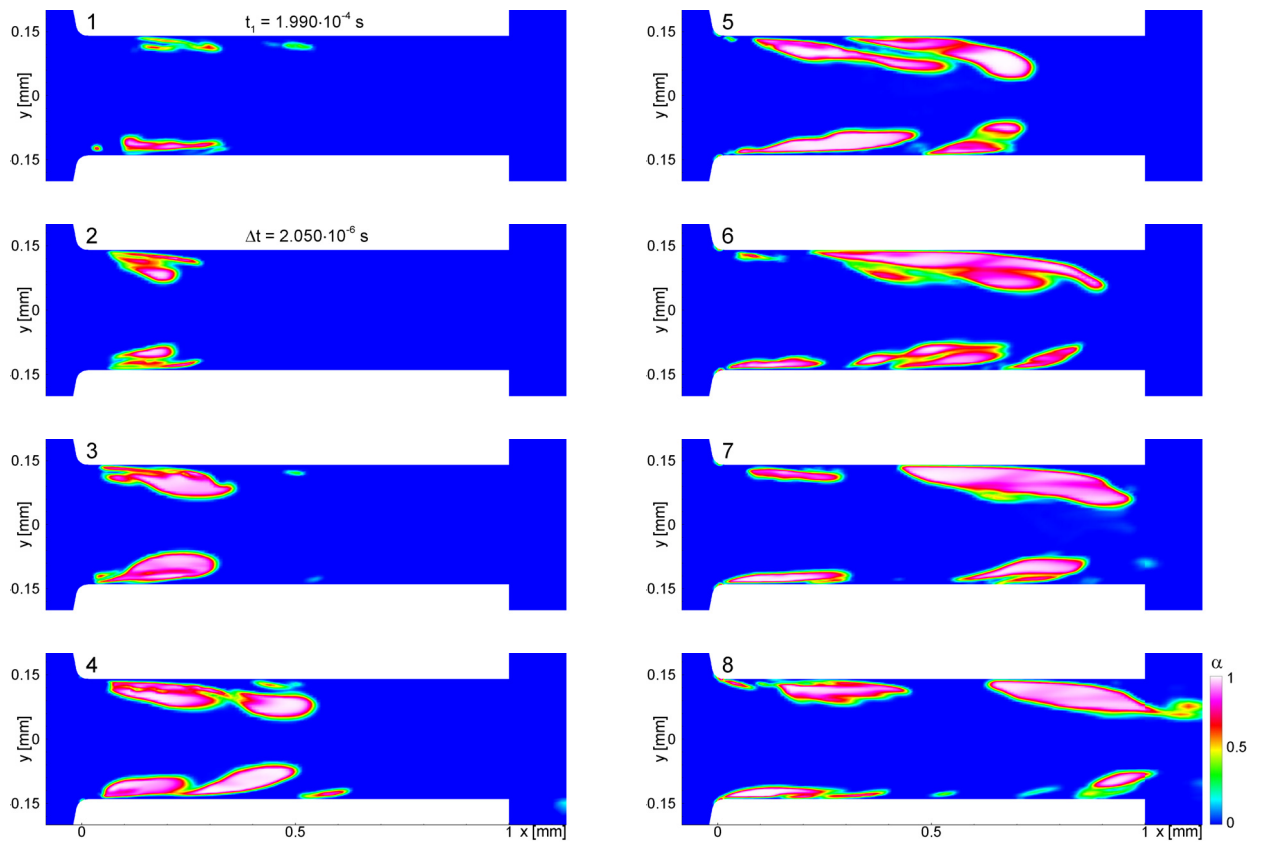


Figure 5.10: Unsteady and asymmetric high frequency void fraction formation in cavitating flow through 2-D plane injection nozzle at $t_1 = 1.990 \cdot 10^{-4}\text{s}$, time interval $\Delta t_{1-8} = 1.639 \cdot 10^{-5}\text{s}$, $p_{in} = 80\text{bar}$, $p_{out,mix} = 26\text{bar}$, $T_{init} = 293\text{K}$, $\Delta t_{CFD} = 10^{-9}\text{s}$, second order in space and in time.

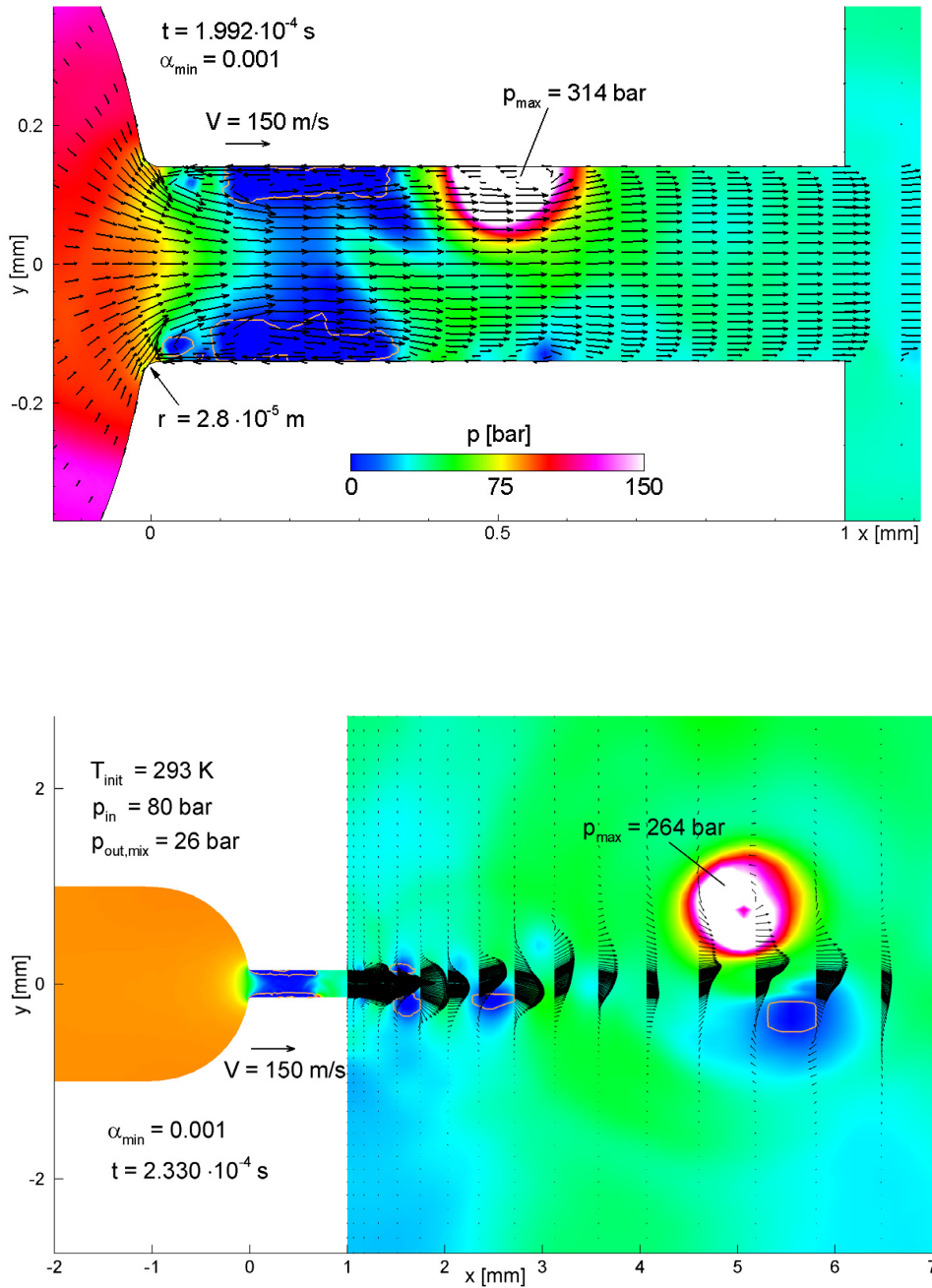


Figure 5.11: Instantaneous formation of a strong shock after violent cloud collapse in the nozzle bore hole (top), inside the outflow domain (bottom), $p_{\max} = 314 \text{ bar}$, $p_{\text{in}} = 80 \text{ bar}$, $p_{\text{out,mix}} = 26 \text{ bar}$, $T_{\text{init}} = 293 \text{ K}$, $\Delta t_{CFD} = 10^{-9} \text{ s}$, second order in space and in time.

5.1.2 3-D Injection Nozzle with Swirl

Because cavitation in injection nozzles cannot be avoided and as it is always accompanied by erosion, especially at the inlet of the nozzle bore hole, active control of the static pressure in this region can be achieved by superimposing appropriate vortex flow. The vortex flow would separate the cavity from the nozzle bore holes and would avoid the contact of the solid surfaces with the cavity structure. The 3-D injection nozzle geometry with 4 quasi-tangential admission openings at the inlet and the corresponding computation mesh is presented in Fig. 5.12. In order to reduce the calculation time, a 90° section (82000 nodes) together with periodic boundaries is simulated. The meridional cross section of this 3-D test case is identical with the layout of the 2-D nozzle model of the previous section. Therefore, the diameter of the bore hole is 0.28 mm , the nozzle length is 1.0 mm and the radius of the wall curvature at the inlet into the

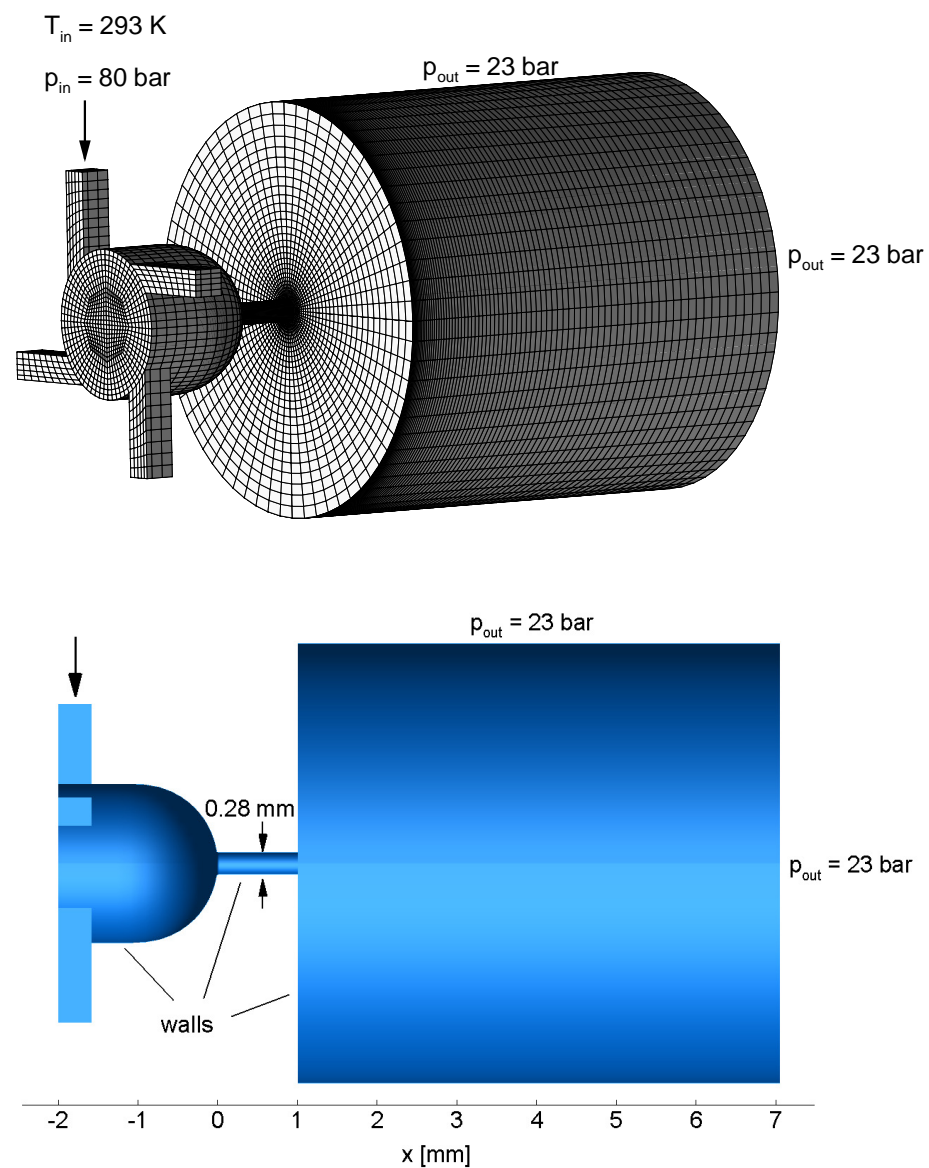


Figure 5.12: 3-D injection nozzle with tangential inlets, geometry and corresponding grid with outflow domain.

bore hole is $r = 2.8 \cdot 10^{-5} m$.

Because of the faster decay of disturbances in 3-D flow, the pressure boundary condition of the outflow regime is prescribed by a constant value $p_{out} = 23 bar$. The inlet pressure and temperature are $p_{in} = 80 bar$ and $T_{init} = 293 K$ respectively. The resulting swirl number Sw , as the ratio of reference values of the circumferential velocity v_ϕ and the axial velocity v_x , is in the range of 0.67 and 0.79, depending on the reference location and on the existence of cavitation or not. This parameter is an important indicator for vortex breakdown if it exceeds a certain value. $Sw < 1$ indicates that vortex breakdown is not to be expected, at least not in single-phase flow. As vortex flow acts as a flow control tool, a more predictable flow pattern is expected in this case as opposed to the highly non-periodic behavior seen in the previous section. The integrated vapor volume of the entire computational domain (Fig. 5.13) confirms the global periodic nature of the process with an average shedding frequency of $f_{cycle} \approx 59 kHz$.

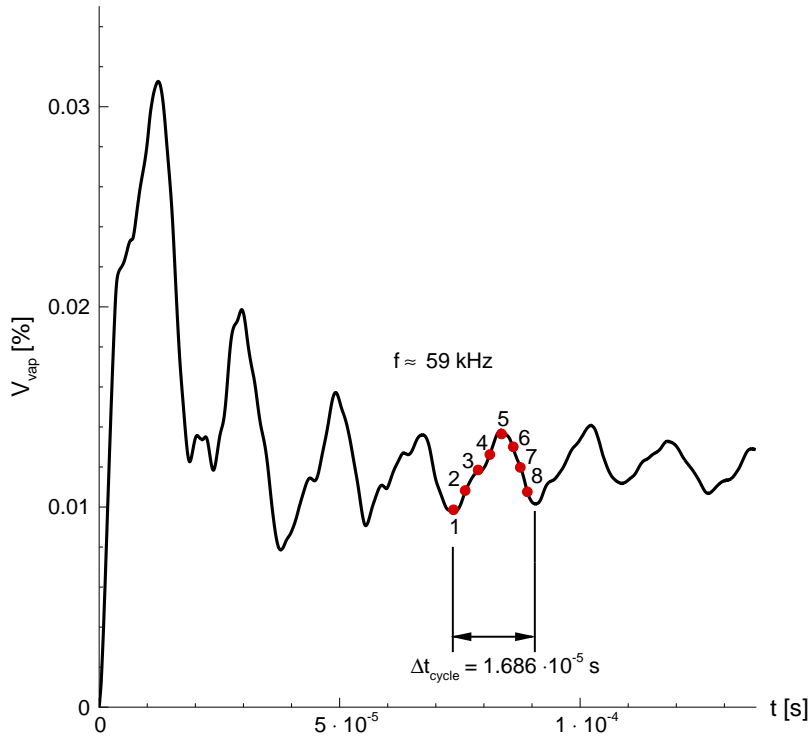


Figure 5.13: Time history of the integrated vapor volume V_{vap} , $p_{in} = 80 bar$, $p_{out} = 23 bar$, $T_{init} = 293 K$, $\Delta t_{CFD} = 10^{-9} s$, second order in space and in time.

The pictures of the sequence given in Fig. 5.14 are directly correlated with the discrete points 1-8 of Fig. 5.13. The presented cavitation cycle starts at $t_1 = 7.390 \cdot 10^{-5} s$ and covers a time interval of $\Delta t_{cycle} = 1.686 \cdot 10^{-5} s$. From these pictures it is quite obvious that the dominating part of the flow inside the injection nozzle remains steady. The significant advantage of the superimposed vortex is the complete separation of the cavity from the nozzle walls. Therefore, this configuration avoids direct contact of the collapsing vapor clouds with the structure and thus minimizes the erosion problem substantially. Moreover, the constant pressure ratio of 80/23 bar establishes a swirl number of $Sw = 0.67$ at the radial position $R = r_{max} = 0.14 mm$ in the nozzle exit plane.

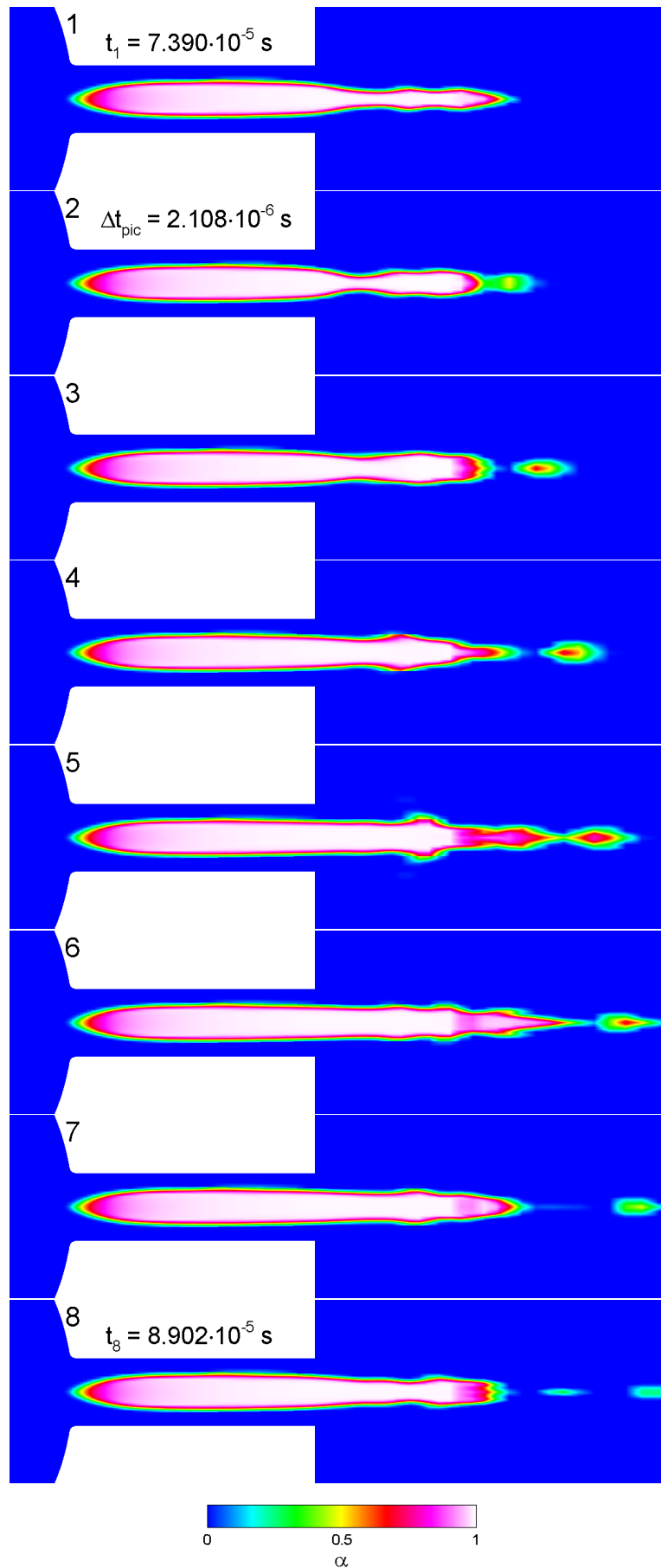


Figure 5.14: Unsteady periodic void fraction formation in cavitating flow through 3-D injection nozzle at $t_1 = 7.390 \cdot 10^{-5} \text{ s}$, time interval $\Delta t_{\text{cycle}} = 1.686 \cdot 10^{-5} \text{ s}$, $f_{\text{cycle}} \approx 59 \text{ kHz}$, $p_{\text{in}} = 80 \text{ bar}$, $p_{\text{out}} = 26 \text{ bar}$, $T_{\text{init}} = 293 \text{ K}$, $\Delta t_{\text{CFD}} = 10^{-9} \text{ s}$, second order in space and in time.

The enlargement given by Fig. 5.15 resolves details in the collapse region and the reverse flow after condensation of the vapor. This shedding behavior is not vortex breakdown, it is actually the corresponding mechanism as known from re-entry jets with cloud separation from the sheet cavities seen in wing type bodies [107].

The resulting steady mass flow defect due to cavitation is $\Delta\dot{m}/\dot{m}_{single-phase} = 17\%$ and is therefore of the same order as in the 2-D plane test cases.

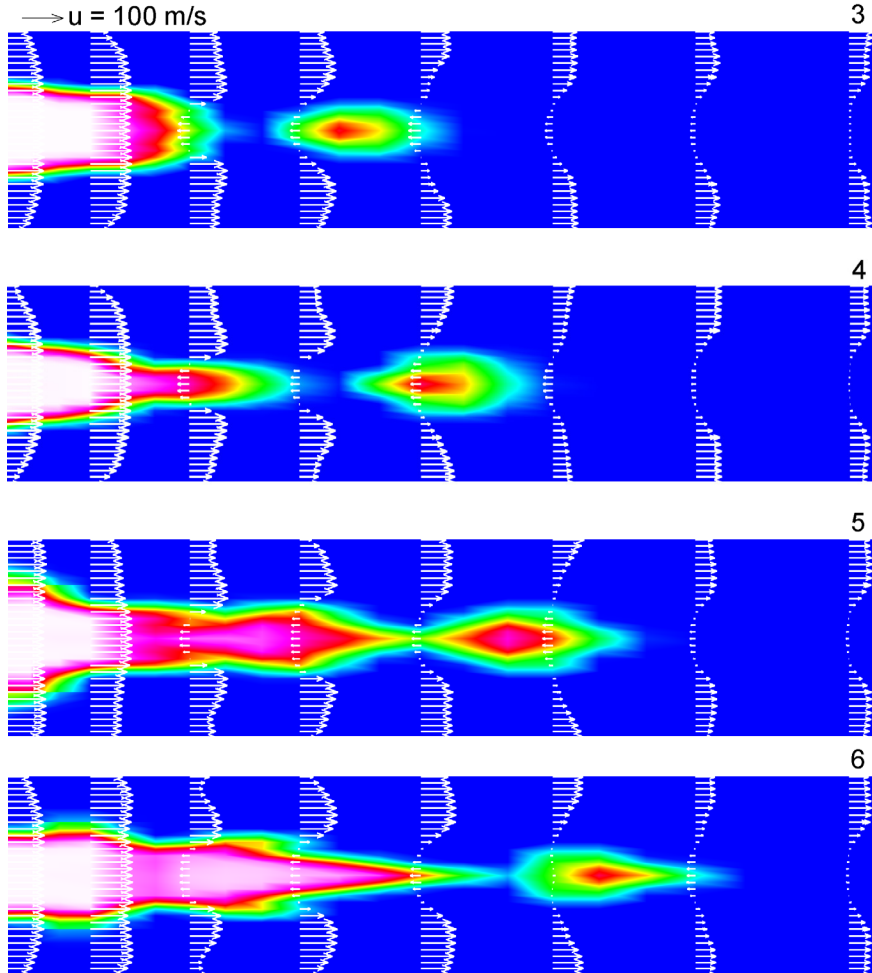


Figure 5.15: Close-up of the collapsing vapor vortex - enlargement of external flow region according to pictures 3-6 of Fig. 5.14. $p_{in} = 80 \text{ bar}$, $p_{out} = 23 \text{ bar}$, $T_{init} = 293 \text{ K}$, $\Delta t_{CFD} = 10^{-9} \text{ s}$, second order in space and in time.

To give an overall impression of the velocity field, streamtraces starting from the inlets to the outflow exit are generated (Fig. 5.16). One can also observe the acceleration in the convergent nozzle part and the rotational symmetric vapor core, which is made visible by iso-surfaces of void fraction $\alpha_{min} = 0.05$ (blue core).

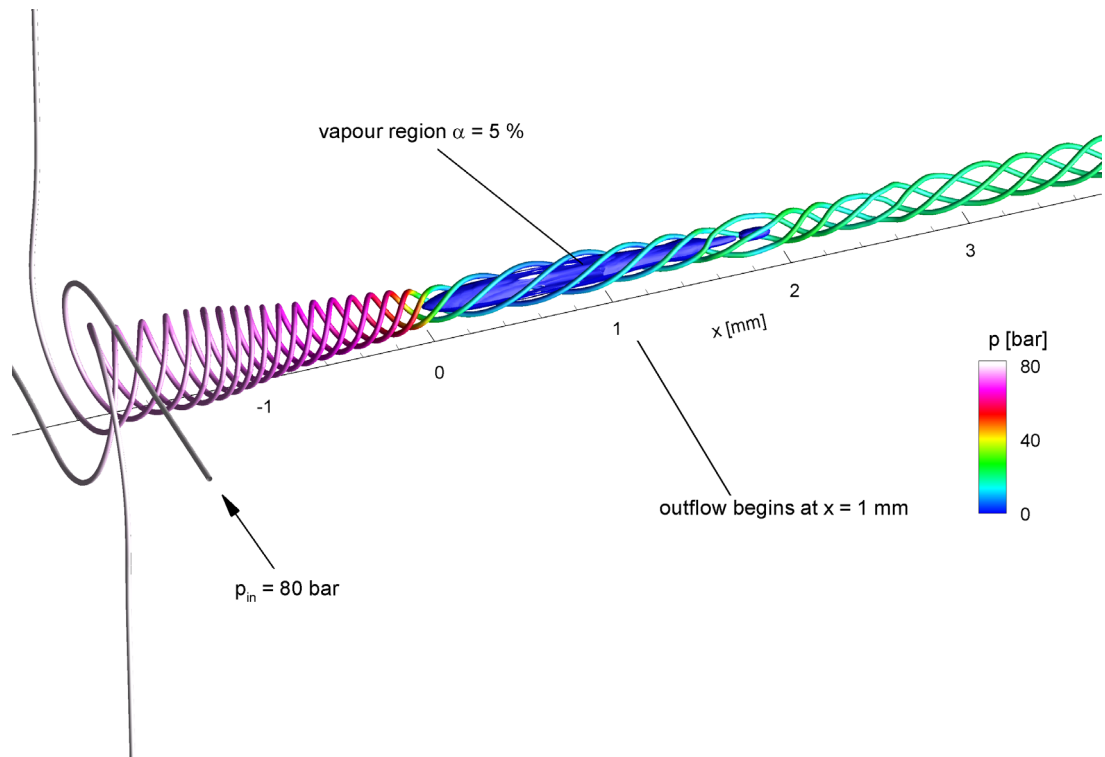


Figure 5.16: Streamtraces through the 3-D nozzle corresponding to the time instant 5 in Fig. 5.14, colored with the static pressure values. Cavitation region is made visible by iso-surfaces of void fraction $\alpha_{min} = 0.05$. $p_{in} = 80 \text{ bar}$, $p_{out} = 23 \text{ bar}$, $T_{init} = 293 \text{ K}$, $\Delta t_{CFD} = 10^{-9} \text{ s}$, second order in space and in time.

5.1.3 3-D Injection Nozzle with Swirl and Divergence

To provide a better understanding of the swirl flow and its interaction with the main flow dynamics, the injection nozzle studied earlier is slightly modified. The parallel bore hole is replaced with a divergent channel having a 50% larger diameter at the exit plane. Figure 5.17 (top) shows the injection nozzle geometry and the applied boundary conditions. The mesh size is the same as the previous calculation and as before to reduce the calculation time, a 90° section together with periodic boundaries is simulated. The diameter of the bore hole is 0.28 mm at the inlet plane and 0.42 mm at the exit plane, the nozzle length is 1.0 mm and the radius of the wall curvature at the inlet into the bore hole is $r = 2.8 \cdot 10^{-5}\text{ m}$. The cylindrical wall of the bore hole has a smooth divergence following a quadratic function. The detail of the computational mesh around the bore hole can be seen in Fig. 5.17 (bottom).

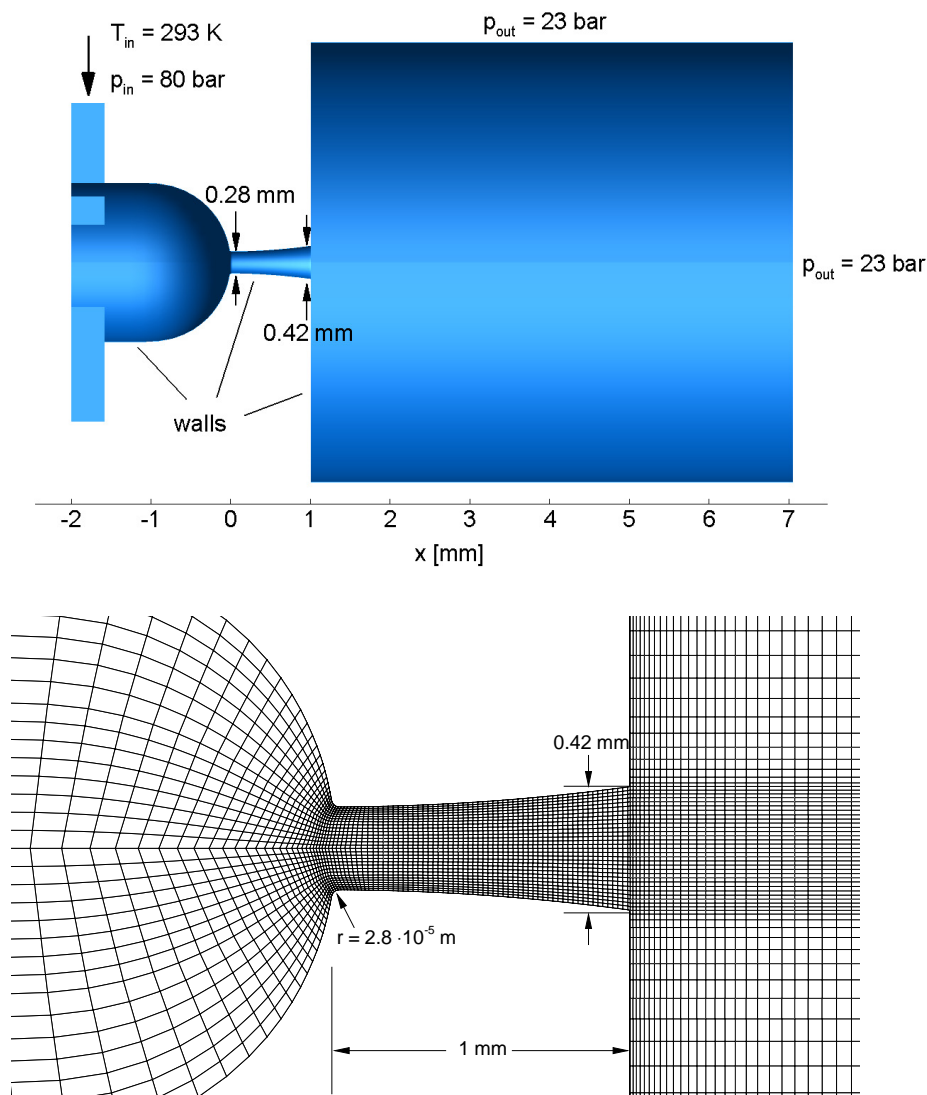


Figure 5.17: 3-D injection nozzle geometry with tangential inlets and the corresponding boundary conditions (top). Detail of the computational mesh around the bore hole (bottom).

The same boundary conditions are applied as the previous calculation, where the inlet pressure and temperature are $p_{in} = 80\text{ bar}$ and $T_{init} = 293\text{ K}$ respectively, and at the

outflow domain a constant pressure value $p_{out} = 23 \text{ bar}$ is prescribed. The integrated vapor volume curve of the entire computational domain (Fig. 5.18) shows a periodic character of the flow field, but it is not as predictable as the previous case. This is mainly due to the effect of the divergence of the bore hole. Although vortex flow acts as a flow control mechanism and stabilizes the flow dynamics, the divergent geometry acts on the opposite sense by decreasing the axial velocity component and increasing the static pressure in the flow direction. Therefore, when the pressure increase interacts with the main cavity structure it causes partial collapses and destroys the stability of the core flow.

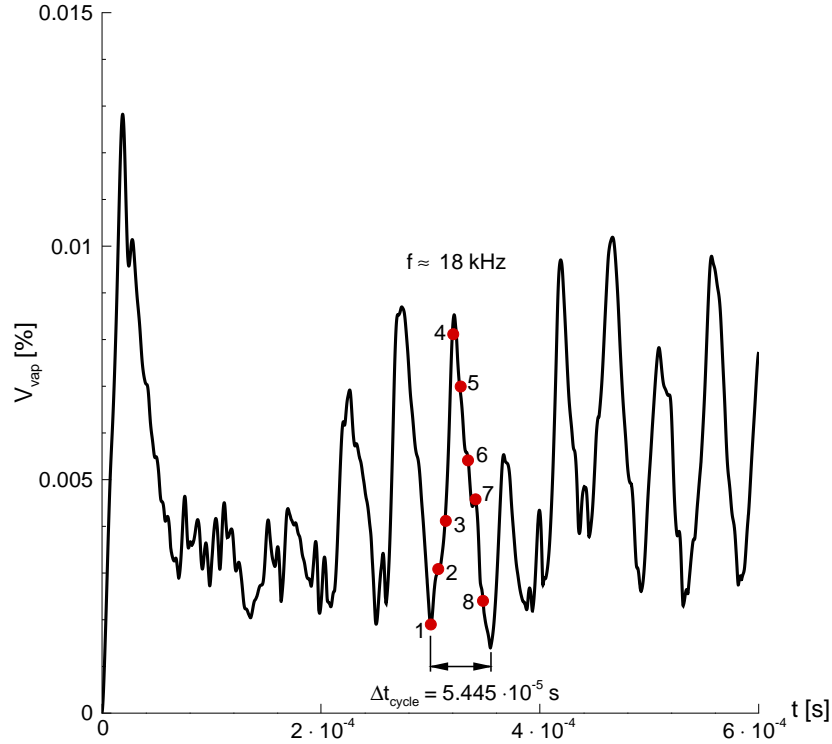


Figure 5.18: Time history of the integrated vapor volume V_{vap} , $p_{in} = 80 \text{ bar}$, $p_{out} = 23 \text{ bar}$, $T_{init} = 293 \text{ K}$, $\Delta t_{CFD} = 10^{-9} \text{ s}$, second order in space and in time.

Figure 5.19 presents the picture series of the investigated cavitation cycle as shown in Fig. 5.18. The given cavitation cycle starts at $t_1 = 3.004 \cdot 10^{-4} \text{ s}$ and covers a time interval of $\Delta t_{cycle} = 5.445 \cdot 10^{-5} \text{ s}$. If we examine these pictures and compare it with Fig. 5.14, we immediately see that the stable portion of the cavity is completely destroyed and cloud shedding mechanism now takes place inside the bore hole. Moreover, fragmentation of the cavitation cloud and small scale structures are visible in all of the pictures. It should be also noted that, the cavitation structures are still separated from the nozzle walls and direct contact of the cavity with the solid walls is again avoided. For this case the constant pressure ratio of $80/23 \text{ bar}$ establishes a maximum swirl number of $Sw = 0.41$ at the radial position $R = r_{max} = 0.21 \text{ mm}$ in the nozzle exit plane.

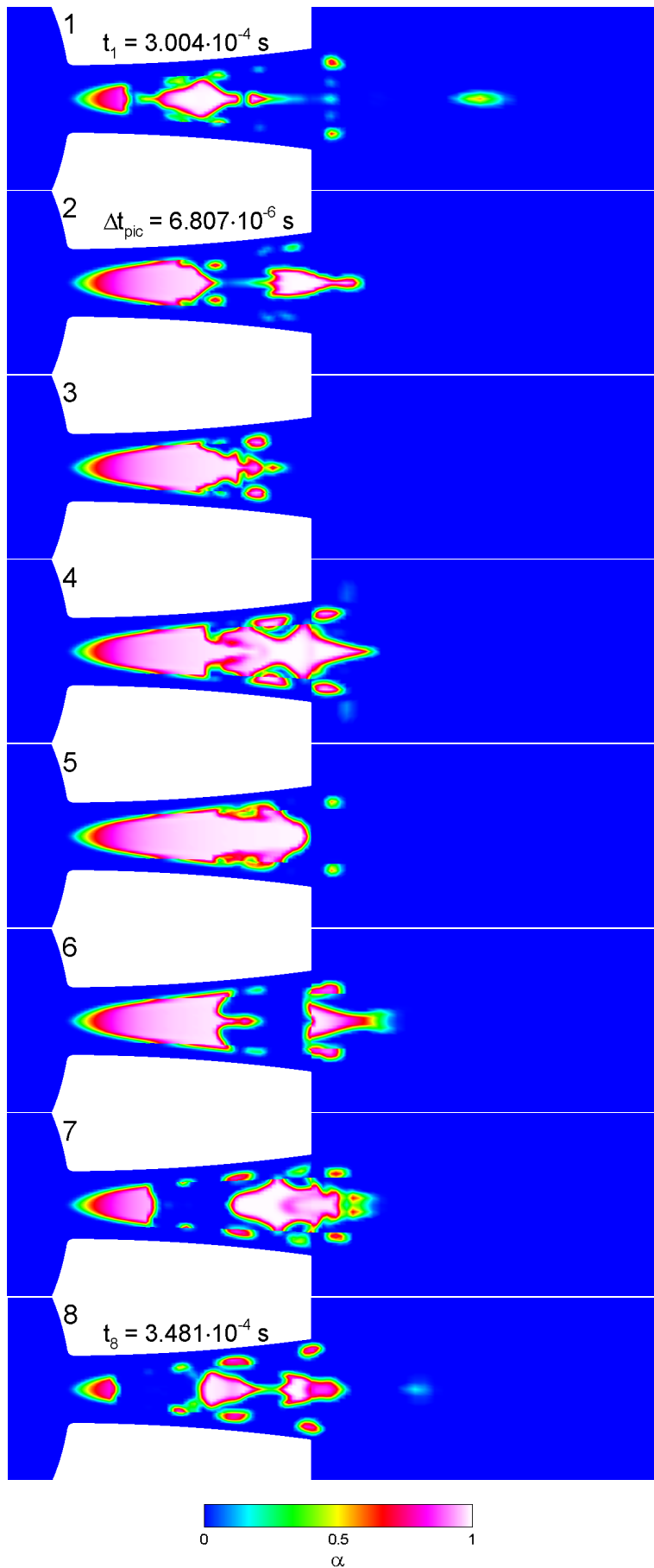


Figure 5.19: Unsteady periodic void fraction formation in cavitating flow through 3-D injection nozzle at $t_1 = 3.004 \cdot 10^{-4} s$, time interval $\Delta t_{cycle} = 5.445 \cdot 10^{-5} s$, $f_{cycle} \approx 18 kHz$, $p_{in} = 80 bar$, $p_{out} = 26 bar$, $T_{init} = 293 K$, $\Delta t_{CFD} = 10^{-9} s$, second order in space and in time.

The enlargement given by Fig. 5.20 resolves the details inside the bore hole. Pictures 3 and 4 show the growth of the cavity inside the nozzle. Between time instants 4 and 5 the tip of the cavity separates from the main body and collapses in the downstream. This collapse initiates re-entry jets that are seen in picture 5 and when they interact with the main cavitation structure, cloud separation occurs, which can be seen in picture 6. Therefore, whole flow dynamics is similar to the previously investigated case and both are analogous to the cloud shedding mechanisms seen in hydrofoils (see section 5.2).

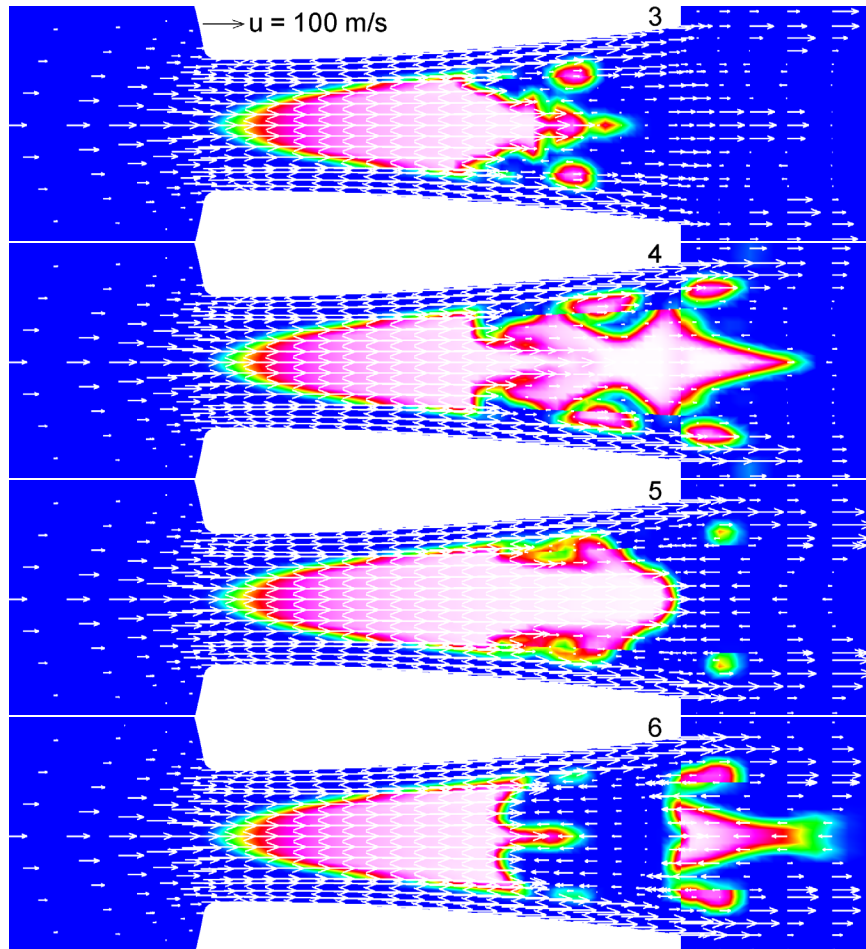


Figure 5.20: Close-up of the collapsing vapor vortex - enlargement of bore hole region according to pictures 3-6 of Fig. 5.19. $p_{in} = 80 \text{ bar}$, $p_{out} = 23 \text{ bar}$, $T_{init} = 293 \text{ K}$, $\Delta t_{CFD} = 10^{-9} \text{ s}$, second order in space and in time.

As the unsteady cloud shedding mechanism takes place inside the bore hole, the resulting mass flow defect due to cavitation is also unsteady with an average magnitude of $\Delta \dot{m} / \dot{m}_{single-phase} = 40\%$. This value is higher than the previous test cases, which is due to the enlarged cavitation region within the bore hole.

5.1.4 3-D Multi-hole Injection Nozzle

As a third 3-D flow example a multi-hole injection nozzle is considered. Figure 5.21 depicts a 180 degree section of a multi-hole fuel injection geometry (left). The position of the needle is fixed at its maximum lift. Six cylindrical bore holes are connected to the lower part of the sack volume.

The inner diameter of the nozzle is 3.9 mm and the needle diameter is 3.26 mm . The length of the bore hole is 1 mm and its diameter is 0.22 mm . The inlet of the bore holes are rounded with a radius of wall curvature of $r = 2.8 \cdot 10^{-5}\text{ m}$. This ensures that the single-phase flow remains attached at the inlet of the bore hole.

The discretization of the flow domain is given by Fig. 5.21 (right). The 6-fold symmetry of the injector geometry allows for the numerical analysis of a periodic 60 degree configuration. At the outlet of the bore hole an outflow domain is added in order to simulate the arising flow field outside of the nozzle as well. The finest mesh used for this calculation consists of 85 blocks and $4 \cdot 10^5$ cells (Fig 5.21 - right).

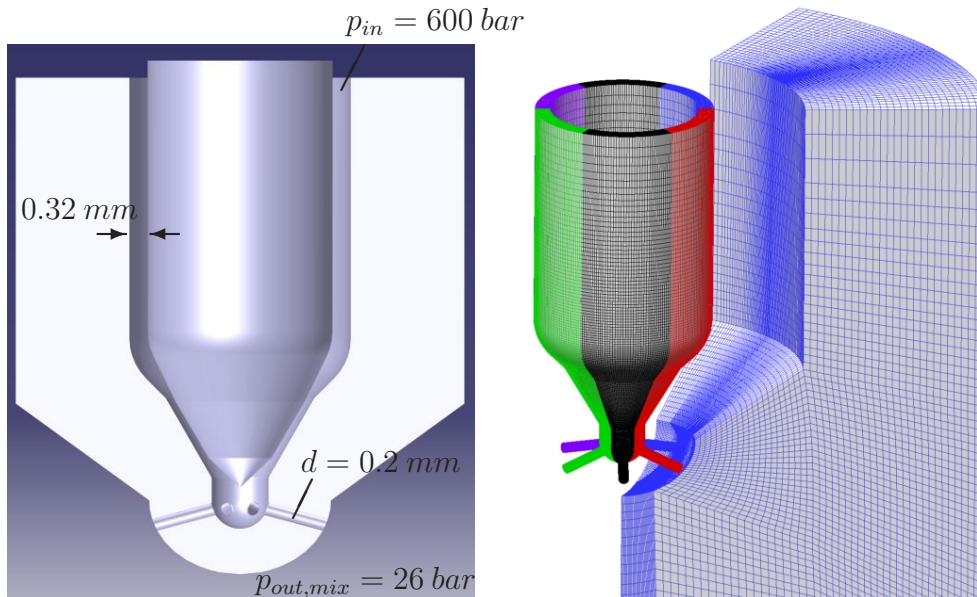


Figure 5.21: 3-D 6-hole injection nozzle, geometry and corresponding grid with outflow domain. Each 60 degree section consists of $4 \cdot 10^5$ cells.

Again, the entire numerical domain initially contains pure water at rest at $p_{out,mix} = 26\text{ bar}$, $T_{init} = 333\text{ K}$. At the inlet the prescribed rail pressure is $p_{in} = 600\text{ bar}$.

Figure 5.22 shows the time history of the integrated vapor volume V_{vap} and mass flow rate \dot{m} plotted against the logarithmic time axis. The graphs demonstrate a strong transient behavior of the flow field, which is converging asymptotically to a steady state value at time $t \approx 10^{-4}\text{ s}$. However, comparison of the final value with the maximum and minimum values during the transient flow development demonstrates the necessity of time accurate simulations of the injection process, especially if pilot or multi-injection strategies are considered. Moreover, this unsteady behavior is also observed for the mass flow rates at the inlet and the outlet of the injection system, which highlights the compressible effects of the liquid fluid and the wave dynamics as

dominating features. This observation is important, as any incompressible formulation would enforce a divergence free velocity field and thus, the equality of mass flow rates throughout the simulation.

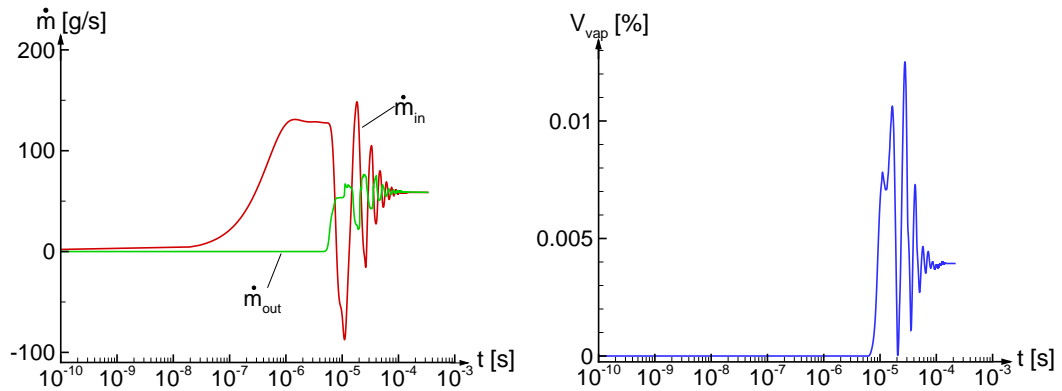


Figure 5.22: Time history of the integrated vapor volume V_{vap} [% total volume of the computational domain], $p_{in} = 600 \text{ bar}$, $p_{out,mix} = 26 \text{ bar}$, $T_{init} = 333 \text{ K}$, $\Delta t_{CFD} = 10^{-10} \text{ s}$, second order in space and in time.

Figures 5.23 and 5.24 depict flow features arising at the time scale $\Delta t \approx 10^{-6} \text{ s}$. Due to the initially enforced pressure jump $\Delta p = p_{in} - p_{out,mix} = 574 \text{ bar}$ a shock instantaneously forms and propagates through the nozzle. The resulting post shock velocity \hat{u} can be estimated by the characteristic compatibility conditions [138]

$$\hat{u} = \frac{p_{in} - p_{out,mix}}{\rho \cdot c}. \quad (5.4)$$

Together with the given conditions and the properties of water at $T_{init} = 333 \text{ K}$, the post shock velocity \hat{u} turns out to be 38.2 m/s .

The shock strength as well as the post shock velocity remain unaltered as long as the wave propagates through the constant area gap between the needle and the inner nozzle wall. As the initial shock reaches the convergent part of the annular gap, area contraction and wall curvature enforce shock focussing and shock deflection respectively (Pics. 1-2 of Fig. 5.23). Downstream of the needle tip the shock front remains no longer planar (Pic. 3). As soon as it interacts with the bore hole inlets diffraction takes place. The diffraction results in a wave propagating towards the bottom of the sack and nearly planar wave fronts traveling through the bore holes (Pic. 4).

When the primary shock focuses at the bottom of the sack the maximum instantaneous pressure rise $p_{max} = 2163 \text{ bar}$ in the system is observed (Fig. 5.24 - left). As the shocks reach the exits of the bore holes, reflected rarefaction waves propagate inside the holes. This expansion is strong enough to reduce the static pressure to p_{sat} and thus to enforce acoustic cavitation (Fig. 5.24 - right).

Figure 5.25 depicts the instantaneous flow field corresponding to a violent collapse and resulting shock formation at $t = 2.04 \cdot 10^{-5} \text{ s}$ inside the nozzle bore hole. This leads to a maximum pressure of $p_{max} = 1029 \text{ bar}$, which is about twice the inlet pressure $p_{in} = 600 \text{ bar}$. The corresponding Mach number of the shock front is $M_s = 1.02$. Moreover, the cavitation regions at the bore hole inlet and near the collapse are visible as orange lines of $\alpha_{min} = 0.001$.

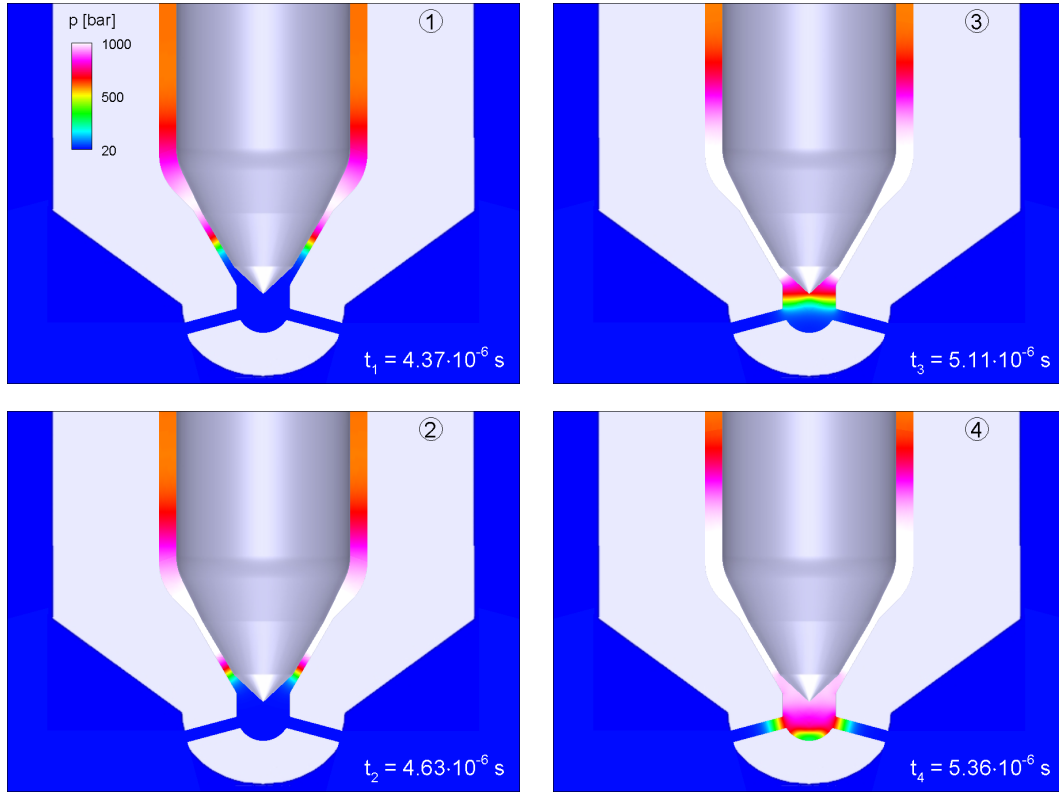


Figure 5.23: Pressure contours showing the pure liquid wave dynamics inside the nozzle as consequence of the initiated shock wave, time interval $\Delta t_{1-4} = 5.36 \cdot 10^{-6} \text{ s}$, $p_{in} = 600 \text{ bar}$, $p_{out,mix} = 26 \text{ bar}$, $T_{init} = 333 \text{ K}$, $\Delta t_{CFD} = 10^{-10} \text{ s}$, second order in space and in time.

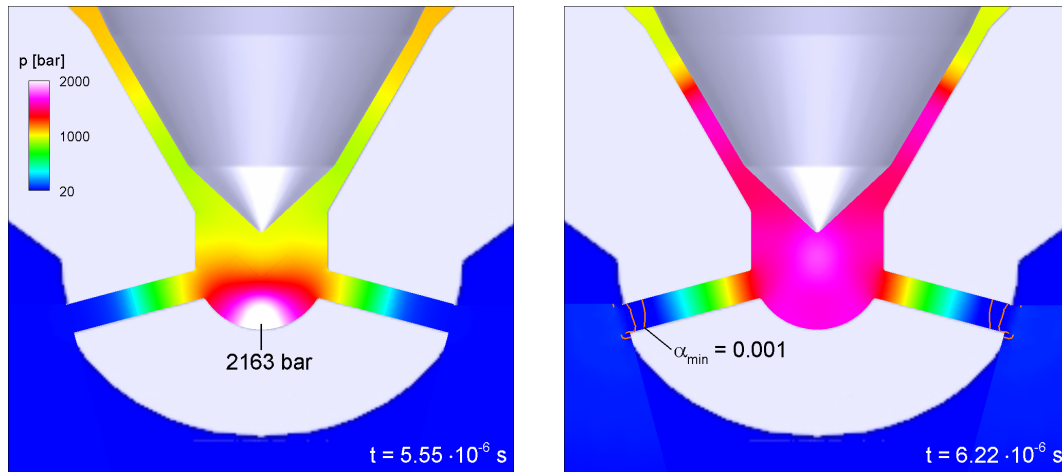


Figure 5.24: Shock wave inside the sack-hole, $p_{max} = 2163 \text{ bar}$ (top), acoustic cavitation in the bore holes (orange lines - bottom), $p_{in} = 600 \text{ bar}$, $p_{out,mix} = 26 \text{ bar}$, $T_{init} = 333 \text{ K}$, $\Delta t_{CFD} = 10^{-10} \text{ s}$, second order in space and in time.

For the prescribed pressure difference $\Delta p = p_{in} - p_{out} = 574 \text{ bar}$ at $t \geq 10^{-4} \text{ s}$ this strong wave motion is no longer present and a stationary cavitation pattern establishes inside the bore holes. The flow field reaches a steady state and thus the vapor volume

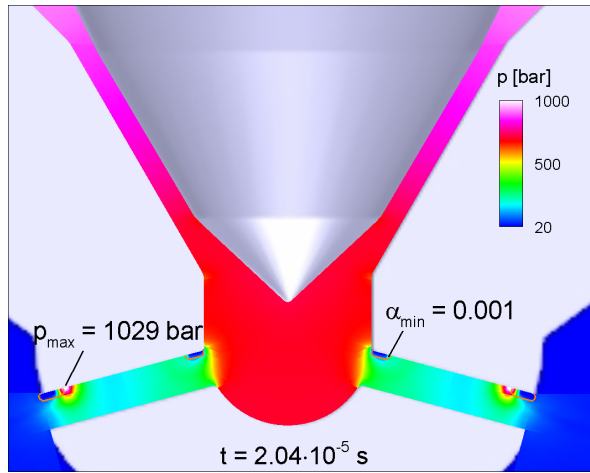


Figure 5.25: Instantaneous formation of a strong shock after violent cloud collapse in the nozzle bore hole at $t = 2.04 \cdot 10^{-5} s$, $p_{max} = 1029 bar$, $p_{in} = 600 bar$, $p_{out,mix} = 26 bar$, $T_{init} = 333 K$, $\Delta t_{CFD} = 10^{-10} s$, second order in space and in time.

as well as the mass flow remain constant. In Fig. 5.26 the resulting steady state supercavitation structure at the meridional plane of the injector is presented.

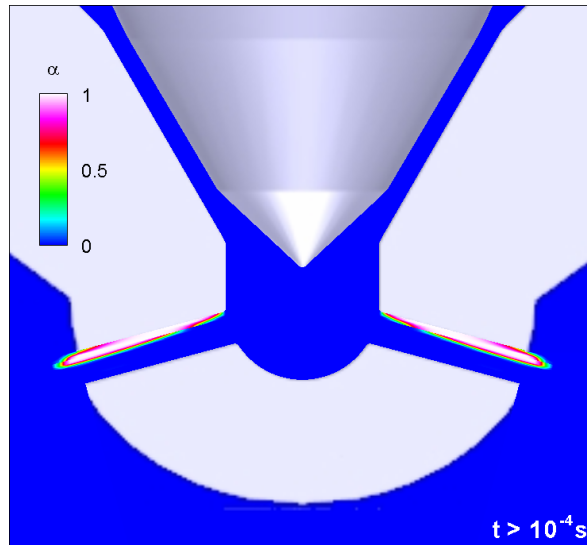


Figure 5.26: Vapor volume fraction α . 3-D steady-state supercavitation inside the bore holes - meridional plane at $t \geq 10^{-4} s$, mass flow defect $\Delta \dot{m} / \dot{m}_{single-phase} = 24\%$, $p_{in} = 600 bar$, $p_{out,mix} = 26 bar$, $T_{init} = 333 K$, $\Delta t_{CFD} = 10^{-10} s$, second order in space and in time.

Figure 5.27 shows the isolated 3-D view of the steady cavity structure inside the bore hole (top). At the bore hole inlet the vapor pocket is nearly circular shaped. Slightly downstream of the inlet the structure is confined to the upper part of the spray hole. The bottom picture in Fig. 5.27 shows a similar view of an injection nozzle from the experiments performed by Busch [15] with $p_{in} = 600 bar$, $p_{out} = 1 bar$. Here, the cavitation regions inside the bore hole appear as dark areas.

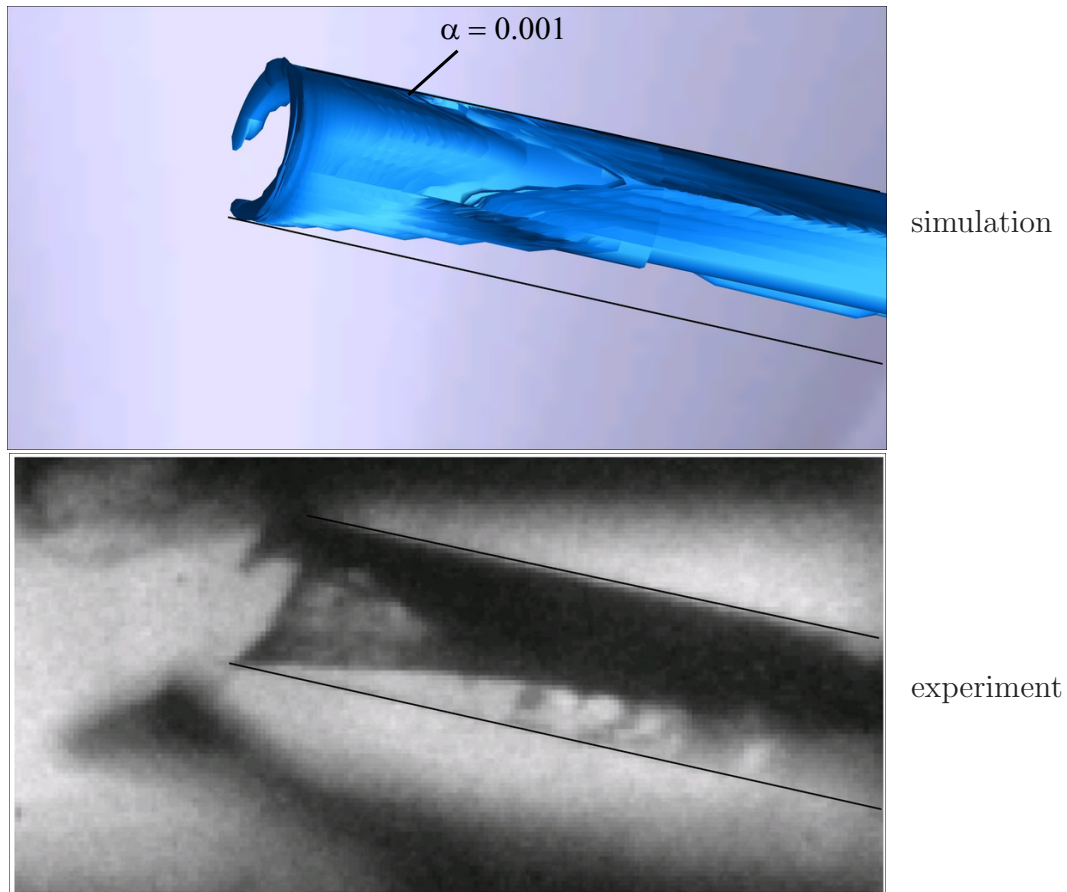


Figure 5.27: Isolated 3-D perspective view of the calculated cavitation pattern (blue surface) inside the bore hole at $t \geq 10^{-4}$ s, $p_{in} = 600$ bar, $p_{out,mix} = 26$ bar, $T_{init} = 333$ K (top). Cavitation pattern (dark area) inside the bore hole from the experiment of Busch [15], $p_{in} = 600$ bar, $p_{out} = 1$ bar (bottom).

The resulting contraction of the effective bore hole exit area due to the cavitation region decreases the mass flow. Here we observe a reduction of the discharge of the nozzle to 76% of its theoretical maximum value. This defect can be interpreted as a 24% reduction of the outlet area. Chaves et al. [19] report comparable discharge defects in several experimental investigations. It is also known that for sufficiently large pressure differences $\Delta p = p_{in} - p_{out}$ no further increase of the mass flow is achievable, even if the outlet pressure is significantly decreased [102]. In order to simulate and predict this effect, without changing the inlet pressure, a series of outlet pressures of 60, 40, 26 and 15 bar are tried. In all cases the numerically obtained mass flows are equal while the integrated vapor volume V_{vap} increases accordingly.

5.2 Hydraulic Machinery

The cavitating flows in hydraulic machinery demonstrate different characteristics than the injection nozzles studied previously. The main differences lie in the flow velocities and the geometrical scale of the applications. Hydraulic machinery applications are generally large-scale and operate within low velocities. Therefore, sheet cavities with resulting break-up, together with cloud shedding and subsequent collapses of these clouds are commonly seen in these flows. This collapse-like re-condensation of vapor clouds has already been seen and studied in the previous sections. These collapses result in strong noise production and erosion in hydraulic machines. The collapse mechanism of a single isolated bubble is explained in chapter 1 and simulated in the previous chapter. Experimental observations indicate a comparable behavior for bubble clouds as well, in spite of being much more complicated due to various bubble-bubble interaction processes [61],[67]. However, the reported maximum intensity of those shock waves not only varies according to the operating conditions for a given setup but it seems to be strongly dependent on the properties of the selected measurement equipment. The range of maximum instantaneous pressure variations reported in the literature covers the huge interval of $O(1)$ bar to $O(100)$ bar [92]. These instantaneous pressure loads due to the collapses are believed to be related to erosion critical areas.

In this section, first results from a 2-D planar hydrofoil are presented and then a 3-D twisted wing geometry is investigated in detail with experimental comparison.

5.2.1 2-D NACA 0015 Hydrofoil

Figure C.8 depicts the computational domain and the corresponding boundary conditions for this test case.

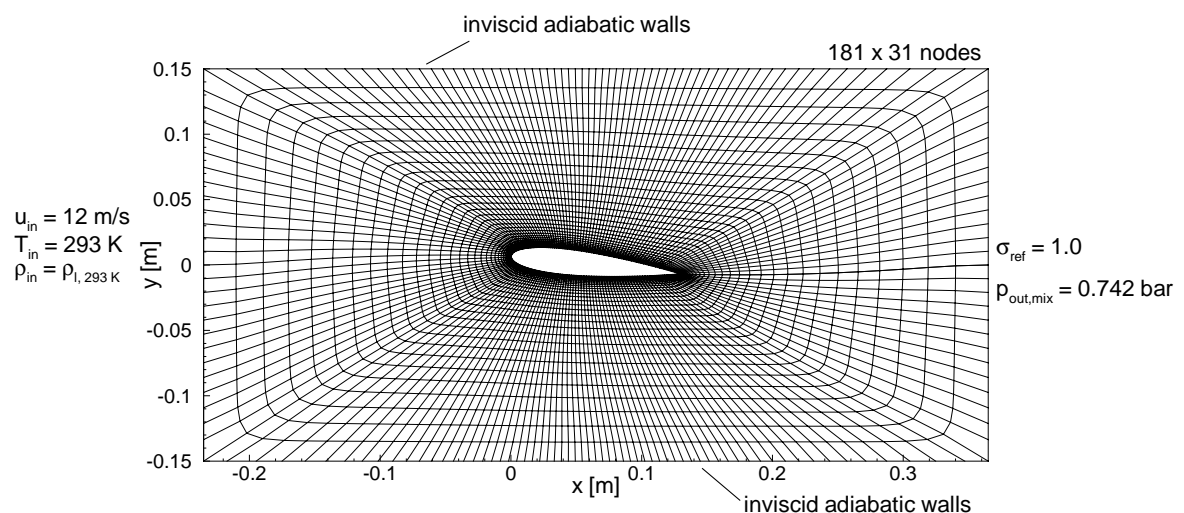


Figure 5.28: 2-D NACA 0015 hydrofoil - computational domain and boundary conditions. Chord length $c = 0.13$ m, angle of attack $\alpha = 6^\circ$, channel height 0.3 m, channel length 0.6 m. Water inflow from left to right, inlet conditions $u_{in} = 12$ m/s, $T_{init} = 293$ K, outlet condition $p_{out,mix} = 0.742$ bar, reference cavitation number $\sigma_{ref} = 1.0$.

The hydrofoil geometry is the standard NACA 0015 at 6° angle of attack with a chord

length of 0.13 m . The inflow velocity is 12 m/s , at the outlet the mixed reflecting non-reflecting boundary condition is applied with $p_{out,mix} = 0.742\text{ bar}$ and the reference cavitation number is set to be $\sigma_{ref} = 1.0$.

Figure 5.29 represents one cycle of the periodic formation of a sheet cavity and the corresponding cloud shedding in a sequence of 8 pictures.

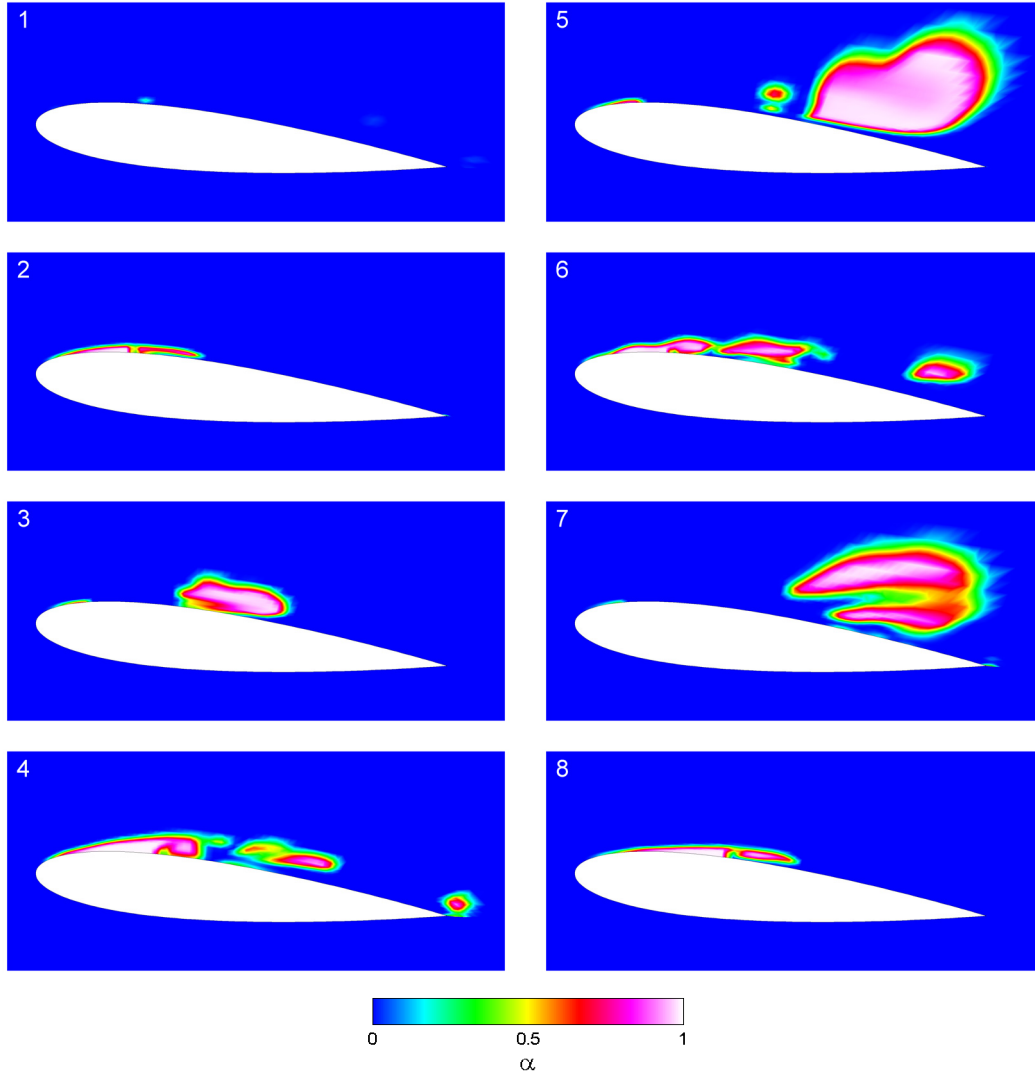


Figure 5.29: Unsteady shedding mechanism of cavitation cycle, $f_{cycle} = 8.93\text{ Hz}$, $\Delta t_{1-8} = 1.12 \cdot 10^{-1}\text{ s}$, $u_{in} = 12\text{ m/s}$, $T_{init} = 293\text{ K}$, $p_{out,mix} = 0.742\text{ bar}$, $\sigma_{ref} = 1.0$, $\Delta t_{CFD} = 10^{-7}\text{ s}$, second order in space and in time.

In Fig. 5.30 the distribution of the time averaged normal and tangential forces (lift and drag forces) per unit meter in depth, together with the vapor volume fraction within one cycle are demonstrated. The dynamic behavior of the shedding mechanism results in strongly time dependent lift and drag variations. The dominating peak values indicate instantaneous negative lift force pulses. The main reasons for the inversion of the normal force direction are either the formation of expansion waves as reflections of shocks at phase boundaries with constant pressure, or the pressure raise due to shocks impacting on the suction side.

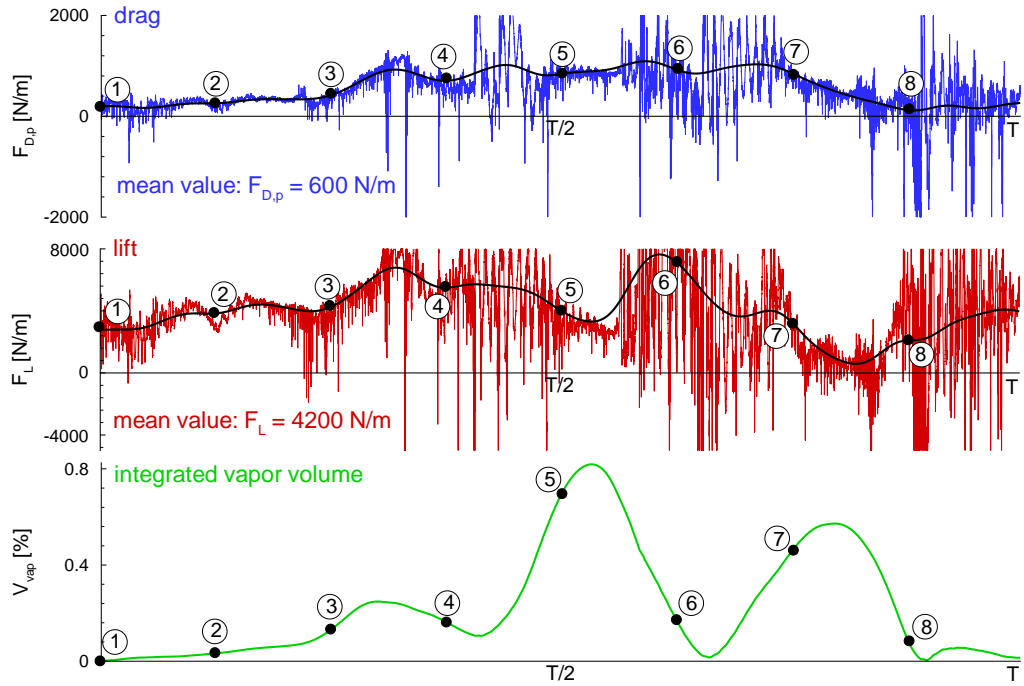


Figure 5.30: Time history of drag force $F_{D,p}$ [N/m], lift force F_L [N/m] and integrated vapor volume V_{vap} , $f_{cycle} = 8.93$ Hz. The black dots numbered 1-8 correspond to the 8 instances in time presented in Fig. 5.29. $u_{in} = 12$ m/s, $T_{init} = 293$ K, $p_{out,mix} = 0.742$ bar, $\sigma_{ref} = 1.0$, $\Delta t_{CFD} = 10^{-7}$ s, second order in space and in time.

A more detailed investigation of the forces acting on the wing is performed through the enlargement of the scaling at the ordinate and the subsequent zooming in on a collapse situation (Fig. 5.31). Figure 5.31 (top) resolves the maximum values of the instantaneous lift force per unit meter in depth up to ± 50000 N/m. It should be noted that the flow around such a 2-D foil geometry with a finite span always develops highly three-dimensional and strongly influenced by alternating sidewall effects. Therefore, this kind of a maximum load is not experienced along the entire span.

To analyze the correlation of the instantaneous peak values of the lift force with the macroscopic structure of the global flow field, the time resolution in Fig. 5.31 is increased stepwise by zooming close to 3 time instants. Zoom 3 of Fig 5.31 enlarges the time interval of $\Delta t = 6 \cdot 10^{-5}$ s with indication of the position of three flow visualizations (pictures 1-3 of Fig. 5.32) within this interval. The time increment between the pictures is $\Delta t_{pic} = 2.1 \cdot 10^{-5}$ s, which is two orders larger than the numerical time step used in the calculation, $\Delta t_{CFD} = 10^{-7}$ s.

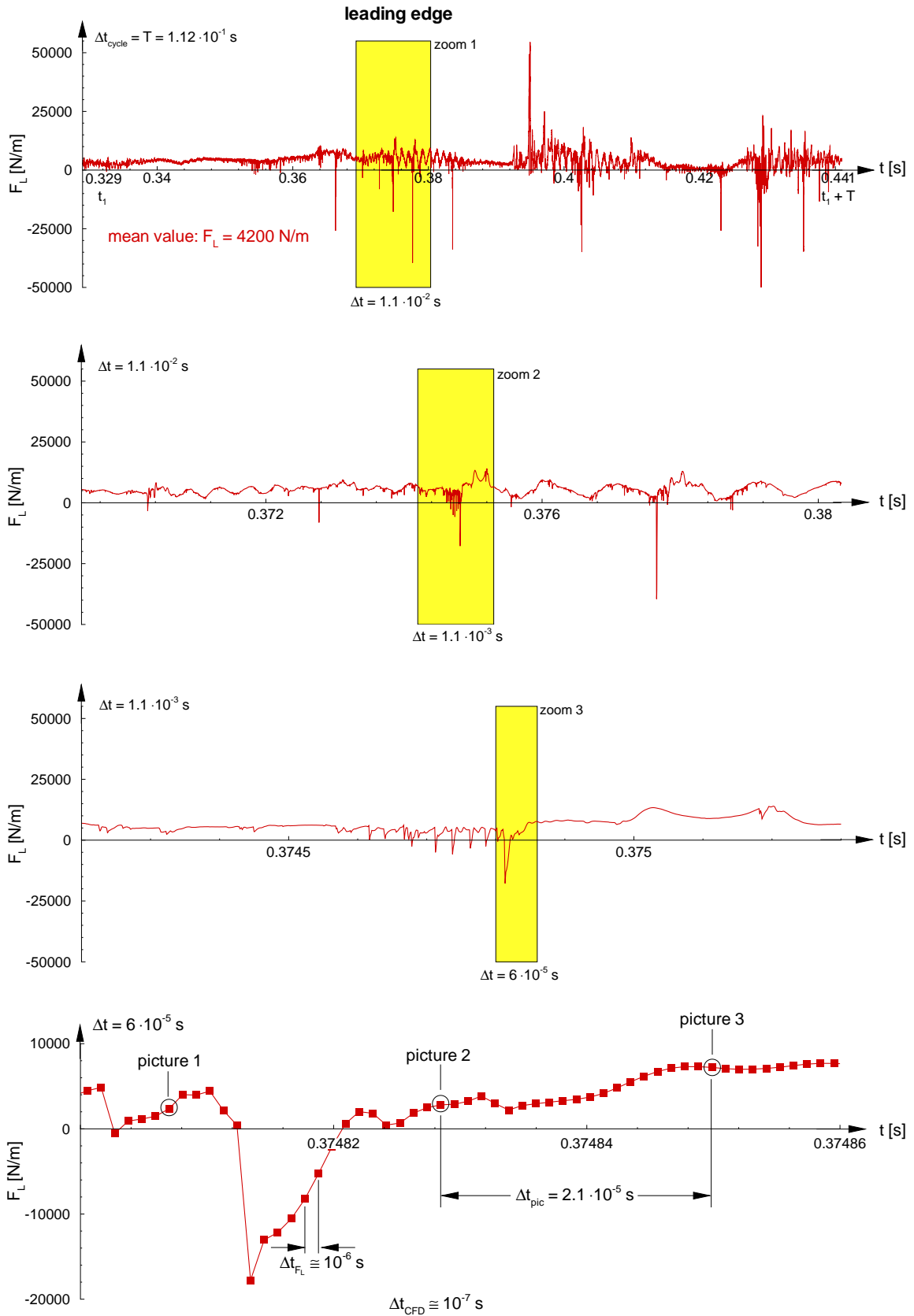


Figure 5.31: Shock formation at the leading edge. High resolution zoom 1 (top) to zoom 3 (bottom) of lift force variation of Fig. 5.30, $f_{\text{cycle}} = 8.93$ Hz. $u_{\text{in}} = 12$ m/s, $T_{\text{init}} = 293$ K, $p_{\text{out,mix}} = 0.742$ bar, $\sigma_{\text{ref}} = 1.0$, $\Delta t_{\text{CFD}} = 10^{-7}$ s, second order in space and in time.

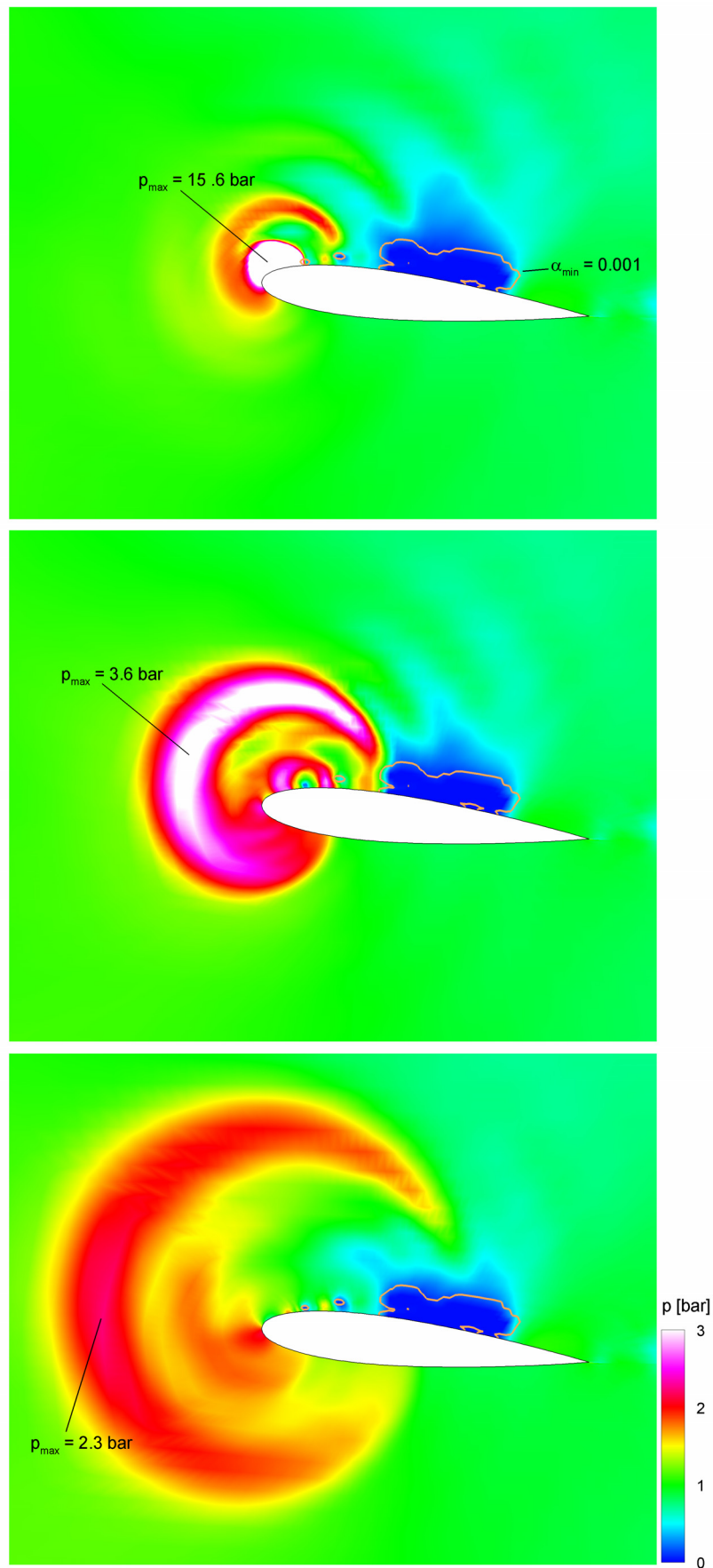


Figure 5.32: Instantaneous shock emerging after cloud collapse at the leading edge at 3 instants in time within the interval $\Delta t_{1-3} = 4.2 \cdot 10^{-5}$ s, according to indication of picture 1-3 of Fig. 5.31 (bottom). $u_{in} = 12$ m/s, $T_{init} = 293$ K, $p_{out,mix} = 0.742$ bar, $\sigma_{ref} = 1.0$, $\Delta t_{CFD} = 10^{-7}$ s, second order in space and in time.

Figure 5.32 highlights details of the correlated instantaneous flow field with the formation of a cylindrical shock at the leading edge and its fast propagation into the oncoming flow. This shock forms instantaneously after the collapse of a small vapor cloud at the leading edge. Because the shock front spreads with approximately 1500 m/s into a flow field with an average convective flow speed of the order of 10 m/s , the front remains perfectly circular. On top (picture 1), the pressure increase through the shock is about 15 bar . Compared with the average static pressure of $p \approx 0.7\text{ bar}$ in the main flow the pressure ratio across this shock is $\hat{p}/p \approx 20$ (Fig. 5.33). In single-phase gas dynamics such a strong pressure ratio requires a pre-shock Mach number above 4 [138]. However, because of the different acoustic impedance of the liquid component, the shock Mach number remains close to one, $M_s = 1.001$. Figure 5.33 depicts the static pressure decay along the radial direction shown.

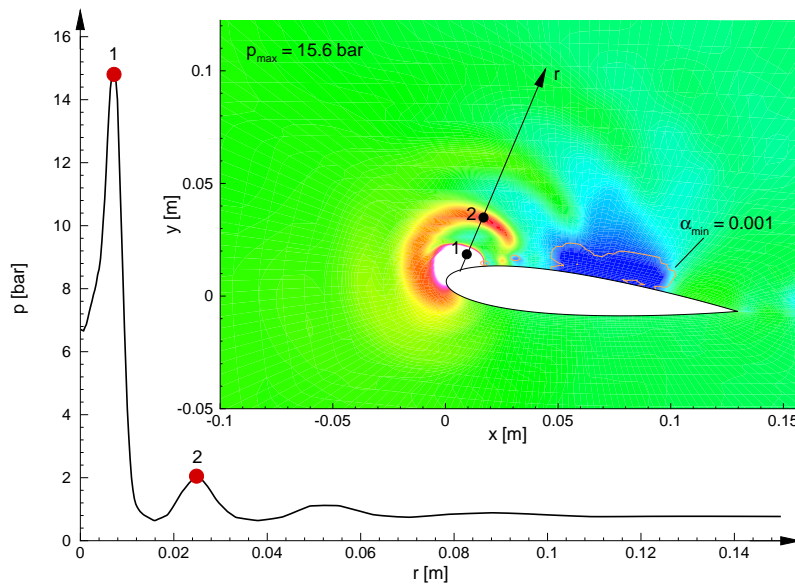


Figure 5.33: Radial pressure decay after cloud collapse at the leading edge with formation of instantaneous shock, according to picture 1 (top) of Fig. 5.32. $u_{in} = 12\text{ m/s}$, $T_{init} = 293\text{ K}$, $p_{out,mix} = 0.742\text{ bar}$, $\sigma_{ref} = 1.0$, $\Delta t_{CFD} = 10^{-7}\text{ s}$, second order in space and in time.

Similar to the leading edge case, Fig. 5.34 demonstrates the instantaneous peak values of the lift force for a collapse at the trailing edge. The time resolution in Fig. 5.34 is increased again stepwise by zooming close to 3 time instants close to the maximum positive pulse of the order of $+50000\text{ N/m}$. Zoom 3 of Fig 5.34 enlarges the time interval of $\Delta t = 1.1 \cdot 10^{-4}\text{ s}$ with indication of the position of three flow visualizations (pictures 1-3 of Fig. 5.35) within this interval. In Fig 5.35 (picture 3) the circular shock front encloses the entire hydrofoil with a maximum strength at the pressure side of 11 bar . This is the reason for the extraordinary high lift force F_L at this instant. At the origin (Fig. 5.35 - picture 1) the maximum static pressure ratio across the emerging shock is about 50 and the shock front starts to propagate in the surrounding liquid phase with $M_s = 1.003$. For comparison, a static pressure ratio of 50 requires in classical gas dynamics a shock Mach number $M_s = 6.5$ [138].

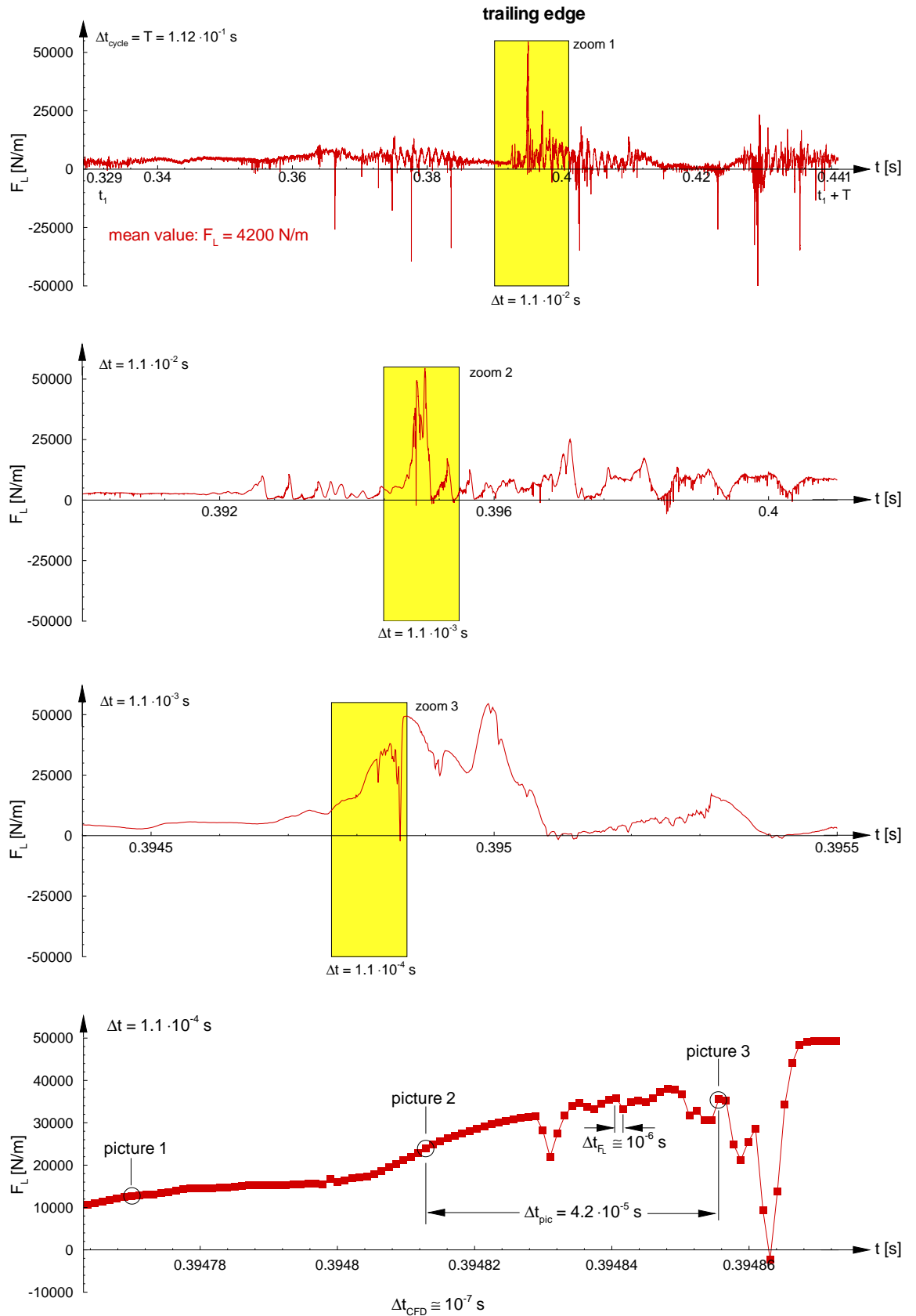


Figure 5.34: Shock formation at the trailing edge. High resolution zoom 1 (top) to zoom 3 (bottom) of lift force variation of Fig. 5.30, $f_{\text{cycle}} = 8.93 \text{ Hz}$. $u_{\text{in}} = 12 \text{ m/s}$, $T_{\text{init}} = 293 \text{ K}$, $p_{\text{out,mix}} = 0.742 \text{ bar}$, $\sigma_{\text{ref}} = 1.0$, $\Delta t_{\text{CFD}} = 10^{-7} \text{ s}$, second order in space and in time.

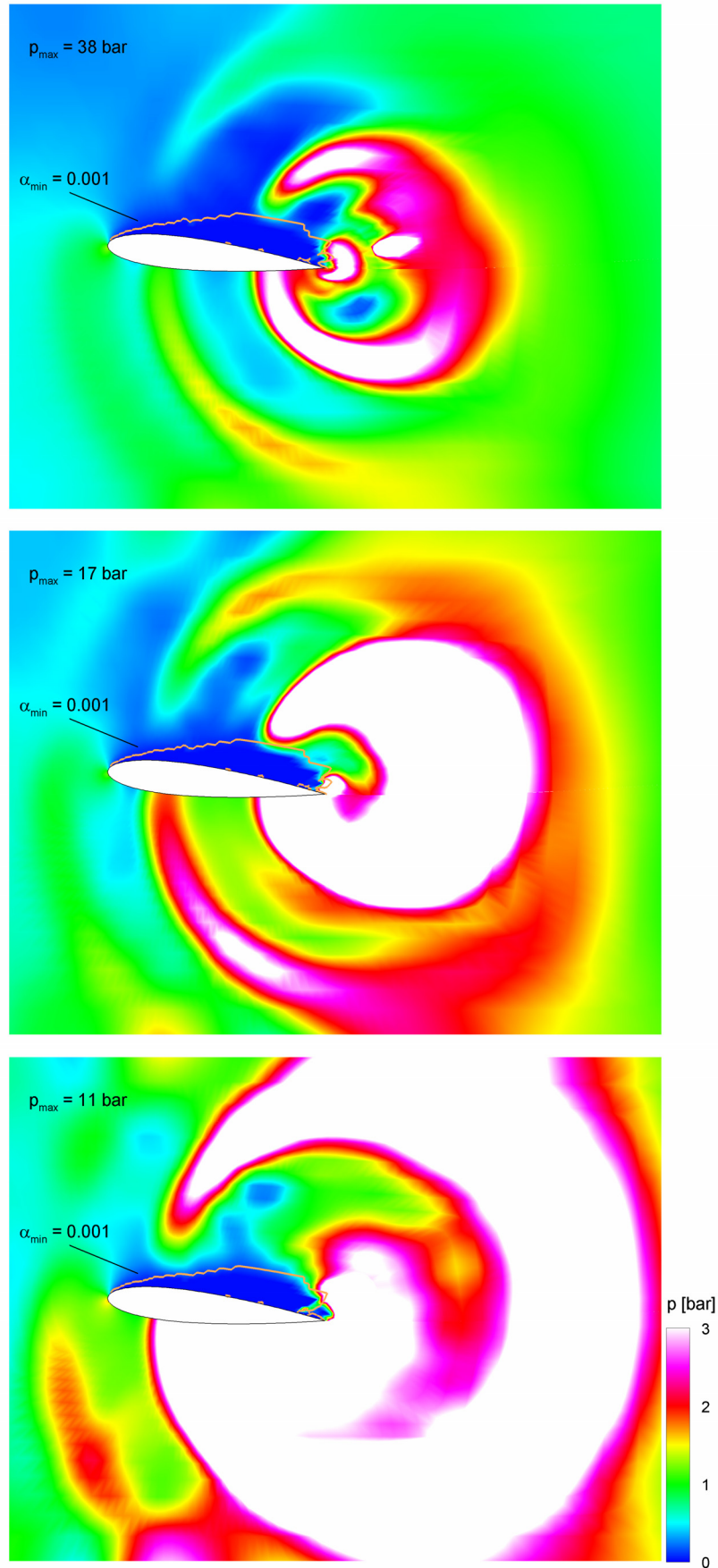


Figure 5.35: Instantaneous shock emerging after cloud collapse at the trailing edge at 3 instants in time within the interval $\Delta t_{1-3} = 8.4 \cdot 10^{-5}$ s, according to indication of picture 1-3 of Fig. 5.34 (bottom). $u_{in} = 12$ m/s, $T_{init} = 293$ K, $p_{out,mix} = 0.742$ bar, $\sigma_{ref} = 1.0$, $\Delta t_{CFD} = 10^{-7}$ s, second order in space and in time.

Figure 5.36 depicts the static pressure decay along the radial direction corresponding to picture 2 of Fig. 5.35.

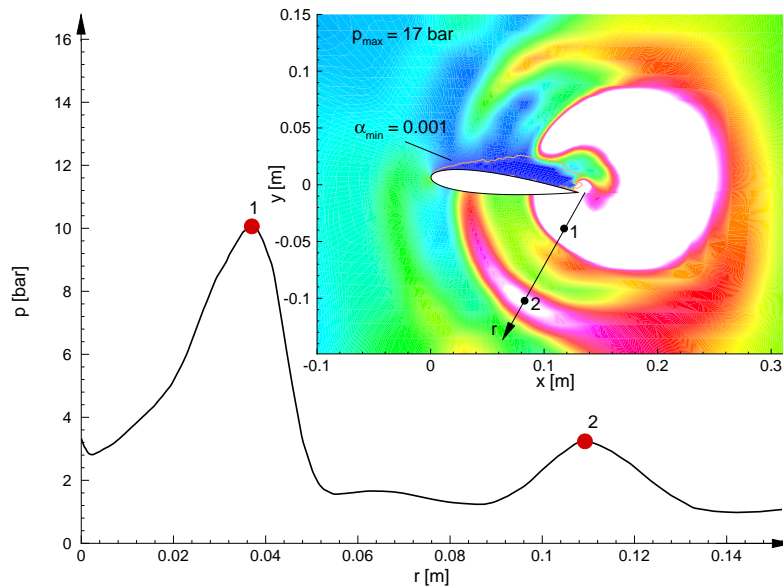


Figure 5.36: Radial pressure decay after cloud collapse at the trailing edge with formation of instantaneous shock, according to picture 2 (middle) of Fig. 5.32. $u_{in} = 12\text{m/s}$, $T_{init} = 293\text{K}$, $p_{out,mix} = 0.742\text{ bar}$, $\sigma_{ref} = 1.0$, $\Delta t_{CFD} = 10^{-7}\text{ s}$, second order in space and in time.

In Fig. 5.35 another important aspect of such simulations concerning the treatment of strong wave propagation can be seen. It was already mentioned in chapter 3 that in order to achieve a realistic flow domain with respect to experimental investigations, the numerical reflection associated with the inflow and outflow boundaries should be minimized. Hence the applied so-called mixed pressure boundary conditions that ensure that oncoming waves can pass through the interface at the outlet via time dependent damping parameters. Instantaneously the waves pass through the cross section without any reflection. With increasing time, amplitude and extension of weak wave reflections increase so that a given value of the static pressure $p_{out,mix}$ at the outlet asymptotically can be maintained.

One interesting observation from the cavitation experiments is that unsteady cavitation dynamics can generate vapor formation at the pressure side of hydrofoils. This is driven by instantaneous pressure decrease at the pressure side as a result of expansion waves and wave reflections inside the system. Typically, violent shocks and intense expansion waves follow each other in rapid succession. Figure 5.37 shows, as before, stepwise increased time resolution of the lift force. Zoom 2 of Fig 5.37 enlarges the time interval of $\Delta t = 8 \cdot 10^{-4}\text{ s}$ with indication of the position of picture series 1-15 of Fig. 5.38, within this interval. The shown picture series covers a time interval of $\Delta t_{1-15} = 2.995 \cdot 10^{-4}\text{ s}$. The first column of Fig. 5.38 visualizes (from top to bottom) the instantaneous propagation of an expansion wave (dark blue region) at the pressure side of the hydrofoil from the trailing edge toward the leading edge (pictures 1-5), followed by the subsequent inversion of this wave motion, high pressure recovering and the formation of a circular shock front, when the vapor starts to collapse close to the

trailing edge (pictures 13-15).

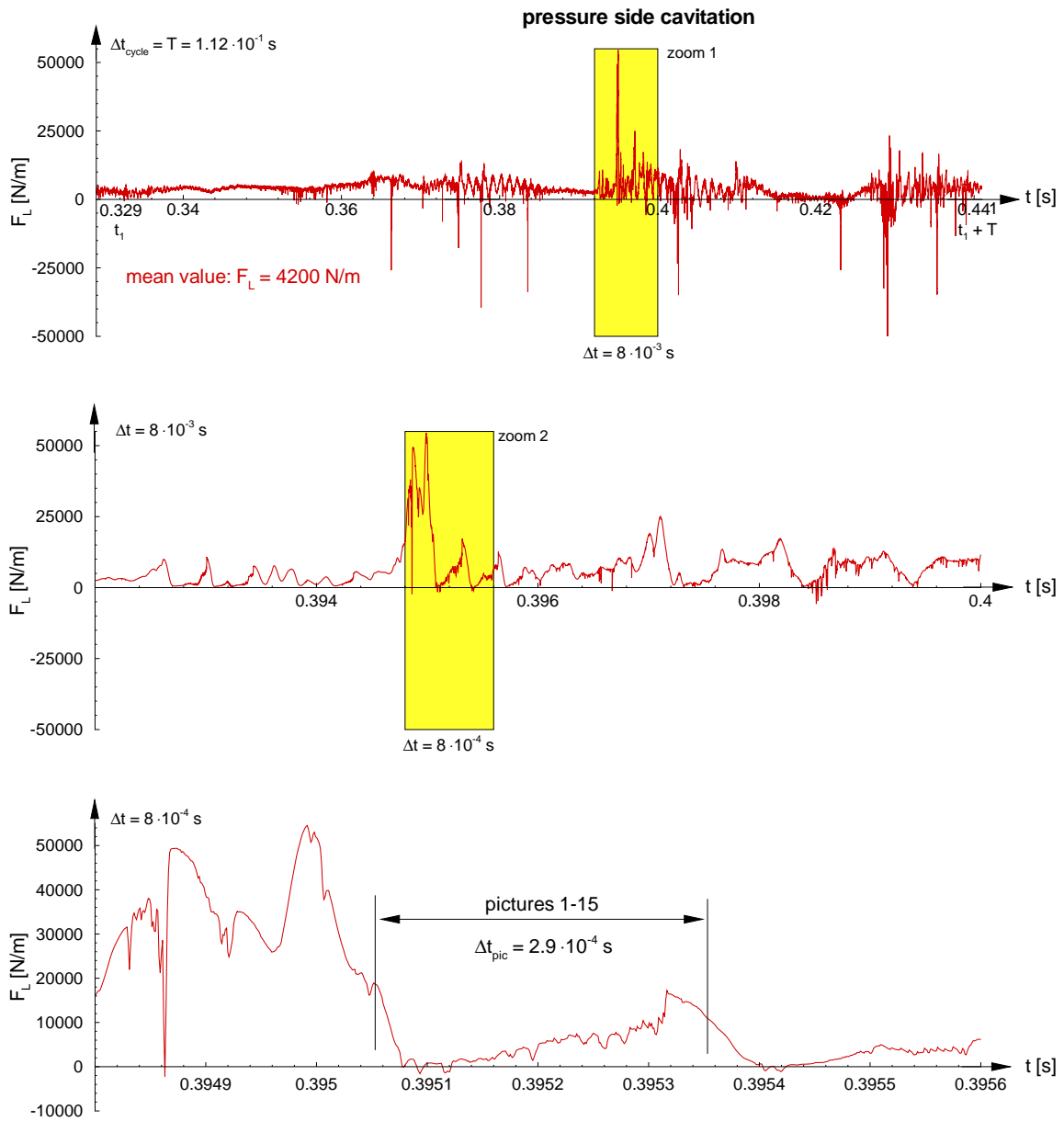


Figure 5.37: Instantaneous pressure side cavitation.. High resolution zoom 1 (top) to zoom 2 (bottom) of lift force variation of Fig. 5.30, $f_{\text{cycle}} = 8.93 \text{ Hz}$, $u_{\text{in}} = 12 \text{ m/s}$, $T_{\text{init}} = 293 \text{ K}$, $p_{\text{out,mix}} = 0.742 \text{ bar}$, $\sigma_{\text{ref}} = 1.0$, $\Delta t_{\text{CFD}} = 10^{-7} \text{ s}$, second order in space and in time.

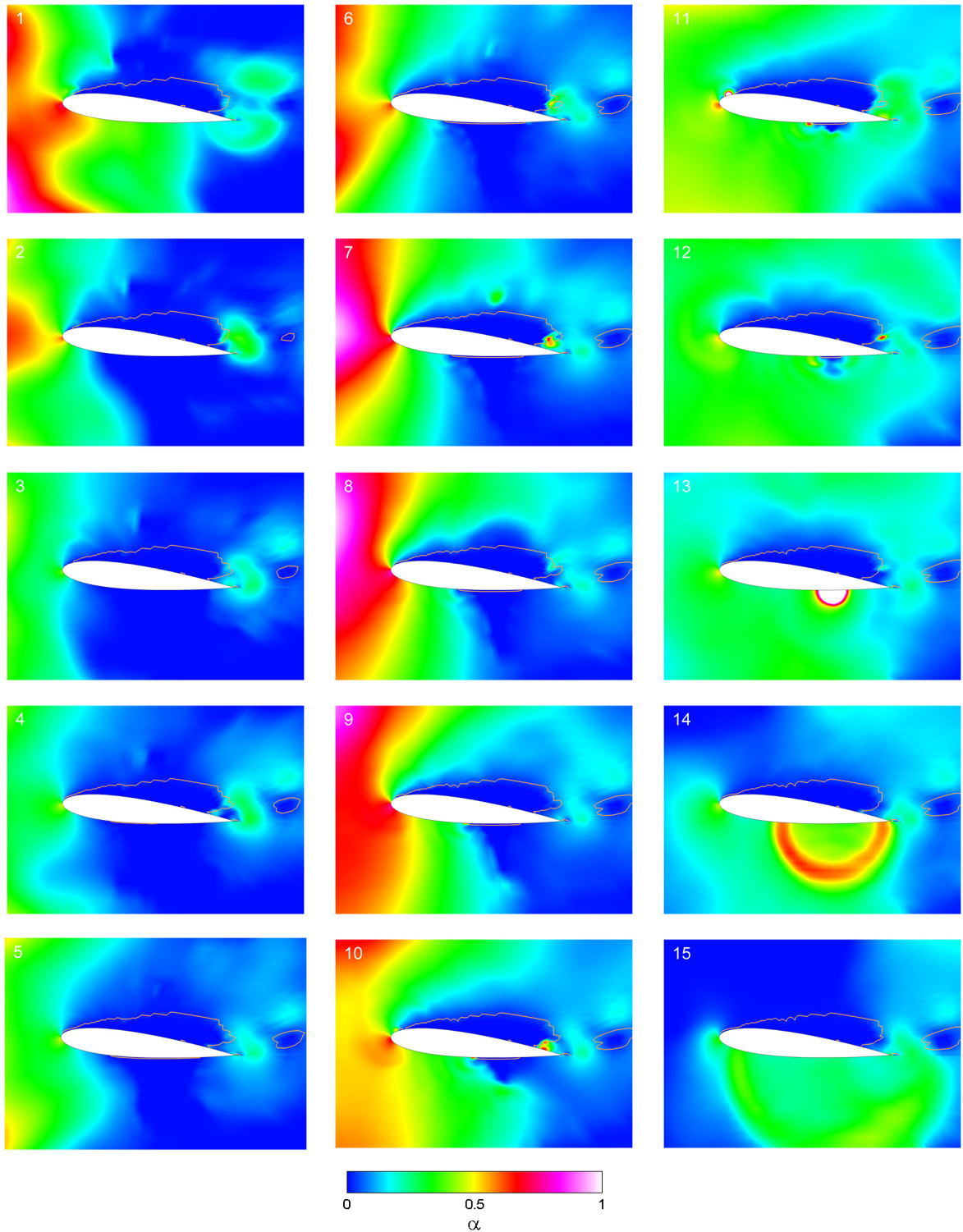


Figure 5.38: Instantaneous pressure side cavitation emerging after violent cloud collapse at the trailing edge at 15 instants in time within the interval $\Delta t_{1-15} = 2.995 \cdot 10^{-4} s$, according to indication of picture 1 - 15 of Fig. 5.37 (bottom). $u_{in} = 12 m/s$, $T_{init} = 293 K$, $p_{out,mix} = 0.742 bar$, $\sigma_{ref} = 1.0$, $\Delta t_{CFD} = 10^{-7} s$, second order in space and in time.

During the first time increments shown, a thin sheet cavity forms at the pressure side (Fig. 5.38, pictures 2-5). In picture 6 the recovered higher ambient pressure initiates a global shrinking of the vapor region. A small fragment collapses (picture 11) while the remaining domain shrinks with increasing speed. At the last stages (between picture 12 and 13), prior to the final collapse, the velocity field close to the vapor domain behaves like a sink relative to the mean flow.

5.2.2 3-D NACA 0009 Twisted Wing - Half Wing Calculation

Due to the inherent instability of the cavitation process, the time dependent development and shedding behavior of a 2-D hydrofoil are not perfectly two-dimensional and remain unpredictable to a certain extent. Therefore, in order to study the true 3-D character of the cavitating flows around wing type bodies, three-dimensional simulations are needed.

Figure 5.39 depicts the numerical test section consisting of a rectangular flow domain with the dimensions $0.3 \times 0.3 \times 1.0 \text{ m}$. The hydrofoil is placed at the center of the test section and defined by the NACA 0009 profile with chord length 0.15 m . The profile is twisted relative to midspan plane to obtain a varying angle of attack from -1° at the sidewalls to $+10^\circ$ at midspan. Therefore, the interaction of the cavitation pattern with the sidewalls of the test section is avoidable for a certain range of operating conditions [24]. Furthermore, this setup and other comparable geometries are experimentally investigated in detail by Foeth [32] and Foeth et al. [33], where it is demonstrated that the described hydrofoil is suitable to study well defined and repeatable shedding structures.

The experimentally observed flow field is symmetric with respect to the midspan up to small scale fluctuations. This motivates **first a symmetric numerical treatment** of the test section in order to reduce the computational effort. Therefore, only **half** of the depicted flow domain is simulated here. Then in the subsequent section, the **full wing calculation** and the **asymmetric behavior** of the cavitation dynamics will be shown.

Numerical Simulation

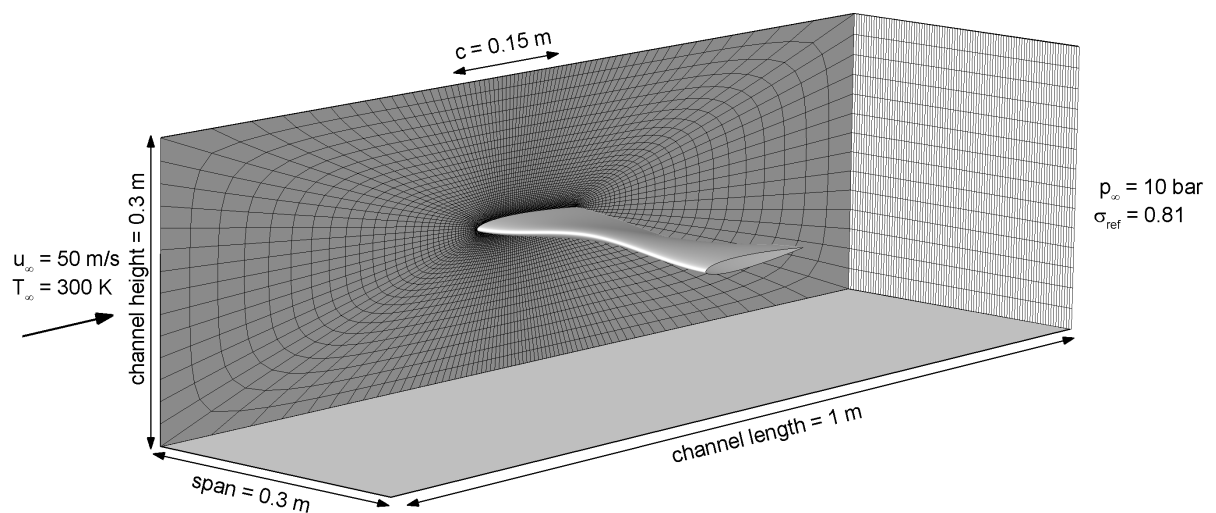


Figure 5.39: 3-D twisted NACA 0009 hydrofoil - computational domain and boundary conditions. Chord length $c = 0.15 \text{ m}$, span $s = 0.3 \text{ m}$, angle of attack -1° (walls) and $+10^\circ$ (midspan), channel height 0.3 m , channel length 1 m . Water inflow from left to right, inlet conditions $u_\infty = 50 \text{ m/s}$, $T_\infty = 300 \text{ K}$, outlet condition $p_\infty = 10 \text{ bar}$, reference cavitation number $\sigma_{ref} = 0.81$. Grid: $3 \cdot 10^5$ hexahedrons.

The computational mesh consists of 300000 hexahedrons, the spatial resolution is refined close to the surface of the hydrofoil. Thereby we obtain cell lengths of $1\text{ mm} \leq l_J \leq 5\text{ mm}$ of those computational cells, where two-phase flow is supposed to occur. Experimental investigations show that the maximum radius of the vapor bubbles for the considered cloud cavitation pattern is of the order of 1 mm . Therefore, the applied spatial resolution describes the behavior of the vapor clouds.

At the inlet domain pure liquid water flows with a velocity of $u_\infty = 50\text{ m/s}$ and a temperature of $T_\infty = 300\text{ K}$. At the outlet plane the reference static pressure is prescribed as $p_\infty = 10\text{ bar}$. Therefore, according to Eq. 1.9, the reference cavitation number σ_{ref} is found as $\sigma_{ref} = 0.81$. It should be remembered that both inlet and outlet boundaries are described by mixed reflecting and non-reflecting boundary conditions and hence the prescribed values are asymptotically reached in the course of the simulation. The flow conditions and the mesh resolution require a numerical time step of $\Delta t_{CFD} = 4.5 \cdot 10^{-8}\text{ s}$. The initialization of the domain is achieved by a steady state solution of the single-phase pure water simulation by applying the same boundary conditions as for the two-phase simulation. This methodology is plausible since it has been observed in the test calculations that different initializations of the domain give matching results. The time history of the integrated vapor volume V_{vap} of the whole calculation is given in Fig. 5.40.

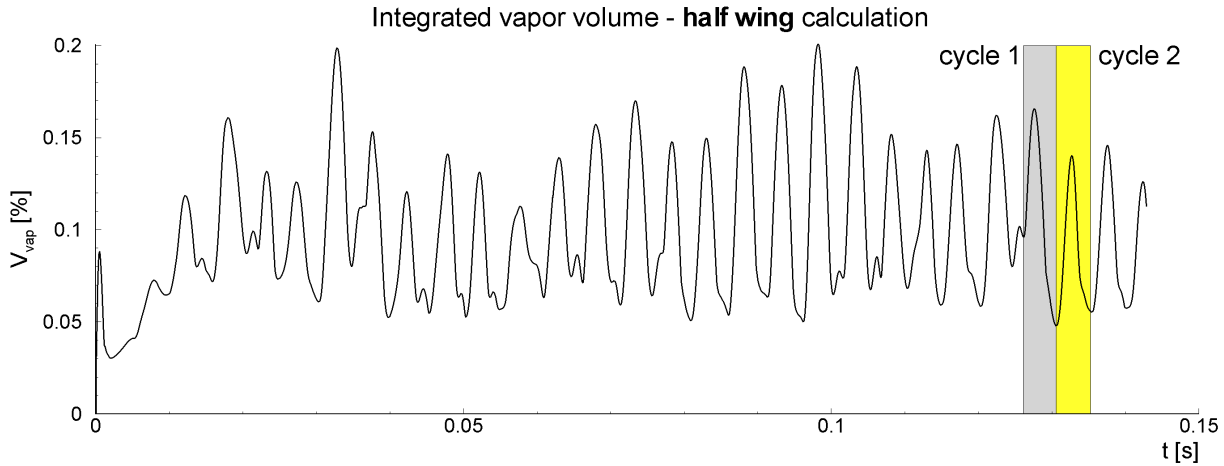


Figure 5.40: Time history of the integrated vapor volume V_{vap} [% total volume of the computational domain]. **Half wing** calculation. Investigated cycles 1 and 2 are highlighted. NACA 0009 hydrofoil, -1° (walls) and $+10^\circ$ (midspan), $u_\infty = 50\text{ m/s}$, $T_\infty = 300\text{ K}$, $p_\infty = 10\text{ bar}$, $\sigma_{ref} = 0.81$, $\Delta t_{CFD} = 4.5 \cdot 10^{-8}\text{ s}$, second order in space and in time.

Figure 5.41 depicts the integrated vapor volume V_{vap} for the last calculated 9 periods. In total, more than twenty shedding cycles are calculated in a real time interval of 0.15 s as shown in the previous figure. The fast Fourier transform of the whole calculation gives an average frequency of $\bar{f} \approx 220\text{ Hz}$, this value is constant up to 5%. The investigated cycles 1 and 2 are highlighted in the figure.

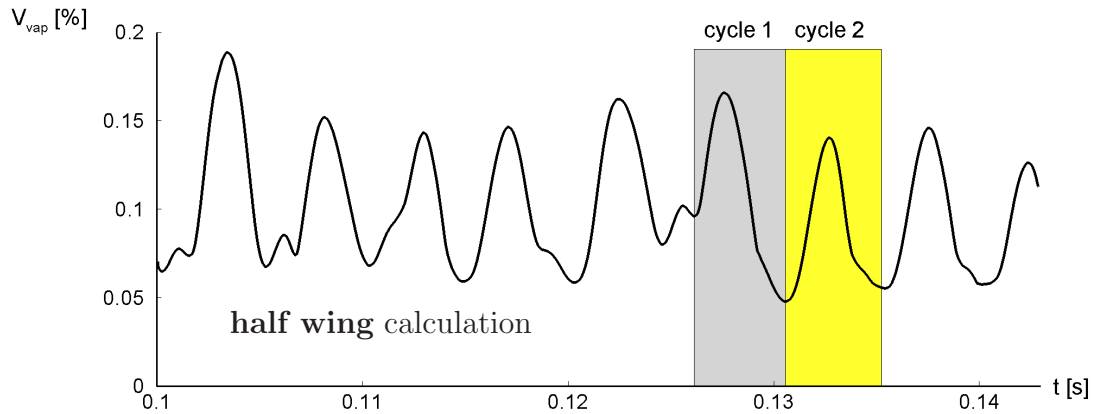


Figure 5.41: Time history of the integrated vapor volume V_{vap} [% total volume of the computational domain]. **Half wing** calculation. Investigated cycles 1 and 2 are highlighted. NACA 0009 hydrofoil, -1° (walls) and $+10^\circ$ (midspan), $u_\infty = 50 \text{ m/s}$, $T_\infty = 300 \text{ K}$, $p_\infty = 10 \text{ bar}$, $\sigma_{ref} = 0.81$, $\Delta t_{CFD} = 4.5 \cdot 10^{-8} \text{ s}$, grid: $3 \cdot 10^5$ hexahedrons, second order in space and in time.

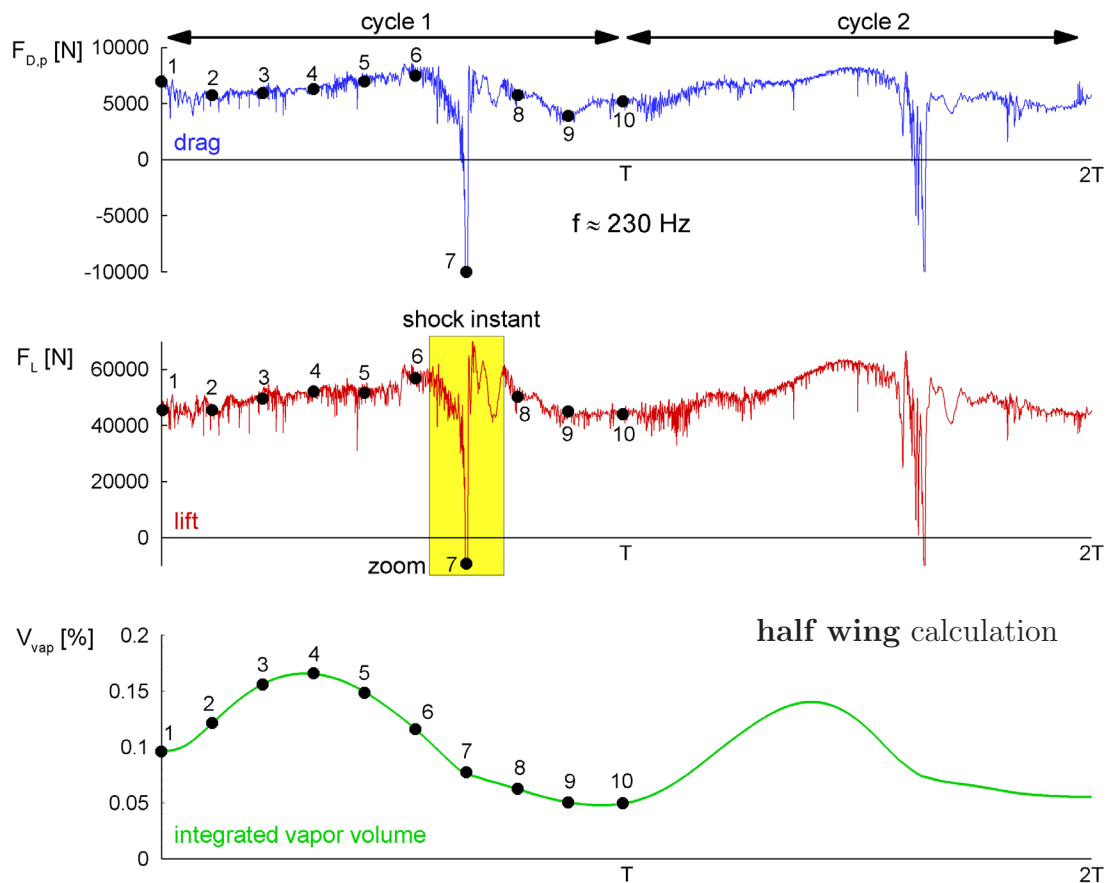


Figure 5.42: Time history of drag force $F_{D,p}$ [N], lift force F_L [N] and integrated vapor volume V_{vap} , $f_{cycle} \approx 230 \text{ Hz}$. **Half wing** calculation. The black dots numbered 1-10 correspond to the 10 instances in time presented in Fig. 5.43. NACA 0009 hydrofoil, -1° (walls) and $+10^\circ$ (midspan), $u_\infty = 50 \text{ m/s}$, $T_\infty = 300 \text{ K}$, $p_\infty = 10 \text{ bar}$, $\sigma_{ref} = 0.81$, $\Delta t_{CFD} = 4.5 \cdot 10^{-8} \text{ s}$, grid: $3 \cdot 10^5$ hexahedrons, second order in space and in time.

The dynamic behavior of the shedding mechanism results in strongly time dependent lift and drag variations. Figure 5.42 depicts the time history of drag force $F_{D,p}$, lift force F_L and integrated vapor volume V_{vap} of cycle 1 and of the subsequent cycle 2. Both forces exhibit significant peaks including highly negative values subsequent to the collapse corresponding to time instant 7. The shedding mechanism of cycle 1 is analyzed in Figs. 5.43 and 5.44 at ten representative instants in time within the time interval $\Delta t_{1-10} = 4.416 \cdot 10^{-3} s$. The pictures in Fig. 5.43 depict perspective views of the hydrofoil together with iso-surfaces of the void fraction composed of all cells with $\alpha_{min} = 0.05$.

At the first instant in time the formation of an attached sheet cavity close to the leading edge of the hydrofoil is observed. Slightly upstream of the trailing edge a horseshoe shaped detached cloud is visible. The vertical elongation of this cloud is of the order of 50% of the chord length. At the second instant in time the previously attached sheet separates from the hydrofoil due to the onset of reverse flow between the cavity and the surface of the hydrofoil. At the leading edge of the hydrofoil the reformation of the attached sheet cavity takes place. Furthermore, the cloud located close to the trailing edge recondenses. The third instant is similar to the second one, where the sheet cavity at the leading edge grows and the detached cloud convects to the downstream. The cloud cavity over the trailing edge grows again in this instant due to the expansion caused by the previous recondensation. In the pictures corresponding to the fourth and fifth instants in time the attached sheet cavity at the leading edge reaches its maximum length and the detached cloud is still connected to the sheet. Here the re-entry jet below the cloud is no longer formed by pure reverse flow but includes a significant spanwise velocity component, i.e. a side re-entrant jet [32], [33], [61], [62]. The collision of the re-entrant flow with the side entrant jets below the vapor cloud causes the cloud to separate completely from the suction side of the hydrofoil. Thereby, the formation of vortices takes place that superimpose on to the main flow and accelerate the cloud downstream. This behavior is observed within various experimental setups and analyzed in detail [92], [32], [67].

Between the time instants five and seven the cloud undergoes a strong compression that is initiated by the surrounding pressure field, where it shrinks in size and convects through the downstream (picture 6). Picture 7 of Fig. 5.43 shows the vapor cloud just before its final collapse occurs. Moreover, two secondary instabilities located at the closure of the triangularly shaped sheet cavity indicate vortex structures due to side entrant flow.

At the last instants in time (pictures 8 and 9) a series of small scale vapor structures close to the trailing edge are observed. One of them is located nearly at the same position as the previously collapsed cloud. Indeed, this structure forms due to the post-expansion corresponding to the collapse induced shock. Cycle 1 ends with time instant ten, where the attached sheet cavity close to the leading edge starts to develop again and the detached cloud above the trailing edge, which is seen in time instant one, begins to grow behind the sheet cavity.

half wing calculation

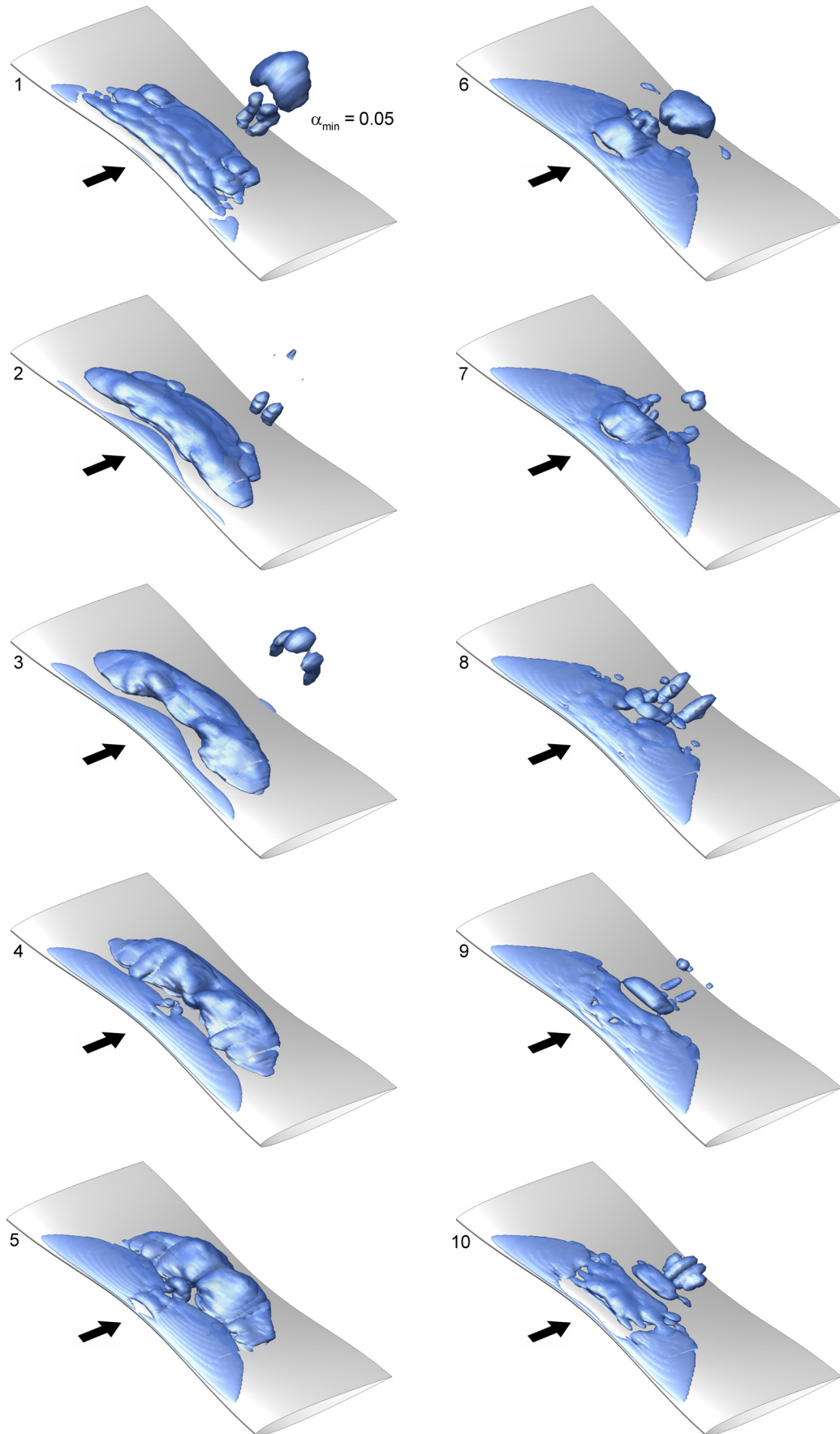


Figure 5.43: Unsteady shedding mechanism, cavitation cycle 1, $f \approx 230 \text{ Hz}$, $\Delta t_{1-10} = 4.416 \cdot 10^{-3} \text{ s}$. NACA 0009 hydrofoil, -1° (walls) and $+10^\circ$ (midspan), $u_\infty = 50 \text{ m/s}$, $T_\infty = 300 \text{ K}$, $p_\infty = 10 \text{ bar}$, $\sigma_{ref} = 0.81$, $\Delta t_{CFD} = 4.5 \cdot 10^{-8} \text{ s}$, second order in space and in time.

half wing calculation

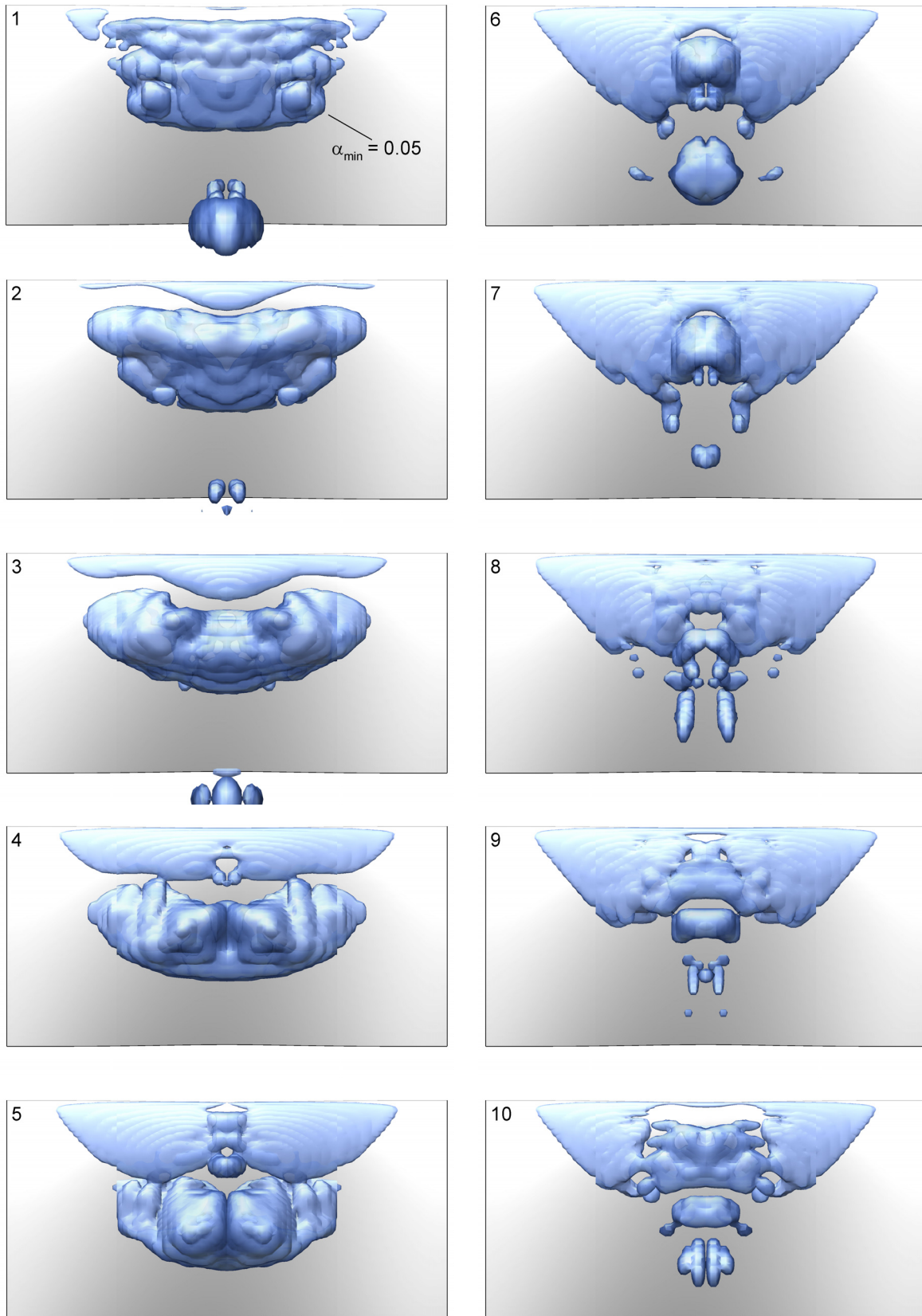


Figure 5.44: Unsteady shedding mechanism, cavitation cycle 1, top view, $f \approx 230 \text{ Hz}$, $\Delta t_{1-10} = 4.416 \cdot 10^{-3} \text{ s}$. NACA 0009 hydrofoil, -1° (walls) and $+10^\circ$ (midspan), $u_\infty = 50 \text{ m/s}$, $T_\infty = 300 \text{ K}$, $p_\infty = 10 \text{ bar}$, $\sigma_{ref} = 0.81$, $\Delta t_{CFD} = 4.5 \cdot 10^{-8} \text{ s}$, grid: $3 \cdot 10^5$ hexahedrons, second order in space and in time.

The lift and drag force curves given in Fig. 5.42 require further attention. Both forces exhibit significant peaks including highly negative values subsequent to the collapse corresponding to time instant 7 in Figs. 5.42 and 5.43. Here, the small vapor cloud located above the trailing edge of the hydrofoil collapses violently and the resulting 3-D shock front propagates through the domain. The zoom area of Fig. 5.42 is enlarged in Fig. 5.45, which corresponds to a time interval of $\Delta t = 7.5 \cdot 10^{-4} s$.

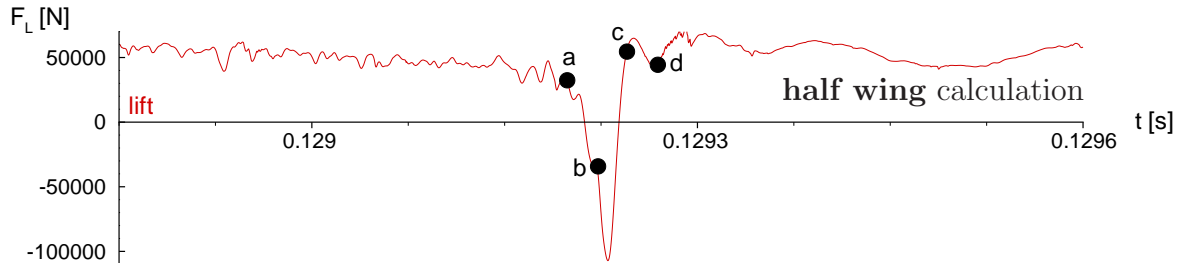


Figure 5.45: Lift force $F_L [N]$ corresponding to zoom area of Fig. 5.42 showing instantaneous 3-D shock formation emerging after cloud collapse at the trailing edge. **Half wing** calculation. The black dots named *a-d* correspond to the 4 instances in time presented in Fig. 5.46. NACA 0009 hydrofoil, -1° (walls) and $+10^\circ$ (midspan), $u_\infty = 50 m/s$, $T_\infty = 300 K$, $p_\infty = 10 bar$, $\sigma_{ref} = 0.81$, $\Delta t_{CFD} = 4.5 \cdot 10^{-8} s$, second order in space and in time.

The black dots named *a-d* correspond to the 4 instances in time presented in Fig. 5.46, where $\Delta t_{a-d} = 7.05 \cdot 10^{-5} s$. This picture series presents the evolution of the collapse and the subsequent shock propagation in detail by using the static pressure contours at the midspan plane as well as at the surface of the hydrofoil. In time instants *a* and *b* the small vapor cloud located above the trailing edge shrinks as a result of the surrounding pressure field. Time instant *b* corresponds exactly to point 7 of the previous picture series. The collapse takes place just after time instant *b* as suggested by the sudden drop in the lift curve and picture *c* shows the flow domain subsequent to the collapse. The maximum pressure behind the shock reaches 230 bar. This leads to an instantaneous maximum pressure of 105 bar on the surface of the hydrofoil, directly after the shock impinges on the suction side, which is depicted by the negative peak in the lift curve between the time instants *b* and the *c*. In the process strongly decreasing lift and drag forces are observed for a time interval of $14 \cdot 10^{-6} s$.

Picture *d* illustrates more interesting gas dynamic details of the interaction of a shock with two-phase boundaries enclosing constant pressure regimes. As the vapor regions have much less acoustic impedance than that of the liquid, a portion of the shock reflects from those regions as rarefaction waves and the remaining portion propagates around two-phase regions.

The shock intensity and the propagation dynamics of the waves are driven by the inertia effects and viscosity plays a minor role. The inclusion of viscous effects in the simulation would cause no significant differences on the lift and the drag curves depicted earlier.

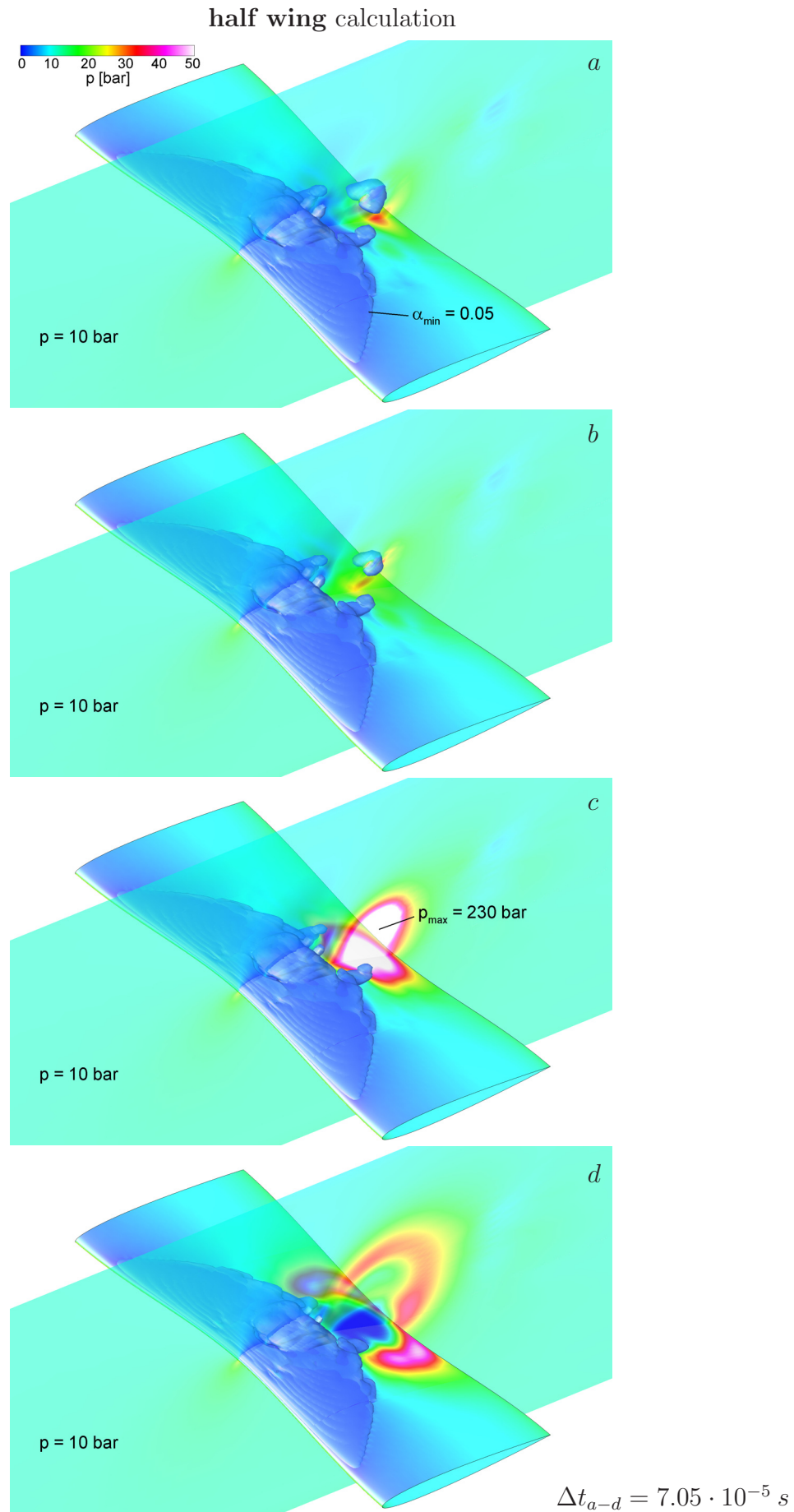


Figure 5.46: Instantaneous 3-D shock front emerging after cloud collapse at the trailing edge. **Half wing** calculation. NACA 0009 hydrofoil, -1° (walls) and $+10^\circ$ (midspan), $u_\infty = 50 \text{ m/s}$, $T_\infty = 300 \text{ K}$, $p_\infty = 10 \text{ bar}$, $\sigma_{ref} = 0.81$, $\Delta t_{CFD} = 4.5 \cdot 10^{-8} \text{ s}$, second order in space and in time.

Experimental Comparison

As mentioned earlier Foeth has performed various twisted wing experiments and visualized the resulting unsteady cavity structures and shedding behavior through PIV methods [32]. In the experiments, he used different hydrofoil profiles with different twist angles. The calculations presented in this subsection correspond to a 3-D NACA 0009 hydrofoil with a total twist angle of 11° , where the angle of attack is -1° at the walls and $+10^\circ$ at midspan.

In his Ph.D. thesis, Foeth used this geometrical setup and analyzed experimentally with different flow conditions. The experiments were performed with an inlet velocity of $u_\infty = 7 \text{ m/s}$ and a reference cavitation number of $\sigma_{ref} = 0.81$. Whereas in the calculations a higher inlet velocity ($u_\infty = 50 \text{ m/s}$) is chosen in order to accelerate the numerical solution. But to achieve a comparable flow, outlet pressure is adjusted so that ($p_\infty = 10 \text{ bar}$) the same reference cavitation number $\sigma_{ref} = 0.81$ is obtained. Therefore, in the calculation similarity with respect to the geometry and the cavitation number is achieved.

On the next page a series of three instants in time depicts visualizations from the experiment of Foeth [32] and the corresponding numerical simulation. The numerical visualizations of these three instants in time belong to cavitation cycle 1 (pictures 2, 5 and 6) shown in Figs. 5.43 and 5.44. Figure 5.47 is the integrated vapor volume curve of cycle 1 with the corresponding points of the discussed time instants.

The comparison of the global flow structure as well as of fine details such as the secondary instabilities leads to the conclusion that numerical simulation reproduces the experimental observations accurately. Moreover, the shedding frequency and the resulting Strouhal number are comparable to the experimental values. The numerically predicted Strouhal number is $St_{calc} \approx 0.27$ (based on the cavity length, which is about 40% of the chord length). From the experimentally visualized shedding cycle a Strouhal number of $St_{exp} \approx 0.22$ is estimated. It should be noted that the exact visualization of the maximum length of the attached cavity might incorporate some uncertainty.

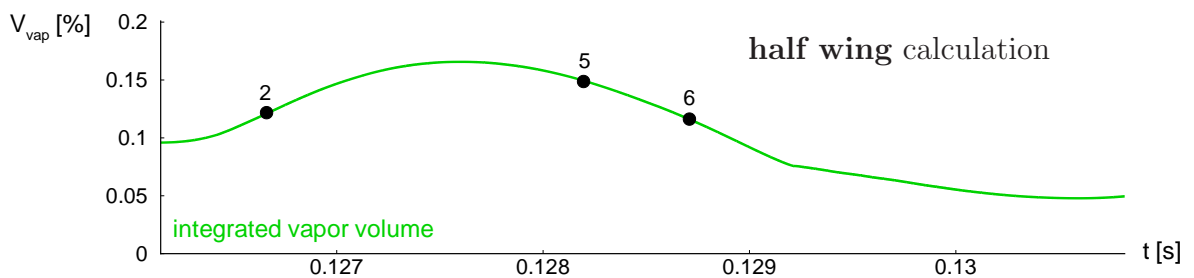


Figure 5.47: The black dots marked as 2,5 and 6 correspond to the 3 instances in time presented in Fig. 5.48. **Half wing** calculation. NACA 0009 hydrofoil, -1° (walls) and $+10^\circ$ (midspan), $u_\infty = 50 \text{ m/s}$, $T_\infty = 300 \text{ K}$, $p_\infty = 10 \text{ bar}$, $\sigma_{ref} = 0.81$, $\Delta t_{CFD} = 4.5 \cdot 10^{-8} \text{ s}$, grid: $3 \cdot 10^5$ hexahedrons, second order in space and in time.

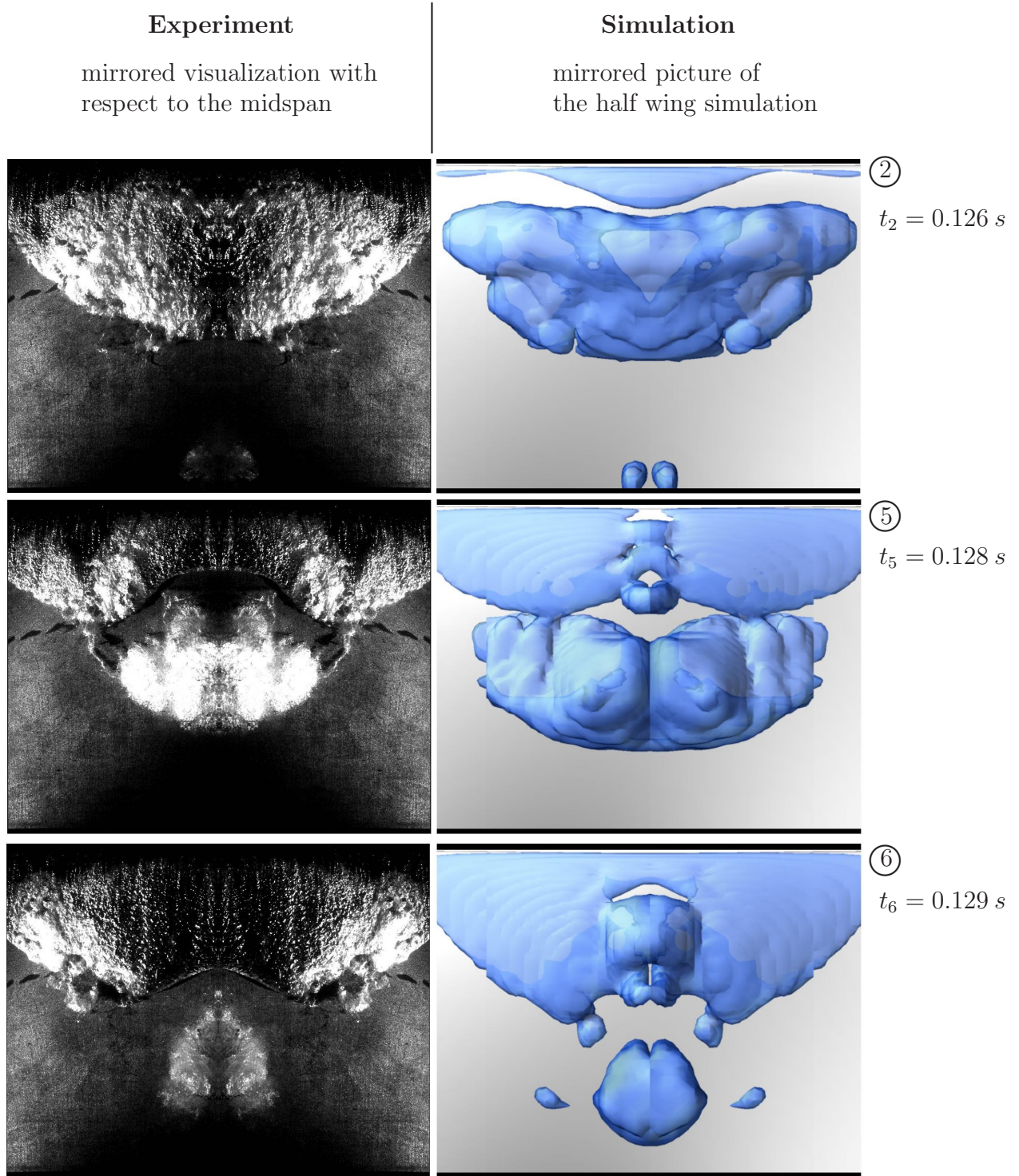


Figure 5.48: 3-D twisted NACA 0009 hydrofoil, experimental results from Foeth [32] (left), numerical calculation (right). Iso surfaces of void fraction with $\alpha_{min} = 0.05$ at 3 instances from cavitation cycle 1 (right). Angle of attack -1° (walls) and $+10^\circ$ (midspan). Experiment: $u_\infty = 7 \text{ m/s}$, $\sigma_{ref} = 0.81$, $St_{exp} \approx 0.22$. **CATUM** simulation: $u_\infty = 50 \text{ m/s}$, $T_\infty = 300 \text{ K}$, $p_\infty = 10 \text{ bar}$, $\sigma_{ref} = 0.81$, $St_{calc} \approx 0.27$, $\Delta t_{CFD} = 4.5 \cdot 10^{-8} \text{ s}$, grid: $3 \cdot 10^5$ hexahedrons, second order in space and in time.

5.2.3 3-D NACA 0009 Twisted Wing - Full Wing Calculation

Although it is experimentally confirmed and shown by Foeth [32] that the investigated twisted wing geometry experiences symmetrical cavitation dynamics at large scales with respect to the midspan, small scale structures, especially at the closure regions of the cavities exhibit asymmetric behavior as discussed in the same work.

This subsection presents the results from the **full wing calculation** of the 3-D twisted wing geometry introduced in the previous subsection. The same computational domain given by Fig. 5.39 is used in the calculation, but this time full wing is simulated by using $6 \cdot 10^5$ hexahedrons. To ensure that the symmetry breakup is purely a physical phenomenon, a **perfectly symmetrical mesh** is generated with respect to the midspan. For that purpose, the computational mesh used in the previous section is

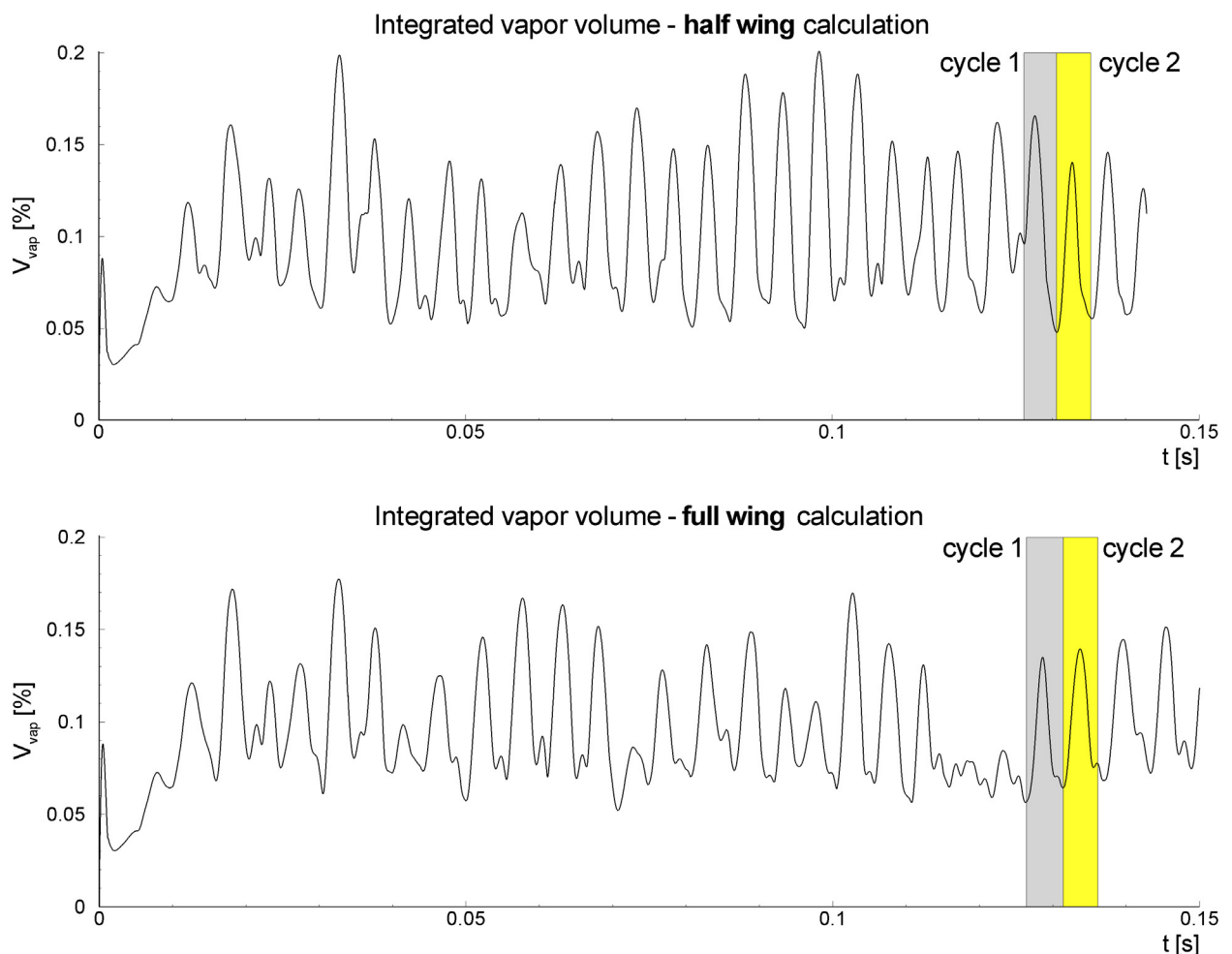


Figure 5.49: Time history of the integrated vapor volume V_{vap} [% total volume of the computational domain]. Comparison of **half wing calculation** ($3 \cdot 10^5$ hexahedrons, top) with **full wing calculation** ($6 \cdot 10^5$ hexahedrons, bottom). Investigated cycles 1 and 2 are highlighted. NACA 0009 hydrofoil, -1° (walls) and $+10^\circ$ (midspan), $u_\infty = 50$ m/s, $T_\infty = 300$ K, $p_\infty = 10$ bar, $\sigma_{ref} = 0.81$, $\Delta t_{CFD} = 4.5 \cdot 10^{-8}$ s, second order in space and in time.

mirrored with respect to the symmetry axis by using our in-house mesh generation tool. Moreover, in order to achieve a one-to-one comparison with the previous half wing calculation, exactly the same initialization and flow conditions are applied in the simulation. At the inlet domain pure liquid water flows with a velocity of $u_\infty = 50 \text{ m/s}$ and a temperature of $T_\infty = 300 \text{ K}$. At the outlet plane the reference static pressure is prescribed as $p_\infty = 10 \text{ bar}$, which results in a reference cavitation number $\sigma_{ref} = 0.81$. As before, the initialization of the domain is achieved by a steady state solution of the single-phase pure water simulation by applying the same boundary conditions as for the two-phase simulation. Figure 5.49 shows the time history of the integrated vapor volume both for the half and full wing cases for the complete calculation. It can be seen from the figure that the frequency and the amplitude of the cavitation dynamics are comparable in both calculations, as are the investigated cycles.

The following figure depicts the integrated vapor volume V_{vap} of the half and full wing calculations zoomed around the investigated cavitation cycles 1 and 2. The fast Fourier transform of the whole calculation gives an average frequency of $\bar{f} \approx 205 \text{ Hz}$ for the full wing calculation, this value is constant up to 5%.

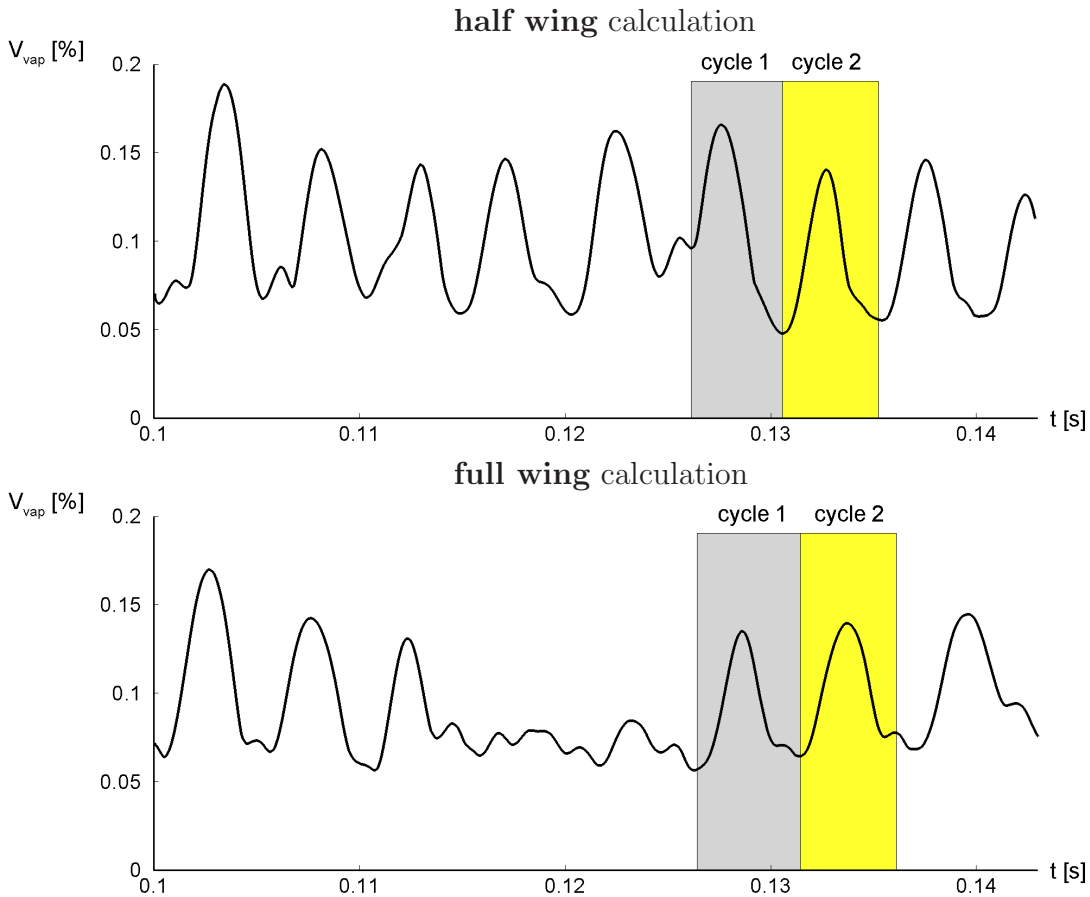


Figure 5.50: Close-up view, time history of the integrated vapor volume V_{vap} [% total volume of the computational domain]. Comparison of **half wing calculation** (top) with **full wing calculation** (bottom). Investigated cycles 1 and 2 are highlighted. NACA 0009 hydrofoil, -1° (walls) and $+10^\circ$ (midspan), $u_\infty = 50 \text{ m/s}$, $T_\infty = 300 \text{ K}$, $p_\infty = 10 \text{ bar}$, $\sigma_{ref} = 0.81$, $\Delta t_{CFD} = 4.5 \cdot 10^{-8} \text{ s}$, grid: $6 \cdot 10^5$ hexahedrons, second order in space and in time.

As before, the dynamic behavior of the shedding mechanism results in strongly time dependent lift and drag variations. Figure 5.51 depicts the time history of the drag force $F_{D,p}$, the lift force F_L and the integrated vapor volume V_{vap} of the cycle 1 and of the subsequent cycle 2. The shedding mechanism of cycle 1 is analyzed in Figs. 5.52 and 5.53 at ten representative instants in time within the time interval $\Delta t_{1-10} = 4.995 \cdot 10^{-3} s$. The pictures in Fig. 5.52 depict perspective views of the hydrofoil together with iso-surfaces of the void fraction composed of all cells with $\alpha_{min} = 0.05$. Whereas Fig. 5.53 shows the same sequence as seen from above.

One can immediately recognize the asymmetry of the cavitation cloud by examining Figs. 5.52 and 5.53. At the first instant in time an attached sheet cavity at the leading edge of the hydrofoil is observed. Although the shape of the cavity is asymmetric, it resembles the triangular structure as seen in the half wing calculation. Above the trailing edge a small vapor cloud is visible, but only on one half of the hydrofoil. At the second instant in time the sheet cavity and the small vapor cloud convect further downstream. The third instant is similar to the second instant of the previous half wing calculation (picture 2 of Figs. 5.43 and 5.44), where the attached sheet cavity separates from the hydrofoil due to the onset of reverse flow between the cavity and

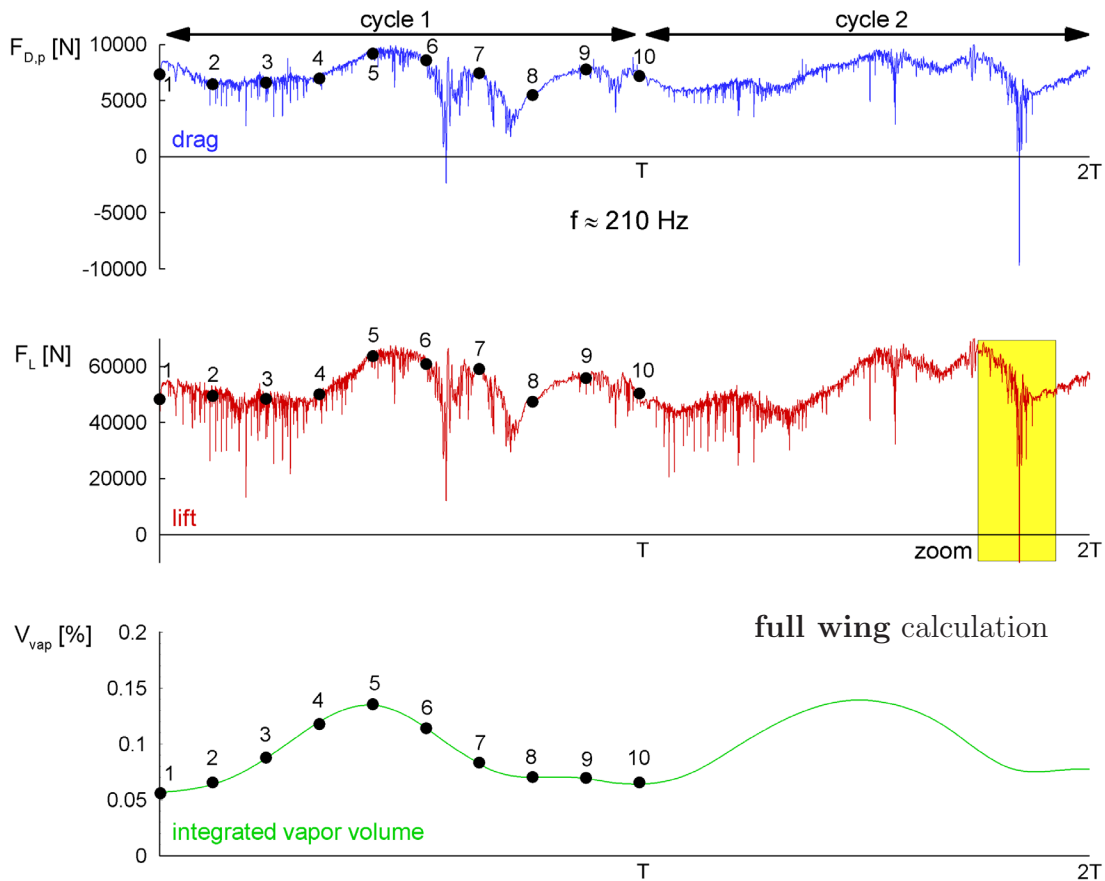


Figure 5.51: Time history of drag force $F_{D,p}$ [N], lift force F_L [N] and integrated vapor volume V_{vap} , $f_{cycle} \approx 210 Hz$. **Full wing** calculation. The black dots numbered 1-10 correspond to the 10 instances in time presented in Figs. 5.52 and 5.53. NACA 0009 hydrofoil, -1° (walls) and $+10^\circ$ (midspan), $u_\infty = 50 m/s$, $T_\infty = 300 K$, $p_\infty = 10 bar$, $\sigma_{ref} = 0.81$, $\Delta t_{CFD} = 4.5 \cdot 10^{-8} s$, grid: $6 \cdot 10^5$ hexahedrons, second order in space and in time.

the surface. At the leading edge of the hydrofoil an attached sheet cavity starts to reform. In addition to that, the cloud over the trailing edge recondenses and is no longer present. During the fourth and fifth instants the sheet cavity at the leading edge grows further and the detached cloud convects to the downstream. As discussed in the previous subsection, re-entry jet below the cloud includes significant spanwise velocity components (side re-entrant jet). The collision of the re-entrant flow with the side entrant jets below the cloud causes the cloud to separate completely from the suction side of the hydrofoil (time instant 6). This time due to the asymmetry of the flow dynamics, side entrant jets have different velocities. Therefore the cloud structure is completely asymmetric, being larger on the right hand side of the hydrofoil. At time instants 7 and 8 the cloud undergoes a strong compression that is initiated by the surrounding pressure field, so it shrinks in size and convects downstream (picture 8). Meanwhile, the attached sheet cavity at the leading edge reaches its maximum length. Picture 9 of Figs. 5.52 and 5.53 shows the vapor cloud just before its final collapse. Moreover, as before, secondary instabilities located at the closure of the triangularly shaped sheet cavity indicate vortex structures due to side entrant flow. Cycle 1 ends with time instant 10, where the attached sheet cavity at the leading edge has the same structure as time instant one.

full wing calculation

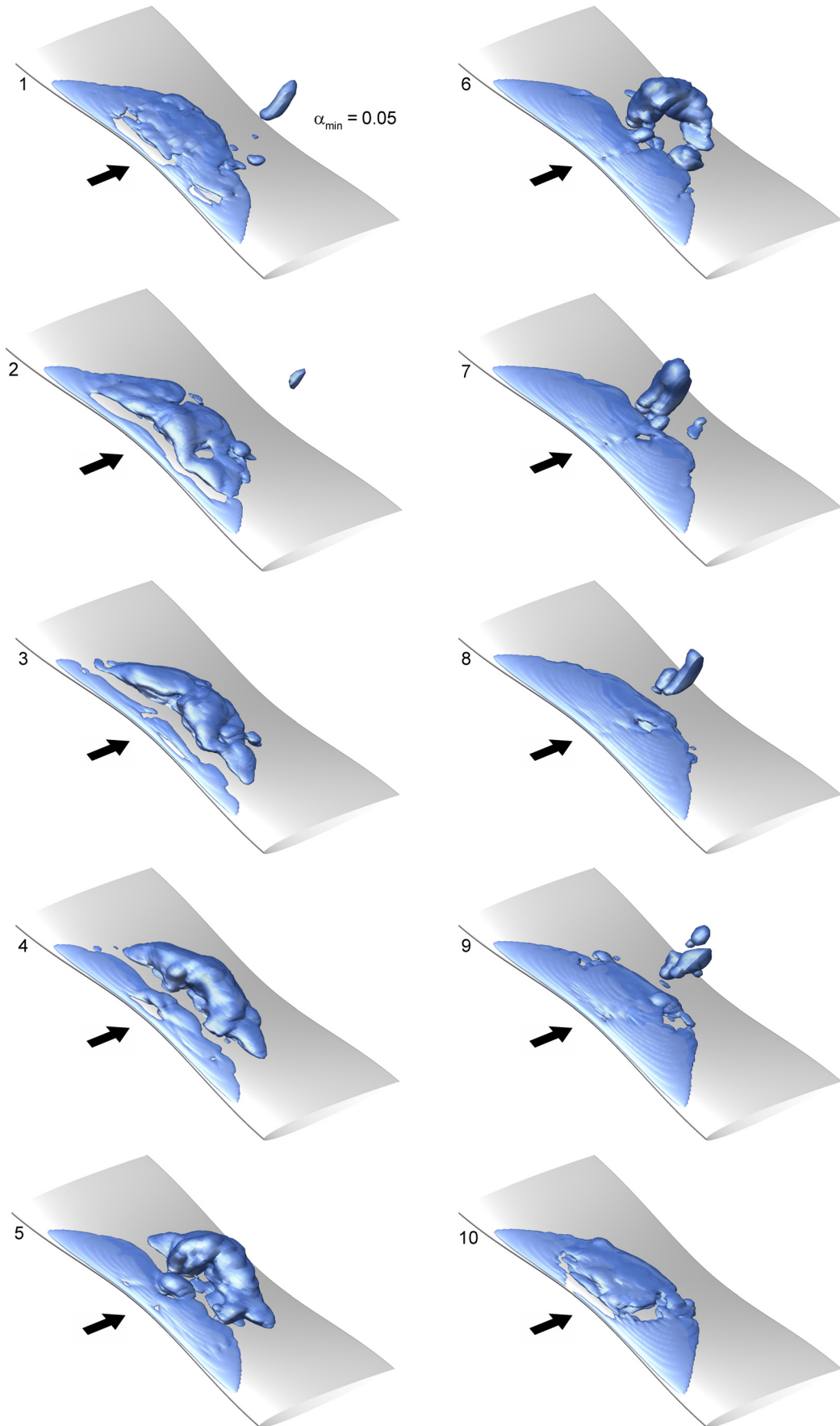


Figure 5.52: Unsteady shedding mechanism, cavitation cycle 1, $f \approx 210 \text{ Hz}$, $\Delta t_{1-10} = 4.995 \cdot 10^{-3} \text{ s}$. NACA 0009 hydrofoil, -1° (walls) and $+10^\circ$ (midspan), $u_\infty = 50 \text{ m/s}$, $T_\infty = 300 \text{ K}$, $p_\infty = 10 \text{ bar}$, $\sigma_{ref} = 0.81$, $\Delta t_{CFD} = 4.5 \cdot 10^{-8} \text{ s}$, second order in space and in time.

full wing calculation

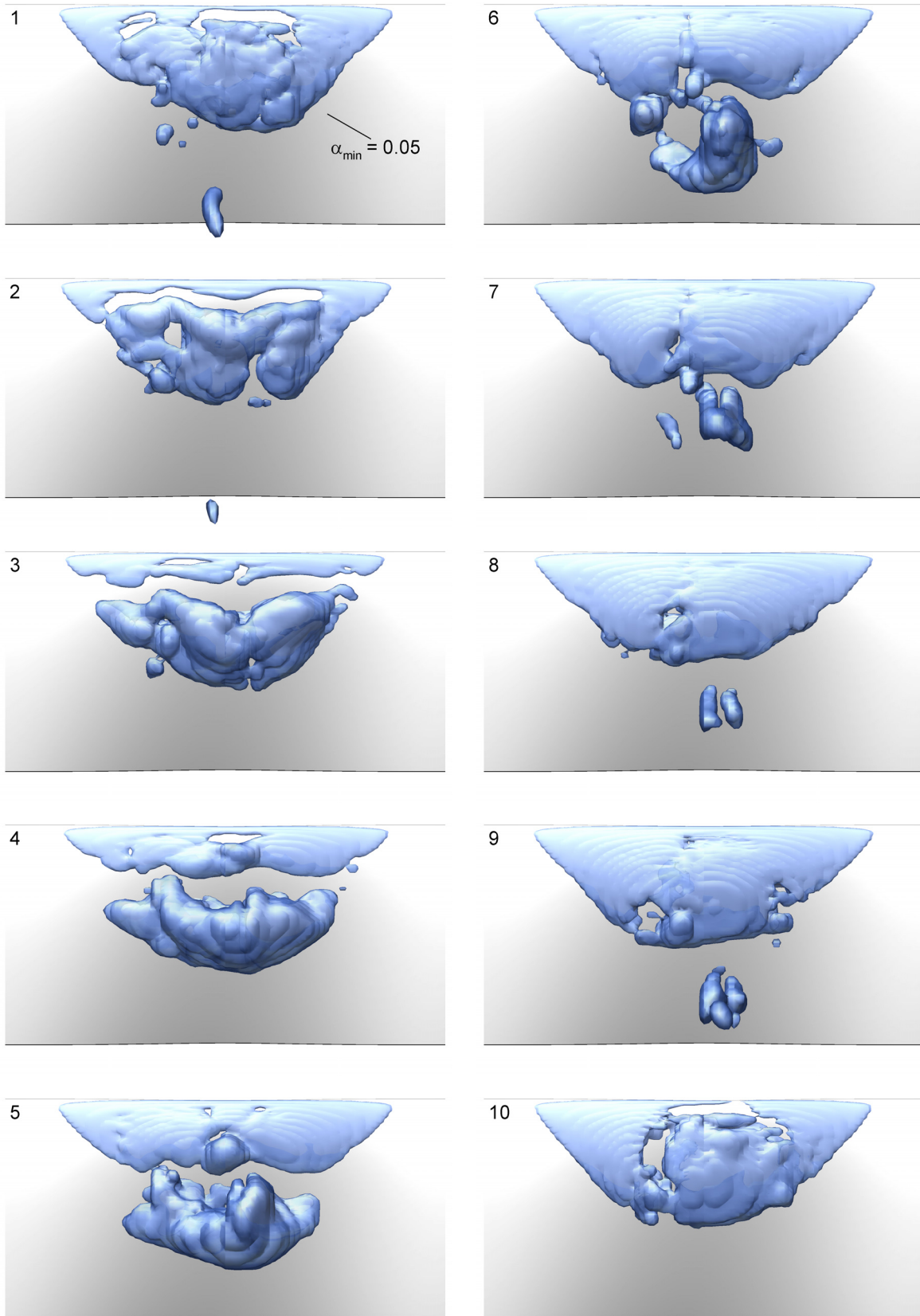


Figure 5.53: Unsteady shedding mechanism, cavitation cycle 1, top view, $f \approx 210 \text{ Hz}$, $\Delta t_{1-10} = 4.995 \cdot 10^{-3} \text{ s}$. NACA 0009 hydrofoil, -1° (walls) and $+10^\circ$ (midspan), $u_\infty = 50 \text{ m/s}$, $T_\infty = 300 \text{ K}$, $p_\infty = 10 \text{ bar}$, $\sigma_{ref} = 0.81$, $\Delta t_{CFD} = 4.5 \cdot 10^{-8} \text{ s}$, grid: $6 \cdot 10^5$ hexahedrons, second order in space and in time.

As before, the lift and drag force curves given in Fig. 5.51 exhibit significant peaks including negative values subsequent to collapses. The zoom area of Fig. 5.51 is enlarged in Fig. 5.54, which corresponds to a time interval of $\Delta t = 8.1 \cdot 10^{-4} s$. Here, a small vapor cloud located above the midspan of the hydrofoil and another vapor cloud just standing on the surface collapse and result in 3-D shock fronts that propagate through the domain.

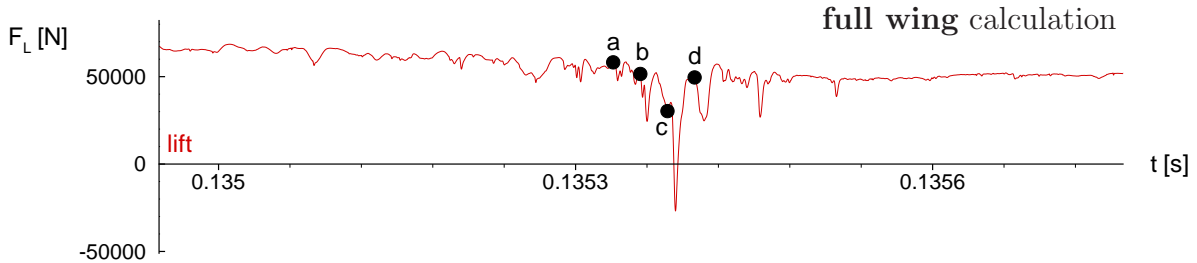


Figure 5.54: Lift force $F_L [N]$ corresponding to zoom area of Fig. 5.50 showing instantaneous 3-D shock formation emerging after cloud collapse near the trailing edge. **Full wing** calculation. The black dots named *a-d* correspond to the 4 instances in time presented in Fig. 5.55. NACA 0009 hydrofoil, -1° (walls) and $+10^\circ$ (midspan), $u_\infty = 50 m/s$, $T_\infty = 300 K$, $p_\infty = 10 bar$, $\sigma_{ref} = 0.81$, $\Delta t_{CFD} = 4.5 \cdot 10^{-8} s$, grid: $6 \cdot 10^5$ hexahedrons, second order in space and in time.

The black dots named *a-d* correspond to the 4 instances in time presented in Fig. 5.55, where $\Delta t_{a-d} = 6.84 \cdot 10^{-5} s$. This picture series presents the collapse of two vapor structures close to the midspan plane of the hydrofoil. The time instants *a* and *b* show the vapor structures before the collapse. The collapse takes place just after the time instant *b* and picture *c* shows the flow domain subsequent to the collapse. There is a sudden drop in the lift curve between time instants *c* and *d*, which is due to the impingement of the collapse induced shocks on the surface of the hydrofoil. The maximum pressure behind the shock reaches $250 bar$. Whereas, the collapse near the surface results in a maximum pressure of $50 bar$ on the surface of the hydrofoil. Thereby, strongly decreasing lift and drag forces are observed for a time interval of $5 \cdot 10^{-5} s$.

The full wing calculation furthermore allows us to analyze the symmetry break-up process in detail. In order to understand it better, a number of monitor points are prescribed on the hydrofoil surface and the pressure p , the spanwise velocity component w , and the vapor volume fraction α are recorded at each point for the overall calculation. Figure 5.56 depicts these monitor points on the surface of the hydrofoil. Note that three pairs of points are used and the points in each pair are located perfectly symmetric to each other with respect to the midspan. The results from the pair located near the trailing edge (monitor pair 1, Fig. 5.56) will be discussed only, as it is seen that at this location symmetry break-up occurs earlier than all of the other pairs. Figure 5.57 (top) shows the static pressure signals recorded by the right (red lines) and left (blue lines) monitor points. At the bottom, the integrated vapor volume V_{vap} is also given. It is seen from the figure that a very short time after the simulation starts, the recorded values deviate from each other. Therefore, to see the deviation clearly, the first $0.02 s$ of the simulation is zoomed in. The zoomed view (Fig. 5.58) shows that shortly after the second order scheme is switched-on, symmetry is no longer present.

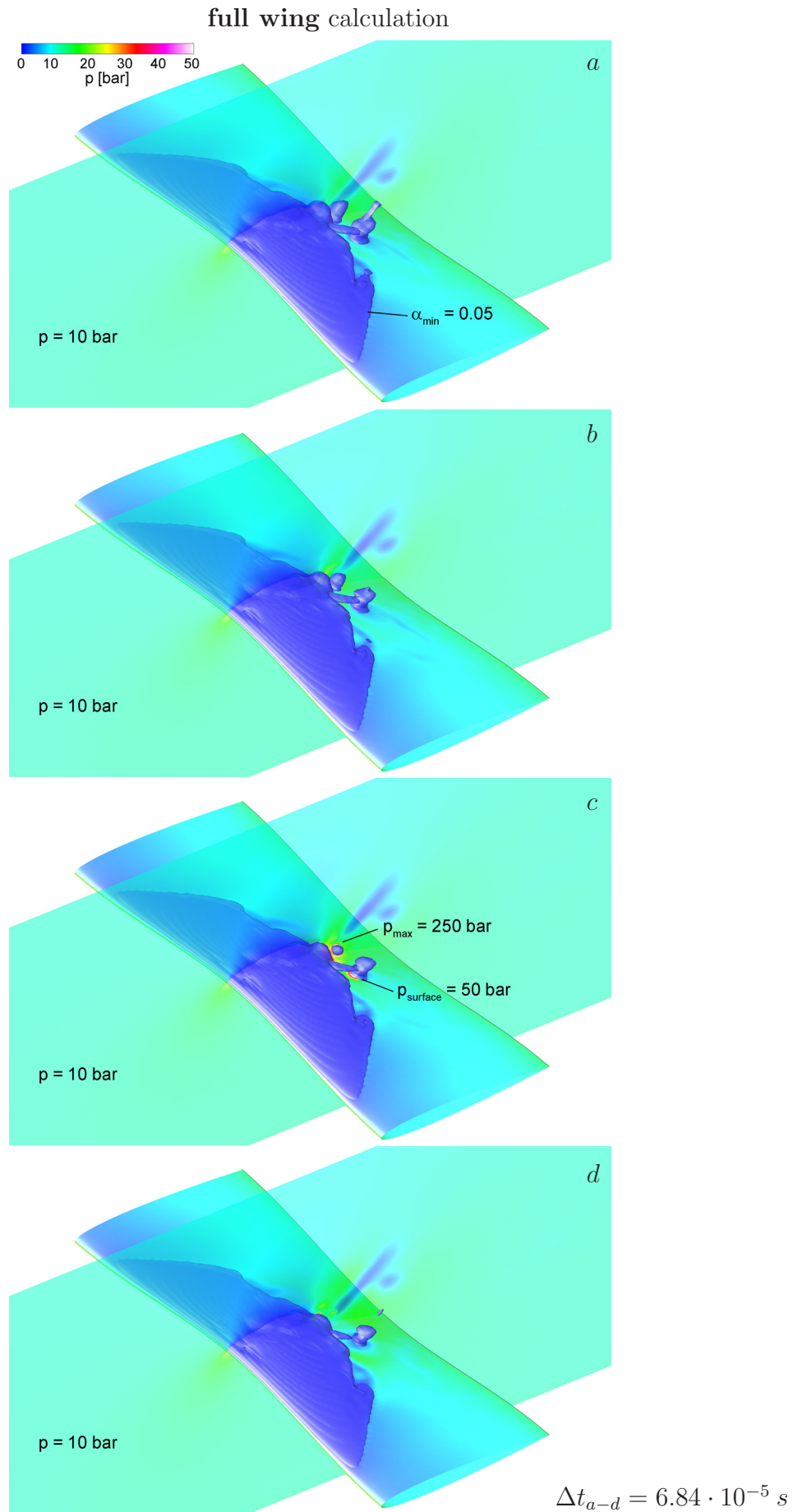


Figure 5.55: Instantaneous shock fronts due to collapses at the midspan. **Full wing** calculation. NACA 0009 hydrofoil, -1° (walls) and $+10^\circ$ (midspan), $u_\infty = 50 \text{ m/s}$, $T_\infty = 300 \text{ K}$, $p_\infty = 10 \text{ bar}$, $\sigma_{ref} = 0.81$, $\Delta t_{CFD} = 4.5 \cdot 10^{-8} \text{ s}$, grid: $6 \cdot 10^5$ hexahedrons, second order in space and in time.

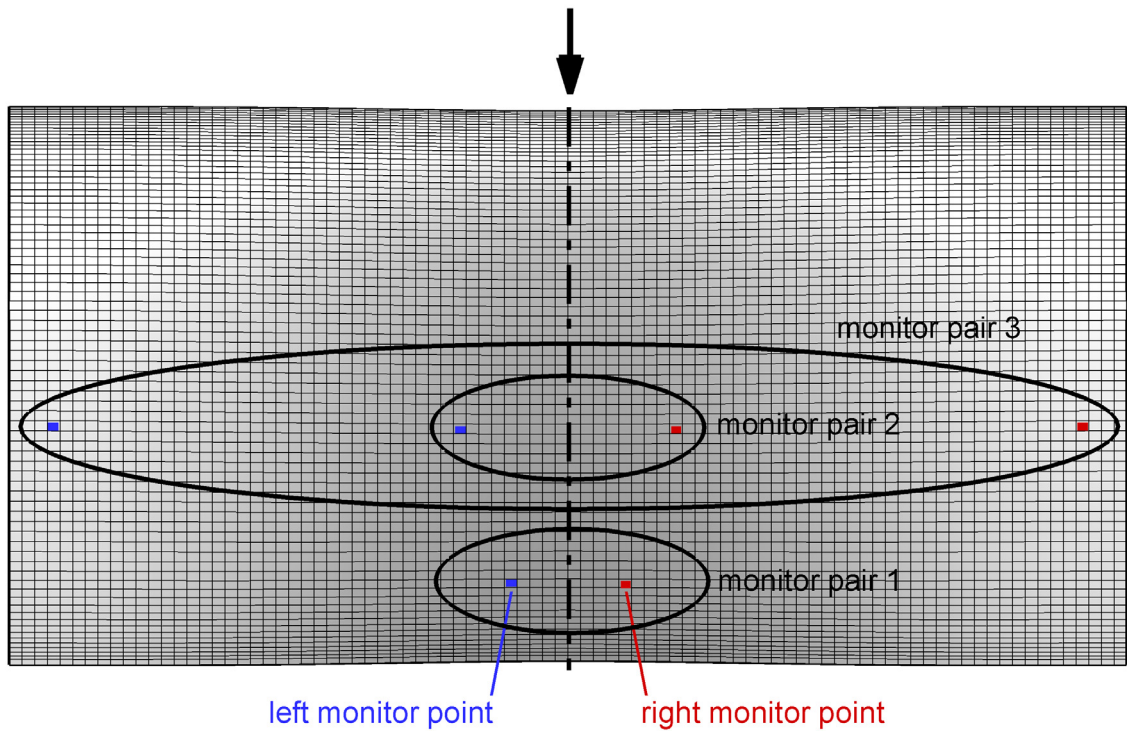


Figure 5.56: Location of the right and left monitor points on the surface of the hydrofoil. **Full wing** calculation. NACA 0009 hydrofoil, -1° (walls) and $+10^\circ$ (midspan), $u_\infty = 50\text{m/s}$, $T_\infty = 300\text{K}$, $p_\infty = 10\text{bar}$, $\sigma_{ref} = 0.81$, $\Delta t_{CFD} = 4.5 \cdot 10^{-8}\text{s}$, grid: $6 \cdot 10^5$ hexahedrons.

A similar analysis is performed for the spanwise velocity component w . Figure 5.59 (top) shows the magnitudes of the spanwise velocity component recorded by the right (red lines) and left (blue lines) monitor points (pair 1). At the bottom, the integrated vapor volume V_{vap} curve is given again for comparison. As before a very short time after the simulation starts, the recorded values deviate from each other. One should here note that, for a perfectly symmetric flow domain spanwise velocity components should have the same magnitude but opposite sign at the symmetric locations. Figure 5.60 (top) depicts the zoomed view of the recorded values. To see the deviation easily, the difference between the left and right values of the spanwise velocity component $\Delta w = w_L - w_R$ is also calculated and plotted in Fig. 5.60 (bottom). As expected, the difference between the left and right values is zero at the beginning of the calculation. After the second order scheme is switched-on, symmetry continues for a while but then slowly breaks-up.

The asymmetric flow dynamics and the symmetry break-up process discussed here have also seen in the 2-D injection nozzle simulation (section 5.1.1) and discussed in detail. As before, Fig. 5.61 depicts the normalized static pressure difference Δp in logarithmic scale given by

$$\log_{10}(\Delta p + \varepsilon) = \log_{10} \left(\frac{|p_{up} - p_{low}|}{p_{01}} + \varepsilon \right), \quad (5.5)$$

recorded at the monitor pair 1. The pressure difference value is normalized by the inlet total pressure p_{01} and a cut-off value of $\varepsilon = 10^{-9}$ is used.

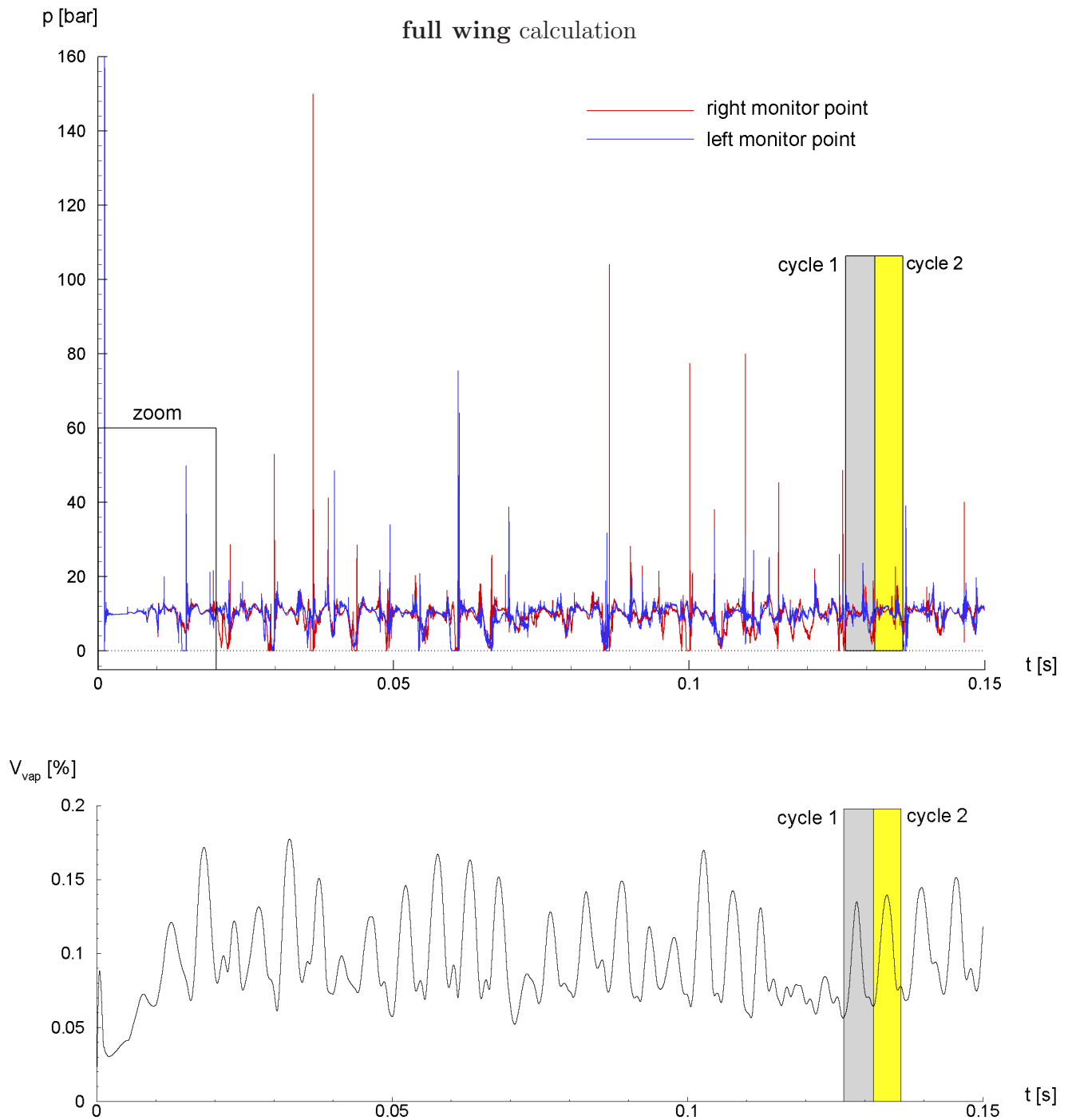


Figure 5.57: Pressure signals recorded by the right (red lines) and left (blue lines) monitor points (top). Integrated vapor volume V_{vap} (bottom). **Full wing** calculation. NACA 0009 hydrofoil, -1° (walls) and $+10^\circ$ (midspan), $u_\infty = 50$ m/s, $T_\infty = 300$ K, $p_\infty = 10$ bar, $\sigma_{ref} = 0.81$, $\Delta t_{CFD} = 4.5 \cdot 10^{-8}$ s, grid: $6 \cdot 10^5$ hexahedrons, second order in space and in time.

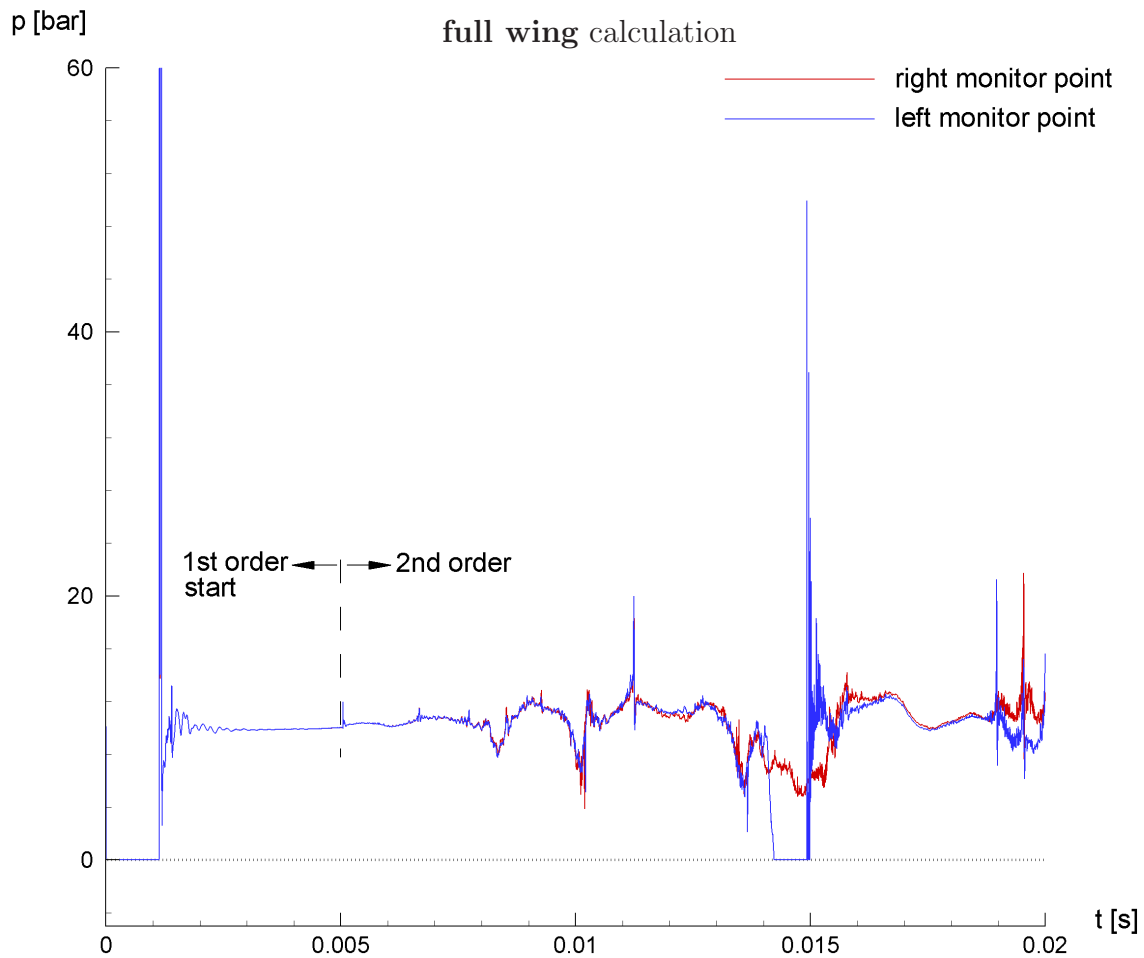


Figure 5.58: Pressure signals corresponding to the zoom area of Fig. 5.57, demonstrating the break-up of the symmetry. **Full wing** calculation. NACA 0009 hydrofoil, -1° (walls) and $+10^\circ$ (midspan), $u_\infty = 50 \text{ m/s}$, $T_\infty = 300 \text{ K}$, $p_\infty = 10 \text{ bar}$, $\sigma_{ref} = 0.81$, $\Delta t_{CFD} = 4.5 \cdot 10^{-8} \text{ s}$, grid: $6 \cdot 10^5$ hexahedrons, second order in space and in time.

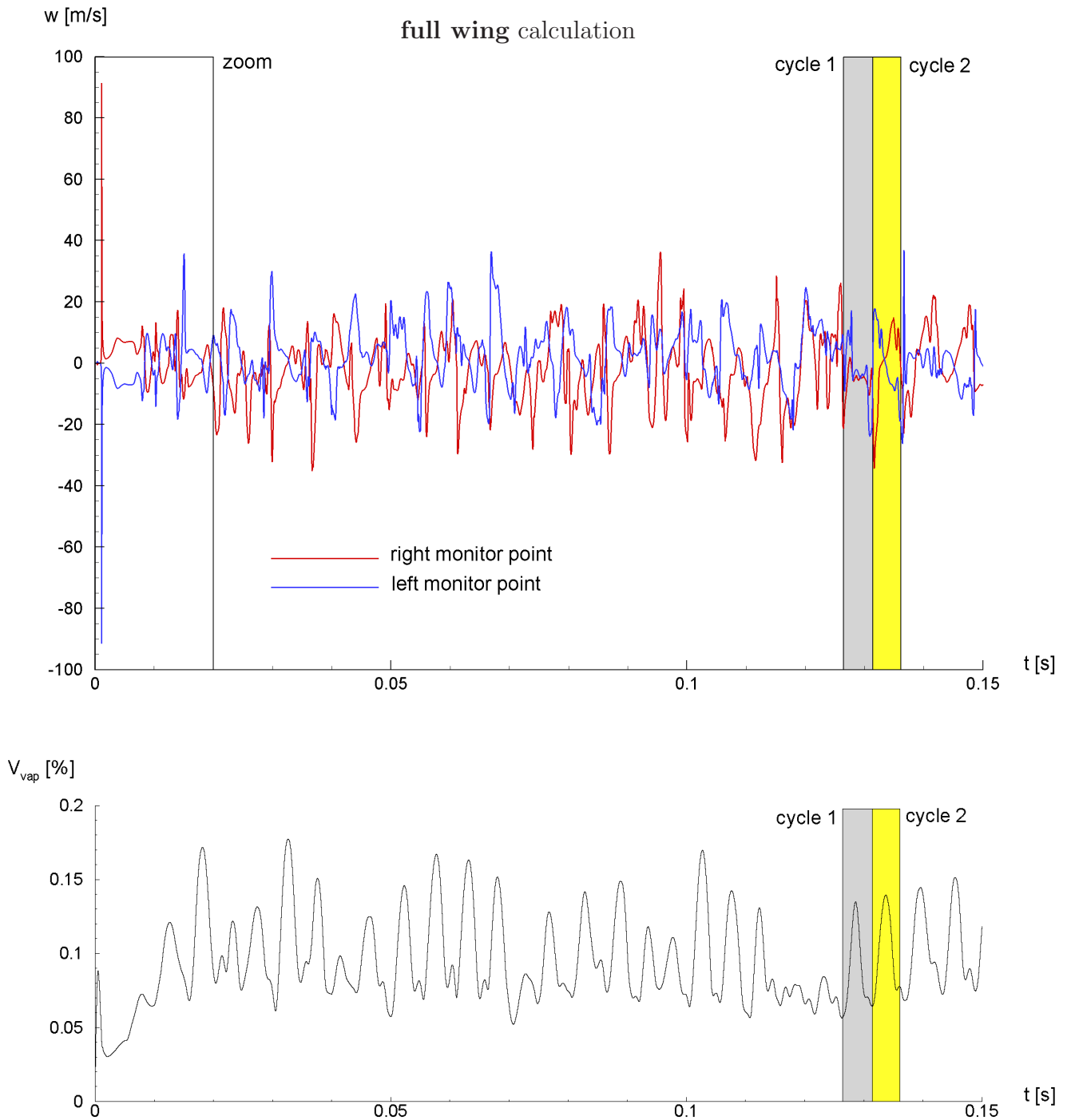


Figure 5.59: Spanwise velocity component w recorded by the right (red lines) and left (blue lines) monitor points (top). Integrated vapor volume V_{vap} (bottom). **Full wing** calculation. NACA 0009 hydrofoil, -1° (walls) and $+10^\circ$ (midspan), $u_\infty = 50$ m/s, $T_\infty = 300$ K, $p_\infty = 10$ bar, $\sigma_{ref} = 0.81$, $\Delta t_{CFD} = 4.5 \cdot 10^{-8}$ s, grid: $6 \cdot 10^5$ hexahedrons, second order in space and in time.

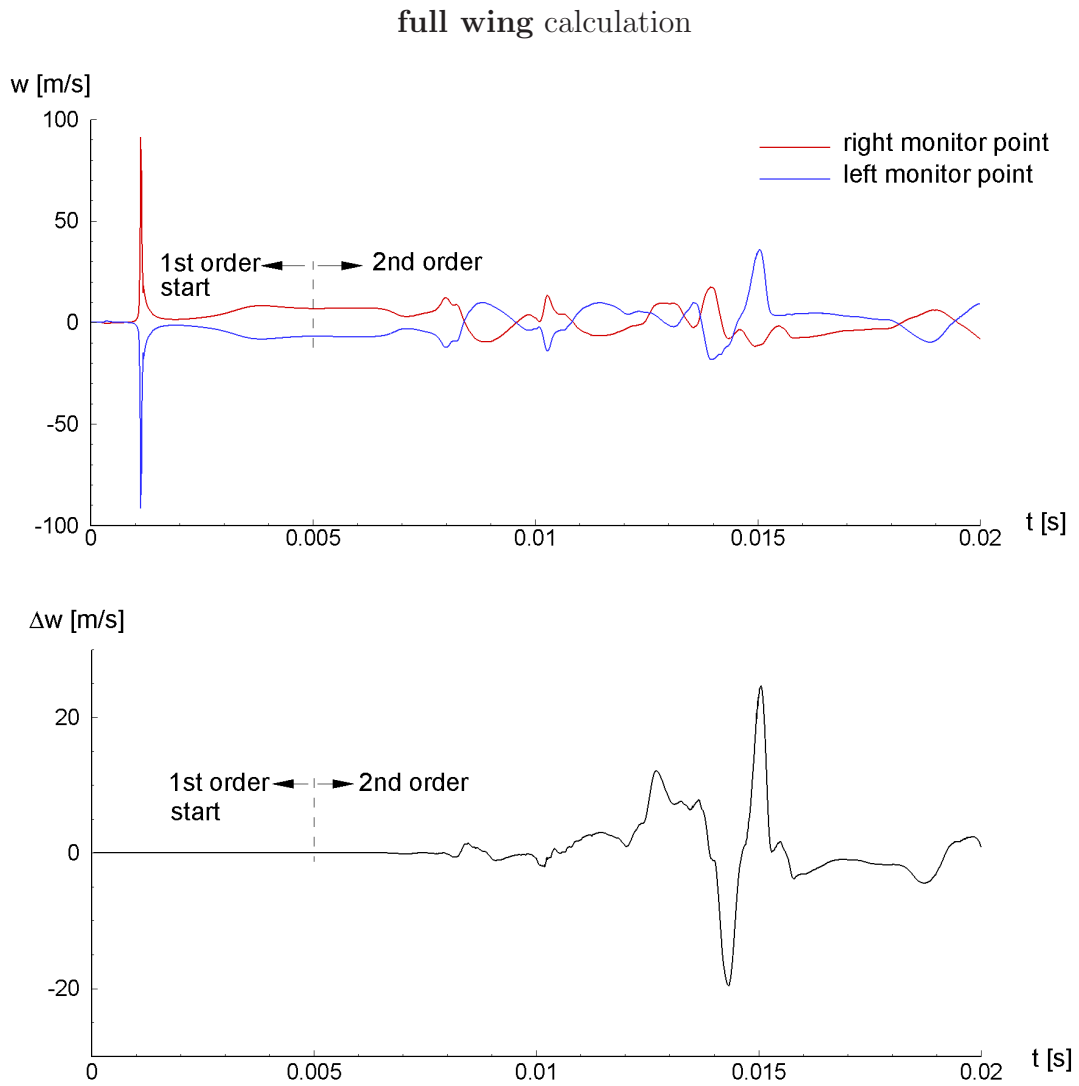


Figure 5.60: Spanwise velocity component w corresponding to the zoom area of Fig. 5.59 (top). Difference between right and left values of the spanwise velocity $\Delta w = w_L - w_R$, demonstrating the break-up of the symmetry. Integrated vapor volume V_{vap} (bottom). **Full wing** calculation. NACA 0009 hydrofoil, -1° (walls) and $+10^\circ$ (midspan), $u_\infty = 50$ m/s, $T_\infty = 300$ K, $p_\infty = 10$ bar, $\sigma_{ref} = 0.81$, $\Delta t_{CFD} = 4.5 \cdot 10^{-8}$ s, grid: $6 \cdot 10^5$ hexahedrons, second order in space and in time.

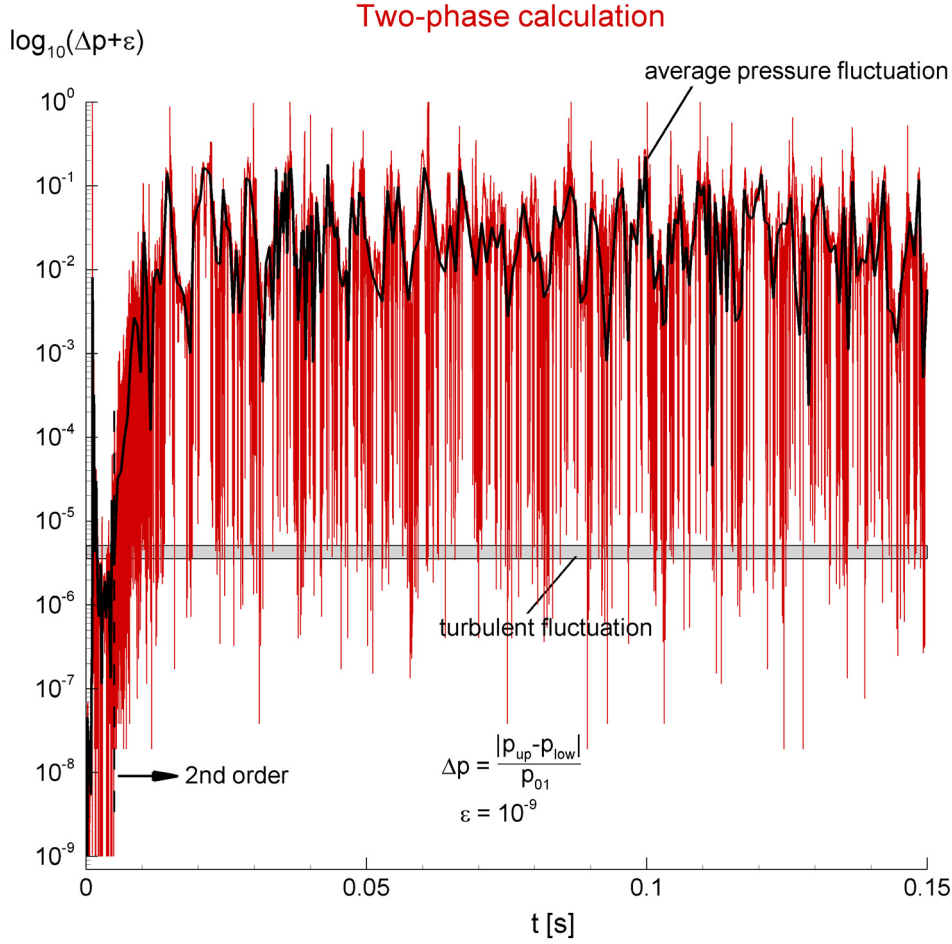


Figure 5.61: Time dependent normalized static pressure difference Δp , **full wing calculation**, logarithmic scale. NACA 0009 hydrofoil, -1° (walls) and $+10^\circ$ (midspan), $u_\infty = 50 \text{ m/s}$, $T_\infty = 300 \text{ K}$, $p_\infty = 10 \text{ bar}$, $\sigma_{ref} = 0.81$, $\Delta t_{CFD} = 4.5 \cdot 10^{-8} \text{ s}$, grid: $6 \cdot 10^5$ hexahedrons, second order in space and in time.

Figure 5.61 clearly shows that the instability in the flow field starts to grow already from the beginning of the simulation and it fluctuates continuously as the transient solution proceeds.

A pressure fluctuation level due to turbulence is determined for the considered flow conditions, where the Reynolds number based on the chord length is $Re_c \approx 10^6$ and assuming a lower turbulence intensity Tu value on the order of $\sim 10^3$ as before, i.e.

$$Tu = \frac{\sqrt{u' \cdot u'}}{\bar{u}} \approx 10^{-3}. \quad (5.6)$$

For a mean velocity of $\bar{u} = 50 \text{ m/s}$, turbulent fluctuation velocity u' can be found by using the above equation as, $|u'| = 0.05 \text{ m/s}$. This velocity corresponds to a pressure fluctuation which can be approximated as

$$p' \approx \frac{1}{2} \rho u'^2 = \frac{1}{2} \cdot 1000 \cdot 0.05^2 = 1.25 \text{ Pa}. \quad (5.7)$$

Normalizing this value with respect to the inlet total pressure $p_{01} \approx 10 \text{ bar}$ and taking the logarithm of it results in the gray bar depicted in Fig. 5.61.

As a result, it is seen that the **full wing** calculation is almost symmetric with respect to large scale cavitation dynamics but asymmetric behavior is observed in terms of small scale structures and especially at the regions of cavity closure and in the vicinity of collapses.

In terms of symmetry break-up investigation, a comparable analysis with respect to the single phase solution as in the case of the 2-D injection nozzle is not performed, which would require an extensive amount of additional computational time. Moreover, from the previous experience it is known that single-phase flow is stable within small perturbations (numerical noise) and remains symmetric. Therefore, no additional information is expected from the single-phase solution of the 3-D twisted wing.

This calculation is performed by using $6 \cdot 10^5$ hexahedrons divided equally into two blocks. The total physical time of 0.15 s took 12 days on two processors (Dell Precision 390 workstation with 2 processors). The inclusion of viscous effects would require the resolution of the boundary layer which would increase the mesh count approximately 2 times. Together with a standard two-equation turbulence model and a wall resolution of $y^+ \approx 1$, one can estimate that the overall CPU requirement would increase 150 times, which would result in a required calculation time of 1800 days or 5 years. This requirement further increases by a factor of 30 if third order discretizations are used instead of the current second order scheme. Such high CPU requirements can of course be reduced by using more processors and code optimization but this simple estimation shows the challenge of the investigated flow problem in terms of the CPU requirements. Therefore, the current inviscid model is well suited for the applications that are considered in this thesis, as the unsteady cavitation dynamics and their collapse mechanisms are inertia controlled.

The following experimental visualization is taken from Foeth [33]. It is a slightly different but comparable geometry with a twisted NACA 0009 hydrofoil and an angle of attack of 1° at the walls and $+9^\circ$ at the midspan. The reference cavitation number in this experiment is $\sigma_{ref} = 0.77 \pm 7.4\%$ and the flow velocity is $u_\infty = 7.04 \pm 1.16\% m/s$.

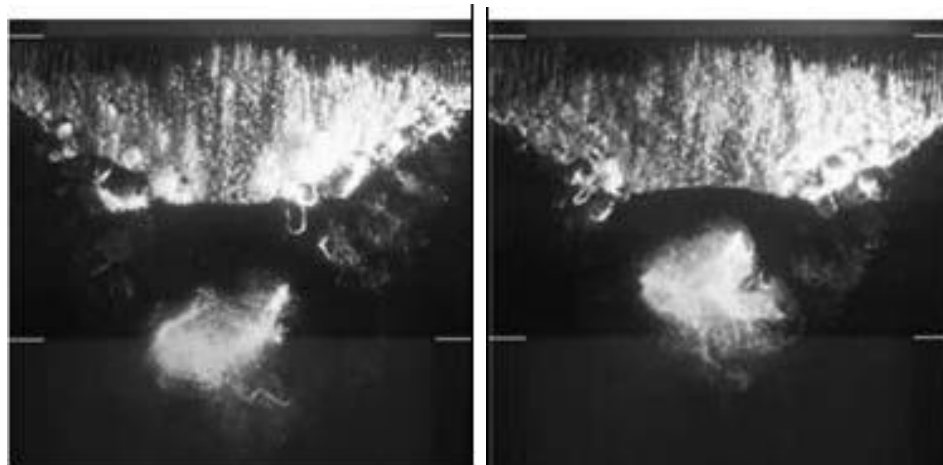


Figure 5.62: Experimental visualization of asymmetric cavitation structure [33]. NACA 0009 hydrofoil, 1° (walls) and 9° (midspan), $u_\infty = 7.04 \pm 1.16\% m/s$, $0.77 \pm 7.4\%$.

Figure 5.62 shows two time instants in the shedding cycle of the cavitating flow. From the pictures one can recognize the small scale asymmetry of the cavitation structure

although the global structure of the cavity pattern remains symmetric. This experimental visualization is in good agreement with our results that are presented in this section, where the global cavity structure is almost symmetric with respect to the midspan but small scale asymmetry is present especially around the closure regions and collapses.

In order to resolve large scale asymmetry of the cavitation structures of a symmetric body a very fine computational mesh is required globally. This investigation is part of the Ph.D. thesis of Schmidt and it is discussed there in detail [104].

Chapter 6

Conclusions

6.1 Summary

In the course of this thesis, a state of the art 3-D compressible flow solver - **CATUM** - has been developed in order to simulate liquid and two-phase flows with special emphasis on the arising shock and wave dynamics inside the flow field.

Simulation of unsteady cavitating flows is an important subject of computational fluid dynamics. Both in academia and in industry researchers have been using different numerical methods in order to predict characteristics of such flows. Most of the methods in literature rely on incompressible treatment of the flow field and time-averaged or long time behavior of the flow variables. Whereas our fundamental interests in the ongoing research project are the time accurate resolution of the cavitation dynamics – mainly the short time scale flow characteristics of the applications – and the arising wave propagation phenomenon due to continuous phase transition processes and their interaction with the flow field. Therefore, the compressibility has to be taken into account in the solution procedure as well as a high temporal resolution to resolve the wave dynamics and detect regions of instantaneous high pressure loads resulting from violent collapses of cavitation regions. Moreover, it is known that inertia effects are dominant in the flows considered here and thus viscous effects are neglected in the formulation.

The full compressible equation system is coupled through a combined equation of state defining all the phases under consideration. The liquid phase is defined by a modified Tait equation, the vapor phase is given by the ideal gas equation and the two-phase regions are calculated through saturation conditions. Therefore, the applied two-phase model assumes thermodynamic equilibrium of the phases. Moreover, as the physical model is directly based on the integral average properties of the arising flow field, no additional specification of small scale structures, like initial bubble concentration or radius, is required. The well known Riemann approach is used in the numerical scheme. But this approach fails in the limit of multidimensional low Mach number flows (low Mach number problem) and requires substantial modifications to achieve accurate solutions in the regions of pure liquid where $M \rightarrow 0$. As a result, we developed a modified numerical flux for cavitating flows based on the characteristic theory and equipped with an asymptotically consistent pressure flux which ensures accurate

solutions for $M \rightarrow 0$ as well. At the inlet and the outlet of the discretized solution domain, weakly reflective boundary conditions are applied. Contrary to classical non-reflective boundary conditions, a prescribed pressure $p_{out,mix}$ is ensured asymptotically with this approach.

The developed code is verified through a series of single and two-phase shock tube problems. The accuracy of the proposed two-phase model is tested against the solution of the Rayleigh-Plesset equation for the Besant problem, where a perfect agreement with the analytical solution is found.

Two application areas are considered in this thesis. First one focuses on the micro-scale and high-speed internal flows in fuel injection systems. Whereas the second application area corresponds to cavitating flows around hydraulic machinery such as ship propellers and pump or turbine blades, which are characterized by large-scale, low-speed flows.

The importance and the necessity of the compressible treatment of these flow problems is shown by the detection of wave dynamics as the essential and dominating feature of the temporal flow development. Furthermore, the observed unsteady flow phenomena manifest the necessity of time accurate calculations with numerical time steps down to $\Delta t_{CFD} = 10^{-10} s$ in order to predict short time flow characteristics. Moreover, collapse induced shocks are resolved in all of the applications that are considered. The locations as well as the intensities of these loads are thought to be related to erosion critical areas. The arising cavitation pattern in the 3-D multi hole injection nozzle and the shedding characteristics of the 3-D twisted wing match the experimental observations [15], [19], [32].

Thus, one can conclude that the proposed model is well applicable to predict the cavitation dynamics of the complex flow applications.

6.2 Recommendations for Further Development

As **CATUM** is developed in a modular and structured basis, extensions and modifications can be implemented in a straightforward manner.

From the code-development point of view, especially the input and initialization structure of the code can be improved. Similarly, for the pre-processing phase mentioned a graphical user interface would be extremely useful and would serve as a starting point for a complete solver package.

As this code is always thought to be the heart of our multi-purpose solution package for compressible flow dynamics including pure liquids and phase transition, chemical reaction and heat addition, the physical modeling of homogeneous and heterogeneous condensation is regarded to be the next important step in the modeling. In addition to that an extensive knowhow in the physics and the numerics of condensing flows is already present in the research group [105], [42], [37].

For liquid and two-phase flows, implementation of a non-condensable gas component is currently under development and the preliminary tests show that cavitation behavior can be effected strongly by the amount of the initial gas content. Another improvement has been foreseen as the inclusion of a second (gas) component into the flow field,

resulting in a multi-phase/multi-component model. Thus, it would be possible to simulate the gas outflow situation in an injection nozzle calculation.

As discussed in the appendix, **CATUM** has already been extended to viscous flows using URANS equations. The initial tests are performed with single-phase laminar ideal gas flows and the subsequent implementation and verification of the $k - \omega$ turbulence model. In the current development state **CATUM** is able to simulate single-phase compressible laminar and turbulent ideal gas flows. Moreover, Lauer [63] has extended the turbulence modeling capability of **CATUM** through the Wilcox Stress- ω Reynolds-stress model. Although it has been shown in this thesis that the cavitation dynamics of the considered flow examples are mainly inertia dominated, the effects of viscosity are always important in the flow development. Hence, in this authors opinion, completing and verifying the viscous formulation for two-phase cavitating flows should be the next enhancement in **CATUM**, as a single-phase ideal gas version has already been completed and tested. One important difficulty in such a formulation is that a widely applicable and accepted two-phase turbulence model does not exist and the existing ones should be tuned according to the cavitating flow in consideration. This step needs an extensive literature survey and well documented validation test cases.

Further investigations are planned for the 3-D twisted wing case, which will include statistical analysis of the observed effects, like instantaneous maximum pressure loads on the surface and their frequency of appearance as well as one-to-one comparison with recently obtained experimental data.

References

- [1] Adams, N.A., *The use of LES subgrid-scale models for shock capturing*, Int. J. Numer. Meth. Fluids, Vol. 39, pp. 783-797 (2002)
- [2] Adams, N.A., *Turbulente Strömungen Einführung in die Theorie und Berechnung*, lecture notes, Lehrstuhl für Aerodynamik, Technische Universität München (2008)
- [3] D'Agostino, L., Brennen, C.E., *Linearized dynamics of spherical bubble clouds*, Journal of Fluid Mechanics, Vol. 199, pp. 155-176 (1989)
- [4] Alajbegovic A., Meister G., Greif D., Basara B., *Three phase cavitating flows in high-pressure swirl injectors*, Experimental Thermal and Fluid Science, Vol. 26, pp. 677-681 (2002)
- [5] Anderson, J.D., Jr., *Modern Compressible Flow with Historical Perspective*, McGraw-Hill, New York (2003)
- [6] Anderson, J.D., Jr., *Computational Fluid Dynamics The Basics with Applications*, McGraw-Hill, Singapore (1995)
- [7] ANSYS-CFX, <http://www.ansys.com/Products/cfx.asp>
- [8] Arakeri, V.H., *Viscous effects on the position of cavitation separation from smooth bodies*, Journal of Fluid Mechanics, Vol. 68, pp. 779-799 (1975)
- [9] AVL-FIRE, <http://http://www.avl.com>
- [10] Besant, W., *Hydrostatics and Hydrodynamics*, Cambridge University Press (1859)
- [11] Blake, J.R., Gibson, D.C., *Cavitation bubbles near boundaries*, Ann. Rev. Fluid Mechanics, Vol. 19, 99-123 (1977)
- [12] Bode, J., Meier, G.E.A., Rein, M. in *Adiabatic Waves in Liquid-Vapor Systems*, eds. Meier, G.E.A., Thompson, P.A., Springer-Verlag, Berlin (1990)
- [13] Brennen, C.E., *Cavitation and Bubble Dynamics*, Oxford Engineering Science Series, Oxford University Press, New York (1995)
- [14] Briggs, L.J., *Limiting negative pressure of water*, Journal of Applied Physics, Vol. 21, pp. 721-722 (1950)
- [15] Busch, R., *Untersuchung von Kavitationsphänomenen in Dieseleinspritzdüsen*, Ph.D. Thesis, Universität Hannover, Hannover (2001)

- [16] CD-ADAPCO Star-CD,
<http://www.cd-adapco.com/products/STAR-CD/index.html>
- [17] Cengel, Y.A., Boles, M.A., *Thermodynamics an Engineering Approach*, McGraw-Hill, New York (1994)
- [18] Chahine, G.L., *Experimental and asymptotic study of non-spherical bubble collapse*, Appl. Sci. Res., Vol. 38, pp. 187-197 (1982)
- [19] Chaves, H., Knapp, M., Kubitzek, A., Obermeier, F., Schneider, T., *Experimental study of cavitation in the nozzle hole of Diesel injectors using transparent nozzles*, SAE Paper 950290, pp. 645-657 (1995)
- [20] Chen, Y., Heister, S.D., *Two-phase modeling of cavitating flows*, Journal of Computers & Fluids, Vol. 24, pp. 799-809 (1995)
- [21] Chorin, A.J., *The numerical solution of the Navier-Stokes equations for an incompressible fluid*, Bull. Am. Math. Soc., Vol. 73, pp. 928-931 (1967)
- [22] P.H. Cook, McDonald, M.A., Firmin, M.C.P., *Airfoil RAE 2822 - Pressure Distributions, and Boundary Layer and Wake Measurements*, AGARD-AR-138 (1979)
- [23] Coutier-Delgosha, O., Reboud, J.L., Delannoy, Y., *Numerical simulation of the unsteady behavior of cavitating flows*, Int. J. Numer. Meth. Fluids, Vol. 42, pp. 527-548 (2003)
- [24] Dang, J., *Numerical Simulation of Unsteady Partial Cavity Flows*, Ph.D. Thesis, Technical University of Delft (2000)
- [25] Dear, J.P., Field, J.E., *A study of the collapse of arrays of cavities*, Journal of Fluid Mechanics, Vol. 190, pp. 409-425 (1988)
- [26] Delale, C.F., Okita, K., Matsumoto, Y., *Steady-state cavitating nozzle flows with nucleation*, Journal of Fluids Engineering, Vol. 127, pp. 770-777 (2005)
- [27] Delale, C.F., Schnerr, G.H., Sauer J., *Quasi-one-dimensional steady-state cavitating nozzle flows*, Journal of Fluid Mechanics, Vol. 427, pp. 167-204 (2001)
- [28] Dymond, J.H., Malhotra, R., *The Tait equation: 100 years on*, International Journal of Thermophysics, Vol. 9, pp. 941-951 (1988)
- [29] Favre, A., *Equations des gaz turbulents compressible: 1. Formes general*, Journal de Mécanique, Vol. 4, pp. 361-390 (1965)
- [30] Franc, J.-P., Michel, J.-M., *Fundamentals of Cavitation*, Kluwer Academic Publishers, Dordrecht (2004)
- [31] Franc, J.-P., Michel, J.-M., *Attached cavitation and the boundary layer: Experimental and numerical treatment*, Journal of Fluid Mechanics, Vol. 154, pp. 63-90 (1985)
- [32] Foeth, E.J., *The Structure of Three-Dimensional Sheet Cavitation*, Ph.D. Thesis, Technical University of Delft (2008)

- [33] Foeth, E.J., van Doorne, C.W.H., van Terwisga, T., *Time resolved PIV and flow visualization of 3D sheet cavitation*, Experiments in Fluids, Vol. 40, pp. 503-513 (2006)
- [34] Fujikawa, S., Akamatsu, T., *Effects of non-equilibrium condensation of vapor on the pressure wave produced by the collapse of a bubble in a liquid*, Journal of Fluid Mechanics, Vol. 97, pp. 481-512 (1980)
- [35] Gilmore, F.R., *The growth and collapse of a spherical bubble in a viscous compressible liquid*, Cal. Inst. Techn. Hydro. Labo., Rpt. 26-4 (1952)
- [36] Godunov, S.K., *A difference scheme for numerical computation of discontinuous solution of hydrodynamic equations*, Math. Sb., Vol. 47, pp. 271-306 (1959), in Russian, translated U.S. Joint Publications Research Service, JPRS 7226 (1969)
- [37] Goodheart, K.A., *3-D Transonic Flow Dynamics with Nonequilibrium Condensation*, Ph.D. Thesis, Technische Universität München, Munich (2004)
- [38] Guillard, H., Viozat, C., *On the behavior of upwind schemes in the low Mach number limit*, Journal of Computers & Fluids, Vol. 28, pp. 63-86 (1999)
- [39] Hammitt, F.G., *Cavitation and Multiphase Flow Phenomena*, McGraw-Hill, New York (1980)
- [40] Harten, A., *High resolution schemes for hyperbolic conservation laws*, Journal of Computational Physics, Vol. 49, pp. 357-393 (1983)
- [41] Hayward, A.T.J., *Compressibility equations for liquid: a comparative study*, British Journal of Applied Physics, Vol. 18, pp. 965-977 (1967)
- [42] Heiler, M., *Instationäre Phänomene in homogen/heterogen kondensierenden Düsen- und Turbinenströmungen*, Ph.D. Thesis, Universität Karlsruhe (TH) (1999)
- [43] Hickling, R., Plesset, M.S., *Collapse and rebound of a spherical bubble in water*, Physics of Fluids, Vol. 7, pp. 7-14 (1964)
- [44] Hirsch, C., *Numerical Computation of Internal & External Flows, Fundamentals of Computational Fluid Dynamics*, Butterworth-Heinemann, Great Britain (2007)
- [45] Hirschfelder, J.O., Curtiss, C.F., Bird, R.B., *Molecular Theory of Gases and Liquids*, John Wiley & Sons, New York (1954)
- [46] Huuva, T., *Large Eddy Simulation of Cavitating and Non-cavitating Flow*, Ph.D. Thesis, Department of Shipping and Marine Technology, Chalmers University of Technology, Göteborg, Sweden (2008)
- [47] IAPWS, *International association for the properties of water and steam*, <http://www.iapws.org/>
- [48] Ikeda, T., Yoshizawa, S., Tosaki, M., Allen, J.S., Takagi, S., Ohta, N., Kitamura, T., Matsumoto, Y., *Cloud cavitation control for lithotripsy using high intensity focused ultrasound*, Ultrasound Med. Biol., Vol. 32, pp. 1383-1397 (2006)

- [49] Ivany, R.D., Hammit, F.G., *Cavitation bubble collapse in viscous compressible liquids - numerical analysis*, Journal of Basic Engineering, Vol. 87, pp. 977-985 (1965)
- [50] Ivany, R.D., Hammit, F.G., Mitchell, T.M., *Cavitation bubble collapse observations in a venturi*, Journal of Basic Engineering, Vol. 88, pp. 649-657 (1966)
- [51] Iivings, M.J., Causon, D.M., Toro, E.F. *On Riemann Solvers for Compressible Liquids*, Int. J. Numer. Meth. Fluids, Vol. 28, pp. 395-418 (1998)
- [52] Jameson, A., Schmidt, W., Turkel, E., *Numerical simulation of the Euler equations by finite volume methods using Runge-Kutta time stepping schemes*, AIAA 5th Computational Fluid Dynamics Conference, AIAA Paper 81-1259 (1981)
- [53] Kedrinskii, V.K., *Hydrodynamics of Explosion*, Springer-Verlag, Berlin (2005)
- [54] Kinjo, T., Matsumoto, M., *Cavitation process and negative pressure*, Fluid Phase Equilibria, Vol. 144, pp. 343-350 (1998)
- [55] Kolev, N., *Multiphase Flow Dynamics*, Springer-Verlag, Berlin (2002)
- [56] Koop, A.H., Hoeijmakers, H.W.M., Schnerr, G.H., *Barotropic flow modelling of sheet cavitation*, In: Proceedings EFMC6 - Euromech Fluid Mechanics Conference, Stockholm, Sweden, June 26-30, 2006, ed. Fransson, J.H.M., KTH Mechanics, Stockholm (2006)
- [57] Kubota, A., Kato, H., Yamaguchi, H., Maeda, M., *Unsteady structure measurement of cloud cavitation on a foil section using conditional sampling technique*, Journal of Fluids Engineering, Vol. 111, pp. 205-210 (1989)
- [58] Kuiper, G., *Cavitation research and ship propeller design*, Applied Scientific Research, Vol. 58, pp. 33-50 (1998)
- [59] Kunz, R.F., Boger, D.A., Stinebirt, D.R., Chyczewski, T.S., Lindau, J.W., Gibeling, H.J., Venkateswaran, S., Govindan, T.R., *A preconditioned Navier-Stokes method for two-phase flows with application to cavitation prediction*, Journal of Computers & Fluids, Vol. 29, pp. 849-875 (2000)
- [60] Laney, C.B., *Computational Gasdynamics*, Cambridge University Press, Cambridge (1998)
- [61] de Lange, D.F., de Bruin, G.J., *Sheet cavitation and cloud cavitation, re-entrant jet and three-dimensionality*, Appl. Sci. Res., Vol. 58, pp. 91-114 (1998)
- [62] de Lange, D.F., de Bruin, G.J., van Wijngaarden, L., *Numerical modeling of unsteady 2D sheet cavitation*, La Houille Blanche, Vol. 4/5, pp. 89-95 (1997)
- [63] Lauer, E., *Implementierung Kompressibler Reynoldsspannungsansätze und Vergleich mit Wirbelviskositätsmodellen*, Diplomarbeit, Technische Universität München, Munich (2007)
- [64] Launder, B.E., Sharma, B.I., *Application of the energy dissipation model of turbulence to the calculation of flow near a spinning disc*, Letters in Heat and Mass Transfer, Vol. 1, pp. 131-138 (1974)

- [65] Lauterborn, W., Ohl, C.-D., *The peculiar dynamics of cavitation bubbles*, Applied Scientific Research, Vol. 58, pp. 63-76 (1998)
- [66] Leer, B. van, *Towards the Ultimate Conservative Difference Scheme V. A Second-Order Sequel to Godunov's Method*, Journal of Computational Physics, Vol. 32, pp. 101-136 (1979)
- [67] Le, Q., Franc, J.-P., Michel, J.-M., *Partial cavities: Global behavior and mean pressure distribution*, Journal of Fluids Engineering, Vol. 115, pp. 243-248 (1993)
- [68] LeVeque, R.J., *Numerical Methods for Conservation Laws*, Birkhuser Verlag, (1992)
- [69] LeVeque, R.J., *Finite Volume Methods for Hyperbolic Problems*, Cambridge University Press, Cambridge (2002)
- [70] Liou, M.-S., Steffen, C.J., Jr., *A new flux splitting scheme*, Journal of Computational Physics, Vol. 107, pp. 23-39 (1993)
- [71] Liou, M.-S., *A sequel to AUSM, Part II: AUSM⁺-up for all speeds*, Journal of Computational Physics, Vol. 214, pp. 137-170 (2006)
- [72] Liou, M.-S., *A sequel to AUSM: AUSM⁺*, Journal of Computational Physics, Vol. 129, pp. 364-382 (1996)
- [73] Liou, M.-S., *Ten years in the making-AUSM-family*, NASA/TM-2001-210977, AIAA Paper 2001-2521 (2001)
- [74] Liu, Z., Brennen, C.E., *Cavitation nuclei population and event rates*, Journal of Fluids Engineering, Vol. 120, pp. 728-737 (1998)
- [75] Martynov, S., *Numerical Simulation of the Cavitation Process in Diesel Fuel Injectors*, Ph.D. Thesis, University of Brighton (2005)
- [76] Mathieu, J., Scott, J. *An Introduction to Turbulent Flow*, Cambridge University Press, Cambridge (2000)
- [77] Maxwell, J.C., *The Scientific Papers of James Clerk Maxwell, Vol. 2*, Cambridge University Press, Cambridge (1995)
- [78] Meister, A., *Asymptotic single and multiple scale expansions in the low Mach number limit*, SIAM J. Appl. Math., Vol. 60, pp. 256-271 (1999)
- [79] Munz, C.-D., Roller, S., Klein, R., Geratz, K.J., *The extension of incompressible flow solvers to the weakly compressible regime*, Journal of Computers & Fluids, Vol. 32, pp. 173-196 (2003)
- [80] NASA, NPARC Alliance web page,
<http://www.grc.nasa.gov/WWW/wind/valid/validation.html>
- [81] Nave, C.R., <http://hyperphysics.phy-astr.gsu.edu/hbase/hph.html>, Georgia State University, Department of Physics and Astronomy (2006)

- [82] Oden, J.T., Reddy, J.N., *An Introduction to the Mathematical Theory of Finite Elements*, John Wiley & Sons, New York (1976)
- [83] Oldenbourg, R., *Properties of Water and Steam in SI-Units*, Springer-Verlag, Berlin (1989)
- [84] Paillère, H., Corre, C., García Cascales, J.R., *On the Extension of the AUSM+ Scheme to Compressible Two-Fluid Models*, Journal of Computers & Fluids, Vol. 32, pp. 891-916 (2003)
- [85] Philipp, A., Lauterborn, W., *Cavitation erosion by single laser-produced bubbles*, Journal of Fluid Mechanics, Vol. 361, pp. 75-116 (1998)
- [86] Plesset, M.S., *The dynamics of cavitation bubbles*, ASME Journal of Applied Mechanics, Vol. 16, pp. 228-231 (1949)
- [87] Plesset, M.S., Prosperetti, A., *Bubble dynamics and cavitation*, Ann. Rev. Fluid Mechanics, Vol. 9, pp. 145-185 (1977)
- [88] Plesset, M.S., Chapman, R.B., *Collapse of an initially spherical cavity in the neighborhood of a solid boundary*, Journal of Fluid Mechanics, Vol. 47, pp. 283-290 (1971)
- [89] Plesset, M.S., Zwick, S.A., *The growth of a vapor bubble in superheated liquids*, Journal of Applied Physics, Vol. 25, pp. 493-498 (1954)
- [90] Pope, S.B., *Turbulent Flows*, Cambridge University Press, Cambridge (2000)
- [91] Rayleigh, Lord, *On the pressure developed in a liquid during the collapse of a spherical cavity*, Phil. Mag., Vol. 34, pp. 94-94 (1917)
- [92] Reisman, G.E., Wang, Y.-C., Brennen, C.E., *Observations of shock waves in cloud cavitation*, Journal of Fluid Mechanics, Vol. 355, pp. 255-283 (1998)
- [93] Roosen P., Kluitmann S., Knoche K.-F., *Untersuchung und Modellierung des transienten Verhaltens von Kavitationserscheinungen bei ein- und mehrkomponentigen Kraftstoffen in schnell durchströmten Düsen*, Abschlußbericht zur ersten Antragsperiode des DFG-Schwerpunktprogramms, Transiente Vorgänge in mehrphasigen Systemen mit einer oder mehreren Komponenten, Aachen (1994)
- [94] Rudy, D.H., Strickwerda, J.D., *A non-reflecting outflow boundary condition for subsonic Navier-Stokes calculations*, Journal of Computational Physics, Vol. 36, pp. 55-70 (1980)
- [95] Sato, K., Saito, Y., *Unstable cavitation behavior in circular cylinder orifice flow*, In: Proceedings of the 4th Int. Symp. on Cavitation, CALTECH, Pasadena, USA (2001)
- [96] Sauer, J., *Instationär kavitierende Strömungen - Ein neues Modell, basierend auf Front Capturing (VoF) und Blasendynamik*, Ph.D. Thesis, Universität Karlsruhe (TH) (2000)

- [97] Saurel, R., Cocchi, J.P., Butler, P.B., *Numerical Study of Cavitation in the Wake of a Hypervelocity Underwater Projectile*, Journal of Propulsion and Power, Vol. 15, No. 4, pp 513-522 (1999)
- [98] Saurel, R., Abgrall, R., *A multiphase Godunov method for compressible multifluid and multiphase flows*, Journal of Computational Physics, Vol. 150, pp. 425-467 (1999)
- [99] Schlichting, H., Gersten, K., *Grenzschicht-Theorie*, Springer-Verlag, Berlin (1997)
- [100] Schmidt, D.P., Rutland, C.J., Corradini, M.L., Roosen, P., Genge, O., *Cavitation in two-dimensional asymmetric nozzles*, SAE paper 1999-01-0518 (1999)
- [101] Schmidt, S.J., *Ein Verfahren zur präzisen Berechnung dreidimensionaler, reibungsfreier Idealgasströmungen über dem gesamten Kompressibilitätsbereich*, Diplomarbeit, Technische Universität München, Munich (2005)
- [102] Schmidt S.J., Sezal I.H., Schnerr G.H., Thalhamer M., Frster M., *Compressible simulation of liquid/vapour two-phase flows with local phase transition*, In: 6th International Conference on Multiphase Flow, ICMF 2007, Leipzig, Germany, July 9 - 13 (2007)
- [103] Schmidt, S.J., Sezal, I.H., Schnerr, G.H., Thalhamer, M., *Riemann techniques for the simulation of compressible liquid flows with phase-transition at all Mach numbers - shock and wave dynamics in cavitating 3-D micro and macro systems*, In: 46th AIAA Aerospace Sciences Meeting and Exhibit, Reno, Nevada, AIAA paper 2008-1238 (2008)
- [104] Schmidt, S.J., *Modellbildung und Simulation der wellen- und hydrodynamischen Phänome in kompressiblen Flüssigkeiten mit Phasenübergang*, Ph.D. Thesis, Fakultät für Maschinenwesen, Technische Universität München, Munich (2009)
- [105] Schnerr, G.H., *Homogene Kondensation in stationären transsonischen Strömungen durch Lavaldüsen und um Profile*, Habilitation, Fakultät für Maschinenbau, Universität Karlsruhe (TH) (1985)
- [106] Schnerr, G.H., *Modeling and computation of unsteady cavitating flows based on bubble dynamics*, in Numerical Simulation of Incompressible Flows, ed. Hafez, M.M., World Scientific, pp. 544-576 (2003)
- [107] Schnerr, G.H., Schmidt, S.J., Sezal, I.H., Thalhamer, M., *Shock and wave dynamics of compressible liquid flows with special emphasis on unsteady load on hydrofoils and on cavitation in injection nozzles*, Invited Lecture, In: Proceedings CAV2006 - Sixth International Symposium on Cavitation, September 11-15 2006, The Netherlands, CD-ROM publication (2006)
- [108] Schnerr, G.H., Sezal, I.H., Schmidt, S.J., *Numerical investigation of 3-D cloud cavitation with special emphasis on collapse induced shock dynamics*, Physics of Fluids, Vol. 20, 040703 (2008)

- [109] Senocak, I., Shyy, W., *A pressure based method for turbulent cavitating flow computations*, Journal of Computational Physics, Vol. 176, pp. 363-383 (2002)
- [110] Shima, A., *Studies on bubble dynamics*, Shock Waves, Vol. 7, pp. 33-42 (1997)
- [111] Shin, B.R., Yamamoto, S., Yuan, X., *Application of preconditioning method to gas-liquid two-phase flow computations*, Journal of Fluids Engineering, Vol. 126, pp. 605-612 (2004)
- [112] Shu, C.-W., *Essentially Non-Oscillatory and Weighted Essentially Non-Oscillatory Schemes for Hyperbolic Conservation Laws*, NASA/CR-97-206253 (1997)
- [113] Sod, G.A., *A survey of several finite-differences methodes for systems of nonlinear hyperbolic conservation laws*, Journal of Computational Physics, Vol. 27, pp. 1-31 (1978)
- [114] Spalart, P.R., Allmaras, S.R., *A one-equation turbulence model for aerodynamic flows*, AIAA-paper 92-439 (1992)
- [115] Tecplot Inc., TECPLOT,
<http://www.tecplot.com/>
- [116] Thalhamer, M., *Multiblock-Parallelisierung auf strukturierten Hexaedernetzen*, Semesterarbeit, Technische Universität München, Munich (2008)
- [117] Thompson, P.A., *Compressible Fluid Dynamics*, McGraw-Hill, (1972)
- [118] Tomita, Y., Shima, A., *Mechanisms of impulsive pressure generation and damage pit formation by bubble collapse*, Journal of Fluid Mechanics, Vol. 169, pp. 535-564 (1986)
- [119] Toro, E.F., *Riemann Solvers and Numerical Methods for Fluid Dynamics*, Springer-Verlag, Berlin (1999)
- [120] Trevena, D.H., *Cavitation and the generation of tension in liquids*, J. Phys. D: Appl. Phys., Vol. 17, pp. 2139-2164 (1984)
- [121] Turkel, E., *Preconditioning methods for solving incompressible and low-speed compressible equations*, Journal of Computational Physics, Vol. 72, pp. 277-298 (1987)
- [122] Turkel, E., *Review of preconditioning methods for fluid dynamics*, Applied Numerical Mathematics, Vol. 12, pp. 257-284 (1993)
- [123] Turkel, E., Radespiel, R., Kroll, N., *Assessment of preconditioning methods for multi-dimensional aerodynamics*, Journal of Computers & Fluids, Vol. 26, pp. 613-634 (1997)
- [124] Vincenti, W.G., Kruger, C.H., Jr., *Introduction to Physical Gas Dynamics*, John Wiley & Sons, New York (1965)

- [125] Vogel, A., Lauterborn, W., Timm, R., *Optical and acoustic investigations of the dynamics of laser-produced cavitation bubbles near solid boundaries*, Journal of Fluid Mechanics, Vol. 206, pp. 299-338 (1989)
- [126] Wallis, W., *One Dimensional Two-Phase Flow*, McGraw-Hill, New York (1975)
- [127] Wang, G., Senocak, I., Shyy, W., Ikohagi, T., Cao, S., *Dynamics of attached turbulent cavitating flows*, Progress in Aerospace Sciences, Vol. 37, pp. 551-581 (2001)
- [128] Weiss, J.M., Smith, W.A., *Preconditioning applied to variable and constant density flows*, AIAA Journal, Vol. 41, pp. 27-33 (2003)
- [129] White, F.M., *Viscous Fluid Flow*, McGraw-Hill, New York (2005)
- [130] Wieghardt, K., Tillman, W., *On the Turbulent Friction Layer for Rising Pressure*, NACA TM-1314 (1951)
- [131] Wilcox, D.C., *Turbulence Modeling for CFD*, DCW Industries, Inc., La Canada, California (2002)
- [132] Wilcox, D.C., *Multiscale model for turbulent flows*, AIAA Journal, Vol. 26, pp. 1311-1320 (1988)
- [133] Woodward, P., Colella, P. *The numerical simulation of two-dimensional fluid flow with strong shocks*, Journal of Computational Physics, Vol. 54, pp. 115-173 (1984)
- [134] Xiao, C., Heyes, D.M., *Cavitation in stretched liquids*, Proc. Royal Soc. Ser. A, Vol. 458, pp. 889-910 (2002)
- [135] Young, F.R., *Cavitation*, Imperial College Press, London (1999)
- [136] Yuan W., Schnerr G.H., *Cavitation in injection nozzles - effect of injection pressure fluctuations*, In: Proceedings of the 4th Int. Symp. on Cavitation, CALTECH, Pasadena, USA (2001)
- [137] Yuan, W., Schnerr, G.H., *Numerical simulation of two-phase flow in injection nozzles: Interaction of cavitation and external jet formation*, Journal of Fluids Engineering, Vol. 125, pp. 963-969. (2003)
- [138] Zierep, J., *Theoretische Gasdynamik*, G. Braunn, Karlsruhe, reprint of 3rd edition (1991)

Appendix A

Physical Constants and Relations

A.1 Saturation Variables

In the two-phase modeling that is implemented, the vapor and the liquid phases are assumed to be in thermodynamic equilibrium. Therefore, the corresponding saturation conditions are defined by $T_{vap} = T_{liq} = T_{sat}$ and $p = p_{sat}(T_{sat})$. Introducing the following temperature function

$$\theta = 1 - \frac{T}{T_{cr}}, \quad (\text{A.1})$$

where the critical conditions for water are

$$\begin{aligned} T_{cr} &= 647.096 \text{ K}, \\ p_{cr} &= 22.064 \cdot 10^6 \text{ Pa}, \\ \rho_{cr} &= 322.0 \text{ kg/m}^3. \end{aligned} \quad (\text{A.2})$$

Using the above definitions, saturation pressure p_{sat} , liquid saturation density $\rho_{l,sat}$ and vapor saturation density $\rho_{v,sat}$ are defined by Oldenbourg as follows [83]

$$\ln \left(\frac{p_{sat}}{p_{cr}} \right) = \frac{T_{cr}}{T_{sat}} [a_1\theta + a_2\theta^{1.5} + a_3\theta^3 + a_4\theta^{3.5} + a_5\theta^4 + a_6\theta^{7.5}], \quad (\text{A.3})$$

$$\frac{\rho_{l,sat}}{\rho_{cr}} = 1 + b_1\theta^{\frac{1}{3}} + b_2\theta^{\frac{2}{3}} + b_3\theta^{\frac{5}{3}} + b_4\theta^{\frac{16}{3}} + b_5\theta^{\frac{43}{3}} + b_6\theta^{\frac{110}{3}}, \quad (\text{A.4})$$

$$\ln \left(\frac{\rho_{v,sat}}{\rho_{cr}} \right) = c_1\theta^{\frac{2}{6}} + c_2\theta^{\frac{4}{6}} + c_3\theta^{\frac{8}{6}} + c_4\theta^{\frac{18}{6}} + c_5\theta^{\frac{37}{6}} + c_6\theta^{\frac{71}{6}}. \quad (\text{A.5})$$

Parameters of the given saturation equations are summarized in Table A.1.

Table A.1: Parameters of the saturation equations from Oldenbourg [83]

Index	a	b	c
1	-7.85823	1.99206	-2.02957
2	1.83991	1.10123	-2.68781
3	-11.7811	-0.512506	-5.38107
4	22.6705	-1.75263	-17.3151
5	-15.9393	-45.4485	-44.6384
6	1.77516	$-6.75615 \cdot 10^5$	-64.3486

A.2 Liquid and Gas Constants

Constants used in liquid water, water vapor and ideal gas equation of states are summarized in this section. The equations are already given in chapter 2 and repeated below for convenience.

Liquid Water

$$p = p(\rho, T) = B \left[\left(\frac{\rho}{\rho_{l,sat}(T)} \right)^n - 1 \right] + p_{sat}(T), \quad (\text{A.6})$$

$$e = e(T) = c_{v,liq} \cdot (T - T_{ref}) + e_{l0}, \quad (\text{A.7})$$

$$c_{liq} = \sqrt{\frac{n}{\rho}(p + B)}. \quad (\text{A.8})$$

Table A.2: Thermodynamic constants in equations of state and sonic speed definition of liquid water

B [Pa]	n	$c_{v,liq}$ [J/kg · K]	T_{ref} [K]	e_{l0} [J/kg]
$3.3 \cdot 10^8$	7.15	4186	273.15	617

Water Vapor - Ideal Gas Constants

$$p = \rho R_{vap} T, \quad (\text{A.9})$$

$$e = c_{v,vap} \cdot (T - T_{ref}) + L_{vap,ref} + e_{l0}, \quad (\text{A.10})$$

$$c_{vap} = \sqrt{\kappa R_{vap} T}. \quad (\text{A.11})$$

Table A.3: Thermodynamic constants in equations of state and sonic speed definition of water vapor

$R_{vap} [J/kg \cdot K]$	$c_{v,vap} [J/kg \cdot K]$	$T_{ref} [K]$	$L_{vap,ref} [J/kg \cdot K]$	$e_{l0} [J/kg]$	κ
461.5	1410.8	273.15	$2501.3 \cdot 10^3$	617	1.327

Air - Ideal Gas Constants

$$p = \rho R_{air} T, \quad (\text{A.12})$$

$$e = c_{v,air} \cdot T, \quad (\text{A.13})$$

$$c_{air} = \sqrt{\kappa R_{air} T}. \quad (\text{A.14})$$

Table A.4: Thermodynamic constants in equations of state and sonic speed definition of air

$R_{air} [J/kg \cdot K]$	$c_{v,air} [J/kg \cdot K]$	$c_{p,air} [J/kg \cdot K]$	κ
287.1	717.75	1004.85	1.4

Appendix B

Viscous Flow Formulation

As mentioned earlier, all the application simulations in this thesis are performed using inviscid formulation. This assumption is plausible since the inertia effects are dominant in these flows. But still viscous flow dynamics has effects on the flow field, especially when boundary layer separation is expected. Moreover, apart from cavitating flows since **CATUM** is planned as a complete simulation package for complex single and multi-phase compressible flows, simulation of viscous flow equations is unconditionally required. This is performed as a final step in the current thesis. It should be noted that, the implementation is in the actual development and only **single-phase ideal gas flow** case is considered here.

B.1 Navier-Stokes Equations

The flow of a viscous fluid is governed by Navier-Stokes equations. Analog to chapter 2 the compressible Navier-Stokes equations without body forces and volumetric heating can be written in vector form as

$$\frac{\partial \mathbf{q}}{\partial t} + \frac{\partial \mathbf{f}}{\partial x} + \frac{\partial \mathbf{g}}{\partial y} + \frac{\partial \mathbf{h}}{\partial z} = 0, \quad (\text{B.1})$$

whereas the vectors in the viscous case are defined as follows

$$\mathbf{q} = \begin{pmatrix} \rho \\ \rho u \\ \rho v \\ \rho w \\ \rho E \end{pmatrix}, \quad \mathbf{f} = \begin{pmatrix} \rho u \\ \rho u^2 + p - \tau_{xx} \\ \rho uv - \tau_{xy} \\ \rho uw - \tau_{xz} \\ \rho uH - u\tau_{xx} - v\tau_{xy} - w\tau_{xz} + q_x \end{pmatrix},$$

$$\mathbf{g} = \begin{pmatrix} \rho v \\ \rho vu - \tau_{yx} \\ \rho v^2 + p - \tau_{yy} \\ \rho vw - \tau_{yz} \\ \rho vH - u\tau_{yx} - v\tau_{yy} - w\tau_{yz} + q_y \end{pmatrix}, \quad \mathbf{h} = \begin{pmatrix} \rho w \\ \rho wu - \tau_{zx} \\ \rho wv - \tau_{zy} \\ \rho w^2 + p - \tau_{zz} \\ \rho wH - u\tau_{zx} - v\tau_{zy} - w\tau_{zz} + q_z \end{pmatrix}. \quad (\text{B.2})$$

The components of the shear stress and heat flux are given by

$$\begin{aligned}
\tau_{xx} &= 2\mu \frac{\partial u}{\partial x} - \frac{2}{3}\mu \left(\frac{\partial u}{\partial x} + \frac{\partial v}{\partial y} + \frac{\partial w}{\partial z} \right) \\
\tau_{yy} &= 2\mu \frac{\partial v}{\partial y} - \frac{2}{3}\mu \left(\frac{\partial u}{\partial x} + \frac{\partial v}{\partial y} + \frac{\partial w}{\partial z} \right) \\
\tau_{zz} &= 2\mu \frac{\partial w}{\partial z} - \frac{2}{3}\mu \left(\frac{\partial u}{\partial x} + \frac{\partial v}{\partial y} + \frac{\partial w}{\partial z} \right) \\
\tau_{xy} &= \tau_{yx} = \mu \left(\frac{\partial v}{\partial x} + \frac{\partial u}{\partial y} \right) \\
\tau_{xz} &= \tau_{zx} = \mu \left(\frac{\partial u}{\partial z} + \frac{\partial w}{\partial x} \right) \\
\tau_{yz} &= \tau_{zy} = \mu \left(\frac{\partial w}{\partial y} + \frac{\partial v}{\partial z} \right) \\
q_x &= -\lambda \frac{\partial T}{\partial x} \\
q_y &= -\lambda \frac{\partial T}{\partial y} \\
q_z &= -\lambda \frac{\partial T}{\partial z},
\end{aligned} \tag{B.3}$$

where μ is the coefficient of molecular viscosity and λ is the heat conductivity of the considered fluid. Total energy and total enthalpy are defined as before

$$E = e + \frac{1}{2}(u^2 + v^2 + w^2), \quad H = E + \frac{p}{\rho}. \tag{B.4}$$

The system of Navier-Stokes equations should be coupled through an equation of state, which is the ideal gas law for the current status.

B.2 Favre Averaged Navier-Stokes Equations

The equation system given by B.1-B.2 is in fact governs both laminar and turbulent flows. Therefore, its solution would give an exact definition of the flow field with defined initial and boundary conditions. But it requires direct numerical simulation (DNS) of the entire turbulent spectrum to smallest scale, which is not possible with the current computing power for the Reynolds number range and geometrical length scale of the practical applications [131]. Thus, for the solution of the system, the unsteady turbulent fluctuations should be expressed in terms of time-averaged quantities and random fluctuations, which introduces additional unknown terms into system. Therefore, the closure of the new system is completed with an appropriate turbulence model.

In order to predict the turbulent fluctuations in compressible flow, density weighted time averaging of Favre [29] is applied. The Favre-average for a scalar f is defined as

$$f = \tilde{f} + f'' , \quad (\text{B.5})$$

with fluctuation part f'' and mass-averaged part \tilde{f}

$$\tilde{f} = \frac{\overline{\rho f}}{\bar{\rho}} , \quad (\text{B.6})$$

where

$$\overline{\rho f} = \lim_{t \rightarrow \infty} \frac{1}{t} \int_{t_0}^{t_0 + \Delta t} \rho f dt . \quad (\text{B.7})$$

Favre-averaging is used for the velocity components u , v , w , internal energy e , temperature T and turbulence model variables. Whereas, the density ρ and the pressure p are averaged by using the conventional Reynolds (time) averaging, i.e.

$$\rho = \bar{\rho} + \rho' \quad (\text{B.8})$$

$$p = \bar{p} + p' , \quad (\text{B.9})$$

where

$$\bar{\rho} = \lim_{t \rightarrow \infty} \frac{1}{t} \int_{t_0}^{t_0 + \Delta t} \rho dt , \quad \bar{p} = \lim_{t \rightarrow \infty} \frac{1}{t} \int_{t_0}^{t_0 + \Delta t} p dt , \quad (\text{B.10})$$

and ρ' , p' corresponds to the fluctuations in density and pressure respectively. To illustrate the averaging procedure of the governing equations one can consider the continuity equation and start with the conventional Reynolds averaging both for the density ρ and the velocity components u_i . Using the Einstein summation rules, the continuity equation reads

$$\frac{\partial}{\partial t} \rho + \frac{\partial}{\partial x_i} (\rho u_i) = 0 , \quad (\text{B.11})$$

with averaged variables

$$\frac{\partial}{\partial t} (\bar{\rho} + \rho') + \frac{\partial}{\partial x_i} (\bar{\rho} u_i + \rho' u_i + \bar{\rho} u'_i + \rho' u'_i) = 0 . \quad (\text{B.12})$$

The next step is time averaging the whole equation. Using the following definitions; $\overline{\tilde{f}} = \tilde{f}$ and $\overline{f'} = 0$ [131], the Reynolds averaged continuity equation becomes

$$\frac{\partial}{\partial t} \bar{\rho} + \frac{\partial}{\partial x_i} (\bar{\rho} u_i + \overline{\rho' u'_i}) = 0 . \quad (\text{B.13})$$

For the closure of this equation a correlation between ρ' and u'_i is needed. From the definition of the Favre-average B.6 one can write

$$\bar{\rho} \tilde{u}_i = \overline{\rho u_i} , \quad (\text{B.14})$$

using the Reynolds averaging for the right hand side of this equation results in

$$\bar{\rho} \tilde{u}_i = \overline{\rho u_i} = \overline{\bar{\rho} u_i + \rho' u_i + \bar{\rho} u'_i + \rho' u'_i} = \overline{\bar{\rho} u_i} + \overline{\rho' u'_i} . \quad (\text{B.15})$$

Substituting the above given result in Eq. B.13 gives the Favre-averaged continuity equation

$$\frac{\partial}{\partial t} \bar{\rho} + \frac{\partial}{\partial x_i} (\bar{\rho} \tilde{u}_i) = 0. \quad (\text{B.16})$$

One can directly see that continuity equation has the same form as the laminar case therefore, averaging did not introduce any additional terms.

The flow variables that are used in the averaged equations are defined as follows

$$\begin{aligned} u_i &= \tilde{u}_i + u_i'' \\ \rho &= \bar{\rho} + \rho' \\ p &= \bar{p} + p' \\ h &= \tilde{h} + h'' \\ e &= \tilde{e} + e'' \\ T &= \tilde{T} + T'' \\ q_j &= \bar{q}_j + q_j'. \end{aligned}$$

The set of Navier-Stokes equations in Favre-averaged form is given below. As their derivation is cumbersome, momentum and energy equations are written directly.

$$\frac{\partial \bar{\rho}}{\partial t} + \frac{\partial (\bar{\rho} \tilde{u}_i)}{\partial x_i} = 0, \quad (\text{B.17})$$

$$\frac{\partial (\bar{\rho} \tilde{u}_i)}{\partial t} + \frac{\partial (\bar{\rho} \tilde{u}_j \tilde{u}_i)}{\partial x_j} = -\frac{\partial \bar{p}}{\partial x_j} + \frac{\partial}{\partial x_j} (\bar{\tau}_{ij} - \overline{\rho u_j'' u_i''}), \quad (\text{B.18})$$

$$\begin{aligned} &\frac{\partial}{\partial t} \left(\bar{\rho} \tilde{E} + \frac{\overline{\rho u_i'' u_i''}}{2} \right) + \frac{\partial}{\partial x_j} \left(\bar{\rho} \tilde{u}_j \tilde{H} + \tilde{u}_j \frac{\overline{\rho u_i'' u_i''}}{2} \right) \\ &= \frac{\partial}{\partial x_j} \left(-\bar{q}_j - \overline{\rho u_j'' h''} + \bar{\tau}_{ij} u_i'' - \overline{\rho u_j'' \frac{u_i'' u_i''}{2}} \right) \\ &\quad + \frac{\partial}{\partial x_j} [\tilde{u}_i (\bar{\tau}_{ij} - \overline{\rho u_j'' u_i''})]. \end{aligned} \quad (\text{B.19})$$

The momentum equation differ from the laminar case by the appearance of the Favre-averaged Reynolds-stress tensor,

$$\bar{\rho}(\tau_{ij})_T = -\overline{\rho u_i'' u_j''}. \quad (\text{B.20})$$

The energy equation includes more terms that should be clarified. First one is the double correlation between u_i'' and itself. This is the kinetic energy per unit volume of turbulent fluctuations, which is usually defined as turbulence kinetic energy k

$$\bar{\rho}k = \frac{\overline{\rho u_i'' u_i''}}{2}. \quad (\text{B.21})$$

The next additional term is the correlation between u_i'' and h'' on the right hand side, which is the turbulent heat flux, i.e.

$$q_{T_j} = \overline{\rho u_j'' h''}. \quad (\text{B.22})$$

The remaining two terms $\overline{\tau_{ij} u_i''}$ and $\overline{\rho u_j'' \frac{u_i'' u_i''}{2}}$ correspond to molecular diffusion and turbulent transport of turbulence kinetic energy respectively. Due to arising additional terms, the closure of the equation system requires the definition of them in terms of the known flow variables. Following the well known Boussinesq assumption, the turbulent shear stress can be related to the mean strain through the definition of a scalar turbulent eddy viscosity, μ_T [90]. Thus, with this assumption Eq. B.20 takes the following form

$$\bar{\rho}(\tau_{ij})_T = -\overline{\rho u_i'' u_j''} = \mu_T \left[\left(\frac{\partial \tilde{u}_i}{\partial x_j} + \frac{\partial \tilde{u}_j}{\partial x_i} \right) - \frac{2}{3} \frac{\partial \tilde{u}_k}{\partial x_k} \delta_{ij} \right] - \frac{2}{3} \bar{\rho}k \delta_{ij}. \quad (\text{B.23})$$

At this point one can use the Prandtl number Pr and define its counterpart, turbulent Prandtl number Pr_T as

$$Pr = \frac{c_p \mu}{\lambda}, \quad Pr_T = \frac{c_p \mu_T}{\lambda_T}. \quad (\text{B.24})$$

For the turbulent heat flux term B.22 one can simply use the classical analogy that is given in the laminar case and obtain

$$q_{T_j} = \overline{\rho u_j'' h''} = -\frac{c_p \mu_T}{Pr_T} \frac{\partial \tilde{T}}{\partial x_j}. \quad (\text{B.25})$$

The molecular diffusion and the turbulent transport of turbulence kinetic energy terms are usually ignored, which is quite accurate if the Mach numbers in the flow field are up to the supersonic range [131]. However, when hypersonic regime is of interest their effect should be included. With the following definitions of Favre-averaged ideal gas equation, total energy and total enthalpy the set of Favre-averaged Navier-Stokes equation is completed

$$\bar{p} = \bar{\rho} R \tilde{T} \quad (\text{B.26})$$

$$\bar{E} = \tilde{e} + \frac{1}{2} \tilde{u}_i \tilde{u}_i + k \quad (\text{B.27})$$

$$\bar{H} = \tilde{h} + \frac{1}{2} \tilde{u}_i \tilde{u}_i + k. \quad (\text{B.28})$$

In the above given formulation the only missing relation is the definition of turbulence kinetic energy k , which is introduced in Eq. B.21. Its definition depends on the turbulence model that is chosen and will be explained in the next section. From this point on the averaged variables are not explicitly displayed.

B.3 Single-phase Turbulence Modeling

Although the advancement of computing power favors the use of LES (Large Eddy Simulation) and related complex modeling strategies (see Adams [1], [2]), two-equation models are still in great use due to their relatively simple formulation, applicability and validation.

Most of the two-equation turbulence models use a relation for turbulence kinetic energy k . But the choice for the second transport variable was long time under discussion. The most used variable is the turbulent dissipation rate ϵ . A dimensional analysis results in the following relation

$$\mu_T \sim \rho \frac{k^2}{\epsilon}. \quad (\text{B.29})$$

Launder and Sharma [64] suggested a transport equation for ϵ and corresponding closure relations, which became the famous k - ϵ model that is being used for decades. Wilcox [132] defined specific dissipation rate ω instead of the turbulent dissipation rate ϵ and proposed the following definition for the turbulent viscosity

$$\mu_T = \rho \frac{k}{\omega}. \quad (\text{B.30})$$

The current implementation of the turbulence modeling considers only the single-phase ideal gas case of the k - ω turbulence model.

B.3.1 Wilcox k - ω Model

The transport equations for the turbulent kinetic energy k and specific dissipation rate ω are written as follows [131]

$$\frac{\partial(\rho k)}{\partial t} + \frac{\partial(\rho u_j k)}{\partial x_j} = \tau_{ij} \frac{\partial u_i}{\partial x_j} - \rho \beta^* k \omega + \frac{\partial}{\partial x_j} \left[(\mu + \sigma^* \mu_T) \frac{\partial k}{\partial x_j} \right] \quad (\text{B.31})$$

$$\frac{\partial(\rho \omega)}{\partial t} + \frac{\partial(\rho u_j \omega)}{\partial x_j} = \alpha \frac{\omega}{k} \tau_{ij} \frac{\partial u_i}{\partial x_j} - \rho \beta \omega^2 + \frac{\partial}{\partial x_j} \left[(\mu + \sigma \mu_T) \frac{\partial \omega}{\partial x_j} \right]. \quad (\text{B.32})$$

Closure coefficients and auxiliary relations are

$$\alpha = \frac{13}{25}, \quad \beta = \beta_0 f_\beta, \quad \beta^* = \beta_0^* f_{\beta^*}, \quad \sigma = \sigma^* = 0.5, \quad (\text{B.33})$$

$$\beta_0 = \frac{9}{125}, \quad f_\beta = \frac{1 + 70\chi_\omega}{1 + 80\chi_\omega}, \quad \chi_\omega \equiv \left| \frac{\Omega_{ij}\Omega_{ji}S_{ki}}{(\beta_0^*\omega)^3} \right|, \quad (\text{B.34})$$

$$\beta_0^* = \frac{9}{100}, \quad f_{\beta^*} = \begin{cases} 1, & \chi_k \leq 0 \\ \frac{1 + 680\chi_k^2}{1 + 400\chi_k^2}, & \chi_k > 0 \end{cases}, \quad \chi_k \equiv \frac{1}{\omega^3} \frac{\partial k}{\partial x_j} \frac{\partial \omega}{\partial x_j}. \quad (\text{B.35})$$

The mean rotation Ω_{ij} and the mean strain-rate S_{ij} tensors are defined by

$$\Omega_{ij} = \frac{1}{2} \left(\frac{\partial u_i}{\partial x_j} - \frac{\partial u_j}{\partial x_i} \right), \quad S_{ij} = \frac{1}{2} \left(\frac{\partial u_i}{\partial x_j} + \frac{\partial u_j}{\partial x_i} \right). \quad (\text{B.36})$$

The $\tau_{ij} \frac{\partial u_i}{\partial x_j}$ term encountered in the transport equations is called the turbulent production term P . Using the definition of the Reynolds-stress tensor given by Eq. B.23 one can write

$$P = \tau_{ij} \frac{\partial u_i}{\partial x_j} = \left[\mu_T \left[\left(\frac{\partial u_i}{\partial x_j} + \frac{\partial u_j}{\partial x_i} \right) - \frac{2}{3} \frac{\partial u_k}{\partial x_k} \delta_{ij} \right] - \frac{2}{3} \rho k \delta_{ij} \right] \frac{\partial u_i}{\partial x_j}. \quad (\text{B.37})$$

For stability reasons one needs to limit the specific dissipation rate [37], i.e.

$$\omega = \max \left[\omega, \beta^* \sqrt{\frac{8S_{ij}^2}{3}} \right]. \quad (\text{B.38})$$

The numerical implementation of the turbulence model will be given in the next section.

B.4 Numerical Formulation

The numerical formulation of **CATUM** is already discussed in chapter 3. For the implementation of viscous effects, diffusive fluxes and turbulence model equations should be discretized and appropriate boundary conditions are needed for the slip-walls.

B.4.1 Nondimensionalization of the Variables

It is an usual practice to cast the Navier-Stokes equations and turbulence model relations into dimensionless form. This technique normalizes the flow variables between 0 and 1. The dimensionless form is obtained by using reference flow variables in the following way

$$\begin{aligned} x^* &= \frac{x}{l_{ref}}, & y^* &= \frac{y}{l_{ref}}, & z^* &= \frac{z}{l_{ref}}, \\ u^* &= \frac{u}{c_{ref}}, & v^* &= \frac{v}{c_{ref}}, & w^* &= \frac{w}{c_{ref}}, \\ \rho^* &= \frac{\rho}{\rho_{ref}}, & p^* &= \frac{p}{\rho_{ref} c_{ref}^2}, & T^* &= \frac{T}{T_{ref}}, & e^* &= \frac{e}{c_{ref}^2}, & h^* &= \frac{h}{c_{ref}^2}, \\ \mu^* &= \frac{\mu}{\mu_{ref}}, & k^* &= \frac{k}{c_{ref}^2}, & \omega^* &= \frac{\omega}{c_{ref}/l_{ref}}, \end{aligned} \quad (\text{B.39})$$

where l_{ref} is the characteristic length of the problem and other reference values are defined as

$$T_{ref} = T_{01} \quad (\text{B.40})$$

$$\rho_{ref} = \frac{p_{01}}{RT_{01}} \quad (\text{B.41})$$

$$c_{ref} = \sqrt{\kappa RT_{01}} \quad (\text{B.42})$$

$$\mu_{ref} = \mu(T_{01}) . \quad (\text{B.43})$$

The reference Reynolds number can then be written as

$$Re_{ref} = \frac{\rho_{ref} c_{ref} x_{ref}}{\mu_{ref}} . \quad (\text{B.44})$$

Therefore, all flow variables in the equations are expressed in terms of their dimensionless forms and implemented in the numerical model accordingly.

B.4.2 Governing Equations with k - ω Turbulence Model

For the numerical solution of the turbulent flows Navier-Stokes equations given in section B.1 is reformulated as follows

$$\frac{\partial \mathbf{q}}{\partial t} + \frac{\partial \mathbf{f}_c}{\partial x} + \frac{\partial \mathbf{g}_c}{\partial y} + \frac{\partial \mathbf{h}_c}{\partial z} - \left(\frac{\partial \mathbf{f}_v}{\partial x} + \frac{\partial \mathbf{g}_v}{\partial y} + \frac{\partial \mathbf{h}_v}{\partial z} \right) = \mathbf{s} , \quad (\text{B.45})$$

where the flux vectors are divided into convective and viscous parts and a source term \mathbf{s} appears on the right hand side because of the turbulence model, i.e.

$$\mathbf{q} = \begin{pmatrix} \rho \\ \rho u \\ \rho v \\ \rho w \\ \rho E \\ \rho k \\ \rho \omega \end{pmatrix} , \quad \mathbf{f}_c = \begin{pmatrix} \rho u \\ \rho u^2 + p \\ \rho uv \\ \rho uw \\ \rho uH \\ \rho uk \\ \rho u\omega \end{pmatrix} , \quad \mathbf{g}_c = \begin{pmatrix} \rho v \\ \rho v^2 + p \\ \rho vw \\ \rho vH \\ \rho vk \\ \rho v\omega \end{pmatrix} , \quad \mathbf{h}_c = \begin{pmatrix} \rho w \\ \rho w^2 + p \\ \rho wv \\ \rho wH \\ \rho wk \\ \rho w\omega \end{pmatrix} ,$$

$$\mathbf{f}_v = \begin{pmatrix} 0 \\ \tau_{xx} \\ \tau_{xy} \\ \tau_{xz} \\ u\tau_{xx} + v\tau_{xy} + w\tau_{xz} - q_x \\ \mu_k k_x \\ \mu_\omega \omega_x \end{pmatrix} , \quad \mathbf{g}_v = \begin{pmatrix} 0 \\ \tau_{yx} \\ \tau_{yy} \\ \tau_{yz} \\ u\tau_{yx} + v\tau_{yy} + w\tau_{yz} - q_y \\ \mu_k k_y \\ \mu_\omega \omega_y \end{pmatrix} , \quad (\text{B.46})$$

$$\mathbf{h}_v = \begin{pmatrix} 0 \\ \tau_{zx} \\ \tau_{zy} \\ \tau_{zz} \\ u\tau_{zx} + v\tau_{zy} + w\tau_{zz} - q_z \\ \mu_k k_z \\ \mu_\omega \omega_z \end{pmatrix} , \quad \mathbf{s} = \begin{pmatrix} 0 \\ 0 \\ 0 \\ 0 \\ 0 \\ \rho P - \rho \beta^* k \omega \\ \rho \alpha \frac{\omega}{k} P - \rho \beta \omega^2 \end{pmatrix} ,$$

where turbulence production term P is defined in Eq. B.37 and

$$k_x = \frac{\partial k}{\partial x}, \quad k_y = \frac{\partial k}{\partial y}, \quad k_z = \frac{\partial k}{\partial z},$$

$$\mu_k = \mu + \sigma^* \mu_T, \tag{B.47}$$

$$\mu_\omega = \mu + \sigma \mu_T.$$

The components of shear stress and heat flux are already defined in Eq. B.3, with only difference that the coefficient of dynamic viscosity μ have to be replaced everywhere by effective viscosity μ_{eff}

$$\mu_{eff} = \mu + \mu_T, \tag{B.48}$$

where μ is the molecular viscosity and μ_T is the turbulent viscosity defined by Eq. B.30 for the single-phase k - ω model.

B.4.3 Discussion about Two-phase Turbulence Modeling

As mentioned earlier, currently only single-phase turbulence modeling is implemented in **CATUM**. A two-phase turbulence modeling for cavitating flows is planned for future versions of the code. This section discusses briefly the two-phase turbulence modeling strategies that are encountered in the literature and that are used by other research groups.

Similar to the single-phase flows, the most frequently used turbulence models in cavitating flows are also two equation models that are based on the Boussinesq eddy viscosity approach [59], [127], [137]. In these models the molecular viscosity of the mixture μ_m is calculated through the convex combination of the vapor and the liquid viscosities by using the void fraction α as

$$\mu_m = \alpha \cdot \mu_{vap} + (1 - \alpha) \cdot \mu_{liq}. \tag{B.49}$$

Wang et al. [127] implemented a k - ϵ turbulence model with wall functions to calculate cavitating flows. They also modified the original empirical model constants for the two-phase formulation. Whereas, Kunz et al. [59] used a standard k - ϵ model in their calculations of cavitating flows.

The two equation models, which are developed for single-phase flows, have a tendency to overestimate viscous effects in two-phase regions. Therefore, they need empirical corrections to model parameters [127], [137]. These corrections mainly account for lowering the eddy viscosity of the mixture region with high gas or vapor contents. Yuan and Schnerr [137] implemented the original single-phase version of the k - ω turbulence model with wall functions to calculate the cavitating flows in injection nozzles. Subsequently, they modified the turbulent viscosity definition with a density dependent function as introduced by Coutier-Delgosha et al. [23], which results in a lower turbulent viscosity in two-phase region and therefore viscous effects are scaled correctly in two-phase domains.

In a recent investigation Huuva [46] used LES to calculate cavitating flows around hydrofoils and compared its results with RANS calculation. In this research he didn't

introduce any additional explicit length scales and modifications in the LES formulation and used the mixture viscosity definition as given by Eq. B.49. It is concluded in the research that LES is advantageous over RANS calculations as it is able to predict both the average and the instantaneous flow field with better accuracy but it still needs more understanding especially in the case of two-phase modeling.

As a result, most of the efforts to calculate cavitating flows with turbulence models are based on the current models for single-phase flows with empirical or problem dependent corrections. Therefore, turbulence modeling for cavitating flows is still an uncertain area because to date, no model has been evaluated against well-established experimental evidences [127].

B.4.4 Diffusive Flux Calculation

The convective fluxes are calculated according to chapter 3 with the addition of two new transport equations for turbulent kinetic energy k and specific dissipation rate ω . The diffusive fluxes on the other hand, need a different consideration as gradients of the flow variables appear in the transport equations. They are calculated by using the method of help cells, which is demonstrated by the grey volume Ω_{help} in Fig. B.1 for the fluxes in x -direction.

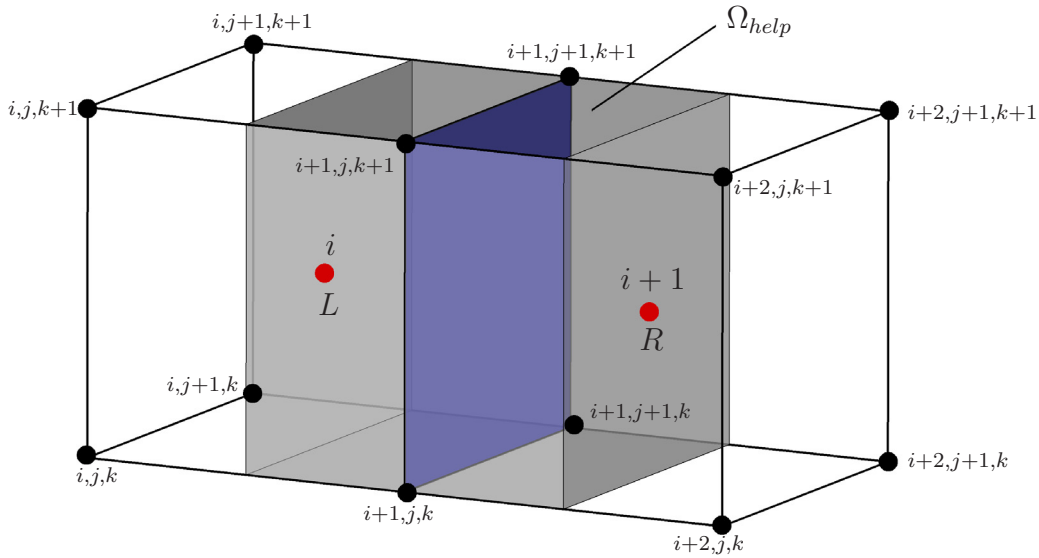


Figure B.1: Discretization of the 3-D numerical domain for diffusive fluxes. The gradients are calculated using help cell (grey volume).

The gradients at the interface surface $(i+1/2)$ -blue surface- between the computational cells are calculated according to the Green's formula. For any flow variable ϕ

$$\left(\frac{\partial \phi}{\partial x}\right)_{i+1/2,j} = \frac{1}{\Omega_{help}} \int_{\Omega_{help}} \frac{\partial \phi}{\partial x} d\Omega_{help} = \frac{1}{\Omega_{help}} \int_{\Gamma_{help}} \phi dS_x \quad (\text{B.50})$$

gives its gradient in the x -direction. The surface integral on the right hand side is evaluated for every surface of the help cell using the x -normal of the surface. The gradients of the variables in y and z -directions are calculated similarly by using the help cells in the corresponding directions.

The turbulence production term P given by Eq. B.37 also includes the gradients of the velocity components. But this time they must be evaluated not on the cell faces but at the cell center. Therefore, help cells are not needed and Eq. B.50 is evaluated directly for the considered computational cell.

B.4.5 Boundary Conditions

The boundary conditions in viscous flows are also calculated according to section 3.6 of chapter 3 by using two ghost-cells in every direction. The only difference is the no-slip boundary conditions for the viscous solid walls, where all velocity components reduce to zero. According to Fig. 3.7 the values at the ghost-cells are given as

$$\begin{aligned}
 \rho_{i,2} &= \rho_{i,3} \\
 \mathbf{v}_{i,2} &= -\mathbf{v}_{i,3} \\
 p_{i,2} &= p_{i,3} \\
 \rho_{i,1} &= \rho_{i,4} \\
 \mathbf{v}_{i,1} &= -\mathbf{v}_{i,4} \\
 p_{i,1} &= p_{i,4} .
 \end{aligned} \tag{B.51}$$

Moreover, turbulent kinetic energy and specific dissipation rate in the ghost-cells are calculated from Wilcox [131] as

$$\begin{aligned}
 k_{i,2} &= -k_{i,3} \\
 \omega_{i,2} &= \omega_{i,2} = \frac{6}{\beta_0} \frac{\mu}{\rho y_3^2} ,
 \end{aligned} \tag{B.52}$$

and

$$\begin{aligned}
 k_{i,1} &= -k_{i,4} \\
 \omega_{i,1} &= \omega_{i,4} = \frac{6}{\beta_0} \frac{\mu}{\rho y_4^2} ,
 \end{aligned} \tag{B.53}$$

where y_3 and y_4 are the cell center distances of cells $(i, 3)$ and $(i, 4)$ to the considered wall.

B.5 Test Case Calculations for Single-phase Ideal Gas Flows

To verify the implementation of the viscous effects into the code several standard test calculations are performed. First, laminar case is considered to see if the diffusive fluxes are correctly calculated. Thus, a laminar flat plate flow is performed and compared with the analytical solution. Then, the turbulence model is verified through a turbulent plate simulation and 2-D transonic flow over RAE 2822 airfoil.

B.5.1 Laminar Flat Plate

The laminar flat plate flow is a standard test case to verify the calculation of laminar viscous effects. In this calculation a subsonic parallel flow with $M_\infty = 0.3$ and $Re_l = 10^5$ is considered. Figure B.2 depicts the flow geometry, where the solid wall starts at $x = 0$. The figure is not drawn to scale and the upper wall is twice the plate length away from the lower boundary. The mesh used in the calculation consists of 55×55 cells, which are refined on the plate and at the stagnation point $x = 0$.

The calculated dimensionless velocity profile u/u_∞ is compared with the Blasius solution [99].

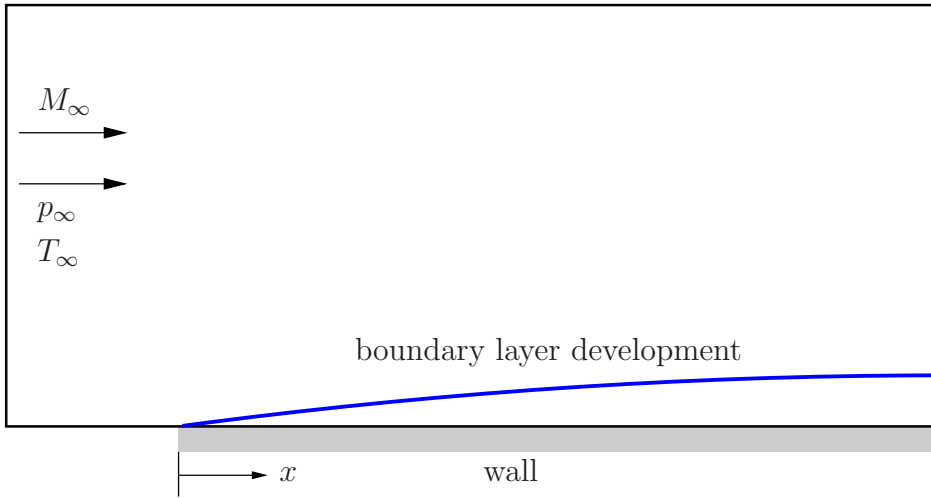


Figure B.2: The sketch of the flow domain used in boundary layer calculations.

The wall friction coefficient c_f is also compared with the analytical solution over the flat plate. The local friction coefficient is given by

$$c_f = \frac{\tau_w}{\frac{1}{2}\rho u_\infty^2}, \quad (\text{B.54})$$

where τ_w is the wall shear stress defined as

$$\tau_w = \mu \left. \frac{\partial u}{\partial y} \right|_w \quad (\text{B.55})$$

Figure B.3 shows the numerical solution for the velocity profile u/u_∞ and skin friction coefficient c_f compared with the analytical solution of Blasius [99].

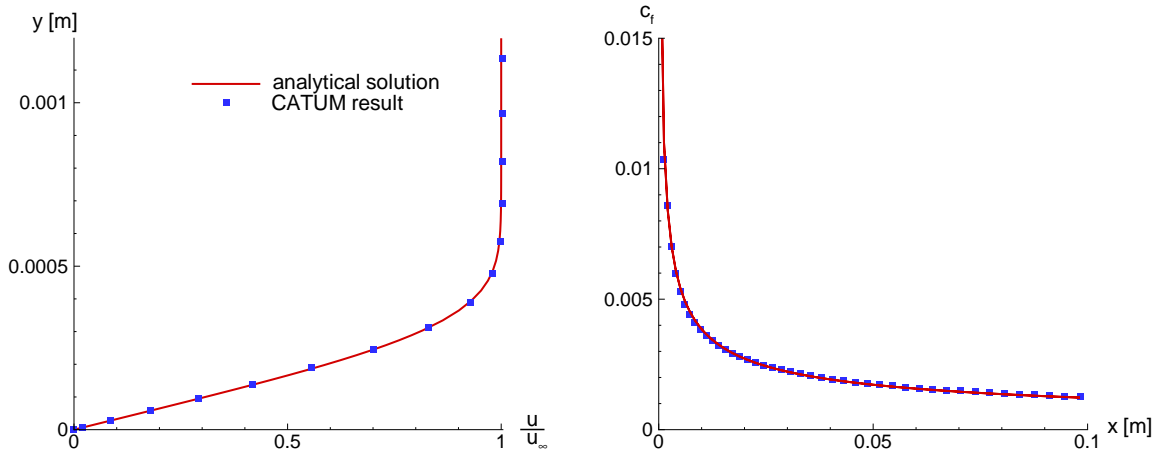


Figure B.3: Laminar flat plate results, velocity profile u/u_∞ (left), skin friction coefficient c_f (right). Red line: analytical solution of Blasius [99], blue dots: **CATUM** calculation.

It is clear from the figures that the laminar flat plate results fit very good with the analytical solution.

B.5.2 Turbulent Flat Plate

As implementation of turbulence model equations is cumbersome and relatively complicated, it is very likely that errors can occur during coding. Therefore, turbulence modeling of a CFD code have to be tested carefully. Similar to the laminar case, a turbulent flow over a flat plate is chosen as a first test case. The flow field is similar to the laminar case given by Fig B.2 but with different scaling. The reference calculation and the mesh is taken from “Computational Fluid Dynamics Validation and Verification Web Page” of NPARC Alliance [80]. The flow conditions are given as $M_\infty = 0.2$, $p_\infty = 1 \text{ bar}$, $T_\infty = 294.44 \text{ K}$ and the length of the flat plate is $l = 5.089 \text{ m}$. The calculation is performed by using $k - \omega$ turbulence model with an initial turbulence intensity of $Tu = 5\%$ and $\mu_T = 10\mu$. Following figure shows the skin friction coefficient c_f over the flat plate compared with the experiment of Wieghardt [130]. The flat plate length is non-dimensionalized by using the Reynolds number as

$$Re_x = \frac{\rho_\infty u_\infty x}{\mu_\infty}. \quad (\text{B.56})$$

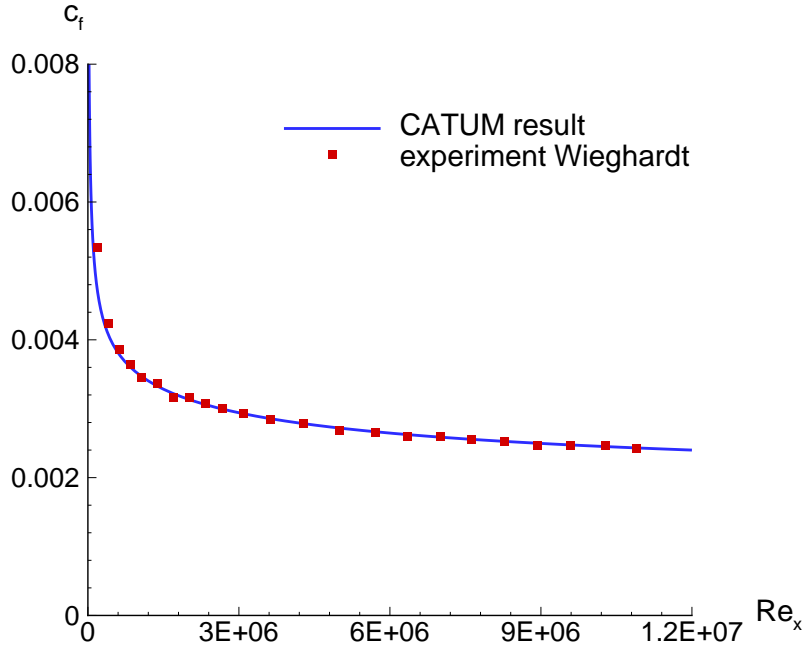


Figure B.4: Turbulent flat plate result, skin friction coefficient c_f . Red points: experiment of Wieghardt [130], blue line: **CATUM** calculation.

The agreement between the calculation and the experimental data shows that the k - ω turbulence model correctly predicts the flow characteristics.

B.5.3 RAE 2822 Airfoil

As a second verification test case, transonic flow over RAE 2822 airfoil is considered. This configuration is a classical test case for external flow calculations and the experimental data is available [22]. The geometry and the reference data are again taken from the NPARC Alliance web site [80]. Figure B.5 depicts the flow domain and the mesh used in the calculation with an enlarged view over the airfoil. The mesh corresponds to a $y^+ \approx 1$ with 15-20 mesh points inside the boundary layer and therefore, turbulence model equations are integrated to the wall without any need for wall functions.

The experimental values are corrected and specified in the NPARC Alliance site [80] as

Table B.1: Flow conditions for the RAE 2822 test case, chord length $c = 0.1$ m.

Mach number	angle of attack	Reynolds number
$M_\infty = 0.729$	$\alpha = 2.31^\circ$	$Re_{c,\infty} = 6.5 \cdot 10^6$

These conditions correspond to case 6 of the experiments performed by Cook [22]. Figure B.6 compares the measured pressure coefficient c_p with the numerical results, where

$$c_p = \frac{p - p_\infty}{\frac{1}{2}\rho_\infty u_\infty^2}. \quad (\text{B.57})$$

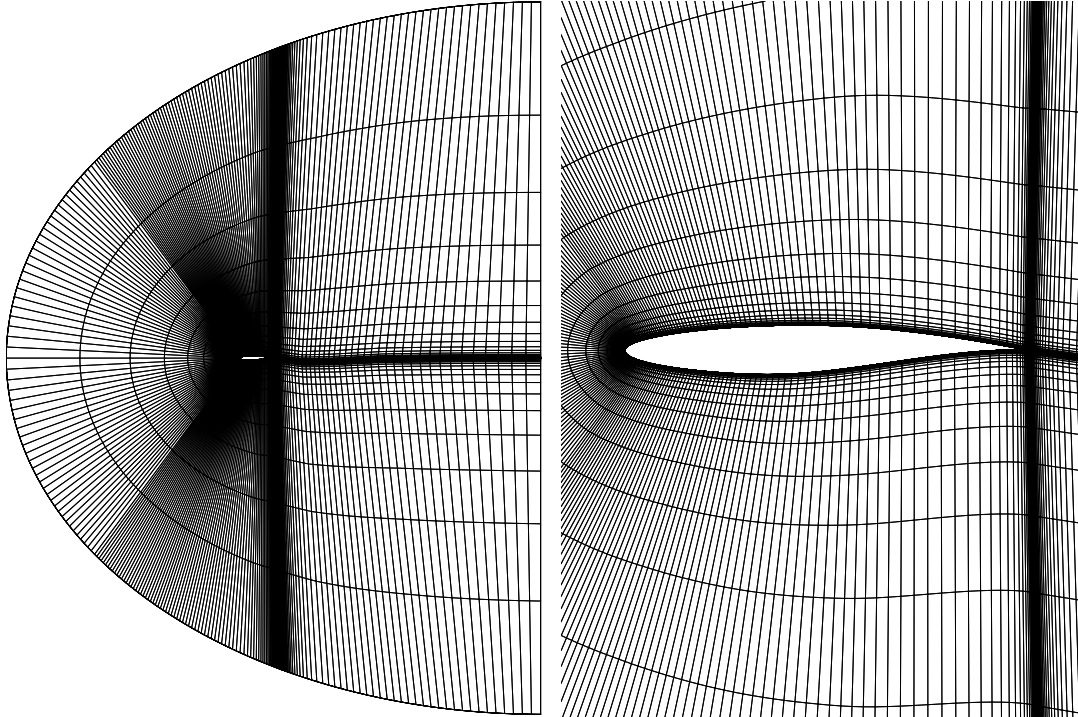


Figure B.5: RAE 2822 flow domain and mesh with 349×40 cells (left). Closeup view of the airfoil (right). $y^+ \approx 1$.

The comparison also includes two calculations from the NPARC site [80], where NASA NPARC and WIND codes are used (green and black lines respectively). The blue line corresponds to the current calculation with $k - \omega$ turbulence model, whereas NASA calculations are performed by using Spalart-Allmaras model [114].

The current calculation is started as turbulent from the beginning. Therefore, the leading edge compression is underestimated (effect 1), which is mainly due to the laminar separation around the leading edge. From the comparison it can be seen that all calculations follow the same trend on the suction side and they fall below the experimental values (effect 2). The shock location is best caught by the **CATUM** calculation (effect 3) but the trailing edge separation is also underestimated in our calculation (effect 4).

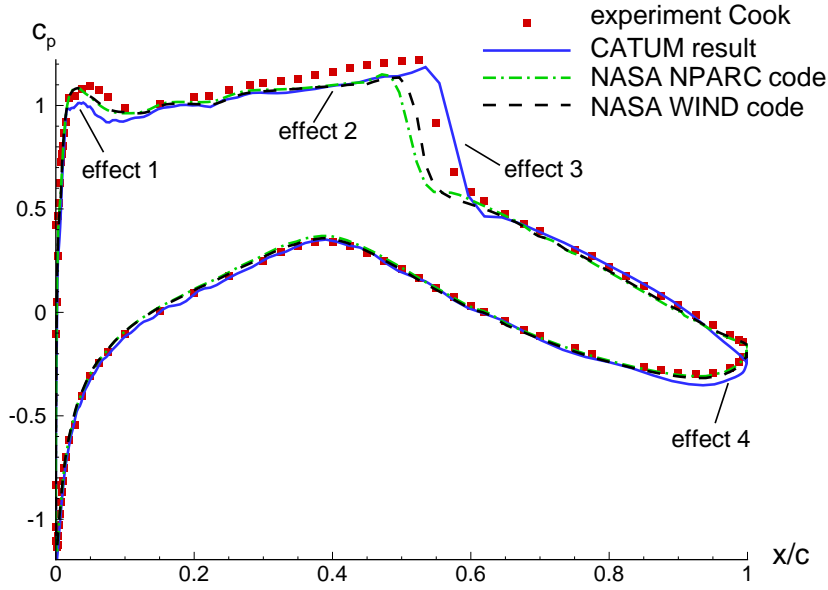


Figure B.6: Pressure coefficients over the RAE 2822 airfoil.

B.6 Outlook

In this chapter the extension of **CATUM** for viscous flow calculations is introduced. In the current development state **CATUM** is able to simulate **single-phase** compressible laminar and turbulent ideal gas flows. As a turbulence model two equation $k - \omega$ turbulence model is implemented and verified. Additionally, Lauer [63] has extended the turbulence modeling capability of **CATUM** through the Wilcox Stress- ω Reynolds-stress model.

As shown in the previous sections, the preliminary results of viscous flow calculations for laminar and turbulent boundary layers and turbulent RAE 2822 airfoil calculation are satisfactory. But as the formulation is still in the development phase, additional tests are needed.

It should be noted that the current implementation considers only single-phase ideal gas flow. As discussed in section B.4.3 extension of the current model to two-phase cavitating flow is possible with some corrections to the model parameters.

Hence, completing and verifying the viscous formulation for two-phase cavitating flows should be the next enhancement in **CATUM**, as a single-phase ideal gas version has already been implemented. As already mentioned, one important difficulty in such a formulation is that a widely applicable and accepted two-phase turbulence model does not exist and the existing ones should be tuned according to the cavitating flow in consideration. This step needs an extensive literature survey and well documented validation test cases.

Appendix C

CATUM Manual

This section is included to give an overview of the internal structure of the **CATUM** and to explain how to setup a run and start the simulation.

CATUM is developed initially for 3-D single block structured grids using FORTRAN 90 language. Afterwards, it is parallelized as multi block structured via MPI libraries by Thalhamer [116]. Both serial and parallel versions of the code can run under Windows and Linux operating systems and in Linux clusters. The details of the parallelization and parallel run setup can be found in the mentioned work.

As already discussed in chapter 3, the flow domain consists of non-overlapping hexahedra cells in ijk order. The ijk ordering of the flow domain is the necessary condition for structured grids and each index corresponds to a cartesian coordinate direction, i.e. $i \rightarrow x$, $j \rightarrow y$ and $k \rightarrow z$. Following figure is repeated here to explain the geometry calculation procedure inside the code.

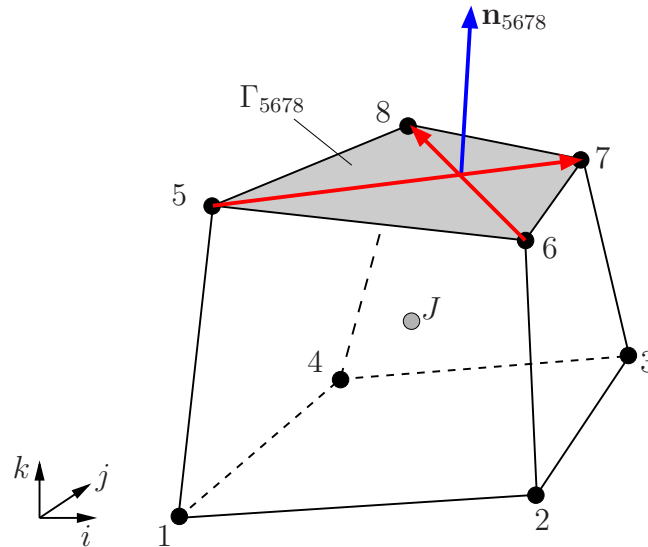


Figure C.1: Surface area of Γ_{5678} and corresponding normal vector \mathbf{n}_{5678} .

The normal vectors are named according to the direction of the surfaces, i.e. $i \rightarrow \xi$, $j \rightarrow \eta$ and $k \rightarrow \zeta$. Therefore the normal vector \mathbf{n}_{5678} of the given surface can be written as

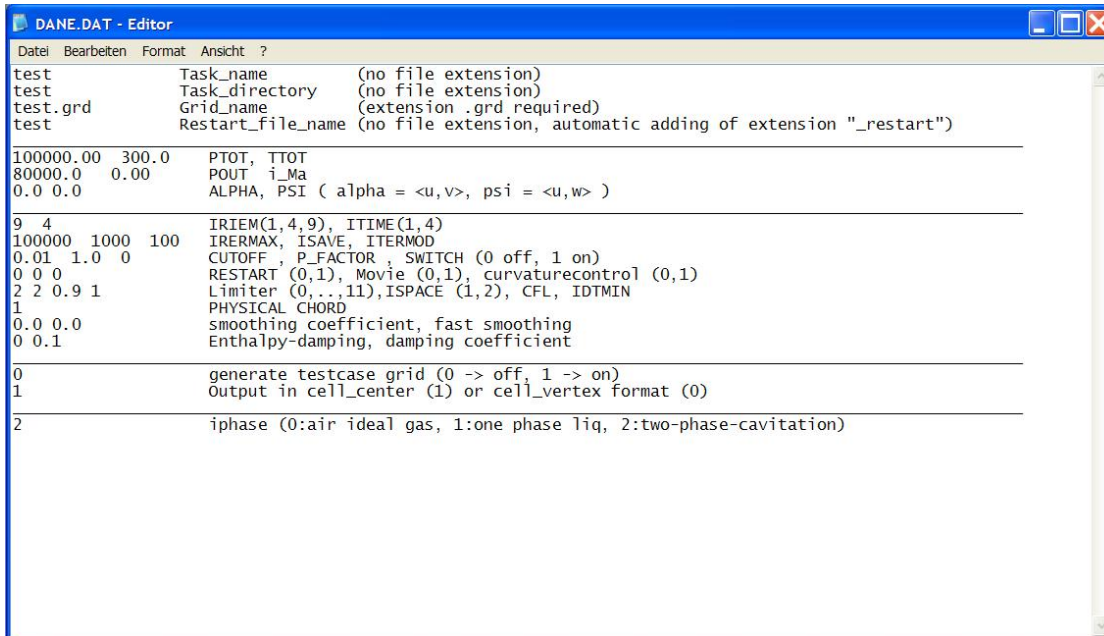
$$\mathbf{n}_{5678} = \boldsymbol{\zeta}_{5678} = \frac{\mathbf{x}_{68} \times \mathbf{x}_{57}}{\|\mathbf{x}_{68} \times \mathbf{x}_{57}\|} = \zeta_x \mathbf{i} + \zeta_y \mathbf{j} + \zeta_z \mathbf{k}, \quad (\text{C.1})$$

where ζ_x , ζ_y and ζ_z are the components of the normal vector in the corresponding spatial directions. Similarly, the normal vectors of the surfaces Γ_{2367} and Γ_{3478} are given by

$$\begin{aligned} \mathbf{n}_{2367} &= \boldsymbol{\xi}_{2367} = \xi_x \mathbf{i} + \xi_y \mathbf{j} + \xi_z \mathbf{k}, \\ \mathbf{n}_{3478} &= \boldsymbol{\eta}_{3478} = \eta_x \mathbf{i} + \eta_y \mathbf{j} + \eta_z \mathbf{k}. \end{aligned} \quad (\text{C.2})$$

The volume of each control volume is calculated according to the method described in chapter 3. The geometry calculation is performed in the subroutine “new_geo”.

CATUM requires two input files to start a simulation. One is the data file that defines the settings of the run and the other one is the grid file that defines the geometry. The data file is named as DANE.DAT and has the following structure.



```

DANE.DAT - Editor
Datei Bearbeiten Format Ansicht ?
test Task_name (no file extension)
test Task_directory (no file extension)
test.grd Grid_name (extension .grid required)
test Restart_file_name (no file extension, automatic adding of extension "_restart")
-----
100000.00 300.0 PTOT, TTOT
80000.0 0.00 POUT i_Ma
0.0 0.0 ALPHA, PSI ( alpha = <u,v>, psi = <u,w> )
-----
9 4 IRIEM(1,4,9), ITIME(1,4)
100000 1000 100 IRERMAX, ISAVE, ITERMOD
0.01 1.0 0 CUTOFF, P_FACTOR, SWITCH (0 off, 1 on)
0 0 0 RESTART (0,1), Movie (0,1), curvaturecontrol (0,1)
2 2 0.9 1 Limiter (0,...,11), ISPACE (1,2), CFL, IDTMIN
1 PHYSICAL CHORD
0.0 0.0 smoothing coefficient, fast smoothing
0 0.1 Enthalpy-damping, damping coefficient
-----
0 generate testcase grid (0 -> off, 1 -> on)
1 Output in cell_center (1) or cell_vertex format (0)
-----
2 iphase (0:air ideal gas, 1:one phase liq, 2:two-phase-cavitation)

```

Figure C.2: Input data file DANE.DAT, that defines the settings of the run.

The details of each input line is as follows:

- Line 1: Name of the run (output file is created using this name).
- Line 2: Name of the directory that will be created for the results.
- Line 3: Name of the grid file with extension.
- Line 4: Restart file name if the run is restarted from a previous solution.
- Line 5: The total pressure [Pa] and the total temperature [K] at the inlet.

- Line 6: The static pressure at the outlet [Pa] and inlet Mach number.
- Line 7: The angle of attack and the yaw angle, used for airfoil and wing calculations.
- Line 8: Solver scheme (1: AUSM, 4: HLLC, 9: Hybrid solver) and time integration scheme (1: First order time integration, 4: 4 stage Runge-Kutta method)
- Line 9: Maximum number of iterations, save frequency of the restart file, display frequency of the residual and time step on the screen.
- Line 10: Not used in the current version.
- Line 11: Flag to control if the run will be restarted from a previous solution (0: new run, 1: restart), flag that controls if movie data will be saved (0: no movie data, 1: movie data), flag to switch on curvature corrected wall boundaries (0: no curvature correction, 1: curvature correction).
- Line 12: Limiter function for higher order reconstruction (1: van Albada limiter, 2: van Leer limiter, 3: minmod limiter, 4: superbee limiter, 5: MC limiter), order of the space discretization (1: first order, 2: higher order with limiters), CFL number, flag to control local or global time stepping (0: local time stepping, 1: global time stepping).
- Line 13: Reference length of the problem [m], used in viscous calculations to non-dimensionalize the lengths.
- Line 14: Not used in the current version.
- Line 15: Not used in the current version.
- Line 16: **CATUM** includes a simple grid generator. This feature can be activated by using this flag (0: normal run, 1: grid generator).
- Line 17: The structure of the output file that is written for the TECPLOT program (default value is 1).
- Line 18: Flag that controls the fluid type (1: air as an ideal gas, 2: single-phase liquid water, 2: two-phase water flow with cavitation).

The second input file defines the computational domain by including the coordinates of the grid points in a ordered way. The name of the grid file and the extension should be the same as the one given on line 3 of the DANE.DAT file (see Fig. C.2). The structure of the grid file is depicted in Fig. C.4. The first line contains the maximum grid number at each spatial direction, i.e. i_{max} , j_{max} and k_{max} . Starting with the second line x , y and z coordinates of the grid points are written in ijk order (in meters). For 2-D domains two k -planes are needed for the solver to construct a control volume, i.e. $k_{max} = 2$ for 2-D calculations. To demonstrate the read and write structure of the coordinate points, following pseudo-code can be used.

```

DO K=1,kmax
DO J=1,jmax
DO I=1,imax
      READ(1,*) X(I,J,K),Y(I,J,K),Z(I,J,K)
ENDDO
ENDDO
ENDDO

```

```

189 25 2
-2.000000095E-003 -1.000000047E-003 0.000000000E+000
-1.916500041E-003 -1.000000047E-003 0.000000000E+000
-1.833250048E-003 -1.000000047E-003 0.000000000E+000
-1.750000054E-003 -1.000000047E-003 0.000000000E+000
-1.666750060E-003 -1.000000047E-003 0.000000000E+000
-1.583499950E-003 -1.000000047E-003 0.000000000E+000
-1.500000013E-003 -1.000000047E-003 0.000000000E+000
-1.416499959E-003 -1.000000047E-003 0.000000000E+000
-1.333249966E-003 -1.000000047E-003 0.000000000E+000
-1.249999972E-003 -1.000000047E-003 0.000000000E+000
-1.166749978E-003 -1.000000047E-003 0.000000000E+000
-1.083499985E-003 -1.000000047E-003 0.000000000E+000
-9.94000018E-004 -9.95000132E-004 0.000000000E+000
-9.045000188E-004 -9.909999790E-004 0.000000000E+000
-8.167499909E-004 -9.749999736E-004 0.000000000E+000
-7.290000212E-004 -9.590000263E-004 0.000000000E+000
-6.559999892E-004 -9.32499992E-004 0.000000000E+000
-5.830000155E-004 -9.059999720E-004 0.000000000E+000
-5.235000281E-004 -8.740000194E-004 0.000000000E+000
-4.640000116E-004 -8.420000086E-004 0.000000000E+000
-4.162500263E-004 -8.07499978E-004 0.000000000E+000
-3.685000120E-004 -7.730000070E-004 0.000000000E+000
-3.302500118E-004 -7.387499791E-004 0.000000000E+000
-2.920000115E-004 -7.045000093E-004 0.000000000E+000
-2.617500140E-004 -6.717499928E-004 0.000000000E+000
-2.315000020E-004 -6.389999762E-004 0.000000000E+000
-2.077500103E-004 -6.082499749E-004 0.000000000E+000
-1.840000041E-004 -5.774999736E-004 0.000000000E+000
-1.652500068E-004 -5.492499913E-004 0.000000000E+000
-1.464999950E-004 -5.210000090E-004 0.000000000E+000
-1.320000010E-004 -4.954999895E-004 0.000000000E+000
-1.174999998E-004 -4.69999990E-004 0.000000000E+000
-1.062500014E-004 -4.469999985E-004 0.000000000E+000

```

Figure C.3: Structure of the computational grid file. The name of the grid file is specified in the input file.

As described in chapter 3, **CATUM** includes four kinds of boundary conditions, which are named as inlet, outlet, periodic and wall boundaries. All of these boundary condition types are included in the code for every spatial direction. In the current version the boundary condition settings are not parameterized through the input files. Therefore, the code should be modified according to the flow problem that is going to be solved and then should be compiled with the given boundary conditions. All the possible boundary condition functions are included in the “ghost_cells” subroutine. Automation of this selection process through the input file is thought to be one of the next steps in the code development. Once the executable or the binary file is created, **CATUM** can be started in a directory where all the input files and the executable are present. During the run the residual and time steps can be monitored through the terminal screen and the data file can be plotted after each save sequence.

CATUM results are post-processed by using **TECPLOT** program developed by Tecplot Inc. [115]. The output data is written by employing the point structured data format as explained in the **TECPLOT** manual.

A simplified flow diagram of **CATUM** is presented in the following figure.

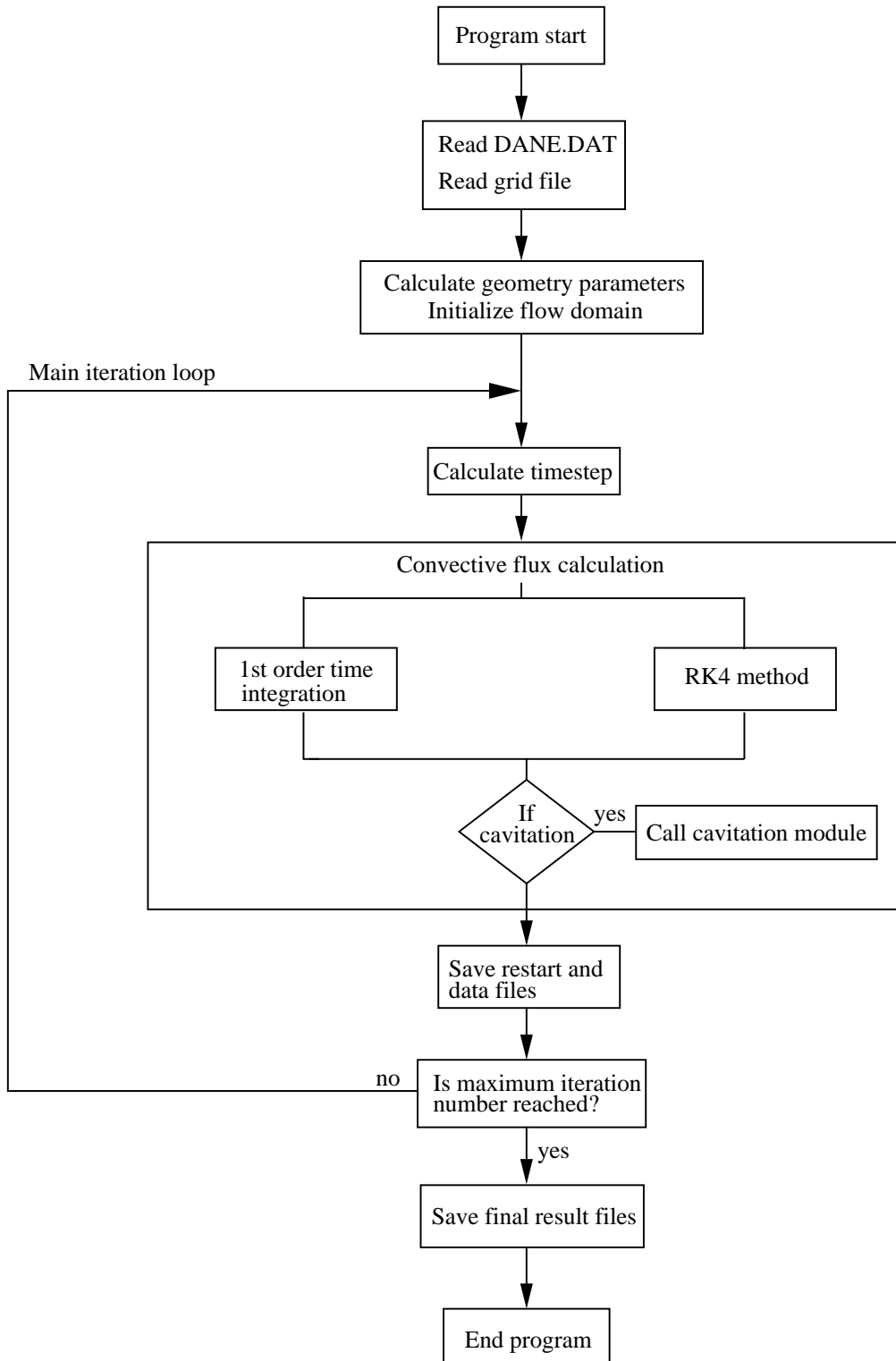


Figure C.4: A simplified flow diagram of CATUM.

C.1 Single-phase Inviscid Ideal Gas Calculation

In this section a single-phase ideal gas calculation will be demonstrated. For that purpose we consider a supersonic air flow over a 2-D circular arc geometry as shown in the following figure.

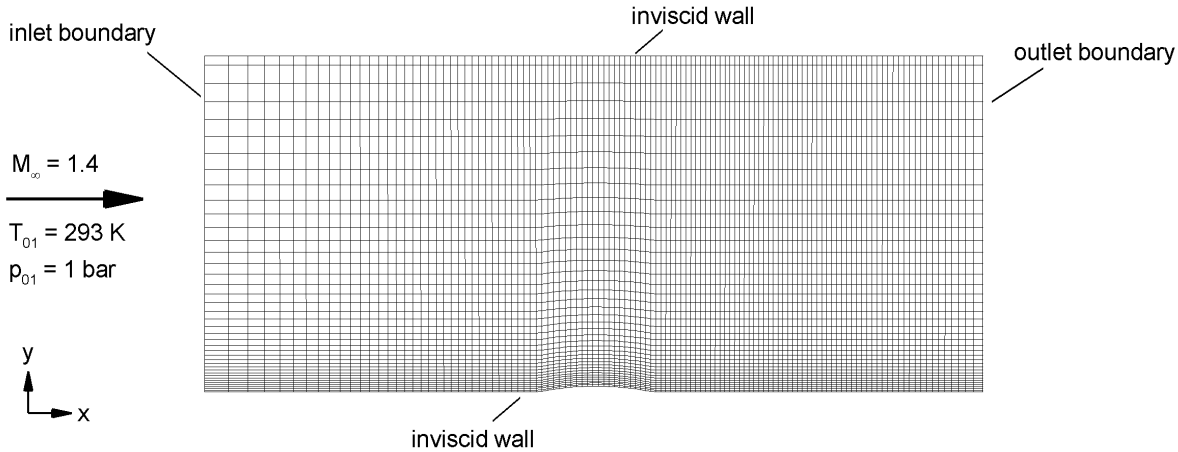


Figure C.5: Computational mesh for the circular arc calculation. Thickness parameter $\tau = 0.1$. 240x80 grid points (every two mesh line is depicted in the figure).

The computational mesh is generated separately and written in a format that **CATUM** can read. The format of the mesh file is given in the previous section. For this example we assume an inlet Mach number of $M_\infty = 1.4$, the inlet total temperature $T_{01} = 293\text{ K}$ and the inlet total pressure $p_{01} = 1\text{ bar}$.

```

DANE_example1.DAT - Editor
Datei Bearbeiten Format Ansicht ?
bump2D      Task_name      (no file extension)
bump2D      Task_directory (no file extension)
bump2D.grd  Grid_name      (extension .grd required)
bump2D      Restart_file_name (no file extension, automatic adding of extension "_restart")
-----
100000.00  293.0    PTOT, TTOT
100000.0  1.40    POUT i_Ma
0.0 0.0    ALPHA, PSI ( alpha = <u,v>, psi = <u,w> )
-----
4 4      IRIEM(1,4,9), ITIME(1,4)
100000 1000 100  IRERMAX, ISAVE, ITERM0D
0.01 1.0 0    CUTOFF , P_FACTOR , SWITCH (0 off, 1 on)
0 0 0      RESTART (0,1), Movie (0,1), curvaturecontrol (0,1)
3 2 1.3 0    Limiter (0,...11), ISPACE (1,2), CFL, IDTMIN
1          PHYSICAL CHORD
0.0 0.0    smoothing coefficient, fast smoothing
0 0.1      Enthalpy-damping, damping coefficient
-----
0          generate testcase grid (0 -> off, 1 -> on)
1          output in cell_center (1) or cell_vertex format (0)
-----
0          jiphase (0:air ideal gas, 1:one phase liq, 2:two-phase-cavitation)

```

Figure C.6: Input data file DANE.DAT for single-phase circular arc calculation.

Figure C.6 shows the input data file DANE.DAT for this calculation. It can be seen from the figure that we choose HLLC Riemann solver and 4-stage Runge-Kutta method

(line 8) with second order space discretization using *minmod* limiter (line 12). The inlet Mach number is given as $M_\infty = 1.4$ (line 6). The inlet total pressure and the inlet total temperature are set to $p_{01} = 1 \text{ bar}$ and $T_{01} = 293 \text{ K}$ respectively (line 5). The calculation uses a *CFL* number of 1.3 and local time stepping algorithm as we are interested in the steady state solution (line 12). Finally, air is set as the working fluid in line 18.

Following Fig. C.4 the boundary conditions should be set manually in the subroutine “ghost_cells” as mentioned earlier. From the geometry, $x = 0$ plane corresponds to the inlet and $x = x_{max}$ plane corresponds to the outlet. Therefore for $i = 1$ plane supersonic inlet boundaries (where the flow variables are prescribed) should be switched on and for $i = i_{max}$ plane standard outlet boundary condition can be used (where pressure is either interpolated from inside for supersonic outflow or pressure outlet condition is imposed when the outflow is subsonic). Inviscid wall boundary condition is chosen for $j = 1$ and $j = j_{max}$ planes. As this is a 2-D calculation the solver does not calculate fluxes in z direction, therefore it is not needed to set any boundary conditions for k -planes. After the boundary conditions are correctly set in the solver, the program should be compiled and linked accordingly and then the binary file can be executed. A converged steady state solution is obtained after 5000 iterations and following figure depicts the Mach number contours plotted by using the TECPLOT program (note that solution domain is mirrored with respect to the x -axis).

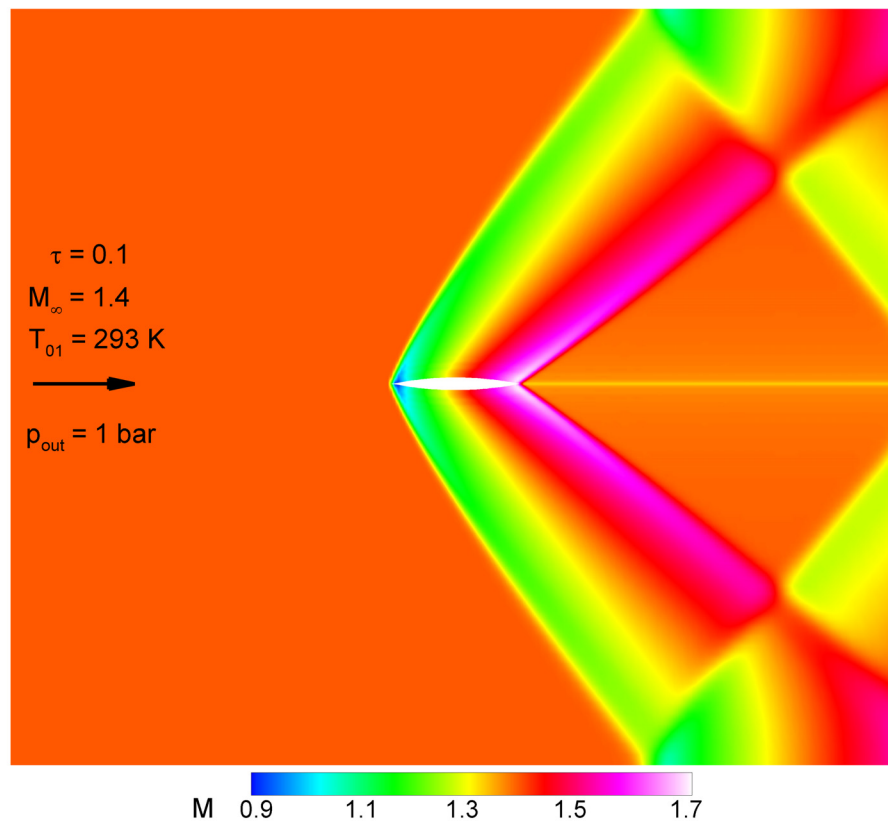


Figure C.7: Mach number contours, circular arc $\tau = 0.1$, $M_\infty = 1.4$, $T_{01} = 293 \text{ K}$ and $p_{out} = 1 \text{ bar}$. Solution is mirrored with respect to the x -axis.

C.2 Single-phase Inviscid Liquid Water Calculation

The second simulation example considers a single-phase steady state liquid flow over a 2-D NACA 0015 hydrofoil. This hydrofoil geometry is the same one that was already introduced in chapter 5 for the two-phase calculation. The following figure shows the computational mesh and the flow conditions.

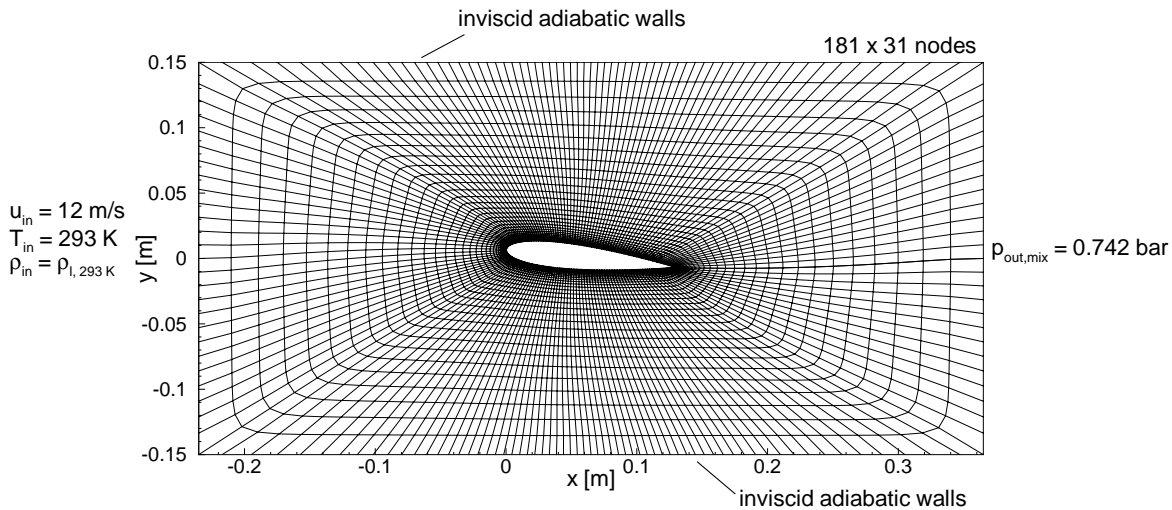


Figure C.8: 2-D NACA 0015 hydrofoil - computational domain and boundary conditions. Chord length $c = 0.13 \text{ m}$, angle of attack $\alpha = 6^\circ$, channel height 0.3 m , channel length 0.6 m . Water inflow from left to right, inlet conditions $u_{in} = 12 \text{ m/s}$, $T_{init} = 293 \text{ K}$, outlet condition $p_{out,mix} = 0.742 \text{ bar}$ (see chapter 3).

The input data file is depicted in Fig. C.9.

```

DANE_example2.DAT - Editor
Datei Bearbeiten Format Ansicht ?
2dnaca Task_name (no file extension)
2dnaca Task_directory (no file extension)
2dnaca0015.grd Grid_name (extension .grd required)
2dnaca Restart_file_name (no file extension, automatic adding of extension "_restart")
-----
100000.00 293.0 PTOT, TTOT
74200.0 1.40 POUT i_Ma
0.0 0.0 ALPHA, PSI ( alpha = <u,v>, psi = <u,w> )
-----
9 1 IRIEM(1,4,9), ITIME(1,4)
100000 1000 100 IRERMAX, ISAVE, ITERMOD
0.01 1.0 0 CUTOFF, P_FACTOR, SWITCH (0 off, 1 on)
0 0 0 RESTART (0,1), Movie (0,1), curvaturecontrol (0,1)
0 1 0.7 0 Limiter (0,...,11), ISPACE (1,2), CFL, IDTMIN
1 PHYSICAL CHORD
0.0 0.0 smoothing coefficient, fast smoothing
0 0.1 Enthalpy-damping, damping coefficient
-----
0 generate testcase grid (0 -> off, 1 -> on)
1 Output in cell_center (1) or cell_vertex format (0)
-----
1 iphase (0:air ideal gas, 1:one phase liq, 2:two-phase-cavitation)

```

Figure C.9: Input data file DANE.DAT for single-phase liquid water calculation.

This calculation will serve as a initial condition for the two-phase cavitation simulation that will be discussed in the next section. Therefore, we use a first order accurate scheme in time and space (lines 8 and 12 respectively) and hybrid solver scheme (line 8). For single-phase water and two-phase cavitation calculations the initial conditions should also be set manually inside the source code by modifying the variables u_{init} and $temp_{init}$ in the subroutine “init_and_restart”. As before, the boundary conditions are given in the subroutine “ghost_cells”. The generated mesh has an o-grid structure around the hydrofoil with a periodicity at $i = 1$ and $i = i_{max}$ planes and the airfoil surface corresponds to $j = 1$ boundary, which is set as an inviscid wall in the subroutine. For this type of o-grid domains around hydrofoils, special care is needed for the $j = j_{max}$ boundary, as both inlet/outlet boundaries and upper and lower walls are on this plane. This distinction is made in the program by setting first the complete $j = j_{max}$ plane as an inviscid wall and then correcting the inlet and the outlet portions according to their start and end indices using the function $jNJ_farfield_3$. In this calculation mixed reflecting/non-reflecting inlet and outlet boundary conditions are used for the pressure calculation (see chapter 3).

Figure C.10 depicts the static pressure contours on the hydrofoil. Note that on the suction side “negative pressure” values are encountered, as the modified Tait equation allows for “negative pressures” for single-phase liquid water calculations.

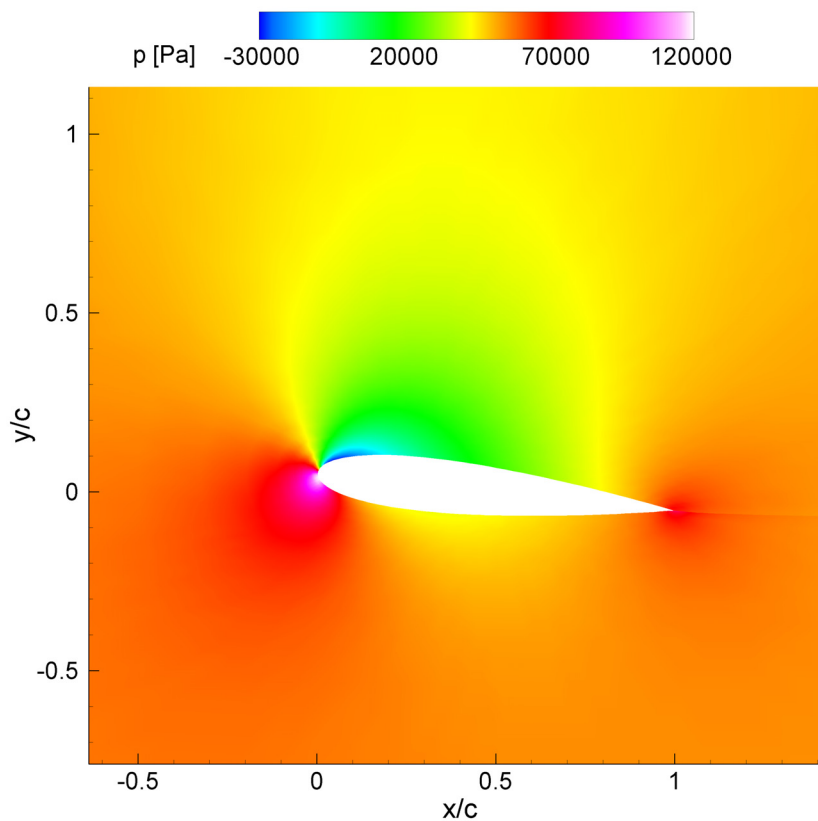


Figure C.10: Pressure contours, 2-D NACA 0015 hydrofoil, **single-phase** water flow, chord length $c = 0.13\text{ m}$, angle of attack $\alpha = 6^\circ$, channel height 0.3 m , channel length 0.6 m . Water inflow from left to right, inlet conditions $u_{in} = 12\text{ m/s}$, $T_{init} = 293\text{ K}$, outlet condition $p_{out,mix} = 0.742\text{ bar}$.

C.3 Two-phase Cavitating Hydrofoil Calculation

In this section we will restart the previous first order single-phase calculation result with switching on the cavitation model and using second order scheme in space and time. The same mesh file is used with the same initial and boundary conditions, so it is not needed to modify anything in the code. Same executable will be started by using the following input data file.

```

DANE_example3.DAT - Editor
Datei Bearbeiten Format Ansicht ?
2dnaca Task_name (no file extension)
2dnaca Task_directory (no file extension)
2dnaca0015.grd Grid_name (extension .grd required)
2dnaca Restart_file_name (no file extension, automatic adding of extension "_restart")

100000.00 293.0 PTOT, TTOT
74200.0 1.40 POUT i_Ma
0.0 0.0 ALPHA, PSI ( alpha = <u,v>, psi = <u,w> )

9 4 IRIEM(1,4,9), ITIME(1,4)
100000 1000 100 IRERMAX, ISAVE, ITERMOD
0.01 1.0 0 CUTOFF, P_FACTOR, SWITCH (0 off, 1 on)
1 1 0 RESTART (0,1), Movie (0,1), curvaturecontrol (0,1)
12 2 0.7 1 Limiter (0,...,11), ISPACE (1,2), CFL, IDTMIN
1 PHYSICAL CHORD
0.0 0.0 smoothing coefficient, fast smoothing
0 0.1 Enthalpy-damping, damping coefficient

0 generate testcase grid (0 -> off, 1 -> on)
1 Output in cell_center (1) or cell_vertex format (0)
2 iphase (0:air ideal gas, 1:one phase liq, 2:two-phase-cavitation)

```

Figure C.11: Input data file DANE.DAT for two-phase cavitating flow calculation. Restart from previous result files.

The hybrid solver and 4-stage Runge Kutta method is used (line 8) together with the second order spatial discretization (line 12). The important modifications in the input file are marked with red circles. As this run will continue from the previous results, the restart flag is set to 1 (line 11). Moreover, as we want to see the **unsteady** results and further post-process them as picture series and movies, movie flag is also set to 1 (line 11). Therefore, at each save frequency a new solution data will be created. In line 12 the **global time stepping** is activated and finally two-phase cavitating flow is set in line 18.

The detailed results of this run are already discussed in chapter 5.2.1 (page 123) with picture series of the unsteady cloud shedding and with the detailed evaluation of the collapse dynamics.